NASA-CR-144886
19790024026

NASA Contractor Report 144886

HiMAT STRUCTURAL DEVELOPMENT DESIGN METHODOLOGY

M. A. Price

Contract NAS4-2560
October 1979

NASA

NASA Contractor Report 144886

HiMAT STRUCTURAL DEVELOPMENT DESIGN METHODOLOGY

M. A. Price
Rockwell International Corporation
Los Angeles, California

Prepared for
Dryden Flight Research Center
under Contract NAS4-2560

National Aeronautics and
Space Administration

1979

FOREWORD

The Phase III HiMAT development was performed at the North American Aircraft Division of Rockwell International, Inc., with L. E. Brown serving as program manager. Contributors to the work reported herein include: Aeroelastic Tailoring, M. A. Price and J. Surdenas; NASTRAN Finite Element Modeling and Sensitivity Studies, D. Kerans; Strain Gage Reduction and Interpretation, J. Lingsweiler and R. Moore; Testing, P. Rogers; Test Data Reduction, D. Kerans, J. Surdenas, J. Lingsweiler, and R. Moore; Flutter Analysis, S. Siegel.

Additional valuable assistance in preparing the report was provided by L. E. Brown, HiMAT Program Manager, E. L. Ruff, HiMAT Engineering Manager, and Dr. L. M. Lackman, Manager of Structures.

Technical assistance by the following is gratefully acknowledged: R. Monaghan and M. DeAngelis of NASA Dryden Flight Research Center; and W. Horsfall and B. Ramsey of Rockwell International.

TABLE OF CONTENTS

TABLE OF CONTENTS - (CONCLUDED)

LIST OF TABLES

LIST OF ILLUSTRATIONS

LIST OF ILLUSTRATIONS - (Continued)

LIST OF ILLUSTRATIONS - (Continued)

LIST OF ILLUSTRATIONS - (Concluded)

HiMAT STRUCTURAL DEVELOPMENT DESIGN METHODOLOGY

By M. A. Price
Rockwell International
North American Aircraft Division
Los Angeles, California

SUMMARY

In order to verify the analytical tools and development techniques used for aeroelastically tailored lifting surfaces, one of the NASA/Rockwell International highly maneuverable advanced technology (HiMAT) aircraft was subjected to an 8g ground test. The comparison of the test results to predicted values indicates that methods are available to adequately predict twist under all loading conditions, provided the material property values are accurately known.

The aircraft, which has approximately 95 percent of the entire outer surface constructed of graphite-epoxy materials, was subjected to a distributed load representing the 8g flight condition. Measurements of wing and canard deflections were taken and twists calculated. These calculated test twists were compared to the predicted twists from the finite element model of the entire aircraft.

The test indicated that the matrix dominated layups used on the wing produced nonlinearities, especially in the transverse coupling term. This nonlinearity adversely affects data reduction of the stresses and correlation with predicted results. Additional testing indicates that stresses are highly sensitive to material property data, and nonlinearity regions are encountered at lower strain levels than previously assumed. Also, the compression modulus enters the nonlinearity region at lower strain levels than the tension modulus.

INTRODUCTION

Rockwell International, under a contract from NASA/Dryden Flight Research Center (DFRC), developed two remotely piloted research vehicles in order to investigate the highly maneuverable aircraft technology (HiMAT) area. In order to improve the maneuvering capability of an aircraft, a twist, local incidence to airstream, criterion was used to design the outboard wing and canard lifting surfaces. This resulted in the use of graphite-epoxy skins in an unbalanced, non-standard laminate orientation. The layup for the wing structural box was

was 35°/±50°, and for the canard, it was 15°/±45°. Approximately 95 percent of the entire outer surface of the aircraft was constructed of graphite-epoxy materials.

This report presents the methodology and analytical tools used to aeroelastically tailor those lifting surfaces. Also in order to verify that the analytic tools predicted the twist correctly, based on these unconventional layups, an 8g deflection test was performed on Air Vehicle No. 2 (A/V-2). The purpose of the test was basically to measure deflections at the 8g design point, calculate canard and wing box twist from those deflections, and compare the results to the predicted twists developed by a NASTRAN solution using a finite element model of the HiMAT aircraft. The correlation of those results is discussed in the body of the report.

This report is presented in two sections. The first section covers aeroelastic tailoring methodology, and the second section covers the test results.

In the aeroelastic tailoring of the HiMAT aircraft, several tailoring computer programs, along with a tailoring procedure, were used to tailor the lifting surfaces of the wing and canards. These programs and their functions are explained and discussed, along with the tailoring procedures.

To verify the structural sizing of the tailored components and to include the interaction between the tailored components and the entire aircraft structure, a finite element model of the HiMAT aircraft was made using NASTRAN. The theoretical verification of the tailored surfaces was performed by the use of this finite element model. The formulation of the finite element model, the design iterations conducted to alter deflections and twists of the tailored surfaces, and the predicted twist and deflection values from this finite element model are presented and discussed. Graphs are presented of the final design predictions.

In the test section of the report, typical data recorded during the test, including flight and ground test strain gages and deflection transducer readings, are presented. The data are reduced, correlated, and discussed.

Also in the test section of the report, test twist versus predicted twist and deflection data are correlated, evaluated, and discussed. The effects of sensitivities on the test results are presented at this time.

And finally, the analytical tools used in tailoring, their effectiveness, and recommendations for improving the tailoring process are presented and discussed.

LIST OF SYMBOLS

AC	advanced composites
A_{ij}	laminate extentional stiffness matrix
B	boron
BL	butt line
BM	bending moment
BP	butt plane
C	chord length
C_{avg}	average chord length
C_l	aerodynamic lift coefficient
C_1, C_2	strain ratios
^oC	degrees centigrade
cm, CM	centimeters
C_p	center of pressure
cu	compression ultimate
$\mathbb{C}_L$	centerline
DOF	degrees of freedom
E	modulus of elasticity in tension or compression
E_Y	laminate transverse-modulus of elasticity
E_X	laminate longitudinal modulus of elasticity
E_L	lamina longitudinal modulus of elasticity
E_T	lamina transverse modulus of elasticity
E_{11}	laminate longitudinal modulus of elasticity
E_{22}	laminate transverse modulus of elasticity
E_{33}	laminate shear modulus
E_{12}, E_{13}, E_{23}	laminate coupling moduli
EI	bending stiffness
E_p	epoxy
F	stress allowable
^oF	degrees fahrenheit
FG	fiberglass
FS	front spar
G	modulus of elasticity in shear
G_r	graphite
G_{XY}	laminate shear modulus

G_{LT}	lamina shear modulus
GJ	torsional stiffness
GVT	ground vibration test
g	acceleration of gravity
H	box beam cross-sectional height
h	altitude
in, IN	inches
I	moment of inertia of cross sectional area
J	polar moment of inertia of cross sectional area
k	k^{th} orientation
k_{ij}	beam stiffness matrix
kg	kilograms
kN	kilonewtons
L, l	lamina longitudinal direction
LE	leading edge
Lb, lb	pounds
LH, LHS	left hand side
M	applied moment, mach nø.
$\underset{\sim}{M}$	load matrix
M	meters
MM	millimeters
N	newtons
$N_{X,Y,Z}$	inertia factors in the X, Y, or Z direction, respectively; running load in X, Y, Z directions, respectively
$\underset{\sim}{N}$	load vector
NL	nonlinear
psi	pounds per square inch
Q_{ij}	lamina reduced stiffness matrix
Q_{ij}^{k}	lamina reduced stiffness matrix of k^{th} layer
$\bar{Q}_{ij}$	transformed reduced lamina stiffness matrix
RS	rear spar
RPRV	remotely piloted research vehicle
RT	room temperature
s	set
SIC	structural influence coefficient
$\underset{\sim}{S}$	deflection matrix
S	symmetric
su	shear ultimate
T	applied torque
TE	trailing edge
t	thickness
t_k	thickness of k^{th} ply of k^{th} segment
tu	tensile ultimate
V	applied shear load

W	box beam width, beam deflection
X_F	aircraft lateral axis
X_C	canard lateral axis
Y_F	aircraft longitudinal axis
Z_F	aircraft vertical axis
Z, 3	lamina vertical direction
%	Percent
α	direction cosine
β	angle between gage axis and finite element axis
δ	deflection
ε_{ij}	strain matrix
$\underset{\sim}{\varepsilon}$	strain vector
ε_x, ε_{xx}	laminate longitudinal strain
ε_y, ε_{yy}	laminate transverse strain
ε_L	lamina longitudinal strain
ε_T	lamina transverse strain
γ_{xy}	laminate shear strain
γ_{LT}	lamina shear strain
μ	Poisson's ratio
μ_{LT}, μ_{TL}	lamina Poisson's ratios
Ω	wing sweep angle
$\Phi_{X, Y}$	wing segment load, beam deflection
ρ	weight per unit volume
σ_x	laminate longitudinal stress
σ_L	lamina longitudinal stress
σ_y	laminate transverse stress
σ_T	lamina transverse stress
τ_{xy}	laminate shear stress
τ_{LT}	lamina shear stress
θ	ply (lamina) orientation
θ_k	ply (lamina) orientation of K^{th} lamina

AEROELASTIC TAILORING METHODOLOGY

Since the HiMAT project is a detail design of an aircraft, the engineering analysis cycle shown in figure 1 represents the aeroelastic tailoring methodology used in tailoring the lifting surfaces of the aircraft. As shown in the figure, three concurrent efforts are performed to accomplish the tailoring.

The tailoring cycle begins with generating aerodynamic coefficients, CC_ℓ/C_{avg} and C_p/Span, in the Aerodynamics Group. These coefficients are a result of aerodynamic theory and wind tunnel testing on the desired airfoil shape, wing planform, and at the flight condition that the desired aerodynamic performance is required. These coefficients, in turn, are then used to define the required tailoring loads that will occur at the desired twist.

These incremental tailoring loads are provided to the External Loads Group, along with a weight distribution and nodal points from the finite element model of the aircraft. From these data, moments, torques, and shears are developed for preliminary tailoring of the lifting surfaces. In addition, the External Loads Group develops grid loads for the finite element model. Preliminary design loads are provided to the Stress Group for aircraft structural sizing.

A parallel effort occurring during the loads work is the configuration and design synthesis used to describe the aircraft lines and geometry. As shown in figure 1, Lofting prepares lines for the lifting surfaces, fuselage, interfaces, and control surfaces. The lines are a function of the required aerodynamic profile. Structural layouts are made of fuselage cross-sections, wing and canard planforms, interfaces, and other pertinent structural components based on the lofted lines. From these layouts, a preliminary structural diagram of the aircraft is produced. In addition, preliminary drawings are made to define the aircraft major structural components. From these drawings, a finite element model is made of the entire aircraft.

As shown in figure 1, these preliminary layouts, along with the loads, are used by the Stress Group for structural sizing of the entire aircraft. This sizing is entered into the finite element model. Structural influence coefficients (SIC's), from the finite element model, and EI/GJ values for the control surfaces are provided to the Flutter Group for flutter analysis of the preliminary layouts.

Concurrent with these two efforts is the preliminary tailoring of the lifting surfaces. As shown in figure 1, tailoring programs AC87 and AC89 are used to define the ply layups required to produce the desired twist. Geometry, loads, and twist requirements are entered into the AC87 tailoring program.

This program then defines a series of layups that meet the twist and strength requirements. AC89 is then used to select the final layup to be entered into the finite element model.

In the engineering analysis cycle shown, the finite element model is made for two purposes. One is to verify that the required twist of the tailored surfaces is achieved, taking into account the surrounding structure and loads, and the other is to verify that the structural integrity of the aircraft has been achieved by checking the internal loads and stresses developed. Once the twist requirement is met and all other structural sizing is provided for the aircraft, structural influence coefficients are determined from the stiffness matrix in the finite element model. The structural influence coefficients are used to establish the jig shape, external loads, and for use in further analytical work in the Aerodynamics, External Loads, and Flutter Groups. Revisions are made to the finite element model based on results from these Groups, and the finite element model is run producing internal loads from which the aircraft structure can be accurately sized, as shown on figure 1. This represents one tailoring cycle. Once this cycle is completed, it is repeated until all disciplines have satisfied their requirements.

In addition, critical load cases are defined by the External Loads Group and run in the finite element model. The critical cases for sizing the aircraft structure are shown in figure 1. The major cases for structurally sizing the aircraft are the 12g, 10g, and 1g yaw case. The other loading cases shown, such as the maximum negative (-6g) case, are used only to design local structure on the fuselage. The design condition used to verify that the lifting surfaces have met the desired structural twists is the 8g load case.

Tailoring begins in the Aerodynamics Group and ends with the Manufacturing Group. In between those extremes are the External Loads, Lines, Design, Stress, Mass Properties, Aeroelastic Tailoring, Structural Dynamics, and Tooling Groups, all interacting with the Aerodynamics and Manufacturing Groups until a compromise is reached to design and build an aircraft that meets the tailoring objectives. This tailoring cycle is repeated until all disciplines have refined their analysis, structural integrity is insured, and the twist requirement is met.

HiMAT Aeroelastic Tailoring Process

The HiMAT wing and canard aeroelastic tailoring process evolved during the development of the RPRV (Remotely Piloted Research Vehicle) project. The procedure was developed specifically for the purpose of achieving particular HiMAT performance goals: superior transonic maneuverability (capability for

a sustained 8g turn at M = 0.9 and h = 7620 m (25,000 feet)), and efficient subsonic cruise capability. In addition, the RPRV had to be structurally adequate to withstand a maximum limit load of 12g's. Ultimate load was defined as 1.5 x limit load.

Early in the HiMAT RPRV design effort, it was decided to meet the wing and canard streamline twist associated with the low drag, subsonic cruise requirements by using wing and canard "jig" shapes and special rigging of their leading and trailing edges. Design of the HiMAT wing and canard primary box structures would then be limited to meeting the 8g maneuver goal twist. That goal is characterized by required wing and canard deformed twist shapes and associated aerodynamic load distributions.

The areas of the HiMAT structure specifically designed to the above aeroelastic requirements are shown as shaded regions in figure 2. They primarily consist of the outboard wings and canards. Tailoring of the wing structure inboard of the vertical tail boom at BP 102.36 cm (40.3 inches) to the 8g aeroelastic constraints could not be accomplished, since other design conditions dictated that structure. The inboard wing area was designed primarily by the landing gear and vertical boom structure and loads. Figure 2 depicts the main structural components of the aircraft, and figure 3 is a photograph of the aircraft as built.

Both canard and outboard wing structures are constructed of front and rear spars and identical upper and lower advanced graphite-epoxy composite covers stabilized by full depth honeycomb core. For this type of construction, the covers are the major structural elements affecting twist; therefore, the emphasis in the aeroelastic tailoring of the wing and canard structures was concentrated on design of the cover laminates in terms of ply distributions and orientations. However, other wing and canard structural elements have an impact on the aeroelastic behavior. The effects of leading edge skin thickness, slotted leading edges, root stiffness at the inboard wing-fuselage intersection, wing tip fin, and other components have been investigated. Their contribution to the lifting surface structural behavior are accounted for in the NASTRAN model. Their impact on the final tailoring of the surfaces is discussed in the Finite Element Model and Analysis section.

The HiMAT canard and outboard wing structural boxes are highly tapered. Use of advanced composite beam theory for preliminary design purposes is therefore acceptable. Aeroelastic tailoring of the wing and canard covers by spanwise only variation of the laminate plies was considered to be the most efficient manufacturing approach to the HiMAT design; therefore, chordwise tailoring was not employed.

The aeroelastic tailoring procedure used in tailoring the HiMAT wing and canards is shown in detail in figure 4. There are basically two phases in the

procedure. The first is preliminary sizing with computer programs AC87 and AC89, and the second is detail design verification based on the finite element model.

As shown in the figure, to initiate the HiMAT aeroelastic design process, the required streamwise twist and associated tailoring loads for the 8g maneuver condition are required. The loads consist of the net effects of the aerodynamic and inertia relief loads. In addition, the net loads for the 12g strength design condition must be known. Based on those loads, the shear (V), moment (M), and torque (T) distributions are defined along the structural box center line for preliminary tailoring and entered into AC87. Box geometry for the AC87 and AC89 preliminary design computer programs is obtained from the wing and canard layouts and entered into the programs.

AS/3501-5 graphite epoxy tape was selected as the advanced composite material system for the canard and outboard wing covers. Its unidirectional lamina properties are shown in table I. As shown in figure 4, those values are entered into AC87, and AC50, Rockwell International materials property computer program (reference 1).

The preliminary sizing of the HiMAT canard and outboard wing cover laminates is then accomplished with the AC87 computer program. In addition to the strength and twist requirements described above, minimum laminate thickness and ply percentages are entered in the program. Use of minimum ply percentages obviates unrealistic cover designs by prohibiting the plies from being oriented in only one direction. For HiMAT, the minimum ply percentages requirement for any layer was arbitrarily set at 20 percent for each of the three orientations $(\theta^{o}_{1}/\theta^{o}_{2}/\theta^{o}_{3})$.

At station 102.36 cm (40.3 inches), the minimum gage constraint was based on the root splice joint design. Subsequent outboard segment cover minimum thickness requirements were selected to give reasonable ply drop-offs. If this is not accomplished, designs with drastic ply drop-offs would result, leading to possible ply delaminations.

In the tailoring process shown on figure 4, in order to reduce the number of laminate configurations examined by AC87 to a reasonable number, only specific families of laminate layups $(\theta^{o}_{1}/\theta^{o}_{2}/\theta^{o}_{3})_{s}$ would be considered. The first layup may be started with the $(\theta^{o}/45^{o}/-45^{o})_{s}$ family, where θ varies from -30^{o} to 30^{o} in 5^{o} increments. The number of 45^{o}s and -45^{o} plies in the final design need not be identical. AC87 would then design each of these laminate configurations for strength and twist requirements as well as the geometric constraints of percentage thickness and individual ply thickness. If no AC87 design is particularly promising, either because of excessive laminate thicknesses or unacceptable twist behavior, a different family of laminate would then be

examined. The next set of families evaluated could be the $(\theta^{o}/+50^{o}/-50^{o})_{s}$ or the $(\theta^{o}/+40^{o}/-40^{o})_{s}$. An important limitation on the value of θ^{o} is that it could not be within 15^{o} of either of the other two directions. Thus, a laminate with almost all the plies oriented in one direction is avoided.

During the tailoring process, when the families do not meet the twist and strength designs, additional families are considered. Consequently, the last two orientations in both cases would be rotated 5^{o}, $(\theta^{o}/+50^{o}/-50^{o})_{s}$ and $(\theta^{o}/+55^{o}/-55^{o})_{s}$. HiMAT experience has shown that only a few such iterations through AC87 are required to produce a reasonable number of candidate laminate configurations that meet the twist and strength requirements.

The AC87 laminate designs are then evaluated by the AC89 deflection analysis program to predict final preliminary twist. Since some did not meet twist requirements, changes were made to the AC87 model in terms of minimum gage and twist requirements, and a new AC87 preliminary sizing effort was undertaken. As soon as AC89 indicated that the AC87 generated laminates are acceptable from an aeroelastic twist point of view, the optimum candidate in terms of twist attained and cover weight is selected. In the HiMAT project, satisfactory aeroelastic twist behavior was a more important design parameter than weight and was used as the selection criterion. However, in all cases the difference in weight between the ply orientation changes was less than 5 percent and considered insignificant at this preliminary design stage.

The selected aeroelastically tailored laminate is then modified to reflect the inboard root splice. This involves the replacement of the graphite-epoxy plies with boron-epoxy plies, so that a joint of adequate strength can be obtained. The resulting layup is processed through the material transformation program, AC84. A deck of data cards reflecting the AC87 and AC89 design layup was then generated from AC84. It describes the tailored laminate in terms of finite element property cards (PTRMEM and PQDMEM) and Hooke's matrix definition cards (MAT2), which are compatible with the wing and canard NASTRAN finite element model. Modifications to the resulting idealization to reflect local laminate build-ups are then performed manually.

A detailed evaluation of the tailored design is accomplished with NASTRAN, as shown in figure 4. Resulting 12g stresses and 8g twists are compared to the strength and twist requirements. Minor modifications are made if inadequacies are evident. The changes are accomplished manually or with AC84. Once an acceptable design is determined, structural influence coefficients for the entire aircraft are calculated with NASTRAN and transmitted to the Aerodynamics, Flutter, and External Loads functional groups for evaluation. After their analysis and the resulting loads and structural sizing changes, the tailoring cycle is repeated until the twist and strength requirements are met.

Once the detailed evaluation of the HiMAT structure indicates an acceptable design, layouts of the canard and wing structure are drawn. Since the laminate layups drawn may not correspond exactly to the desired ones, due to manufacturing or design considerations, a final analysis of the as-drawn wing and canard design is performed to insure structural integrity and twist requirements using the finite element model.

This procedure is used in tailoring both the HiMAT wing and canard lifting surfaces.

Aeroelastic Tailoring Computer Programs

As shown in figure 1, the basic analytical tool used to aeroelastically tailor the HiMAT RPRV wing and canards is the NASTRAN Finite Element Analysis Program. The NASTRAN program is used in order to account for the iterations of the substructure and the tailored surfaces, the effects of the entire aircraft loading on tailoring the surfaces, and the effects of the adjacent structure on the tailored surfaces. However, to solely rely on NASTRAN for design purposes would require numerous iterations. The prohibitive costs and turn-around time associated with such an approach emphasized the need for preliminary level design programs. Since the TS-0 Aeroelastic Tailoring Program (Reference 2) was not operational at Rockwell/LAD, alternate methodology had to be developed. Consequently, Rockwell developed tailoring programs were used in the preliminary sizing of the wing and canard surfaces as input to the finite element model. A short description of each tailoring program used in the HiMAT program is presented below.

AC87 aeroelastic tailoring (strength/twist) program. - The AC87 aeroelastic tailoring computer program is a modified version of a Rockwell developed study program, AC87Q. The intent of both programs is to provide initial cover sizings for the NASTRAN finite element model of the HiMAT wing and canards. The programs and their features are as follows.

The AC87Q and AC87 mathematical model is applicable to a wing or a canard, and consists of a series of full depth honeycomb beams having anisotropic covers (figure 5). The cover laminates consist of plies oriented in three directions, $(\theta^{o}_{1}/\theta^{o}_{2}/\theta^{o}_{3})$. The layups are assumed to be symmetric, but need not be balanced. This means that the number of θ^{o}_{i} laminae on both sides of the laminate midplane are identical, but that the number of θ^{o}_{1}, θ^{o}_{2}, or θ^{o}_{3} plies in the laminate do not have to be equal. There is no chordwise variation of the cover laminates. All skin plies are considered to be constant across a cross-section of the structural box. Plies are dropped off perpendicular to the wing

or canard box centerline. This eases manufacture of a tailored surface by minimizing layup complexity and curing problems of the covers, as well as making their analysis and design more tractable.

The AC87Q lifting surface idealization originally included front and rear spar webs (figure 6). Their ply orientations, however, were limited to the same directions as those used in the cover laminates. Since the skin covers had unconventional orientation, this limitation on the spar designs was deemed unacceptable for HiMAT application. Therefore, in the modified AC87 program, the idealization model excluded the front and rear spar webs and their effects. Consequently, the AC87 model consisted of only identical anisotropic covers, fully supported by a honeycomb core, as shown in figure 7.

In tailoring the surfaces, both the AC87 and AC87Q models were subjected to two sets of design loads. One corresponded to the 12g strength critical condition, while the other represented the 8g aeroelastic tailoring design condition. Both conditions are net summarizations of the aerodynamic loads and the inertia effects. They are expressed in terms of vertical shear, bending, and torsional moment distributions along the wing box center line.

In the AC87Q program the lifting surface box covers carry bending and torsional loads while the spars resist the vertical shear as well as the torsional moment (figure 6). The shear load is disregarded in AC87, since the spars are not included in the structural model (figure 7). The core, in both cases, serves only to stabilize the box covers and to prevent the box cross section from deforming.

Since the box cross sections are assumed to remain plane under the applied loads, the structural deflections can be calculated directly from the cover membrane deformations. The aeroelastic twist requirements can then be redefined in terms of required cover laminate strains. If the laminate strength analysis is also based on a laminate strain failure approach, the aeroelastic tailoring problem becomes a matter of designing a laminate to satisfy the two sets of given loads and corresponding strains. In equation form, this would involve solving the equation:

$$\underset{\sim}{N}^{(\ell)} = \underset{\approx}{A}\underset{\sim}{\varepsilon}^{(\ell)}, \quad \ell = 1,2$$

where

$$\underset{\sim}{N}^{(\ell)} = \left\{N_x, N_y, N_{xy}\right\}^{(\ell)}, \quad \ell = 1,2 \text{ (load vector)}$$

$$\underset{\sim}{\varepsilon}^{(\ell)} = \left\{\varepsilon_{xx}, \varepsilon_{yy}, \tau_{xy}\right\}^{(\ell)}, \quad \ell = 1,2 \text{ (strain vector)}$$

and

$$\underset{\approx}{A}^{(\ell)} = \begin{bmatrix} A_{11} & A_{12} & A_{16} \\ A_{12} & A_{22} & A_{26} \\ A_{16} & A_{26} & A_{66} \end{bmatrix} \quad \text{(laminate extensional stiffness matrix)}$$

$$A_{ij}^{(\ell)} = \sum_{k=1}^{3} Q_{ij}^{(k)} t_k$$

where $Q^{(k)}$ is the lamina stiffness matrix of the k^{th} orientation. Selection of a laminate that satisfies this equation cannot be accomplished directly because the lamina stiffnesses, $Q_{ij}^{(k)}$, are not linear functions of the ply orientation, Q_k. Thus, an indirect solution scheme is required.

The original AC87Q program approach consisted of considering every combination of cover laminate layups, $(\theta^o_1/\theta^o_2/\theta^o_3)$, where θ_k values ranged from -90^o to 90^o in 10^o increments. Each configuration was then strength sized for ply thickness, t_k, at an arbitrary number of strain ratios, $\varepsilon_{yy} = C_1 \varepsilon_{xx}$ and $\gamma_{xy} = C_2 \varepsilon_{xx}$. The resulting box design that gave the best aeroelastic twist distribution was considered the tailored design. Trial evaluation of this procedure indicated that it was too cumbersome to be used effectively and also that it did not provide a high degree of confidence in the optimality of the wing cover laminate design due to the arbitrary formation of the strain ratios used.

The AC87 program was subsequently developed to circumvent these difficulties and is thus more applicable to the design of actual lifting surface structures. In addition, other features were added to the program. These changes were incorporated into AC87 and used, since no tailoring program existed in industry at that time that included these advances.

For example, to insure that realistic laminate layups would be designed, minimum laminate gage and ply percentage limits are included as additional design constraints. Rather than examine every combination of cover laminate orientation, $(\theta^o_1/\theta^o_2/\theta^o_3)$, only user-specified sets of ply directions would be entered into AC87. For each set of laminate orientations, only specific strain ratios which satisfy the aeroelastic twist requirements would be utilized in sizing the laminate thicknesses, t_k. These strain ratio derivations are shown in appendix A. The resulting laminate is then checked in AC87 against the strength and dimensional constraints and revised if a criterion is not satisfied. One minor limitation in the AC87 design procedure is the number of

cover laminate configurations ($\theta^{o}_{1}/\theta^{o}_{2}/\theta^{o}_{3}$) that can be examined per computer run. This is not serious, since engineering judgment can be used to eliminate many unlikely candidate layups, allowing emphasis to be placed on a minor number of potential cover laminate configurations.

AC89 aeroelastic stiffness program. - As was typical with industry programs at the time, the inability of AC87 to account for spars or spar caps limits the accuracy of its predicted aeroelastic wing or canard twists. Consequently, an existing advanced composite beam analysis program, AC89, was used to verify the AC87 twist calculations prior to any NASTRAN analyses. The mathematical simulation of the lifting surface box of AC89 is similar to that of AC87 except that the front and rear spars are considered. In the AC89 model, the spars must have conventional $(0^{o}/\pm45^{o}/90^{o})_{s}$ layups, but do not have to be of the same material as the covers. Their sizing is determined by the Stress Group. There is no strength check or resizing capability in AC89. However, for specified cover laminates, it can generate a set of preliminary structural influence coefficients as well as the beam stiffness matrices, K, which are used for preliminary flutter analysis, as shown on figure 1. This was one of its primary uses. Internally, the program works with the following equation.

For a particular wing box segment, K satisfies the equation

$$\underset{\sim}{M} = \underset{\approx}{K}\,\underset{\sim}{S}$$

or

$$\begin{Bmatrix} V \\ M \\ T \end{Bmatrix} = \begin{bmatrix} K_{11} & K_{12} & K_{13} \\ K_{21} & K_{22} & K_{23} \\ K_{31} & K_{32} & K_{33} \end{bmatrix} \begin{Bmatrix} W \\ \phi_x \\ \phi_y \end{Bmatrix}$$

where V, M, and T are the normal shear, bending, and torsional moments at the outboard end of the beam segment and where w, ϕ_x, and ϕ_y are the corresponding deflections at that point.

Merging the AC87 and AC89 program capabilities was considered, but their program structures were too dissimilar to permit this to be readily accomplished. Consequently, they were run separately and sequentially to provide the ply layup for the finite element model.

AC84 material transformation program. - The prior three programs (AC87, AC87Q, and AC89) defined aeroelastic tailoring layups. The AC84 program converts that information to NASTRAN input.

The NASTRAN model of the HiMAT RPRV uses membrane type finite elements (TRMEM and QDMEM) to simulate the canard and outboard wing skins. The element property data for this type of element consists of the membrane (laminate) thickness and the Hooke's matrix of the constituent material. As can be seen in appendices B and C, the Hooke's matrix formation for anisotropic advanced composite laminates is complex. Manual generation of these matrices would be tedious if an accurate NASTRAN simulation of the AC87 tailored laminate were desired. An interface computer program, AC84, was therefore developed to eliminate this time consuming operation.

AC84 maps the AC87 defined laminate ply distributions onto the NASTRAN simulations of the canard and wing covers. Direct use is made of the existing NASTRAN finite element model's element connectivity and grid coordinate data. The program then calculates each element's average thickness and its associated Hooke's material matrix and provides the required NASTRAN input data cards (PTRMEM, PQDMEM, and MAT2 cards). Once this is accomplished, revision of the data set can be readily revised by time-sharing editing. Thus, changes to the NASTRAN model (to simulate different cover configurations) required little additional effort. Experience has shown that, with AC84, the interfacing between preliminary tailoring and NASTRAN Finite Element Analysis was reduced to about one hour of real time.

Finite Element Model and Analysis

A finite element model was constructed of the entire HiMAT aircraft. This model was used to verify analytically the aeroelastic tailoring of the outboard wing box and the canard box. It was also used to generate internal loads to verify the structural integrity of the lifting surfaces. Also, the model was used to provide structural influence coefficients (SIC's) for external load, aerodynamics, and flutter analysis of the wing and canard. The components of the aircraft modeled are shown in figure 2.

The finite element model of the HiMAT aircraft was constructed using NASTRAN (Reference 3). NASTRAN uses a finite element structural model in which the distributed physical properties of the structure are represented by a finite number of structural elements interconnected at grid points to which loads are applied and displacements are calculated. The grid definition forms the basic framework for the structural model. All the other parts of the structural model are referenced either directly or indirectly to the grid points. Figure 8 is a three-quarter view of the aircraft modeled.

The HiMAT aircraft finite element idealization consists of the following NASTRAN elements: CBAR, CONROD, CQDMEM, CQUAD1, CQUAD2, CSHEAR, CTRIA1, CTRIA2, and CTRMEM. In the actual HiMAT aircraft the real structure consists of end

load-carrying elements, beam elements, and panels. Some panels are shear only, and others are shear plus biaxial in-plane loading. Also, some panels carry bending as well as in-plane shear and in-plane biaxial loading.

The structure was idealized using the above described finite elements as a symmetric half-shell model along the center line of the aircraft. For symmetric load conditions the center line boundaries were symmetric. For the antisymmetric load conditions, a second model was generated, but with antisymmetric center line boundaries. With the two models, all symmetric and antisymmetric design load conditions were checked for balance by use of a loads summation program. This was done in order to avoid using a condition that was unbalanced or incorrect as input to NASTRAN.

The outboard wing box of the HiMAT aircraft is full-depth aluminum honeycomb with graphite-epoxy upper and lower skins and graphite-epoxy front and rear spars. The idealization consisted of use of the CQDMEM panels to model the upper and lower skins, shear panels to model the full-depth honeycomb shear stiffness, and CONRODS to model the core axial stiffness. The front and rear spars were modeled as shear panels for the spar webs and CONRODS to represent the spar caps. The same type of idealization was used to model the canard box.

The fuselage was idealized by using CQDMEM panels and CTRMEM panels to model the skins. Frames at station 438.15 cm (172.5 inches), figure 2, and forward were modeled as two cap frames, i.e. two caps with a shear web between them, joined with inside skin, inlet duct, and other surrounding structure. The aft module frames from station 438.15 cm (172.5 inches) and aft were modeled as CBAR elements with the neutral axis at the proper offset distance.

The inboard wing of the HiMAT aircraft was idealized using CQUAD1 and CTRIA1 sandwich panel elements for the upper and lower skins. The spars and ribs were idealized using CSHEAR elements. Spar caps were idealized using CONROD elements. At this point, it should be pointed out that one of the problems that occurs with the usage of NASTRAN is the possibility of singularity. Elements such as the CQUAD1, CTRIA1, CQUAD2, CTRIA2 are five degree of freedom elements, and if used alone require the sixth degree of freedom to be suppressed. If this is not done, the solution will be singular and the problem will not run; therefore, no solution. If a surface is perfectly flat, the required suppression, which is also considered a reaction if attached to active section properties, will produce no reaction, resulting in proper usage of the element. If the surface is not flat, then the suppressions become undesired reactions that are not proper, and will cause undesirable and incorrect internal loads. The way to avoid this is to use bar elements on all four sides of each CQUAD1 and CQUAD2 element. This permits use of the element, and the result will be correct internal loads with the proper reaction system.

In the development of the sizing for the HiMAT outboard wing and canard, design iterations were conducted of pertinent components of the entire aircraft in order to improve the controlled twist. The investigations conducted were to determine how the various parts of the aircraft structure contributed to the bending and twisting of the wing and canard. The items investigated included:

- Effect of the structural box skins
- Aileron support system
- Slotting of the leading edges
- Leading edge skin thickness
- Effect of spar stiffness
- Effect of wing tip fin
- Effect of external loads
- Varying the root stiffness at the side of the fuselage X_F = 38.10 cm (15 inches)
- Addition of tip mass to the wing and canard
- Evaluating the vertical tail effect

Table II depicts their effect on twist. It should be emphasized that tailoring is a function of load, geometry, design, and sizing. Consequently, the results shown apply only to the unique HiMAT design and would vary to some extent with another design. The sensitivity studies were conducted using the loads specified in figure 1.

As shown in table II, the box skins have the greatest effect on twist. Many configurations of thicknesses and ply layups were studied. The results of those studies are presented in the section entitled "Final Design and Twist Prediction" and since they are extensive they will not be repeated here.

The model of the outboard wing was run with the control surfaces removed. This was done in order to ascertain the effects of the control surfaces on the wing twist. The aileron is supported on three hinges, and because of the flutter requirements, is extremely stiff in both the spanwise and chordwise directions. The removal of the aileron permitted an increase in wing box twist of 0.80 degree. Therefore, the aileron hinges were designed to ensure

no binding, and it is recommended in future designs that only two-point hinge systems or split control surfaces be used. The effect of the elevon on the twist was insignificant.

If a continuous leading-edge segment is used, the resulting loss of box twist is 0.6 degree. Consequently, in order to compensate for this degradation in box twist, the leading edges on both the canard and the wing were slotted. Also, heavier than required leading-edge skin gages inhibit bending and reduce box twist considerably. The wing box leading edge skins were actually manufactured thicker than the required structural sizing. Bending contributes significantly to meeting the twist requirements; consequently, anything that impedes bending, lowers the attainable twist. The resulting loss in twist due to this increase in gage was 0.5 degree, but was compensated for by improvements in box skin and spar layups.

Spar studies with NASTRAN indicated that an increase of 0.3 to 0.4 degree was obtained by minimizing spar thickness and correct ply orientation.

The effect of the winglet is basically to increase the wing shear, bending, and torsion loads. Increasing these loads increases the wing twist approximately 0.3 degree.

Additional studies of the canard and wing twist were made by considering the effect of changing altitudes, and consequently the loads the aircraft would experience Not only was the twist decreased with lower altitudes, but the shape of the twist curve changed radically. The maximum decrease in twist experienced was 0.25 to 1.0 degree, depending on span location.

The planform of a wing is important, since the more sweepback the higher the structural aspect ratio becomes. Consequently, the natural tendency is for the tip deflection and twist to increase with larger sweep angles. However, once the configuration has been set, planform is no longer a factor in sensitivity studies. Although the HiMAT planform was fixed, the root stiffness studies revealed that the design of the inboard wing had a significant effect on the twist and bending. This effect was investigated along with the vertical tail load, the joint at X_F = 102.36 cm (40.3 inches), and tip masses. Since the vertical tail load acts downward, the twist was decreased. In order to compensate for this, the root joint, the inboard wing, and the skin and rib gages at joint 102.36 cm (40.3 inches) were minimized to increase twist. An additional study was made by fixing the outboard wing at X_F = 102.36 cm (40.3 inches) and attaching a wing tip mass of 111.21 N (25 pounds) at X_F = 227.58 cm (89.6 inches). At 8g, the twist due to this mass was 0.93 degree with respect to the support system at X_F = 102.36 cm (40.3 inches) However, with the entire aircraft and 8g load, the effects of the vertical tail down load, inboard wing, fuselage flexibility, and tip mass, only a wing twist increase of 0.15 degree was produced. Since the tip mass did not add significant twist

to the wing and contrary to earlier analysis, did not influence the flutter characteristics of the aircraft it was removed. A similar effect was experienced for the canard.

Concurrent with the above efforts, a detailed flutter analysis was made of the HiMAT aircraft and its major structural components. Partial finite element models were made of the wing and canard boxes to study flutter effects. Similarly, detailed models were made of the aileron, elevon, elevator, and canard flap. Included in the control surface models were the actuator systems and backup structures.

From these studies, the design of the aircraft was changed, incorporating the effects of the above studies until the desired twist of both the canard and wing were met.

Final Design and Twist Predictions

The HiMAT outboard wing and canard were designed using the aeroelastic tailoring process and tools described in the methodology sections. In addition, the design iteration studies of the finite element model and their interactions on the design were discussed. In this section, the actual design of the outboard wing and canard structural box configurations that were manufactured are explained. Results for the progressive steps in the design process are shown in order to demonstrate how the final design was determined. In addition, the selected outboard wing and canard configurations are defined, along with their predicted structural twist and deflection behavior.

HiMAT wing aeroelastic tailoring. - A planview of the HiMAT outboard wing structure that was aeroelastically tailored is shown in figure 9. It also shows the ply orientations, thickness, and number of plies along the wing span. The cross-section of the outboard wing geometry used in the preliminary tailoring phase, AC87 and AC89, is given in figure 10. The nomenclature shown coincides with that used in figure 5 The front and rear spar heights are used only in AC89 to get a more realistic wing structural stiffness definition.

The HiMAT outboard wing was configured to two flight conditions: an 8g maneuver condition and 12g strength condition. The wing was to be designed to display sustained maneuvering capability at the 8g point and was to be structurally adequate for 12g's. The loads for the 8g tailoring condition have an associated required wing twist shape. By subtracting the twist due to structural deformation and anticipated twist increment due to leading and trailing edge devices, the jig shape is obtained.

The resulting outboard wing structural deformations required at the tailoring point are shown in figure 11 and result in a tip twist of approximately 5.5°. This shape was defined by the Aerodynamics Group. The loads for the 12g strength sizing condition are based on the HiMAT outboard wing's stiffness characteristics.

The next air and inertia loads corresponding to the two design conditions were provided by the External Loads Group. These were in terms of grid loads for NASTRAN Finite Element Analyses and as shear, bending and torsional moment distributions along the wing box center line. Winglet effects are included. The two loading cases used as input data for the preliminary tailoring computer programs, AC87 and AC89, are shown in figures 12 and 13.

The primary means of aeroelastically tailoring the outboard wing was by selection of the cover laminate ply orientations, and their corresponding number. The box honeycomb core was selected to prevent core crushing as well as to prevent warping of the wing box cross-sections. Initial trials at design indicated that a very flexible structure was necessary at the outboard wing to meet the twist requirements. To minimize the contribution of the leading edge to total wing stiffness, the leading edges were slotted and made from fiber glass material. Nearly all of the wing stiffness is due to the structural box covers. Therefore, the tailoring effort was concentrated on the judicious design of cover laminates.

The aeroelastic tailoring cycle was initiated by using the AC87 computer program to generate cover designs that met strength and twist requirements for selected laminate ply orientations. The procedure in which the sets of orientations were chosen was to start with a conventional orientation of $(0^o/45^o/-45^o)$ and vary the first orientation, θ_1. Thus AC87 designs for cover laminate orientations $(-30^o/45^o/-45^o)$, $(-20^o/45^o/-45^o)$ . . . $(0^o/45^o/-45^o)$ . . . $(30^o/45^o/-45^o)$ were obtained. The resulting 8g twists calculated by AC87 for this family of orientations $(\theta^o_1/45^o/-45^o)$ are shown in figure 14. The wing cover laminates with negative θ_1 displayed poor twist behavior and are therefore omitted from this figure.

As shown in figure 14, the AC87 designed covers having $(20^o/45^o/-45^o)$ and $(30^o/45^o/-45^o)$ orientations appear promising. To improve the twist, the same procedure was repeated for the $(\theta^o_1/50^o/-50^o)$, $(\theta^o_1/55^o/-55^o)$ and $(\theta^o_1/60^o/-60^o)$ families of cover ply orientations, where θ_1 ranged from 0^o to 30^o. Laminates with negative θ_1 were disregarded, since the results from the $(\theta^o_1/45^o/-45^o)$ family indicated no improvement in wing structural behavior. The 8g structural twists for the $(\theta^o_1/50^o/-50^o)$ covers designed by AC87 are given in figure 15. Since the predicted twist curves matched the desired

aeroelastic curve so closely, the ($20^o/50^o/-50^o$) and ($30^o/50^o/-50^o$) laminates were selected for further investigation. The cover laminate configurations ($\theta^o_1/55^o/-55^o$) and ($\theta^o_1/60^o/-60^o$) sized by AC87 displayed some potential designs that satisfied strength/twist requirements, but were of prohibitive thickness and therefore eliminated.

Consequently, four candidate ply layups that matched the 8g maneuver condition twist were selected from Figure 14 and 15 and verified with the AC89 program. The candidate configurations selected were the ($20^o/45^o/-45^o$), ($30^o/45^o/-45^o$), ($20^o/50^o/-50^o$) and ($30^o/50^o/-50^o$) layups. AC89 twist results using these layups are shown in figure 16. As shown in the figure, the ($30^o/50^o/-50^o$) design is the best choice for further refinement to meet twist. This laminate definition was therefore incorporated into the HiMAT outboard wing NASTRAN finite element model.

A detailed analysis of the tailored structure was performed with NASTRAN. This was done in order to check for strength under the interaction loading of the leading and trailing edge surfaces, winglet, and root interface structure. The 8g streamline twist distributions, calculated from the finite element analyses using the AC87 designed wing cover of ($30^o/50^o/-50^o$), are shown in figure 17. Other than at the front spar/rear spar inboard section, the leading and trailing edge (LE/TE) aerodynamic twist and the front spar and rear spar (FS/RS) twist distributions exhibit good correlation. The latter twists show a good form fit to the required twist shape. The offset is primarily due to the extreme stiffness of the inboard wing. The effects of the chordwise bending of the leading edges and control surfaces do not appear to be important since both the FS/RS and the LE/TE curves match closely.

The AC87 designed ($30^o/50^o/-50^o$) cover laminates exhibited pronounced inbalance of the 50^o and -50^o ply numbers. A more conventional layup having equal numbers of 50^o and -50^o plies is more desirable, since the possibility of laminate warpage during manufacture would be reduced. The AC87 ($30^o/50^o/-50^o$) laminate was therefore revised to balance the 50^o, -50^o ply numbers. The NASTRAN results for this configuration are shown in figure 18. A comparison of figures 17 and 18 shows that there is a small reduction in the twist behavior of the outboard wing when using the balanced ply layup. Examination of the NASTRAN cover element stress results at the 12g strength condition revealed adequate structural integrity, and therefore the balanced design was adopted. Later increases in load indicated a panel with a negative margin of safety in the matrix at ultimate load. The panel was assessed against the impact of tooling changes, mole line constraints, and schedule. It was deemed an acceptable risk, and the balanced design maintained.

As shown in figure 18, the difference between the desired aerodynamic twist and predicted twist is approximately 0.5 degree. This is satisfactory

from an aerodynamic standpoint, but in order to compensate for uncertainties in manufacturing that would possibly increase this difference, the θ^{o}_{1} ply was rotated from 30^{o} to 35^{o}, foregoing another preliminary tailoring iteration. This presupposed that there would be little change in the strength properties of the resulting 35^{o} laminate. Small coupon testing of this laminate at a later date confirmed that assumption. Also, subsequent NASTRAN analyses confirmed that the 35^{o} configuration had the required strength capability, again with one panel indicating a negative margin of safety in the matrix at ultimate load. A few other cover NASTRAN finite elements were marginal strengthwise due to load distribution. The twist distribution for this new cover design ($35^{o}/50^{o}/-50^{o}$) at the 8g twist condition as determined from NASTRAN analyses is shown in figure 19. As shown in figure 19, a closer correlation in magnitude and form are obtained with this ply layup. Structural influence coefficients for the entire aircraft utilizing this wing design were then calculated with NASTRAN and submitted to the Aerodynamics, External Loads and Flutter groups for their verification. Their analysis indicated an adequate design.

Drawings of this cover laminate design were then initiated. However, during this time period, the 8g tailoring condition was changed from an altitude of 9144 M (30,000 feet) to 7620 M (25,000 feet). Rather than redesign the wing to the new conditions, the existing structure was re-analyzed for the revised 8g tailoring condition at the lower altitude using the NASTRAN finite element model. The resulting twist distributions are shown in figure 20. Although the FS/RS twist was reduced to 5.25^{o}, the existing outboard wing design was still considered satisfactory. Consequently, no retailoring of the wing structure was pursued, and the $+35^{o}/\pm 50^{o}$ design was selected for manufacture.

Final wing twist prediction. - As the manufacture of the structural box, leading edge, trailing edge control surfaces, interface joint, inboard wing, and mid-fuselage frames and skins progressed, changes were made to the as-designed condition in order to facilitate packaging, control systems, and manufacturing. All of these changes were incorporated into the finite element model.

As an example, figure 21 shows the desired and actual cover thickness distribution for the outboard wing. It can be seen from the figure that they match quite well, except at the tip. This thickness effect tends to flatten the twist. The desired and actual number of cover plies are shown in figures 22 and 23 for each orientation, $35^{o}/\pm 50^{o}$. Again, the number of plies match well

except at the inboard and outboard wing stations. In the inboard portion, at approximately 50 percent span, $0^{o}/90^{o}$ B/E_p had to be interleaved to meet the required joint thickness and strength, again, reducing the wing twist. At the outboard wing station, approximately 95 percent span, fiber glass was interleaved to meet thickness requirements and strength.

As a result of these changes, the finite element model was run again using the tailoring 8g and strength 12g loading conditions. These cases were run both to verify strength and predict the final wing twist. Figure 24 plots the deflection of the front and rear spar and figure 25 depicts the associated twist. As can be seen from figure 25, there is a noticeable drop in twist from the as-designed aircraft (figure 20) to the actual manufactured aircraft. The twist decreases from 5.25^{o} to 4.95^{o}. The shape of the curve remains about the same.

A similar result is shown for the leading-trailing edge deflection (figure 26) and the twist (figure 27). The twist for the leading-trailing edge (figure 20) drops from 5.56^{o} to 4.95^{o}, as shown in figure 27.

Figures 25 and 27 represent the final predicted twist for the FS/RS and LE/TE surfaces for the outboard wing under the 8g flight loads.

HiMAT canard aeroelastic tailoring. - Aeroelastic tailoring of the HiMAT canard was performed in a manner similar to the outboard wing tailoring procedure. A plan view of the canard structure that was designed is shown in figure 28. Again, ply orientations, thicknesses and number of plies, and local ply increases for hinge fittings are shown in the figure. The cross-section definition of the canard box structure is given in figure 29 It presents the height and width of the box as a function of span percentage. The structural configuration employed is similar to that of the outboard wing, a full depth honeycomb torque box having identical upper and lower anisotropic advanced composite covers and conventional graphite epoxy front and rear spars. As in the wing tailoring, the main means of aeroelastic tailoring the canard was in the design of the cover laminates.

The HiMAT canard was sized to display required aeroelastic behavior at the HiMAT 8g maneuver condition and be strength satisfactory for a load factor of 12g's. The latter load condition is identical to that used for the outboard wings. The corresponding 12g shear, moment and torque distributions for the canard are shown in figure 30. The canard was designed later than wing; consequently, the 8g maneuver condition has already been changed from 9144 M (30,000 feet) to 7620 M (25,000 feet). Design of the canards utilized the new load condition rather than the prior 8g maneuver loads. The associated 8g

aeroelastic tailoring loads are shown in figure 31. The required structural twist for the canard at the revised maneuver condition is given in figure 32. A total structural twist of 3.9 degrees was desired.

The preliminary design of the canard covers was performed by use of the AC87 computer program. Again, the design started with ply layups using the $(0^{o}/45^{o}/-45^{o})$ configuration. Results for the $(\theta^{o}/45^{o}/-45^{o})$ family of laminate orientations are shown in figures 33. The $(15^{o}/45^{o}/-45^{o})$ design shows the most desirable structural behavior in terms of matching the required 8g structural twist requirements. Evaluation of its deflected shape using AC89 showed that the structure was less stiff than indicated by AC87. A weight comparison was made of the candidate ply layups, and the results are plotted on figure 34. As shown in the figure, the layups using θ^{o} equal to negative values incur a weight penalty over those layups with a θ^{o} equal to positive values. Also, the twist is not as good. In order to get the twist closer to the desired shape, the $\theta^{o} = 15^{o}$ plies were modified, resulting in a small increase in weight (figure 34). However, the twist curve was matched closer, as shown in figure 35 The matched twist was improved by adding more 15^{o} plies.

The modified $(15^{o}/45^{o}/-45^{o})$ layup was provided to the NASTRAN finite element model and run under the 8g tailoring load. The results for the twists of front-spar to rear-spar and leading-edge to trailing-edge are plotted in figure 36. As shown in figure 36, the LE/TE and FS/RS twists are identical outboard of the 66 percent station of the structural box. Inboard, the LE/TE match the twist closer, due to the slotting of the leading edge. Figure 37 shows a plot comparison of the AC89 output versus NASTRAN. The AC89 and NASTRAN tracked closely both in magnitude and shape for the FS/RS twist, as shown in the figure, verifying tool correlation.

Final canard twist prediction. - During the drawing layout and actual manufacture of the canard, changes were made for either design or manufacturing considerations. Figure 38 depicts the desired aeroelastic tailoring cover ply thickness versus the as-built thickness. The inboard thicknesses were larger than desired, and although they did not affect the shape of the twist curve to any prohibitive degree, they did reduce the magnitude of twist. Figures 39 and 40 present the desired and actual number of plies used on the aircraft, respectively.

Again, once these changes were incorporated, the finite element model was run using the strength and tailoring loads. Figure 41 depicts the deflections for the front and rear spars, and figure 42 predicts the final twist. As can be seen from the figure, the magnitude of the twist decreases from 4.5^{o} to 4.05^{o}. This closely approximates the desired twist of 3.9^{o}.

A similar change occurred on the leading-trailing edge surfaces. Figure 43 depicts the canard LE/TE deflections, Figure 44 depicts the final leading edge to trailing edge twist of 4.0^{o} versus the desired twist of 3.94^{o}.

TEST PROGRAM AND RESULTS

In order to verify the analytical tools used for aeroelastically tailoring lifting surfaces, one of the NASA/Rockwell HiMAT aircraft was subjected to an 110 percent 8g test load. The test was conducted to verify structural integrity of the aircraft and to verify how well the aeroelastic tailoring was accomplished. This section presents those results. Only test data to 100 percent of the 8g loading were used in the data reduction.

Test Configuration

Figure 45 shows the HiMAT aircraft in the test setup. It is a view looking directly at the aircraft. The test configuration consists of the all-up RPRV aircraft, A/V-2, as specified below:

- Complete airframe with maneuver leading edges on the wing and canard.
- The landing gear was on, but the nose gear skid and oleo structure were removed so that the loading mechanism to apply a 907.2 kg (2000 pound) vertical reaction load at the nose gear could be attained. A dummy oleo was installed in lieu of the aircraft oleo.
- The access panels were installed, including the hydraulic access panel.
- The hydraulic system was operational so that the rudder, aileron, elevon, elevator, and canard flap surfaces could be locked in the trail position.
- There was no nose or aft module ballast.
- No fuel was on board.
- Neither the engine nor the pallet was installed. A dummy engine beam was installed to apply reactions at the engine mounts.
- The aft module was installed for the test.

Test Loads and Procedures

In conducting the 8g structural deflection test, the vehicle reaction points were the air vehicle captive flight hooks. The unbalanced roll component was reacted through the engine mounts. Any other small roll component was reacted through the nose gear axial lug. The canard and outboard wing, (including leading and trailing edge surfaces) the rudder, and the wing tip fin were dead-weighted (zeroed) out. Neither the fuselage nor inboard wing was dead-weighted out.

A distributed 8g structured load was applied to each canard, outboard wing, tip fin, and vertical stabilizer surface by the use of suction pads on the upper surface of the component as shown in figure 45. Also, distributed 8g loads were applied to the leading and trailing edge surfaces of the wing and canard. The loads were applied at room temperature. A 907.2 kg (2000 pound) inertia load was applied to the axle of the nose gear lug. Also, 8g engine inertia loads of 2814.13 kg (6204 pounds) were applied to the three engine mount supports. No loads were applied to the fuselage, inboard wing, or rudder boom. No negative loads were applied. During loading no supporting or loading structure influenced the test results in any manner.

The distributed loads used for the test were the 8g flight loads. These loads were reduced to pad loads and applied to the aircraft. Figure 46 shows the pad identification number used in loading the aircraft wing. Table III presents the pad identification number, pad location, and load magnitude used for the test. Figure 47 and table IV present the locations of the pads on the canard, their pad identification number, and load magnitude. Figures 48 and 49 present rudder and wing tip fin loads and pad locations used in the test.

In conducting the test, the following procedure was used:

- Forty percent of the 8g load was applied to the canard, wing and verticals. Likewise, 40 percent load was applied to the nose gear and engine.

- The loads were applied concurrently, incrementally, and symmetrically about the fuselage. The loads were applied in 10 percent increments.

- The test set-up was checked for proper loading and functioning during this loading phase.

- After this system checkout, the aircraft was loaded to 80 percent of the 8g load in 20 percent increments. From the 80 percent level, the vehicle was loaded to 100 percent of the 8g limit load in 10 percent increments. The strain gage and deflection test data during this loading phase were examined to verify that there were no anomalies.

- After that loading, the aircraft was cycled three times, the gages were zeroed-out, and the aircraft was loaded concurrently, incrementally, and symmetrically in 20 percent increments until 80 percent of the test load was reached.

- When the 80 percent level was reached, the aircraft was loaded in 10 percent increments until 110 percent of the 8g design limit load was reached.

- The load was reduced in the same increments.

- Data were recorded for all gages, including spares. The data were recorded, incrementally, in both loading directions. Only data to the 100 percent level were used for reduction.

Load Correlation

In order to verify that the proper external load was applied to the test aircraft, a series of computer runs were made prior to the test to insure that the applied test load matched the distributed NASTRAN 8g flight load. This was done as follows.

A pad layout of the lifting surface was constructed, as shown in figure 46, for the wing. Pad loads were calculated that represented the applied distributed 8g net flight load. These pad loads were then integrated along the span of the lifting surface and compared to the NASTRAN distributed air load.

Figure 50 shows the correlation between the finite element model distribution and the pad test loads for the wing shear. Also, superimposed on figure 50 is the shear load measured during the test. That value is approximately 1462.41 kg (3224 pounds). As can be seen from figure 50, the correlation between applied test and flight loads is excellent.

For the canard, the forces used to load the structure were applied normal to the canard surface, which is at a 20^{o} dihedral. As shown in figure 51, the correlation between the applied test pad shear loads and the finite element model distribution is good. However, the resulting shear and C_p are slightly inboard of the desired loading. This resulted in a lower moment being applied to the canard, and consequently, a lower twist resulted. Instead of an in-flight twist of approximately 4.0^{o}, as shown in figure 52, for the FS/RS, the test loads predicted a lower twist of 3.8^{o}, as shown on figure 52. For the canard LE/TE, the test loads predicted a twist of 3.8^{o}, as shown in figure 53, versus a flight twist of 4.0^{o}, as shown on figure 44.

Deflection Transducers

Sixty-three deflection transducers were used to measure the deflection of the lifting surfaces. The number of points measured on each surface are as follows:

31 Left-hand wing

24 Left-hand canard

6 Right-hand wing

2 Right-hand canard

Figures 54 and 55 depict the location of the gages on the wing and the canard. Table V specifies the grid location of the gages. The locations of these gages were used in calculating the canard and wing twist due to the test loading.

Also shown in the table are the size, gage direction, and property number of the gages. The size listed is the maximum extension of the gage. All gages were installed and zeroed around their mid-point reading. The accuracy of the gages is one percent. Therefore, as an example, for size 10, the gage reading would have an accuracy of $\pm$.05 inches. All gages read in a vertical direction and the property number is the Rockwell International identification of the gage.

Strain Gages

The strain gages used for the HiMAT static test were divided into two major categories; ground test gages and flight test gages. The ground test gage locations were determined by Rockwell International and the flight test gage locations were specified by NASA.

The purpose of the ground test strain gages was to verify structural load paths, to insure that no component was structurally overloaded, and to reduce recorded test strains to stresses and compare them to the stresses from the finite element model. The ground test gages were mounted externally on the lifting surfaces and were removed after the test. Figures 56 and 57 depict the location of the ground strain gages. Table VI specifies the location and coordinates of the strain gages.

The strain gages specified by NASA/DFRC are still operational and are to be used to record flight loads. Those on the external surfaces have not been removed. Figures 58 and 59 present the NASA/DFRC gages for the wing and canard. Table VII presents the coordinate locations of those gages.

Test instrumentation. - A total of 107 ground type strain gages were installed on the aircraft for the 8g test. In addition, data from 42 prime and 42 spare strain gages installed for the flight program were recorded during the tests. These strain gages are distributed over the airframe as follows:

Ground Test Strain Gages

Fuselage	77
Wing	15
Canard	10
Vertical Stabilizer	2
Tip Fin	3
	107

Flight Test Strain Gages

Wing	20
Canard	8
Tail Boom	8
Actuators	6
	42

Only the wing and canard gages were used in the data reduction. The other gages were used in monitoring the test to insure that no component was over loaded.

As listed below, 34 of the 107 ground installations are three channel 45^{o} rosettes and the remainder are single channel axial and shear strain gages. The 42 flight installations consist of single channel load cells and bending, shear and torsion strain gage bridges.

Ground Test Strain Gages

Type A1-1 Axial	42
Type S1-2 Shear	31
Type R3-1 Rosette	34
	107

Flight Test Strain Gages

Type 30 Bending	16
Types 53, 54 and 56 Shear	19
Type 45 Torsional Shear	1
Type 72 Load Cell	6
	42

The ground test strain gage types are defined in reference 4 and the flight gage types are defined in reference 5.

Test data reduction. - The standard Los Angeles Division computer program for processing structural test data (reference 6) was used to reduce the strain gage data. The only change made for the HiMAT program was to expand the program to cover fully anisotropic material. Previously, the program had been limited to orthotropic material. The equations used by the computer program for the strain to stress reduction are discussed in the following sections for each type of strain gage used.

Ground test strain gages. - The strain gage output for the A1-1 type gage is the axial strain, ε_x. The strain to stress equation is:

$$\sigma_x = E_x \varepsilon_x$$

where E_x is Young's modulus in the strain gage x-direction. Figure 60 describes the reference axis for the ground gages.

The strain gage output for S1-2 is the shear strain γ_{xy}. The strain to stress equation is:

$$\tau_{xy} = G_{xy} \gamma_{xy}$$

where G_{xy} is the shear modulus in the x-y reference system.

The type R3-1 rosette consists of three independent axial strain gages (1, 2 and 3) arranged as shown in figure 60. The x-y reference system is defined by the rosette orientation and the x'-y' axis defines the reference system in the corresponding NASTRAN element. Strain readings from the rosette are reduced to stress in the x'-y' reference system for direct comparison with NASTRAN results.

The rosette output consists of three strains, ε_1, ε_2, ε_3. The strain tensor in the x-y reference system is obtained from ε_1, ε_2, and ε_3 by using the equations:

$$\varepsilon_x = \varepsilon_1$$

$$\varepsilon_y = \varepsilon_3$$

$$\gamma_{xy} = 2\varepsilon_2 - \varepsilon_1 - \varepsilon_3$$

Standard tensor rotation into the finite element model x'-y' reference system gives:

$$\varepsilon_x' = \varepsilon_x \cos^2\theta + \varepsilon_y \sin^2\theta + \gamma_{xy} \sin\theta \cos\theta$$

$$\varepsilon_y' = \varepsilon_x \sin^2\theta + \varepsilon_y \cos^2\theta - \gamma_{xy} \sin\theta \cos\theta$$

$$\gamma_{xy}' = 2(\varepsilon_y - \varepsilon_x) \sin\theta \cos\theta + \gamma_{xy} (\cos^2\theta - \sin^2\theta)$$

Finally, from Hookes' Law, the stress tensor in the x'-y' reference system is:

$$\sigma_x' = E_{11}\,\varepsilon_x' + E_{12}\,\varepsilon_y' - E_{13}\,\gamma_{xy}'$$

$$\sigma_y' = E_{12}\,\varepsilon_x' + E_{22}\,\varepsilon_y' - E_{23}\,\gamma_{xy}'$$

$$\tau_{xy}' = -E_{13}\,\varepsilon_x' - E_{23}\,\varepsilon_y' + E_{33}\,\gamma_{xy}'$$

where the elastic coefficients E are taken directly from the NASTRAN model. The minus signs in the equations are due to the fact that the data reduction program sign convention for shear is opposite to that of NASTRAN. Principal stresses are computed from the cartesian stresses σ_x' σ_y' and τ_{xy}' in the usual way.

Flight test strain gages. - In referring to figure 61, the strain gage bridge output for the type 30 bending gage can be expressed as the average bending strain in the x direction.

$$\varepsilon_{(INDICATED)} = \frac{\varepsilon_{x\ (LOWER)} - \varepsilon_{x\ (UPPER)}}{2}$$

The strain to stress reduction is based on the equation:

$$\sigma_x = E_x\,\varepsilon_x = E_x\,\varepsilon_{(INDICATED)}$$

where E_x is the average (upper and lower) Young's modulus in the x direction. Notice that the correct strain to stress relationship is:

$$\sigma_x = E_{11}\,\varepsilon_x + E_{12}\,\varepsilon_y - E_{13}\,\gamma_{xy}$$

and that the reduction assumes that the $E_{12}\,\varepsilon_y$ and $E_{13}\,\gamma_{xy}$ terms are negligible. This assumption is reasonably valid for bending bridges installed on metal structure because E_{12} is small compared to E_{11} and E_{13} is zero. For bending bridges installed on graphite-epoxy, this assumption leads to

gross errors in the measured stress because E_{12} is not small and E_{13} is not zero. Consequently, stresses between ground type rosettes and adjacent flight type bending gages on graphite-epoxy should not be compared. The only valid comparison is between the rosette strain ε_x and the bending bridge strain ε_x.

The value of the flight bending gages on graphite-epoxy is in measuring flight loads. The ratio between ε_x, ε_y, and γ_{xy} tends to remain reasonably constant in flight. Hence, the measurement of ε_x alone in conjunction with calibration factors obtained during the ground tests gives a reasonable measure of the flight loads.

The gage output for the type 53 and 54 (single surface) and type 56 shear (back-to-back) strain gage is half of the shear strain as shown in figure 61, or it is:

$$\gamma_{(INDICATED)} = \frac{\gamma_{xy}}{2}$$

The shear stress is:

$$\tau_{xy} = G_{xy}\,\gamma_{xy} = 2G_{xy}\,\gamma_{(INDICATED)}$$

where G_{xy} is the shear modulus in the x-y system.

The gage output for the type 45 torsion gage is one-half of the average torsional shear strain or it is:

$$\gamma_{(INDICATED)} = \frac{\gamma_{xy}\ (UPPER) - \gamma_{xy}\ (LOWER)}{4}$$

The torsional shear stress is:

$$\tau_{xy} = G_{xy}\,\gamma_{xy} = 2G_{xy}\,\gamma_{(INDICATED)}$$

where G_{xy} is the shear modulus in the x-y reference system.

The Type 72 load cell strain gage installation was used exclusively on calibrated actuators. The gage output is the strain $\varepsilon_{(INDICATED)}$. The strain to load equation is

$$Load = F\ \varepsilon_{(INDICATED)}$$

where F is a calibration factor derived by test.

Correlation of Strain Gage Readings

This section presents the results of comparing the predicted stresses with the calculated test gage stresses for both the ground and flight test strain gages. Gages were located at maximum stress locations and the number restricted for budgetary considerations. The 8g test proved that the structural load paths occurred as predicted for the wing and canard. Also, there was good correlation of predicted stresses versus test stresses for the canard. The wing correlation was inconsistent and correlated poorly.

Ground-test strain gages-outboard wing and canard. - The 8g static test results were compared with the theoretical results using bar charts. This section presents the results of the comparison for the ground test gages on the outboard wing and canard. Since the gage results are compared with the results of the finite element panel that encloses the gage, refer to figures 56 and 57 to determine the location of the panel and gage being discussed.

Three different stresses, longitudinal (σ_x), transverse (σ_y), and shear (τ_{xy}), are developed in each finite element skin panel. The rosette ground test strain gages record strains in three directions, which are then used to calculate the longitudinal (ε_x), transverse (ε_y), and shear (γ_{xy}) strains. These are then multiplied by the applicable Hooke's matrix to obtain the gage longitudinal (σ_x), transverse (σ_y) and shear (τ_{xy}) stresses that are to be compared with the theoretical finite element panel stresses.

Each one of the three stresses are compared on different charts. Table VIII is a summary of the stresses for the ground test gages and the predicted stresses from the finite element model for the outboard wing and canard. In addition to the stresses, other data listed on the table

are gage number and type, and the percent difference between the average test gage calculations and the predicted stress values. The average test gage stress value calculated was determined by averaging the strain read during the loading and unloading of the test specimen.

The first comparison chart is presented in figure 62. This figure presents a bar chart comparison between the test gage and predicted longitudinal stresses (σ_x) for the ground test gages on the outboard wing. The lamina shear modulus used in the finite element solution is $G_{LT} = 2.413 \times 10^6 \frac{kN}{m^2}$ (0.35×10^6 psi).

As shown in figure 62, the predicted stress is higher at every gage than the test gage calculated stress and reverse magnitude at gages 101 and 102. The two upper surface leading edge gages, 101 and 102, show panel compression while the test gages show tension. The load condition applied during the test resulted in wing up-bending, and logically the upper wing surface should be in compression. Since there were no unusually high loads applied in this area, the gage setup, wiring, and computer readout were verified. No error could be found, so there is no satisfactory answer for the stress reversal at the gages. A similar reversal occurred at gage 110. They are included for completeness.

The first five gages shown in figure 62 (gages 1, 2, 3, 4, and 117) are located on the wing box structure. Examining these values in tabular form we have:

GAGES ON G/Ep EXCEPT 117	PREDICTED STRESS, σ_x kN/m^2 (LBS/IN^2)	GAGE STRESS, σ_x kN/m^2 (LBS/IN^2)	FACTOR (PREDICTED STRESS) / (GAGE STRESS)
1	60099.6 (8716.4)	18523.4 (2686.5	3.2
2	44159.7 (6404.6)	26735.4 (3877.5)	1.65
3	38956.7 (5650.0)	27390.4 (3971.5)	1.42

GAGES ON G/Ep EXCEPT 117	PREDICTED STRESS, σ_x kN/m^2 (LBS/IN^2)	GAGE STRESS, σ_x kN/m^2 (LBS/IN^2)	FACTOR (PREDICTED STRESS) / (GAGE STRESS)
4	16155.0 (2343.0)	3426.8 (497.0)	4.7
117 (B-G/Ep)	69189.0 (10035.0)	37818.0 (5485.0)	1.83

No common factor exists for these gages; however, the load path developed during the test can be observed by comparing the stress results at gages 1 and 117. The location of these gages is snown in figure 56, and as can be seen, they are located in an area of high stress loading. The test gage stress shows that for panel 1021124, the longitudinal stress is σ_x = 18523.4 $\frac{kN}{m^2}$ (2686.5 lbs/in^2) and increases to σ_x = 37818.0 $\frac{kN}{m^2}$ (5485.0 lbs/in^2) in panel 1021134. This load buildup along the rear spar going inboard is typical of swept wing aircraft and confirms the structural load path of the wing.

In comparing gages 2 and 3, by taking the difference between ratioed readings, the difference is approximately 14 percent. This is good correlation between test gage readings. The material is all graphite-epoxy in this area and of the same thickness, 4.27 mm (.186 incn). Gage 4 is located on graphite-epoxy, which is in an area of considerable fiber glass plies. Consequently, this area can be expected to strain greater and indicate a higher factor than the gages 1 to 3. Gage 117 is in the boron-graphite-epoxy area, and its strain can be expected to be lower due to the boron interleaving and thickness compared to gage locations 2 and 3 (t = 7.21 mm (.284 inch) vs. 4.27 mm (.168 inch), respectively).

A plot of the percentage differences in the longitudinal stresses, σ_x, of the test gage readings and predicted readings are shown in figure 63. The gages vary from 0 to 174 percent and the mean value is 85 percent. However, when only the structural box gages are considered, the correlation is better having a mean value of 57 percent. Test gages 108, 3, 2, and 117 have a mean correlation of 37 percent with predicted stresses. Gages 109,

103, 4 and 1 correlate approximately 77 percent with predicted results. Gages 101, 102, and 110 are extremely unreliable, having a reading of 159 percent over the test gage reading.

In figure 64, the transverse (σ_y) stresses are compared, and as can be seen from the figure, they show no common ratio factors. Also, the stress reversals occur not only at gages 101 and 102, but also at gages 1, 103, and 108. The percentage of difference between the stress readings vary from -17 to -112 percent. This erratic behavior indicates that Poisson's ratio is not as predicted, and consequently not only affects these stresses, but also those stresses in the x-direction shown previously on figure 62, which were reduced using the strain gage equations previously described.

Figure 65 shows the shear stress comparison. Again, no common factor is prevalent, and stress reversals occur at test gages 1, 2, 3, 4, 102, 110 and 117. Since the sign convention to develop the gage shear stress is opposite to the convention used in NASTRAN, the sign of the gage shear stress was reversed before the value was plotted. However, even if absolute magnitudes are compared, the stresses differ on an average of 76 percent.

Figures 66, 67 and 68 display the stresses for the ground test gages on the canard. The layup orientation for the canard box was $15^{o}/\pm45^{o}$ and is fiber dominated rather than matrix dominated as was the wing layup. This layup produced better correlation between gage and predicted stress values, especially in the longitudinal (σ_x) direction (figure 66). Gage 105 was installed, but malfunctioned during the test. Consequently, its readings are not shown. The difference between ground and test data is 25 percent. And if only the inboard gages, 5, 6, and 7 are considered, the correlation is very good - being 10 percent. The gage locations are shown in Figure 57.

The transverse stress comparison, figure 67, shows good correlation of data for gages on the canard structural box (gages 5, 6, 7, 8, and 115). Also, the stresses progressively increase along the rear spar going inboard as shown when examining the test gage readings of gages 8, 7, 6, and 5. Again, verifying a correct structural load path for the rear spar; especially, with test gage reading 5 being larger than 6, indicates that the load is definitely not drifting forward.

The shear stress comparison, figure 68, shows that most of the test gages read lower stresses than predicted. However, as shown on the figure,

when considering absolute magnitudes of the stress values, better correlation is achieved for the canard box shear stresses than for the wing.

Flight test strain gages-outboard wing and canard. - Table IX lists the flight test strain gage identification number and the types of gages used on the inboard wing, outboard wing, and canard. From this table, gages on the outboard wing were selected for correlation purposes.

On the outboard wing, the inner row of chordwise bending bridge flight test gages cross the ℄ of the structural box at approximately X_F = 130.3 cm (51.3 inches). The gage numbers are 2020, 1020, 1021, 2021 and are shown in figure 58. The data recorded by these gages can be expressed as the average uniaxial strain between the upper and lower wing skins, and is shown in table X.

In order to compare the test gage strains with predicted strains, the following calculations were performed. For a given finite element panel, the Hookian matrix was inverted and multiplied by the predicted stresses. The results are the predicted strains. In comparing flight test gage results to predicted results, only the longitudinal strain (ε_x) can be examined and compared. The equation governing the longitudinal strain calculation is:

$$\{\varepsilon\} = [E]^{-1}\{\sigma\}$$

The results of these calculations for the skin finite element panels 1021117-1021124, are shown in table XI. Average strain values for the panels have been calculated and are also included in the table.

The data in tables X and XI are graphically displayed in figure 69. Two abscissas are shown on the figure. They represent: (1) the percent chordline distance through panel c.g., and (2) percent chordline location of gages. Also shown are the locations of the NASTRAN panel c.g.'s and the strain gage number. As shown in figure 69, the NASTRAN predicted strains follow the magnitude of the flight test bending strain gages quite well. Also, load path correlation is verified since the rear spar gages, numbers 1021 and 2021, figures 58 and 69, increase in magnitude as the load approaches the rear spar.

For the canard, this same type of investigation could not be made since there is no row of flight gages on the canard.

Strain Gage Analysis

In some cases of correlating wing and canard stresses developed from test data to those developed by finite element analysis, the correlation was good. For example, the outboard wing gages 2 and 3 present a difference of only 14 percent between their gage readings and test results. For the canard, gages 5 and 6 correlated witnin 2 percent of test results.

However, because of discrepancies and inconsistent results, investigations were performed in an attempt to resolve the discrepancies in the reduced data. The studies conducted consisted of investigations of:

- Lamina shear modulus
- Material property data

Lamina shear moduli. - Due to the wing cover construction being $+35^{\circ}/\pm50^{\circ}$, it is matrix dominated, and consequently, the shear modulus term should have a strong effect on the stresses developed. Therefore, the first study conducted was the investigation of the lamina shear modulus.

Conventional graphite/epoxy ply layups usually have a value of lamina shear modulus of 4.689×10^6 kN/m^2 (0.68×10^6 psi). However, from test data and past experience with unconventional layups, Rockwell determined that the lamina shear modulus was more correctly represented by a value of 2.413×10^6 kN/m^2 (0.35×10^6 psi) as specified in table I and was used in the program. However, since discrepancies in the gage readings occurred, it was decided to explore the effect of the shear modulus on the gage readings.

As shown in figures 70 through 72, the lamina shear modulus value was changed to a conventional modulus value of 4.689×10^6 kN/m^2 (0.68×10^6 psi). Calculations were rerun with this value in the finite element model and with test strain gage readings. Only wing box gages 1, 2, 3, 4, and 117 were investigated.

Figure 70 shows the correlation between the test and predicted longitudinal stresses (σ_x). As shown in the figure, correlation is slightly improved for gages 1, 2, 3, and 117 for the conventional shear modulus

value rather than the test modulus. The average stress correlates within 32 percent of the predicted stress, whereas before it correlated within 43 percent of the predicted value as shown on figure 62. Gage 4 results are questionable. In figure 62, where $G_{LT} = 2.413 \times 10^6$ kN/m^2 (0.35×10^6 psi), the predicted stress at gage 4 is almost five times the magnitude of the test stress. However, with the change in shear modulus to 4.689×10^6 kN/m^2 (0.68×10^6 psi), the predicted stress is now approximately 25 percent lower than the test stress; in effect, a gage reversal.

Figure 71 shows the transverse stress (σ_y) comparisons and again inconsistent correlation is observed with sign reversals apparent at gages 1, 4, and 117. However, correlations on figure 64 using the test G_{LT} are better than those on figure 71 using the conventional G_{LT}. This is especially true at gages 2 and 3.

The shear stress comparison, figure 72, does exhibit two common features. The first is that the absolute magnitude of all test gage stresses is higher than the predicted stress at every gage, and secondly, stress reversals occur at every gage. One very interesting fact that can be observed by comparing the data shown in figure 72 with the location of the gages shown in figure 56, is that better correlation exists between predicted and gage results, considering only absolute magnitudes, where the out of plane deflection is small. This indicates that gage shear is adversely affected by vertical deflection.

For the canard, the next three figures show the effect on the stresses of changing the shear modulus, G_{LT}, to the higher value of 4.689×10^6 kN/m^2 (0.68×10^6 psi). The longitudinal stress correlation, figure 73, is improved; however, transverse and shear stress correlations do not improve (figures 74 and 75).

As a result of using conventional shear modulus data, the following table can be constructed:

Better Correlation Using $G_{LT} = N \times 10^6$ kN/m^2

	N		
	σ_x	σ_y	γ_{xy}
Wing	4.689	2.413	2.413
Canard	4.689	2.413	2.413

From the above table, it can be concluded that the conventional shear modulus values of 4.689×10^6 kN/m^2 (0.68×10^6 psi) does improve strain gage correlation in some instances, but the percentage differences between the test and theoretical values remain too high. Increasing the shear modulus decreases Poisson's ratio, which tends to benefit correlation, but it still does not permit correlation among all the gages. Also, there is more sign reversal when using $G_{LT} = 4.689 \times 10^6$ kN/m^2 (0.68×10^6 psi), as can be seen when comparing figures 68 and 75.

In an attempt to obtain additional correlating data for the wing, strain plots were made for the outer row ($X_F \sim 143$ cm) of flight test gages 2025, 1025, 1026, and 2026.

The location of these gages is shown in figure 58. The finite element panels involved are 1021109 thru 1021116. The data for the flight gages are tabulated in table XII and for the panels in table XIII. The results are plotted in figure 76. This figure indicates that the test strain gages are reading low compared to both theoretical solutions. Both moduli give about the same results with the test moduli, $G_{LT} = 4.689 \times 10^6$ kN/m^2 being closer to the test data. A similar plot of flight gages 2020, 1020, 1021, and 2021 on the outboard wing, is shown in figure 77. As shown in the figure, using $G_{LT} = 2.413 \times 10^6$ kN/m^2 results in a better match of the test data than using $G_{LT} = 4.689 \times 10^6$ kN/m^2. The tabulated data for that figure is shown in table X for the gages and tables XI and XIV present the data for the NASTRAN panels.

For the canard, this same type of investigation was made for ground test gages 5 and 6 and finite element panels 5011110 and 5011111. The strain results are shown in figure 78. The indication here is that test results correlate better with $G_{LT} = 4.689 \times 10^6$ kN/m^2 (0.68×10^6 lb/in^2).

The reduction of the test data clearly indicates an inconsistency regardless of the constant value of the shear moduli used. It can be concluded from the reduced readings that the shear moduli of 2.413×10^6 kN/m^2 (0.35×10^6 psi) consistently correlated better than did the value of 4.189×10^6 kN/m^2 (0.68×10^6 psi). However, since neither value gave satisfactory answers repeatedly additional testing is recommended to establish the shear moduli property value.

Material property data. - The primary cause, then, for the inconsistency in the measured and predicted stresses is apparently the original

elastic coefficients and transformations used in the strain to stress reduction. Consequently, the second study investigated the original property data and their effects on the Hookian transformation matrix through AC84.

In the initial design of the aircraft, the ply layup was selected as $+30^{o}/\pm50^{o}$. A test program was conducted for that layup to establish the basic material properties. It was determined through the test program that the properties were linear. Consequently, the stress-strain curves were used as linear values, and the transformations of the elastic coefficients were linear. The final ply layup was changed to $+35^{o}/\pm50^{o}$ for manufacturing considerations; however, past experience indicated that such a small change in θ_1 from 30^{o} to 35^{o} produced negligible changes in material properties. Consequently, property data were extracted from the $+30°/\pm50°$ tests and used in determining property data for the $35^{o}/\pm50^{o}$ layup. Small coupon testing verified that 5^{o} made very little change in material allowables.

Examining the material property at room temperature, as shown in figures 79 through 83, indicates that the material behaves nonlinearly and not linearly as assumed in the design of the aircraft. As shown in figures 80 and 82, transverse nonlinearity occurs at low strain levels for both tension and compression. Also, for both the transverse tension and compression transverse strain values, nonlinearity occurs at lower levels than the nonlinearity effects for the shear strain, (figure 83).

These transverse properties have a pronounced effect on the stress reductions in the wing. For example, consider the computation of the spanwise stress for rosette number 1 at 100 percent load for the 8g condition. The strain to stress equation is:

$$\sigma_x = E_{11}\,\varepsilon_x + E_{12}\,\varepsilon_y - E_{13}\,\gamma_{xy}$$

The measured strains are

$$\varepsilon_x = 1960,\ \varepsilon_y = -1462,\ \gamma_{xy} = -552$$

Substituting the measured strains into the stress equation, the resulting stress in the x-direction of the finite element is:

$$\sigma_x = 37.44\ (1960) + 34.89\ (-1462) + 7.24\ (-552)$$

$$\sigma_x = 73382 - 51009 - 3996 = 18377\ kN/m^2\ (2665\ psi)$$

The elastic coefficient values are developed in Appendix D. Notice that the resulting spanwise stress depends on a small difference of large numbers between longitudinal and transverse strains. This indicates that relatively small errors in the elastic coefficients can be responsible for large discrepancies between measured and predicted stress. Also, as shown in the calculation, a large transverse elastic coefficient (E_{12}) has been developed based on the linear transformation of the stress-strain curves. The large transverse elastic coefficient, then, had a pronounced effect on the resulting stress. Had this value been developed based on the nonlinear curve, as shown in figure 84, its elastic coefficient would be smaller; consequently, the resulting stress shown in the above calculation would be more positive and correlate better with the positive value developed by the finite element model shown in figure 62.

In comparing the stresses in figures 62, 64, and 65, to the crossover nonlinearity stress levels, or strains, of figures 79 through 83, it can be seen that in most cases the finite element model is operating in the region of nonlinearity, usually in a higher nonlinear range than the test gages. However, the elastic coefficients provided to the finite element program were through a linear transformation. Consequently, the predicted stress magnitudes are higher than the aircraft should experience. Due to these nonlinearities in material properties and transformations, the predicted versus test stresses will not correlate in a consistent manner, as is shown, again, by the reduced data on figures 62, 64, and 65.

The canard skins are fiber-dominated due to the $+15^o/\pm45^o$ and will exhibit more linearity than the wing. Further, a similar calculation for the canard demonstrates better correlation between measured and predicted stress and less dominance of the transverse property. For example, for rosette gage 5, the measured strains are:

$$\varepsilon_x = 1569,\ \varepsilon_y = -701,\ \text{and}\ \gamma_{xy} = -134$$

Therefore, the stress is:

$$\sigma_x = 85.22\ (1569) + 22.82\ (-701) + 19.93\ (-134)$$

$$\sigma_x = 133710 - 15997 - 2671 = 115042\ kN/m^2\ (16686\ psi)$$

As the above calculation shows, the transverse property does not have a pronounced effect on stress reduction as in the matrix-dominated designs.

Consequently, for large nonlinearity behavior of materials, such as in the $+35^o/\pm50^o$ layup, stress values cannot be satisfactorily calculated unless the material property data is accurately known and nonlinearities are included in the calculations. For small nonlinearities, stress values can be satisfactorily calculated, as demonstrated by the canard stress calculations.

Test Twist Results

During the 8g test, deflections of the wing and canard were recorded and twist calculations performed based on those deflections. How well the test twists correlated to predicted twists are explained in the following paragraphs.

Figure 85 depicts the plot of front and rear spar deflections produced for both increasing and decreasing test loads. Also plotted on the figure are the predicted deflections. In checking the wing tip maximum deflection points, the correlation was excellent. The rear spar test deflection matched the predicted deflection by 93 percent based on the average readings. The front spar test deflection matched the predicted deflection by 95 percent, based on the average readings. Both the magnitude and the shape of the curves correlate well. The test deflections are presented in table XV.

Figure 86 depicts the test deflections for the leading and trailing edges of the outboard wing. Superimposed on the curves are the predicted deflection points. As shown on the figure, the deflected shape comparison is excellent. Also, the magnitudes are excellent. The leading edge achieved approximately 97 percent of predicted deflection, and the trailing edge achieved approximately 94 percent of predicted deflection based on the average deflections. The plots are shown for increasing and decreasing test loads.

For the 8g test load, figure 87 depicts test results versus predicted deflections for the canard. The upper curve presents deflections between the leading edge and trailing edge, and the lower curve predicts deflections between the front spar and rear spar. Also shown on the test results are predicted deflections. For the trailing edge, the test deflection at the tip are 2 percent higher than predicted and for the leading edge they are 17 percent higher. For the rear spar, the test deflections are 7 percent higher and 2 percent higher for the front spar. Again, the correlation of the test curves to predicted curves is very good

Based on those test deflections, curves were constructed to determine how well predicted twists compared with the twists determined by the test. Figure 88 shows the results for the wing structural box. As shown on this figure, the magnitude of the twist is approximately 4.45^{o} versus the predicted 4.94^{o}, for a correlation of approximately 90 percent. The shape of the curve is fair and it has been predicted that there is little degradation in the aerodynamic performance of the aircraft at the design lift coefficient, C_L=1.0 (Reference 7).

Figure 89 depicts the plots of the twists determined by test results and the predicted twist from the finite element model for the leading and trailing edges of the wing. As shown, the magnitude and shape are much better than that for the wing structural box. The test twist magnitude is approximately 93 percent of the predicted twist. Gage 8004, shown on figure 53, was relocated during the test. Consequently, its reading is neglected and the curve extrapolated to the wing tip station based on the FS/RS twist increasing towards the tip as shown in figure 88.

In conducting the test, the fuselage deflections were recorded and are plotted in figure 90. As shown in the figure, the fuselage deflection has negligible effect on the twist of the wing, which is at approximately 66-71 percent of fuselage length. For the canard, the fuselage effect on twist is also small and amounts to $.099^{o}$ increase over the raw test data presented in table XV. Figure 91 shows the effect of calculating twist with and without the horizontal component of the 20^{o} canted canard. As shown in the figure, the twist increases from $.05^{o}$ at the 40% spar to $.47^{o}$ at the 100% spar when the horizontal deflection component is included in the calculations. A similar effect occurs for the leading and trailing edges of the canard. These corrections were added to the raw test data presented in table XV and are shown in the following figures.

The correlation of twist for the canard structural box with predicted results, is shown in figure 92. The magnitudes were simulated within 87 percent and the shape of the curve was approximated quite well. The results for the canard LE/TE, are shown on figure 93.

Again, the discrepancies between the predicted twist and measured twist are attributed to material properties and nonlinearities; especially, for the matrix dominated layup of the wing. Since a linear value for the elastic constant was used, it has larger predicted value in nigh stress regions. In low stress regions, the predicted elastic constant would more closely approximate test conditions. This can be seen in figure 84 and was explained in the Strain Analysis section.

Because of the use of these higher predicted linear elastic coefficients, the deflections in the inboard high stress region of the wing should be lower than test. The outboard deflections which occur in lower loaded regions should be in the linear portion of its curves and therefore, approximate the test deflections. This phenomenon did occur and is shown in figure 94 for an overlay of predicted versus test deflection for the front and rear spar of the wing.

A similar plot was made for the canard, as shown in figure 95, and again, in higher stress regions, predicted elastic coefficients should be larger than if nonlinearity effects were included. Consequently, inboard predicted deflections should be lower than test deflections. And outboard, in lower stress areas they should match test results closer than inboard deflections. As shown in the figure, the test results confirm this, but more for the rear spar than for the front spar. Again, no direct magnitude comparison can be made, since no non-linearities were included in the predicted elastic coefficients, but the trend can be identified and is unmistakable, as shown on the figure.

Post Test Studies

Since conducting the 8g test on the HiMAT aircraft, additional studies have been performed. One is an additional material characterization test and the other is a post-GVT flutter analysis. This section presents the results of those studies.

Additional material property characterization. - Since the reduced test data did not consistently correlate with predicted stress data, additional testing was conducted of the wing 35°/±50° graphite-epoxy skin layup. Figures 96 to 99 present plots of the stress-strain data for the tension, transverse, compression, and shear tests. The vertical line on the figures indicates the linear versus nonlinear region. The figures indicate that at a very small strain the nonlinear region is reached. Also, the figures display the nonlinearity of the layup.

Calculations were performed using this new test data and comparing the results to the stresses calculated using the material property data assumed in the HiMAT program. Following are the calculations.

For rosette gage number 1,

NASTRAN (Original Test Data)

$$\begin{Bmatrix} \sigma_x \\ \sigma_y \\ \tau_{xy} \end{Bmatrix} = \begin{bmatrix} 37.44 & 34.89 & -7.24 \\ 34.89 & 48.06 & -3.45 \\ -7.24 & -3.45 & 34.20 \end{bmatrix} \begin{Bmatrix} \varepsilon_x \\ \varepsilon_y \\ \gamma_{xy} \end{Bmatrix}$$

At 100 percent, 8g load, the stresses are as follows

$\varepsilon_x = 1959.9$ $\quad \sigma_x = 18381\ kN/m^2$ (2666 psi)

$\varepsilon_y = -1461.8$ $\quad \sigma_y = -3778\ kN/m^2$ (-548 psi)

$\gamma_{xy} = 551.7$ $\quad \tau_{xy} = 9715\ kN/m^2$ (1409 psi)

New Test Data

$$\begin{Bmatrix} \sigma_x \\ \sigma_y \\ \tau_{xy} \end{Bmatrix} = \begin{bmatrix} 36.377 & 28.234 & 1.510 \\ 28.234 & 45.636 & 3.744 \\ 1.510 & 3.744 & 26.924 \end{bmatrix} \begin{Bmatrix} 1959.9 \\ -1461.8 \\ 551.7 \end{Bmatrix}$$

Again, at 100 percent load, and 8g load, the stresses are

ε_x 1959.9 σ_x = 30854 kN/m^2 (4475 psi)

ε_y = -1461.8 σ_y = -9308 kN/m^2 (-1350 psi)

γ_{xy} 551.7 τ_{xy} = 12342 kN/m^2 (1790 psi)

As shown in the calculations, for a small change in the Hookian matrix, a large change in stress magnitude results. Stresses in the longitudinal, transverse, and shear direction, x,y, xy, respectively, increase by approximately 68, 346, and 27 percent due to these small property changes; some of which occur in the nonlinear region of the material. These stress calculations indicate how sensitive the resulting stress magnitudes are to small changes in material properties.

HiMAT post-GVT flutter analysis results. - Flutter analyses for HiMAT were conducted using calculated modes obtained from a mathematical model that was adjusted (Reference 8) to provide an acceptable correlation with ship 2 ground vibration test results. Modes for the symmetric cases for both the unballasted and ballasted vehicle at mid-mission weight were calculated. The ballasted vehicle contained an additional 85.14 kilograms (187.7 pounds) in the forward fuselage to increase longitudinal stability. The unballasted configuration was analyzed at M=0.5, 0.85, 0.95, 1.2, and 1.6. The ballasted configuration was analyzed at M=0.5, 0.85, and 0.95. Doublet Lattice theory aerodynamics with interference effects was used for the subsonic Mach numbers, and Mach Box theory aerodynamics was used for the supersonic Mach numbers. Generalized aerodynamic forces were calculated for the wing, tip fin, vertical tail, and canard. The flutter solutions were obtained at four altitudes (sea level, 4,570, 9,140, and 15,240 meters (sea level, 15K, 30K, and 50K feet)) for each of the Mach numbers using the g-V approach through modal analyses. The match points (zero g crossing at the solution Mach number) were summarized yielding the flutter limits of figures 100 and 101.

Figure 100 shows the flutter limits for the unballasted configuration with no margin and with 44 percent q margin. The no margin limit clears a q of 71,820 Newtons per square meter (N/m^2) (1500 pounds per square foot (PSF))

through M=1.6. The 44 percent q margin limit clears a q of 47,880 N/m^2 (1000PSF) in the supersonic regime. Between M=0.84 and M=1.0 the 44 percent q margin limit extends below 47,880 N/m^2 (1000 PSF) to a minimum of 41,180 N/m^2 (860 PSF) at about M=0.90. Figure 101 shows the flutter limits for the ballasted configuration with no margin and with 44 percent q margin. The no margin limit has a small transonic restriction below 4,570 meters (15000 feet) altitude between M=0.92 and M=1.0. The 44 percent q margin limit clears 43,080 N/m^2 (900 PSF) subsonically and is deduced to clear 47,880 N/m^2 (1000 PSF) supersonically. It is also deduced that the effect of fuel changes will produce only small changes in flutter speed because the fuel is located in the stiff inboard wing where modal motions are relatively small.

CONCLUSIONS

It has been demonstrated by testing the HiMAT aircraft, that it is feasible to use unconventional, unbalanced graphite-epoxy ply layups to controll aerodyanmic twist. In order to predict twist and calculate stresses in unbalanced or highly matrix dominated graphite-epoxy laminates, material properties must be accurately known. The inconsistency between the predicted and measured twist and stress values may be attributed to insufficiently accurate material properties.

The tests further indicated that stress calculations are extremely sensitive to small changes in material property values for matrix dominated ply layups. Also, nonlinear regions are encountered at much lower strain levels than previously assumed, and especially in the transverse property direction. The tests also showed that not only are the compression and tension moduli different, but that the compression modulus is in the nonlinear region at a much lower strain level than is the tension modulus.

RECOMMENDATIONS

Analytical tools exist that can predict layups to produce desired twists, provided material properties are known. It is recommended, however, that additional effort be expended to advance those tools to incorporate more advanced design features. For example, nonlinearities should be incorporated into the preliminary design tools either by curve-fitting routines built into the programs, or options to input test data from which nonlinearity material property data curves are developed. With these nonlinear routines incorporated into the programs, an accurate twist and deflection behavior would be predicted in nonlinear regions.

Also, an automated routine to feed aerodynamic lines to tailoring programs should be developed so that changes can be made rapidly. Likewise, accurate, but preliminary, loads, flutter, divergence, and optimization routines should be included in the tailoring tools and verified against test hardware results. From this output, then, the sizing would automatically be fed into a finite element program to verify the structural integrity of the aircraft and the twist goals.

Rather than run finite element programs in a step-wise function using constant elastic coefficients, the finite element programs should be modified to accept nonlinear material property data. From these property data, then, deflection and stresses would be calculated and could be compared to data calculated from tests. It is especially important to incorporate transverse nonlinearities in order to attain stress correlation for matrix dominated layups.

Additional testing should be conducted on matrix dominated and unbalanced layups to characterize their properties. A better understanding of the stress gradient through the plies, transverse coupling, compression and tension moduli, and out of plane stresses should be establishing by testing. Also, material property sensitivity and coupling-term effects on analytical tools should be assessed.

In order to assess the influence of using low loads in flutter testing, structural influence coefficient tests should be conducted, at low and high load levels, to ascertain their effects on flutter prediction. Additional testing should be done to establish strain gage installations that measure strain through the ply thickness.

Appendix A

AC87 AEROELASTIC TAILORING STRAIN RATIO FORMULATION

Consider a swept wing box of N segments. Each segment is modelled as a set of identical advanced composite covers fully supported by a honeycomb core.

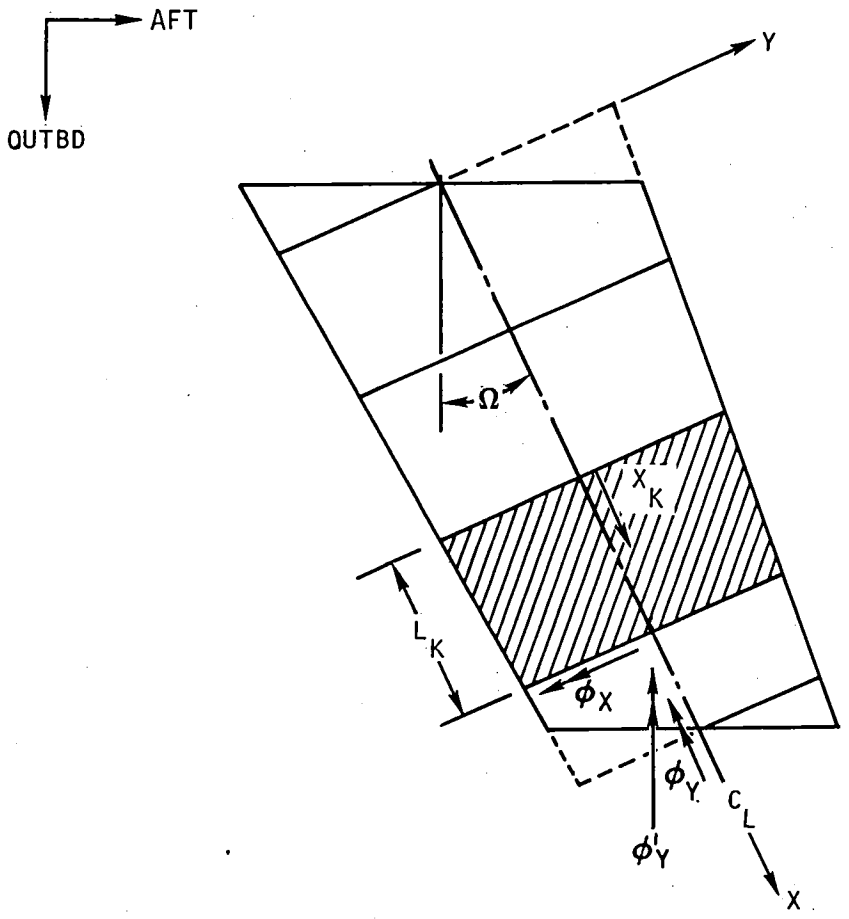

$$\phi'_{y_{(k)}} = \phi_{y_{(k)}} \cos \Omega - \phi_{x_{(k)}} \sin \Omega$$

Let

$$\Delta\phi'_{y_{(k)}} = \phi'_{y_{(k)}} - \phi'_{y_{(k-1)}}$$

$$\Delta\phi_{y_{(k)}} = \phi_{y_{(k)}} - \phi_{y_{(k-1)}}$$

$$\Delta\phi_{x_{(k)}} = \phi_{x_{(k)}} - \phi_{x_{(k-1)}}$$

Then

$$\Delta\phi'_{y_{(k)}} - \phi'_{y_{(k-1)}} = \left[\Delta\phi_{y_{(k)}} \cos\Omega - \Delta\phi_{x_{(k)}} \sin\Omega\right] - \left[\phi_{y_{(k-1)}} \cos\Omega - \phi_{x_{(k-1)}} \sin\Omega\right]$$

But

$$\phi'_{y_{(k-1)}} = \phi_{y_{(k-1)}} \cos\Omega - \phi_{x_{(k-1)}} \sin\Omega$$

Then,

$$\Delta\phi'_{y_{(k)}} = \Delta\phi_{y_{(k)}} \cos\Omega - \Delta\phi_{x_{(k)}} \sin\Omega \qquad (1)$$

For the k^{th} segment,

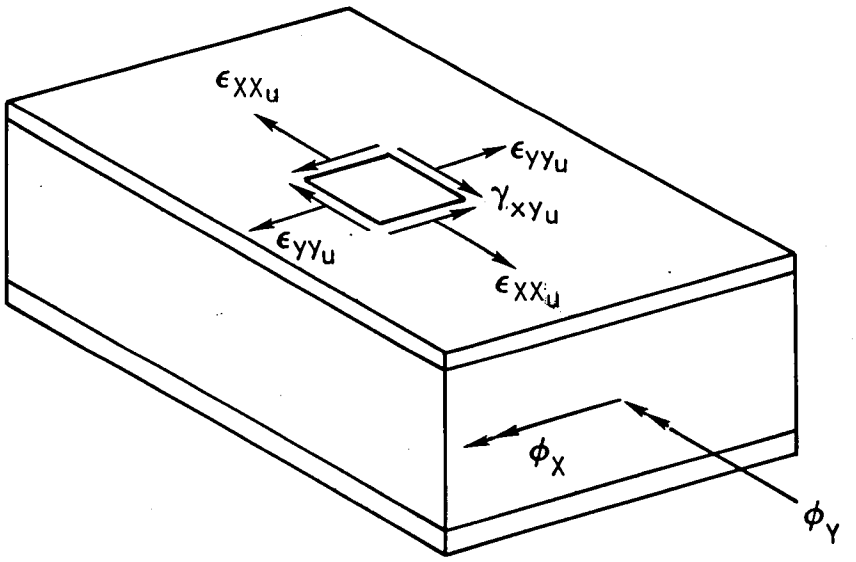

Then

$$\Delta\phi_{x_{(k)}} = \int_0^{L_K} \left[\frac{\epsilon_{xx_L} - \epsilon_{xx_u}}{H_k} \right] dx_k$$

$$\Delta\phi_{y_{(k)}} = \int_0^{L_K} \left[\frac{\gamma_{xy_L} - \gamma_{xy_u}}{2H_k} \right] dx_k$$

If both covers are identical,

$$\epsilon_{xx_u} = -\epsilon_{xx_L}$$

$$\gamma_{xy_u} = -\gamma_{xy_L}$$

Then

$$\Delta\phi_{x_{(k)}} = \int_0^{L_K} \frac{2\varepsilon_{xx_L}}{H_k} dx_k$$

$$\Delta\phi_{y_{(k)}} = \int_0^{L_k} \frac{\gamma_{xy_L}}{H_k} dx_k$$

To simplify analysis/design, assume that the stresses are constant along x_k for the k^{th} segment. Then

$$\Delta\phi_{x_{(k)}} = \frac{2\varepsilon_{xx_L}}{H_k} L_k \tag{2a}$$

$$\Delta\phi_{y_{(k)}} = \frac{\gamma_{xy_L}}{H_k} L_k \tag{2b}$$

Substituting equation (2) into (1)

$$\Delta\phi'_{y_{(k)}} = \frac{\gamma_{xy_L} L_K}{H_k} \cos\Omega - \frac{2\varepsilon_{xx_L} L_K}{H_k} \sin\Omega \tag{3}$$

Rearranging (3)

$$\gamma_{xy_L} = \frac{H_k \Delta\phi'_{y_{(k)}}}{L_k \cos\Omega} + 2\varepsilon_{xx_L} \tan\Omega \tag{4}$$

Since $\Delta\phi'_{y_{(k)}}$ is known for each beam segment, the laminates can be sized for this relationship between axial and sheer strain.

Appendix B

DIRECTION COSINES FOR COMPOSITE SYSTEMS

The following analysis develops the direction cosines for the coordinate system shown.

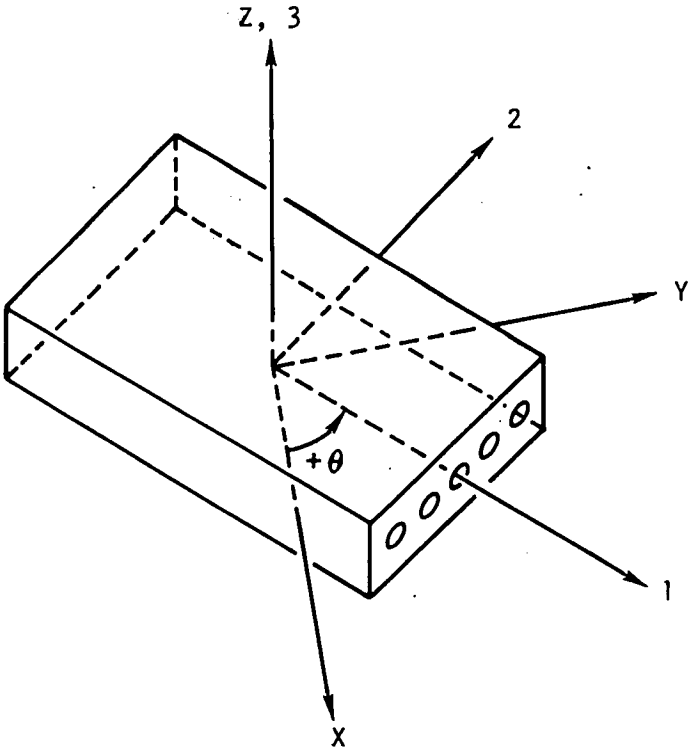

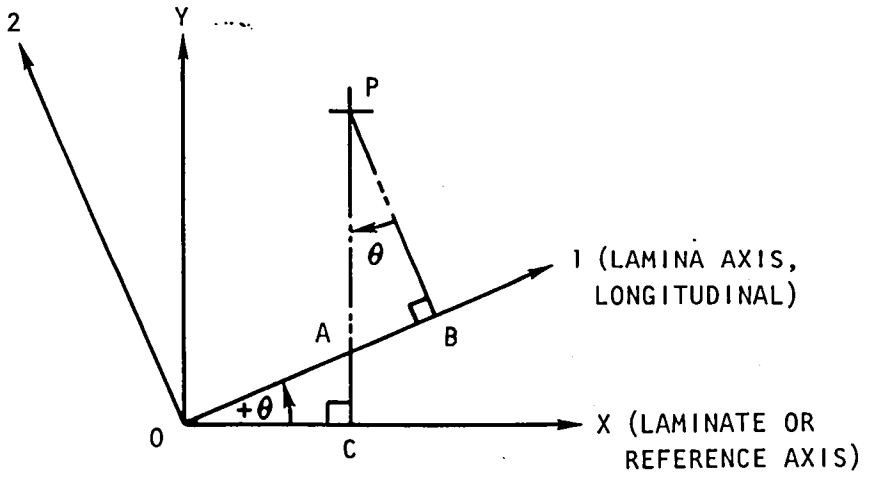

$$l_P = \overline{OA} + \overline{AB}$$

$$\cos \theta = \frac{\overline{OC}}{\overline{OA}}$$

But,

$$\overline{OC} = X_P$$

$$\therefore \overline{OA} = \frac{X_P}{\cos \theta}$$

$$\sin \theta = \frac{\overline{AB}}{\overline{AP}}$$

$$\overline{AB} = \overline{AP} \sin \theta$$

Substituting, we get

$$l_P = \frac{X_P}{\cos \theta} + \overline{AP} \sin \theta$$

$$\overline{AP} = Y_P - \overline{CA}$$

$$\therefore l_P = \frac{X_P}{\cos \theta} + (Y_P - \overline{CA}) \sin \theta$$

$$l_P = \frac{X_P}{\cos \theta} + Y_P \sin \theta - \overline{CA} \sin \theta$$

$$\tan \theta = \frac{\overline{CA}}{\overline{OC}} = \frac{\overline{CA}}{X_P}$$

$$\therefore \overline{CA} = X_P \tan \theta$$

Substituting, we have

$$1_P = \frac{X_P}{\cos \theta} + Y_P \sin \theta - X_P \tan \theta \sin \theta$$

But,

$$\tan \theta = \frac{\sin \theta}{\cos \theta}$$

$$\therefore 1_P = Y_P \sin \theta + \frac{X_P}{\cos \theta} - \frac{X_P \sin^2 \theta}{\cos \theta}$$

$$1_P = Y_P \sin \theta + \frac{X_P}{\cos \theta}(1 - \sin^2 \theta)$$

$$1_P = Y_P \sin \theta + X_P \cos \theta$$

$$\cos \theta = \frac{\overline{BP}}{\overline{AP}}$$

$$\overline{BP} = \overline{AP} \cos \theta$$

$$\overline{BP} = 2_P$$

$$2_P = \overline{AP} \cos \theta$$

$$\overline{AP} = Y_P - \overline{CA}$$

$$\therefore 2P = (YP - \overline{CA}) \cos \theta$$

$$\tan \theta = \frac{\overline{CA}}{\overline{OC}}$$

and

$$\overline{OC} = X_p$$

$$\therefore \overline{CA} = X_p \tan \theta$$

$$2_p = Y_p \cos \theta - X_p \tan \theta \cos \theta$$

$$2_p = Y_p \cos \theta - X_p \sin \theta$$

Expressing the relations in matrix form we have

	X_p	Y_p	Z_p
1_p	cos θ	sin θ	0
2_p	-sin θ	cos θ	0
3_p	0	0	1

These relationships are used in appendix C to develop the stress transformation matrix for the coordinate system.

Appendix C

HOOKIAN TRANSFORMATION MATRICES FOR COMPOSITES

Stress and strain are both second order tensors. A tensor of second order has $3^2 = 9$ components and transforms according to:

$$A'_{ij} = \alpha_{ik}\,\alpha_{jl}\,A_{kl}$$

or

$$\sigma'_{ij} = \alpha_{ik}\,\alpha_{jl}\,\sigma_{kl}$$

Since we are concerned with stress and strain tensors that are symmetric, then

$$\sigma'_{ij} = \sigma_{ji}$$

$$\varepsilon_{ij} = \varepsilon_{ji}$$

and, therefore, the number of independent stresses and strains is reduced to six each. These stresses are summarized in tensor and contracted notation as follows:

Tensor	Contracted
σ_{11}	σ_1
σ_{22}	σ_2
σ_{33}	σ_3
$\tau_{23} = \sigma_{23}$	σ_4
$\tau_{31} = \sigma_{31}$	σ_5
$\tau_{12} = \sigma_{12}$	σ_6

For a rotation about the Z-axis, the stresses transform according to:

$$\{\sigma'\} = [T]\ \{\sigma\}$$

Using the direction cosines for the coordinate system in Appendix B and tensor notation, the T-matrix will now be developed.

$$\sigma'_{11} = \alpha_{11}\,\alpha_{11}\,\sigma_{11}$$

$$\sigma'_{11} = (\cos\theta)(\cos\theta)\,\sigma_{11}$$

$$\sigma'_{11} = (\cos^2\theta)\,\sigma_{11}$$

$$\sigma'_{11} = \alpha_{12}\,\alpha_{12}\,\sigma_{22}$$

$$\sigma'_{11} = (\sin\theta)(\sin\theta)\,\sigma_{22}$$

$$\sigma'_{11} = (\sin^2\theta)\,\sigma_{22}$$

$$\sigma'_{11} = \alpha_{13}\,\alpha_{13}\,\sigma_{33}$$

$$\sigma'_{11} = (0)\ (0)\,\sigma_{33}$$

$$\sigma'_{11} = (0)\,\sigma_{33}$$

$$\sigma'_{11} = \alpha_{12}\,\alpha_{13}\,\sigma_{23}$$

$$\sigma'_{11} = (\sin\theta)(0)\,\sigma_{23}$$

$$\sigma'_{11} = (0)\,\sigma_{23}$$

$$\sigma'_{11} = \alpha_{13}\,\alpha_{11}\,\sigma_{31}$$

$$\sigma'_{11} = (0)(\cos\theta)\,\sigma_{31}$$

$$\sigma'_{11} = (0)\,\sigma_{31}$$

$$\sigma_{11} = \alpha_{11}\,\alpha_{12}\,\sigma_{12}$$

$$\sigma'_{11} = (\cos\theta)(\sin\theta)\,\sigma_{12}$$

$$\sigma'_{11} = \alpha_{13}\,\alpha_{12}\,\sigma_{32}$$

$$\sigma'_{11} = (0)(\sin\theta)\,\sigma_{32}$$

$$\sigma'_{11} = (0)\,\sigma_{32}$$

$$\sigma'_{11} = \alpha_{11}\,\alpha_{13}\,\sigma_{13}$$

$$\sigma'_{11} = (\cos\theta)(0)\,\sigma_{13}$$

$$\sigma'_{11} = (0)\,\sigma_{13}$$

$$\sigma'_{11} = \alpha_{12}\,\alpha_{11}\,\sigma_{21}$$

$$\sigma'_{11} = (\sin\theta)(\cos\theta)\,\sigma_{21}$$

Combining σ'_{21} and σ_{12}:

$$\sigma'_{11} = (2\cos\theta\sin\theta)\,\sigma_{12}$$

$$\sigma'_{22} = \alpha_{21}\,\alpha_{21}\,\sigma_{11}$$

$$\sigma'_{22} = (-\sin\theta)(-\sin\theta)\,\sigma_{11}$$

$$\sigma'_{22} = (\sin^2\theta)\,\sigma_{11}$$

$$\sigma'_{22} = \alpha_{22}\,\alpha_{22}\,\sigma_{22}$$

$$\sigma'_{22} = (\cos\theta)(\cos\theta)\,\sigma_{22}$$

$$\sigma'_{22} = (\cos^2\theta)\,\sigma_{22}$$

$$\sigma'_{22} = \alpha_{23}\,\alpha_{23}\,\sigma_{33}$$

$$\sigma'_{22} = (0)(0)\,\sigma_{33}$$

$$\sigma'_{22} = (0)\,\sigma_{33}$$

$$\sigma'_{22} = \alpha_{22}\,\alpha_{23}\,\sigma_{23}$$

$$\sigma'_{22} = (\cos\theta)(0)\,\sigma_{23}$$

$$\sigma'_{22} = (0)\,\sigma_{23}$$

$$\sigma'_{22} = \alpha_{23}\,\alpha_{21}\,\sigma_{31}$$

$$\sigma'_{22} = (0)(-\sin\theta)\,\sigma_{31}$$

$$\sigma'_{22} = (0)\,\sigma_{31}$$

$$\sigma'_{22} = \alpha_{21}\,\alpha_{22}\,\sigma_{12}$$

$$\sigma'_{22} = (-\sin\theta)(\cos\theta)\,\sigma_{12}$$

$$\sigma'_{22} = \alpha_{23}\,\alpha_{22}\,\sigma_{32}$$

$$\sigma'_{22} = (0)(\cos\theta)\,\sigma_{32}$$

$$\sigma'_{22} = (0)\,\sigma_{32}$$

$$\sigma'_{22} = \alpha_{21}\,\alpha_{23}\,\sigma_{13}$$

$$\sigma'_{22} = (-\sin\theta)(0)\,\sigma_{13}$$

$$\sigma'_{22} = (0)\,\sigma_{13}$$

$$\sigma'_{22} = \alpha_{22}\,\alpha_{21}\,\sigma_{21}$$

$$\alpha'_{22} = (\cos\theta)(-\sin\theta)\,\sigma_{21}$$

Combining σ_{21} and σ_{12}:

$$\sigma'_{22} = (-2\cos\theta\sin\theta)\,\sigma_{12}$$

$$\sigma'_{33} = \alpha_{31}\,\alpha_{31}\,\sigma_{11}$$

$$\sigma'_{33} = (0)(0)\,\sigma_{11}$$

$$\sigma'_{33} = (0)\,\sigma_{11}$$

$$\sigma'_{33} = \alpha_{32}\,\alpha_{32}\,\sigma_{22}$$

$$\sigma'_{33} = (0)(0)\,\sigma_{22}$$

$$\sigma'_{33} = (0)\,\sigma_{22}$$

$$\sigma'_{33} = \alpha_{33}\,\alpha_{33}\,\sigma_{33}$$

$$\sigma'_{33} = (1)(1)\,\sigma_{33}$$

$$\sigma'_{33} = (1)\,\sigma_{33}$$

$$\sigma'_{33} = \alpha_{32}\,\alpha_{33}\,\sigma_{23}$$

$$\sigma'_{33} = (0)(1)\,\sigma_{23}$$

$$\sigma'_{33} = (0)\,\sigma_{23}$$

$$\sigma'_{33} = \alpha_{33}\,\alpha_{31}\,\sigma_{31}$$

$$\sigma'_{33} = (1)(0)\,\sigma_{31}$$

$$\sigma'_{33} = (0)\,\sigma_{31}$$

$$\sigma'_{33} = \alpha_{31}\,\alpha_{32}\,\sigma_{12}$$

$$\sigma'_{33} = (0)(0)\,\sigma_{12}$$

$$\sigma'_{33} = (0)\,\sigma_{12}$$

$$\sigma'_{33} = \alpha_{33}\,\alpha_{32}\,\sigma_{32}$$

$$\sigma'_{33} = (1)(0)\,\sigma_{32}$$

$$\sigma'_{33} = (0)\,\sigma_{32}$$

$$\sigma'_{33} = \alpha_{31}\,\alpha_{33}\,\sigma_{13}$$

$$\sigma'_{33} = (0)(1)\,\sigma_{13}$$

$$\sigma'_{33} = (0)\,\sigma_{13}$$

$$\sigma'_{33} = \alpha_{32}\,\alpha_{31}\,\sigma_{21}$$

$$\sigma'_{33} = (0)(0)\,\sigma_{21}$$

$$\sigma'_{33} = (0)\,\sigma_{21}$$

$$\sigma'_{23} = \alpha_{21}\,\alpha_{31}\,\sigma_{11}$$

$$\sigma'_{23} = (-\sin\theta)(0)\,\sigma_{11}$$

$$\sigma'_{23} = (0)\,\sigma_{11}$$

$$\sigma'_{23} = \alpha_{22}\,\alpha_{32}\,\sigma_{22}$$

$$\sigma'_{23} = (\cos\theta)(0)\,\sigma_{22}$$

$$\sigma'_{23} = (0)\,\sigma_{22}$$

$$\sigma'_{23} = \alpha_{23}\,\alpha_{33}\,\sigma_{33}$$

$$\sigma'_{23} = (0)(1)\,\sigma_{33}$$

$$\sigma'_{23} = (0)\,\sigma_{33}$$

$$\sigma'_{23} = \alpha_{22}\,\alpha_{33}\,\sigma_{23}$$

$$\sigma'_{23} = (\cos\theta)(1)\,\sigma_{23}$$

$$\sigma'_{23} = (\cos\theta)\,\sigma_{23}$$

$$\sigma'_{23} = \alpha_{23}\,\alpha_{31}\,\sigma_{31}$$

$$\sigma'_{23} = (0)(0)\,\sigma_{31}$$

$$\sigma'_{23} = (0)\,\sigma_{31}$$

$$\sigma'_{23} = \alpha_{21}\,\alpha_{32}\,\sigma_{12}$$

$$\sigma'_{23} = (-\sin\theta)(0)\,\sigma_{12}$$

$$\sigma'_{23} = (0)\,\sigma_{12}$$

$$\sigma'_{23} = \alpha_{23}\,\alpha_{32}\,\sigma_{32}$$

$$\sigma'_{23} = (0)(0)\,\sigma_{32}$$

$$\sigma'_{23} = (0)\,\sigma_{32}$$

$$\sigma'_{23} = \alpha_{21}\,\alpha_{33}\,\sigma_{13}$$

$$\sigma'_{23} = (-\sin\theta)(1)\,\sigma_{13}$$

$$\sigma'_{23} = (-\sin\theta)\,\sigma_{13}$$

$$\sigma'_{23} = \alpha_{22}\,\alpha_{31}\,\sigma_{21}$$

$$\sigma'_{23} = (\cos\theta)(0)\,\sigma_{21}$$

$$\sigma'_{23} = (0)\,\sigma_{21}$$

Combining

$$\sigma'_{23} = (\cos\theta)\,\sigma_{23}$$

$$\sigma'_{23} = (-\sin\theta)\,\sigma_{31}$$

$$\sigma'_{31} = \alpha_{31}\,\alpha_{11}\,\sigma_{11}$$

$$\sigma'_{31} = (0)(\cos\theta)\,\sigma_{11}$$

$$\sigma'_{31} = (0)\,\sigma_{11}$$

$$\sigma'_{31} = \alpha_{32}\,\alpha_{12}\,\sigma_{22}$$

$$\sigma'_{31} = (0)(\sin\theta)\,\sigma_{22}$$

$$\sigma'_{31} = (0)\,\sigma_{22}$$

$$\sigma'_{31} = \alpha_{33}\,\alpha_{13}\,\sigma_{33}$$

$$\sigma'_{31} = (1)(0)\,\sigma_{33}$$

$$\sigma'_{31} = (0)\,\sigma_{33}$$

$$\sigma'_{31} = \alpha_{32}\,\alpha_{13}\,\sigma_{23}$$

$$\sigma'_{31} = (0)(0)\,\sigma_{23}$$

$$\sigma'_{31} = (0)\,\sigma_{23}$$

$$\sigma'_{31} = \alpha_{33}\,\alpha_{11}\,\sigma_{31}$$

$$\sigma'_{31} = (1)\,(\cos\theta)\,\sigma_{31}$$

$$\sigma'_{31} = (\cos\theta)\,\sigma_{31}$$

$$\sigma'_{31} = \alpha_{31}\,\alpha_{32}\,\sigma_{12}$$

$$\sigma'_{31} = (0)(0)\,\sigma_{12}$$

$$\sigma'_{31} = (0)\,\sigma_{12}$$

$$\sigma'_{31} = \alpha_{33}\,\alpha_{12}\,\sigma_{32}$$

$$\sigma'_{31} = (1)(\sin\theta)\,\sigma_{32}$$

$$\sigma'_{31} = (\sin\theta)\,\sigma_{32}$$

$$\sigma'_{31} = \alpha_{31}\,\alpha_{13}\,\sigma_{13}$$

$$\sigma'_{31} = (0)(0)\,\sigma_{13}$$

$$\sigma'_{31} = (0)\,\sigma_{13}$$

$$\sigma'_{31} = (0)\,\sigma_{21}$$

Combining

$$\sigma'_{31} = (\cos\theta)\,\sigma_{31}$$

$$\sigma'_{31} = (\sin\theta)\,\sigma_{23}$$

$$\sigma'_{12} = \alpha_{11}\,\alpha_{21}\,\sigma_{11}$$

$$\sigma'_{12} = (\cos\theta)(-\sin\theta)\,\sigma_{11}$$

$$\sigma'_{12} = (-\cos\theta\sin\theta)\,\sigma_{11}$$

$$\sigma'_{12} = \alpha_{12}\,\alpha_{22}\,\sigma_{22}$$

$$\sigma'_{12} = (\sin\theta)(\cos\theta)\,\sigma_{22}$$

$$\sigma'_{12} = (\cos\theta\sin\theta)\,\sigma_{22}$$

$$\sigma'_{12} = \alpha_{13}\,\alpha_{23}\,\sigma_{33}$$

$$\sigma'_{12} = (0)(0)\,\sigma_{33}$$

$$\sigma'_{12} = (0)\,\sigma_{33}$$

$$\sigma'_{12} = \alpha_{12}\,\alpha_{23}\,\sigma_{23}$$

$$\sigma'_{12} = (\sin\theta)(0)\,\sigma_{23}$$

$$\sigma'_{12} = (0)\,\sigma_{23}$$

$$\sigma'_{12} = \alpha_{13}\,\alpha_{21}\,\sigma_{31}$$

$$\sigma'_{12} = (0)(-\sin\theta)\,\sigma_{31}$$

$$\sigma'_{12} = (0)\,\sigma_{31}$$

$$\sigma'_{12} = \alpha_{11}\,\alpha_{22}\,\sigma_{12}$$

$$\sigma'_{12} = (\cos\theta)(\cos\theta)\,\sigma_{12}$$

$$\sigma'_{12} = (\cos^2\theta)\,\sigma_{12}$$

$$\sigma'_{12} = \alpha_{13}\,\alpha_{22}\,\sigma_{32}$$

$$\sigma'_{12} = (0)(\cos\theta)\,\sigma_{32}$$

$$\sigma'_{12} = (0)\,\sigma_{32}$$

$$\sigma'_{12} = \alpha_{11}\,\alpha_{23}\,\sigma_{13}$$

$$\sigma'_{12} = (\cos\theta)(0)\,\sigma_{13}$$

$$\sigma'_{12} = (0)\,\sigma_{13}$$

$$\sigma'_{12} = \alpha_{12}\,\alpha_{21}\,\sigma_{21}$$

$$\sigma'_{12} = (\sin\theta)(-\sin\theta)\,\sigma_{21}$$

$$\sigma'_{12} = (-\sin^2\theta)\,\sigma_{21}$$

Combining

$$\sigma'_{12} = (\cos^2\theta - \sin^2\theta)\,\sigma_{12}$$

In contracted notation the stress transformation equation is:

$$\begin{Bmatrix} \sigma'_1 \\ \sigma'_2 \\ \sigma'_3 \\ \sigma'_4 \\ \sigma'_5 \\ \sigma'_6 \end{Bmatrix} = [T] \begin{Bmatrix} \sigma_1 \\ \sigma_2 \\ \sigma_3 \\ \sigma_4 \\ \sigma_5 \\ \sigma_6 \end{Bmatrix}$$

Where the T-matrix can now be constructed from the tensor values

$$[T] = \begin{bmatrix} \cos^2\theta & \sin^2\theta & 0 & 0 & 0 & 2\cos\theta\sin\theta \\ \sin^2\theta & \cos^2\theta & 0 & 0 & 0 & -2\cos\theta\sin\theta \\ 0 & 0 & 1 & 0 & 0 & 0 \\ 0 & 0 & 0 & \cos\theta & -\sin\theta & 0 \\ 0 & 0 & 0 & \sin\theta & \cos\theta & 0 \\ -\cos\theta\sin\theta & \cos\theta\sin\theta & 0 & 0 & 0 & \cos^2\theta - \sin^2\theta \end{bmatrix}$$

In two dimensions, this rotation simplifies to

$$\begin{Bmatrix} \sigma'_1 \\ \sigma'_2 \\ \tau'_{12} \end{Bmatrix} = \begin{bmatrix} \cos^2\theta & \sin^2\theta & 2\cos\theta\sin\theta \\ \sin^2\theta & \cos^2\theta & -2\cos\theta\sin\theta \\ -\cos\theta\sin\theta & \cos\theta\sin\theta & \cos^2\theta - \sin^2\theta \end{bmatrix} \begin{Bmatrix} \sigma_1 \\ \sigma_2 \\ \tau_{12} \end{Bmatrix}$$

Let

$$m = \cos\theta$$

$$n = \sin\theta$$

$$\begin{Bmatrix} \sigma_1 \\ \sigma'_2 \\ \tau'_{12} \end{Bmatrix} = \begin{bmatrix} m^2 & n^2 & 2mn \\ n^2 & m^2 & -2mn \\ -mn & mn & m^2 - n^2 \end{bmatrix} \begin{Bmatrix} \sigma_1 \\ \sigma_2 \\ \tau_{12} \end{Bmatrix}$$

LAMINA CONSTITUTIVE RELATIONSHIP

For a homogeneous orthotropic material in a plane stress state, the stress-strain on Hooke's law relationships in matrix form are

$$\begin{bmatrix} \sigma_1 \\ \sigma_2 \\ \tau_{12} \end{bmatrix} = \begin{bmatrix} Q_{11} & Q_{12} & 0 \\ Q_{12} & Q_{22} & 0 \\ 0 & 0 & Q_{66} \end{bmatrix} \begin{bmatrix} \varepsilon_1 \\ \varepsilon_2 \\ \gamma_{12} \end{bmatrix}$$

These are the equations necessary to supply the constitutive relationships for the specially orthotropic lamina. The term specially orthotropic is used to distinguish between the constitutive relationships which are referred to the lamina principle axes (1, 2) and those which are referred to as laminate, or reference, axes (x, y).

Normally, the lamina principal axes (1, 2) are not coincident with the reference axes for the laminate, (x, y). When this occurs, the constitutive relations for each individual lamina must be transformed to the laminate reference axes in order to determine the laminate constitutive relationship.

Considering coordinate system shown in Appendix B, along with the defined rotation (+θ), we can write

$$\begin{bmatrix} \sigma_1 \\ \sigma_2 \\ \tau_{12} \end{bmatrix} = [T] \begin{bmatrix} \sigma_x \\ \sigma_y \\ \tau_{xy} \end{bmatrix}$$

$$\begin{bmatrix} \varepsilon_1 \\ \varepsilon_2 \\ \gamma_{12/2} \end{bmatrix} = [T] \begin{bmatrix} \varepsilon_x \\ \varepsilon_y \\ \gamma_{xy/z} \end{bmatrix}$$

However, in this particular instance, the lamina properties are known and therefore,

$$[T][T]^{-1} \begin{bmatrix} \sigma_x \\ \sigma_y \\ \tau_{xy} \end{bmatrix} = [T]^{-1} \begin{bmatrix} \sigma_1 \\ \sigma_2 \\ \tau_{12} \end{bmatrix}$$

$$[T][T]^{-1} \begin{bmatrix} \varepsilon_x \\ \varepsilon_y \\ \gamma_{xy/2} \end{bmatrix} = [T]^{-1} \begin{bmatrix} \varepsilon_1 \\ \varepsilon_2 \\ \gamma_{12/2} \end{bmatrix}$$

or

$$\begin{bmatrix} \sigma_x \\ \sigma_y \\ \tau_{xy} \end{bmatrix} = [T]^{-1} \begin{bmatrix} \sigma_1 \\ \sigma_2 \\ \tau_{12} \end{bmatrix}$$

$$\begin{bmatrix} \varepsilon_x \\ \varepsilon_y \\ \frac{\gamma_{xy}}{2} \end{bmatrix} = [T]^{-1} \begin{bmatrix} \varepsilon_1 \\ \varepsilon_2 \\ \frac{\gamma_{12}}{2} \end{bmatrix}$$

Derivation of $[\bar{Q}]$

$$\begin{bmatrix} \sigma_x \\ \sigma_y \\ \tau_{xy} \end{bmatrix} = [T]^{-1} \begin{bmatrix} \sigma_1 \\ \sigma_2 \\ \tau_{12} \end{bmatrix} \qquad (1)$$

The lamina relationship is

$$\begin{bmatrix} \sigma_1 \\ \sigma_2 \\ \tau_{12} \end{bmatrix} = [Q] \begin{bmatrix} \varepsilon_1 \\ \varepsilon_2 \\ \gamma_{12} \end{bmatrix}$$

Substituting in equation (1), we obtain

$$\begin{bmatrix} \sigma_x \\ \sigma y \\ \tau_{xy} \end{bmatrix} = [\bar{T}]^{-1} [Q] \begin{bmatrix} \varepsilon_1 \\ \varepsilon_2 \\ \gamma_{12} \end{bmatrix} \qquad (2)$$

The R-matrix is now defined so that the more natural strain vectors can be used instead of the modified strain vectors in the strain transformations, as well as in stress-strain law transformations.

$$[R] = \begin{bmatrix} 1 & 0 & 0 \\ 0 & 1 & 0 \\ 0 & 0 & 2 \end{bmatrix}$$

$$\begin{bmatrix} \epsilon_1 \\ \epsilon_2 \\ \gamma_{12} \end{bmatrix} = [R] \begin{bmatrix} \epsilon_1 \\ \epsilon_2 \\ \frac{\gamma_{12}}{2} \end{bmatrix}$$

$$\begin{bmatrix} \epsilon_x \\ \epsilon_y \\ \gamma_{xy} \end{bmatrix} = R \begin{bmatrix} \epsilon_x \\ \epsilon_y \\ \gamma_{xy/2} \end{bmatrix}$$

Substituting in equation (2)

$$\begin{bmatrix} \sigma_x \\ \sigma_y \\ \gamma_{xy} \end{bmatrix} = [T]^{-1} [Q][R] \begin{bmatrix} \epsilon_1 \\ \epsilon_2 \\ \frac{\gamma_{12}}{2} \end{bmatrix} \qquad (3)$$

However, we have

$$\begin{bmatrix} \epsilon_1 \\ \epsilon_2 \\ \frac{\gamma_{12}}{2} \end{bmatrix} = [T] \begin{bmatrix} \epsilon_x \\ \epsilon_y \\ \frac{\gamma_{xy}}{2} \end{bmatrix}$$

Substituting in equation (3), we have

$$\begin{bmatrix} \sigma_x \\ \sigma_y \\ \tau_{xy} \end{bmatrix} = [T]^{-1}\,[Q][R][T] \begin{bmatrix} \varepsilon_x \\ \varepsilon_y \\ \frac{\gamma_{xy}}{2} \end{bmatrix} \tag{4}$$

However,

$$\begin{bmatrix} \varepsilon_x \\ \varepsilon_y \\ \frac{\gamma_{xy}}{2} \end{bmatrix} = [R]^{-1} \begin{bmatrix} \varepsilon_x \\ \varepsilon_y \\ \gamma_{xy} \end{bmatrix}$$

Substituting in equation (4),

$$\begin{bmatrix} \sigma_x \\ \sigma_y \\ \tau_{xy} \end{bmatrix} = [T]^{-1}[Q][R][T][R]^{-1} \begin{bmatrix} \varepsilon_x \\ \varepsilon_y \\ \gamma_{xy} \end{bmatrix}$$

Without going through the derivation, it can be shown that

$$[R][T][R]^{-1} = [T]^{-T}$$

Then, if we use the abbreviation

$$[\overline{Q}] = [T]^{-1}[Q][T]^{-T}$$

The stress-strain relations in XY coordinates are

$$\begin{bmatrix} \sigma_x \\ \sigma_y \\ \tau_{xy} \end{bmatrix} = [\bar{Q}] \begin{bmatrix} \varepsilon_x \\ \varepsilon_y \\ \gamma_{xy} \end{bmatrix} = \begin{bmatrix} \bar{Q}_{11} & \bar{Q}_{12} & \bar{Q}_{16} \\ \bar{Q}_{12} & \bar{Q}_{22} & \bar{Q}_{26} \\ \bar{Q}_{16} & \bar{Q}_{26} & \bar{Q}_{66} \end{bmatrix} \begin{bmatrix} \varepsilon_x \\ \varepsilon_y \\ \gamma_{xy} \end{bmatrix}$$

where the bar over the $\bar{Q}$-matrix denotes that we are dealing with the transformed, reduced stiffnesses instead of the reduced stiffnesses, Q.

The equations for the $\bar{Q}_{ij}$ will now be derived.

$$[T]^{-1} = \begin{bmatrix} m^2 & n^2 & -2mn \\ n^2 & m^2 & 2mn \\ mn & -mn & m^2 - n^2 \end{bmatrix}$$

$$[T]^{-T} = \begin{bmatrix} m^2 & n^2 & mn \\ n^2 & m^2 & -mn \\ -2mn & 2mn & m^2 - n^2 \end{bmatrix}$$

Let

$$[B] = [T]^{-1} [Q]$$

$$= \begin{bmatrix} m^2 & n^2 & -2mn \\ n^2 & m^2 & 2mn \\ mn & -mn & m^2 - n^2 \end{bmatrix} \begin{bmatrix} Q_{11} & Q_{12} & 0 \\ Q_{12} & Q_{22} & 0 \\ 0 & 0 & Q_{66} \end{bmatrix}$$

$$B_{11} = (m^2)(Q_{11}) + (n^2)(Q_{12}) + (0)(-2mn)$$

$$B_{12} = (m^2)(Q_{12}) + (n^2)(Q_{22}) + (0)(-2mn)$$

$$B_{13} = (m^2)(0) + (n^2)(0) + (-2mn)\ (Q_{66})$$

$$B_{21} = (n^2)(Q_{11}) + (m^2)(Q_{12}) + (2mn)(0)$$

$$B_{22} = (n^2)(Q_{12}) + (m^2(Q_{22}) + (2mn)(0)$$

$$B_{23} = (n^2)(0) + (m^2)(0) + (2mn)(Q_{66})$$

$$B_{31} = (mn)(Q_{11}) + (-mn)(Q_{12}) + (m^2 - n^2)(0)$$

$$B_{32} = (mn)(Q_{12}) + (-mn)(Q_{22}) + (m^2 - n^2)(0)$$

$$B_{33} = (mn)(0) + (-mn)(0) + (m^2 - n^2)(Q_{66})$$

$$\therefore [B] = \begin{bmatrix} m^2Q_{11} + n^2Q_{12} & m^2Q_{12} + n^2Q_{22} & (-2mn)(Q_{66}) \\ n^2Q_{11} + m^2Q_{12} & n^2Q_{12} + m^2Q_{22} & (2mn)(Q_{66}) \\ mnQ_{11} - mnQ_{12} & mnQ_{12} - mnQ_{22} & (m^2 - n^2)(Q_{66}) \end{bmatrix}$$

Now,

$$[\bar{Q}] = [B][T]^{-T} = \begin{bmatrix} B_{11} & B_{12} & B_{13} \\ B_{21} & B_{22} & B_{23} \\ B_{31} & B_{32} & B_{33} \end{bmatrix} \begin{bmatrix} m^2 & n^2 & mn \\ n^2 & m^2 & -mn \\ -2mn & 2mn & (m^2 - n^2) \end{bmatrix}$$

$$\bar{Q}_{11} = (B_{11})(m^2) + (B_{12})(n^2) + (B_{13})(-2mn)$$

$$\bar{Q}_{12} = (B_{11})(n^2) + (B_{12})(m^2) + (B_{13})(2mn)$$

$$\bar{Q}_{16} = (B_{11})(mn) + (B_{12})(-mn) + (B_{13})(m^2 - n^2)$$

$$\bar{Q}_{22} = (B_{21})(n^2) + (B_{22})(m^2) + (B_{23})(2mn)$$

$$\bar{Q}_{26} = (B_{21})(mn) + (B_{22})(-mn) + (B_{23})(m^2 - n^2)$$

$$\bar{Q}_{66} = (B_{31})(mn) + (B_{32})(-mn) + (B_{33})(m^2 - n^2)$$

Expanding, we obtain

$$\bar{Q}_{11} = \left(m^2Q_{11} + n^2Q_{12}\right)(m^2) + \left(m^2Q_{12} + n^2Q_{22}\right)(n^2)$$

$$+ (-2mn\ Q_{66})(-2mn)$$

$$\bar{Q}_{11} = m^4Q_{11} + m^2n^2Q_{12} + m^2n^2Q_{12} + n^4Q_{22} + 4m^2n^2Q_{66}$$

$$\bar{Q}_{12} = \left(m^2Q_{11} + n^2Q_{12}\right)(n^2) + \left(m^2Q_{12} + n^2Q_{22}\right)(m^2) + (-2mnQ_{66})(2mn)$$

$$\bar{Q}_{12} = m^2n^2Q_{11} + n^4Q_{12} + m^4Q_{12} + m^2n^2Q_{22} - 4m^2n^2Q_{66}$$

$$\bar{Q}_{16} = \left(m^2Q_{11} + n^2Q_{12}\right)(mn) + \left(m^2Q_{12} + n^2Q_{22}\right)(-mn) + (-2mnQ_{66})$$

$$(m^2 - n^2)$$

$$\bar{Q}_{16} = m^3nQ_{11} + mn^3Q_{12} - m^3nQ_{12} - mn^3Q_{22} - 2m^3nQ_{66} + 2mn^3Q_{66}$$

$$\bar{Q}_{22} = \left(n^2Q_{11} + m^2Q_{12}\right)(n^2) + \left(n^2Q_{12} + m^2Q_{22}\right)(m^2) + (2mnQ_{66})(2mn)$$

$$\bar{Q}_{22} = n^4Q_{11} + m^2n^2Q_{12} + m^2n^2Q_{12} + m^4Q_{22} + 4m^2n^2Q_{66}$$

$$\bar{Q}_{26} = \left(n^2Q_{11} + m^2Q_{12}\right)(mn) + \left(n^2Q_{12} + m^2Q_{22}\right)(-mn) + (2mnQ_{66})(m^2 - n^2)$$

$$\bar{Q}_{26} = mn^3Q_{11} + m^3nQ_{12} - mn^3Q_{12} - m^3nQ_{22} + 2m^3nQ_{66} - 2mn^3Q_{66}$$

$$\bar{Q}_{66} = (mnQ_{11} - mnQ_{12})(mn) + (mnQ_{12} - mnQ_{22})(-mn) + \left(m^2Q_{66} - n^2Q_{66}\right) \times (m^2 - n^2)$$

$$\bar{Q}_{66} = m^2n^2Q_{11} - m^2n^2Q_{12} - m^2n^2Q_{12} + m^2n^2Q_{22} + m^4Q_{66} - 2m^2n^2Q_{66} + n^4Q_{66}$$

Combining terms, the final equations for the transformed, reduced stiffnesses are

$$\bar{Q}_{11} = Q_{11}m^4 + 2(Q_{12} + 2Q_{66})m^2n^2 + Q_{22}n^4$$

$$\bar{Q}_{12} = (Q_{11} + Q_{22} - 4Q_{66})m^2n^2 + Q_{12}(m^4 + n^4)$$

$$\bar{Q}_{22} = Q_{11}n^4 + 2(Q_{12} + 2Q_{66})m^2n^2 + Q_{22}m^4$$

$$\bar{Q}_{66} = (Q_{11} + Q_{22} - 2Q_{12} - 2Q_{66})m^2n^2 + Q_{66}(m^4 + n^4)$$

$$\bar{Q}_{16} = (Q_{11} - Q_{12} - 2Q_{66})nm^3 + (Q_{12} - Q_{22} + 2Q_{66})mn^3$$

$$\bar{Q}_{26} = (Q_{11} - Q_{12} - 2Q_{66})mn^3 + (Q_{12} - Q_{22} + 2Q_{66})m^3n$$

Appendix D

HiMAT PLY ORIENTATION AND HOOKE'S MATRIX

Based on the reduced stiffness equations $[\bar{Q}]$ developed in appendix C, and using the +35°/±50° HiMAT outboard wing lamina orientation, Hooke's matrix [E] is developed for a specific finite element panel. This is done in order to verify the elastic coefficients used in the NASTRAN solution and calculation of stresses based on test strain gage readings.

The ply layup directions for the HiMAT wing are +35°/±50°. The first layup direction is +35° using the coordinate convention developed in appendix B, the rotation angle = -35°. The material properties used are the values from table I.

$$E_1 = E_L = 137.9 \times 10^6 \text{ kN/m}^2 \ (20 \times 10^6 \text{ psi})$$

$$E_2 = E_T = 10.3 \times 10^6 \text{ kN/m}^2 \ (1.49 \times 10^6 \text{ psi})$$

$$G_{LT} = 2.413 \times 10^6 \text{ kN/m}^2 \ (0.35 \times 10^6 \text{ psi})$$

$$\mu_{LT} = 0.3$$

$$\theta = -35°$$

$$m = \cos\theta = 0.81915$$

$$n = \sin\theta = -0.57358$$

$$m^2 = \cos^2\theta = 0.671$$

$$n^2 = \sin^2\theta = 0.32899$$

$$m^3 = \cos^3\theta = 0.54965$$

$$n^3 = \sin^3\theta = 0.1887$$

$$m^4 = \cos^4 \theta = 0.45025$$

$$n^4 = \sin^4 \theta = 0.10823$$

$$\frac{\mu_{TL}}{E_T} = \frac{\mu_{LT}}{E_L}$$

Therefore,

$$\mu_{TL} = \frac{E_T}{E_L} (\mu_{LT})$$

$$\mu_{TL} = \frac{(1.49)(10^6)}{(20)(10^6)} (.3)$$

$$\mu_{TL} = 0.02235$$

$$Q_{11} = \frac{E_{11}}{1 - \mu_{12}\,\mu_{21}} = \frac{(20)(10^6)}{1 - (.3)(.02235)} = 20.14\ (10^6)\ \text{psi}$$

$$Q_{12} = \mu_{21} Q_{11} = 0.45\ (10^6)\ \text{psi}$$

$$Q_{22} = \frac{E_{22}}{1 - \mu_{12}\,\mu_{21}} = 1.5\ (10^6)\ \text{psi}$$

$$Q_{66} = G_{LT} = 0.35\ (10^6)\ \text{psi}$$

Substituting into the transformed reduced stiffness equations we obtain:

$$\overline{Q}_{11} = (20.14)(10^6)(0.45025) + 2\left[(0.45)(10^6) + 2\ (0.35)(10^6)\right]$$

$$(0.671)(0.32899) + (1.5)(10^6)(0.10823)$$

$$\overline{Q}_{11} = 9.7381\ (10^6)$$

$$\bar{Q}_{22} = (20.14)(10^6)(0.10823) + 2\left[(0.45)(10^6) + 2(0.35)(10^6)\right]$$

$$\times (0.671)(0.32899) + (1.5)(10^6)(0.45025)$$

$$\bar{Q}_{22} = 3.36285\ (10^6)$$

$$\bar{Q}_{12} = \left[20.14(10^6) + 1.5(10^6) - 4(0.35)(10^6)\right](0.671)(0.32899)$$

$$+ (0.45)(10^6)(0.45025 + 0.10823)$$

$$\bar{Q}_{12} = 4.71935\ (10^6)$$

$$\bar{Q}_{66} = \left[(20.14)(10^6) + (1.5 \times 10^6) - 2(0.45)(10^6) - 2(0.35)(10^6)\right]$$

$$\times (0.671)(0.32899) + (0.35)(10^6)(0.45025 + 0.10823)$$

$$\bar{Q}_{66} = 4.61935\ (10^6)$$

$$\bar{Q}_{16} = \left[20.14\ (10^6) - 0.45\ (10^6) - 2\ (0.35)(10^6)\right](-0.57358)(0.54965)$$

$$+ \left[0.45\ (10^6) - 1.5\ (10^6) + 2\ (0.35)(10^6)\right](0.81915)(-0.1887)$$

$$\bar{Q}_{16} = -5.93284\ (10^6)$$

$$\bar{Q}_{26} = \left[20.14\ (10^6) - 0.45\ (10^6) - 2\ (0.35)(10^6)\right](0.81915)(-0.1887)$$

$$+ \left[0.45\ (10^6) - 1.5\ (10^6) + 2\ (0.35)(10^6)\right](0.54965)(-0.57358)$$

$$\bar{Q}_{26} = -2.82501\ (10^6)$$

$$\therefore [\bar{Q}]_{(-35°)} = 10^6 \begin{bmatrix} 9.7381 & 4.71935 & -5.93284 \\ 4.71935 & 3.36285 & -2.82501 \\ -5.93284 & -2.82501 & 4.61935 \end{bmatrix}$$

For the +50° layup, $\theta = -50°$, and

$m = 0.64279$

$n = -0.76604$

$m^2 = 0.41318$

$n^2 = 0.58682$

$m^3 = 0.26559$

$n^3 = -0.44953$

$m^4 = 0.17072$

$n^4 = 0.34436$

$Q_{11} = 20.14\ (10^6)$

$Q_{12} = 0.45\ (10^6)$

$Q_{22} = 1.5\ (10^6)$

$Q_{66} = 0.35\ (10^6)$

$$\bar{Q}_{11} = 20.14\ (10^6)(0.17072) + 2\left[0.45\ (10^6) + 2\ (0.35)(10^6)\right]$$

$$\times\ (0.41318)(0.58682) + 1.5\ (10^6)(0.34436)$$

$\bar{Q}_{11} = 4.5125\ (10^6)$

$$\bar{Q}_{22} = 20.14(10^6)(0.34436) + 2\left[0.45\ (10^6) + 2\ (0.35)(10^6)\right]$$

$$\times\ (0.41318)(0.58682) + 1.5\ (106)(0.17072)$$

$$\bar{Q}_{22} = 7.74915\ (10^6)$$

$$\bar{Q}_{12} = \left[20.14\ (10^6) + 1.5\ (10^6) - 1.4\ (10^6)\right]\ (0.41318)(0.58682)$$

$$+\ 0.45\ (10^6)(0.51508)$$

$$\bar{Q}_{12} = 5.13923\ (10^6)$$

$$\bar{Q}_{66} = \left[20.14\ (10^6) + 1.5\ (10^6) - 0.9\ (10^6) - 0.7\ (10^6)\right]\ (0.41318)$$

$$\times\ (0.58682) + 0.35\ (10^6)(0.51508)$$

$$\bar{Q}_{66} = 5.03922\ (10^6)$$

$$\bar{Q}_{16} = \left[20.14\ (10^6) - 0.45\ (10^6) - 0.7\ (10^6)\right]\ (-0.76604)(0.26559)$$

$$+\left[0.45\ (10^6) - 1.5\ (10^6) + 0.7\ (10^6)\right]\ (0.64279)(-0.44953)$$

$$\bar{Q}_{16} = -3.76243\ (10^6)$$

$$\bar{Q}_{26} = \left[20.14\ (10^6) - 0.45\ (10^6) - 0.7\ (10^6)\right]\ (0.64279)(-0.44953)$$

$$+\left[0.45\ (10^6) - 1.5\ (10^6) + 0.7\ (10^6)\right]\ (0.26559)(-0.76604)$$

$$\bar{Q}_{26} = -5.41601\ (10^6)$$

$$\therefore [\bar{Q}]_{(-50°)} = (10^6) \begin{bmatrix} 4.5125 & 5.13923 & -3.76243 \\ 5.13923 & 7.74915 & -5.41601 \\ -3.76243 & -5.41601 & 5.03922 \end{bmatrix}$$

and

$$[\bar{Q}]_{(+50°)} = (10^6) \begin{bmatrix} 4.5125 & 5.13923 & 3.76243 \\ 5.13923 & 7.74915 & 5.41601 \\ 3.76243 & 5.41601 & 5.03922 \end{bmatrix}$$

To check Hooke's matrix values used in the NASTRAN theoretical solution, the following finite element is selected.

Element Type	Element ID	Thickness
CQDMEM	1021114	(0.17325 (in.)

Ply percentage breakdown is:

+35 - 18%

+50 - 41%

-50 - 41%

$$A_{ij} = \left[\Sigma \bar{Q}_{ij} \ (\%t)\right] t_{TOT}$$

$$A_{11} = \left[9.7381 \ (0.18) + (4.5125)(0.41)(2)\right] (10^6)(0.17325)$$

$$A_{11} = 0.94475 \ (10^6)$$

$$A_{22} = \left[3.36285\ (0.18) + 7.74915\ (0.41)(2)\right]\ (10^6)(0.17325)$$

$$A_{22} = 1.20575\ (10^6)$$

$$A_{12} = \left[(4.71935)(0.18) + 5.13923\ (0.41)(2)\right]\ (10^6)(0.17325)$$

$$A_{12} = 0.87728\ (10^6)$$

$$A_{66} = \left[4.61935\ (0.18) + 5.03922\ (0.41)(2)\right]\ (10^6)(0.17325)$$

$$A_{66} = 0.85995\ (10^6)$$

$$A_{16} = \left[-5.93284\ (0.18)\right]\ (10^6)(0.17325)$$

$$A_{16} = -0.18502\ (10^6)$$

$$A_{26} = \left[(-2.82501)(0.18)\right]\ (10^6)(0.17325)$$

$$A_{26} = -0.0881\ (10^6)$$

$$\therefore [A] = (10^6) \begin{bmatrix} 0.94475 & 0.87728 & -0.18502 \\ 0.87728 & 1.20575 & -0.0881 \\ -0.18502 & -0.0881 & 0.85995 \end{bmatrix}$$

$$[E] = 1/t\ [A]$$

			Lb/In.^{2}	N/m^2
E_{11}	=	0.94475/0.17325	= $5.453(10^6)$	$3.76\ (10^{10})$
E_{12}	=	0.87728/0.17325	= $5.064(10^6)$	$3.491(10^{10})$
E_{13}	=	-0.18502/0.17325	= $-1.068(10^6)$	$-0.736(10^{10})$
E_{22}	=	1.20575/0.17325	= $6.96(10^6)$	$4.799(10^{10})$
E_{23}	=	-0.0881/0.17352	= $-0.509(10^6)$	$-0.351(10^{10})$
E_{33}	=	0.85995/0.17325	= $4.964(10^6)$	$3.423(10^{10})$

The values compare with those input to NASTRAN. The magnitudes are not exactly the same because a ply drop occurs across this element in the actual finite-element model.

NASTRAN VALUES (FROM AC84)

		Lb/In.^{2}	N/m^2
E_{11}	=	$5.43(10^6)$	$3.744(10^{10})$
E_{12}	=	$5.06(10^6)$	$3.489(10^{10})$
E_{13}	=	$-1.05(10^6)$	$-0.724(10^{10})$
E_{22}	=	$6.97(10^6)$	$4.806(10^{10})$
E_{23}	=	$-0.50(10^6)$	$-0.345(10^{10})$
E_{33}	=	$4.96(10^6)$	$3.42(10^{10})$

REFERENCES

1. Rockwell LAD Report TFD-75-1180, "AC50 Laminate Design and Analysis," M.C. Less and D. Y. Konishi, dated 2 March 1975.

2. Aeroelastic Tailoring of Advanced Composite Structures, AFF DL-TR-76-100, Volume III, "Modifications and User's Guide for Procedure TSO," February 1978.

3. Rockwell LAD Report NA-78-711, "Rockwell NASTRAN Theoretical Manual Level 17.000," by Rockwell NASTRAN Development Group, dated 8 September 1978.

4. Rockwell LAD Report NA-59-1395, "NAA Structural Strain Gage Procedure," by the NAA Strain Gage Committee, dated 15 August 1959.

5. Rockwell LAD Specification LL40256, "Strain Gage Installation, Flight Test Instrumentation," dated 16 March 1973.

6. Rockwell LAD Report NA-68-52, "LAD Computer Program for Processing Structural Test Data," by A. L. Carter.

7. Rockwell LAD Report DAR32000-14, "Advanced Technology Development, HiMAT System Concept and Utilization," dated September 1977, page 23.

8. Rockwell MAD Report NA 79-366, 'HiMAT Post-GVT Flutter Analysis,' dated July 1979.

Table I

AS/3501-5 G_r/EP TAPE LAMINA PROPERTIES

Material Property	Design Allow RT kN/m^2 (psi)	Design Allow 82.2°C(180°F) kN/m^2 (psi)
F_L^{tu}	1454.8×10^3 (211.0×10^3)	1406.6×10^3 (204.0×10^3)
F_T^{tu}	53.1×10^3 (7.7×10^3)	49.6×10^3 (7.2×10^3)
F_L^{cu}	1454.8×10^3 (211.0×10^3)	1334.5×10^3 (195.0×10^3)
F_T^{cu}	221.3×10^3 (32.1×10^3)	193.7×10^3 (28.1×10^3)
F_{LT}^{su}	71.0×10^3 (10.3×10^3)	64.8×10^3 (9.4×10^3)
E_L	137.9×10^6 (20.0×10^6)	135.1×10^6 (19.6×10^6)
E_T	10.3×10^6 (1.49×10^6)	9.5×10^6 (1.38×10^6)
G_{LT}	2.413×10^6 (0.35×10^6)	2.206×10^6 (0.32×10^6)
μ_{LT}	0.3	0.3
ρ	$1578\ kg/m^3$ ($0.057\ lb/in.^3$)	$1578\ kg/m^3$ ($0.057\ lb/in.^3$)
$t/_{ply}$	0.01334 cm (0.00525 in.)	0.01334 cm (0.00525 in.)

Table II

FINITE ELEMENT MODEL - DESIGN ITERATION STUDIES

Effect on Twist (deg)	Description
±3.0	Effect of structural box skins
-0.80	Aileron support system
+0.60	Slotting leading edges
-0.50	Increasing thicknesses of leading edge skins
+0.35	Effect of spar stiffness
+0.30	Effect of wingtip fin
-0.25/-1.0	Effect of load changes
+0.15	Root stiffness at BL 38.10 cm (15 in.) Addition of tip masses Joints

Table III
WING PAD LOADS

Pad No.	X_F Cm (in.)	Y_F Cm (in.)	Load Newtons (lb)
1	109.98 (43.3)	370.33 (145.8)	889.64 (200.)
2	123.19 (48.5)	383.79 (151.1)	613.85 (138.)
3	135.38 (53.3)	396.49 (156.1)	613.85 (138.)
4	149.10 (58.7)	407.67 (160.5)	613.85 (138.)
5	160.27 (63.1)	419.1 (165.0)	524.89 (118.)
6	171.20 (67.4)	429.77 (169.2)	524.89 (118.)
7	182.63 (71.9)	441.2 (173.7)	524.89 (118.)
8	193.80 (76.3)	452.37 (178.1)	524.89 (118.)
9	204.98 (80.7)	463.55 (182.5)	524.89 (118.)
10	217.93 (85.8)	477.01 (187.8)	524.89 (118.)
11	111.25 (43.8)	396.75 (156.2)	644.99 (145.)
12	122.43 (48.2)	407.16 (160.3)	644.99 (145.)
13	133.86 (52.7)	417.07 (164.2)	644.99 (145.)
14	145.54 (57.3)	427.74 (168.4)	569.37 (128.)
15	157.23 (61.9)	438.4 (172.6)	569.37 (128.)
16	168.4 (66.3)	449.58 (177.0)	569.37 (128.)

Table III
WING PAD LOADS (Continued)

Pad No.	X_F Cm (in.)	Y_F Cm (in.)	Load Newtons (lb)
17	180.34 (71.0)	460.25 (181.2)	489.3 (110.)
18	192.02 (75.6)	471.17 (185.5)	489.3 (110.)
19	203.71 (80.2)	481.84 (189.7)	489.3 (110.)
20	108.97 (42.9)	421.64 (166.0)	133.45 (30.)
21	120.4 (47.4)	438.66 (172.7)	133.45 (30.)
22	134.62 (53.0)	449.07 (176.8)	133.45 (30.)
23	149.10 (58.7)	459.49 (180.9)	133.45 (30.)
24	163.32 (64.3)	469.9 (185.0)	222.41 (50.)
25	177.8 (70.0)	480.06 (189.0)	222.41 (50.)
26	192.02 (75.6)	490.73 (193.2)	222.41 (50.)
27	206.5 (81.3)	501.14 (197.3)	222.41 (50.)
28	222.76 (87.7)	492.76 (194.0)	360.31 (81.)
29	221.74 (87.3)	508.51 (200.2)	271.34 (61.)
30	221.74 (87.3)	529.84 (208.61)	271.34 (61.)
31	127.51 (50.2)	474.73 (186.9)	177.93 (40.)

Table III
WING PAD LOADS (Concluded)

Pad No.	X_F Cm (in.)	Y_F Cm (in.)	Load Newtons (lb)
32	143.26 (56.4)	481.84 (189.7)	177.93 (40.)
33	160.78 (63.3)	491.74 (193.6)	177.93 (40.)
34	175.77 (69.2)	501.65 (197.5)	177.93 (40.)
35	190.25 (74.9)	512.06 (201.6)	177.93 (40.)
36	204.72 (80.6)	521.97 (205.5)	177.93 (40.)

Table IV
CANARD PAD LOADS

Pad No.	X_c Cm (in.)	Y_c Cm (in.)	Load Newtons (1b)
1	32.51 (12.8)	137.67 (54.2)	489.3 (110.)
2	39.37 (15.5)	153.67 (60.5)	934.13 (210.)
3	49.53 (19.5)	169.16 (66.6)	934.13 (210.)
4	60.2 (23.7)	184.15 (72.5)	934.13 (210.)
5	70.61 (27.8)	199.64 (78.6)	934.13 (210.)
6	81.53 (32.1)	212.34 (83.6)	667.23 (150.)
7	90.93 (35.8)	226.06 (89.0)	667.23 (150.)
8	100.33 (39.5)	239.52 (94.3)	667.23 (150.)
9	108.97 (42.9)	252.73 (99.5)	644.99 (145.)
10	118.36 (46.6)	266.19 (104.8)	644.99 (145.)
11	37.59 (14.8)	183.64 (72.3)	444.82 (100.)
12	47.75 (18.8)	204.98 (80.7)	244.65 (55.)
13	60.45 (23.8)	217.93 (85.8)	244.65 (55.)
14	72.9 (28.7)	230.38 (90.7)	244.65 (55.)
15	85.85 (33.8)	243.08 (95.7)	244.65 (55.)

Table IV
CANARD PAD LOADS (Concluded)

Pad No.	X_c Cm (in.)	Y_c Cm (in.)	Load Newtons (lb)
16	44.7 (17.6)	228.6 (90.0)	222.41 (50.)
17	60.45 (23.8)	242.06 (95.3)	222.41 (50.)
18	76.2 (30.0)	255.52 (100.6)	222.41 (50.)
19	97.03 (38.2)	272.03 (107.1)	266.89 (60.)
20	109.73 (43.2)	283.72 (111.7)	266.89 (60.)

Table V

LOCATION OF DEFLECTION TRANSDUCERS

Gage No.	Nominal Grid No.	Location	Coord X_F cm (in.)	Coord Y_F cm (in.)	Coord Z_F cm (in.)	Size	Gage Dir	Prop No.
8001	25	LH wing	225.55 (88.8)	478.54 (188.4)	248.16 (97.7)	10	Vert	S-260164
8002	27	LH wing	224.66 (88.45)	488.82 (192.45)	250.95 (98.8)	10	Vert	S-260161
8003	31	LH wing	223.52 (88.0)	521.97 (205.5)	253.75 (99.9)	15	Vert	S-260180
8004	33	LH wing	224.54 (88.4)	545.85 (214.9)	253.24 (99.7)	15	Vert	S-260188
8005	71	LH wing	203.58 (80.15)	531.62 (209.3)	253.67 (99.87)	10	Vert	S-260162
8006	95	LH wing	212.85 (83.8)	482.85 (190.1)	249.17 (98.1)	10	Vert	S-260812
8007	103	LH wing	199.01 (78.35)	501.78 (197.55)	252.48 (99.4)	10	Vert	S-260874
8008	106	LH wing	185.42 (73.0)	519.05 (204.35)	253.82 (99.93)	10	Vert	S-260875
8009	140	LH wing	206.25 (81.2)	457.83 (180.25)	247.9 (97.6)	10	Vert	S-260876
8010	144	LH wing	197.87 (77.9)	465.58 (183.3)	249.17 (98.1)	10	Vert	S-260879
8011	152	LH wing	179.2 (70.55)	488.19 (192.2)	252.96 (99.59)	10	Vert	S-260880
8012	155	LH wing	168.4 (66.3)	506.73 (199.5)	253.95 (99.98)	10	Vert	S-260881

Table V

LOCATION OF DEFLECTION TRANSDUCERS (Continued)

Gage No.	Nominal Grid No.	Location	Coord X_F cm (in.)	Coord Y_F cm (in.)	Coord Z_F cm (in.)	Size	Gage Dir	Prop No.
8013	186	LH wing	186.18 (73.3)	438.66 (172.7)	247.65 (97.5)	5	Vert	S-260153
8014	193	LH wing	175.51 (69.1)	448.44 (176.55)	248.92 (98.0)	5	Vert	S-260159
8015	201	LH wing	156.84 (61.75)	472.19 (185.9)	253.03 (99.62)	5	Vert	S-260160
8016	228	LH wing	143.64 (56.55)	492.25 (193.8)	254.23 (100.09)	5	Vert	S-260170
8017	239	LH wing	164.34 (64.7)	416.56 (164.0)	248.16 (97.7)	5	Vert	S-260823
8018	243	LH wing	153.67 (60.5)	426.21 (167.8)	248.41 (97.8)	5	Vert	S-260829
8019	251	LH wing	131.19 (51.65)	455.42 (179.3)	252.81 (99.53)	5	Vert	S-260868
8020	254	LH wing	119.89 (47.2)	483.23 (190.25)	254.56 (100.22)	5	Vert	S-260870
8021	274	LH wing	104.65 (41.2)	477.52 (188.0)	254.76 (100.3)	2	Vert	S-260820
8022	278	LH wing	114.55 (45.1)	444.25 (174.9)	252.5 (99.41)	2	Vert	S-260910
8023	299	LH wing	127.51 (50.2)	379.09 (149.25)	246.13 (96.9)	2	Vert	S-260917
8024	303	LH wing	115.57 (45.5)	390.4 (153.7)	248.16 (97.7)	2	Vert	S-260918

Table V

LOCATION OF DEFLECTION TRANSDUCERS (Continued)

Gage No.	Nominal Grid No.	Location	Coord X_F cm (in.)	Coord Y_F cm (in.)	Coord Z_F cm (in.)	Size	Gage Dir	Prop No.
8025	423	LH wing	86.36 (34.0)	438.15 (172.5)	251.92 (99.18)	2	Vert	S-260922
8026	436	LH wing	86.36 (34.0)	405.13 (159.5)	250.11 (98.47)	2	Vert	S-260930
8027	440	LH wing	86.36 (34.0)	357.94 (140.92)	247.04 (97.26)	2	Vert	S-260943
8028	464	LH wing	60.32 (23.75)	438.15 (172.5)	251.0 (98.82)	2	Vert	S-260945
8029	466	LH wing	60.32 (23.75)	405.13 (159.5)	249.88 (98.38)	2	Vert	S-261276
8030	470	LH wing	127.00 (50.0)	357.94 (140.92)	247.9 (97.60)	2	Vert	S-261282
8031	1555	LH can	127.00 (50.0)	268.1 (105.55)	301.75 (118.8)	10	Vert	S-260886
8032	1565	LH can	127.00 (50.0)	277.49 (109.25)	302.77 (119.2)	10	Vert	S-260887
8033	1572	LH can	127.00 (50.0)	290.32 (114.3)	303.78 (119.6)	10	Vert	S-260888
8034	1574	LH can	127.00 (50.0)	306.07 (120.5)	304.29 (119.8)	10	Vert	S-260889
8035	1568	LH can	123.85 (48.76)	287.22 (113.08)	302.51 (119.1)	10	Vert	S-260890
8036	1557	LH can	123.14 (48.48)	271.96 (107.07)	300.99 (118.5)	10	Vert	S-260891

Table V

LOCATION OF DEFLECTION TRANSDUCERS (Continued)

Gage No.	Nominal Grid No.	Location	Coord X_F cm (in.)	Coord Y_F cm (in.)	Coord Z_F cm (in.)	Size	Gage Dir	Prop No.
8037	1561	LH can	116.00 (45.67)	279.6 (110.08)	299.21 (117.8)	10	Vert	S-260892
8038	1564	LH can	105.59 (41.57)	289.76 (114.08)	295.91 (116.5)	10	Vert	S-260898
8039	1522	LH can	109.17 (42.98)	253.16 (99.67)	294.64 (116.0)	5	Vert	S-260871
8040	1526	LH can	99.21 (39.06)	263.07 (103.57)	292.61 (115.2)	5	Vert	S-260885
8041	1529	LH can	86.82 (34.18)	275.44 (108.44)	288.54 (113.6)	5	Vert	S-260894
8042	1530	LH can	114.99 (45.27)	250.9 (98.78)	296.67 (116.8)	5	Vert	S-260897
8043	1511	LH can	84.68 (33.34)	273.74 (107.77)	287.78 (113.3)	5	Vert	S-260895
8044	1485	LH can	97.06 (38.21)	224.15 (88.25)	289.81 (114.1)	5	Vert	S-260908
8045	1487	LH can	89.66 (35.30)	228.07 (89.79)	287.27 (113.1)	5	Vert	S-260909
8046	1491	LH can	76.53 (30.13)	240.84 (94.82)	283.97 (111.8)	5	Vert	S-260157
8047	1494	LH can	61.24 (24.11)	255.93 (100.76)	279.15 (109.9)	5	Vert	S-260873
8048	1460	LH can	79.78 (31.74)	199.64 (78.6)	282.96 (111.4)	2	Vert	S-261284

Table V

LOCATION OF DEFLECTION TRANSDUCERS (Continued)

Gage No.	Nominal Grid No.	Location	Coord X_F cm (in.)	Coord Y_F cm (in.)	Coord Z_F cm (in.)	Size	Gage Dir	Prop No.
8049	1462	LH can	71.30 (28.07)	203.96 (80.3)	281.18 (110.7)	2	Vert	S-261290
8050	1466	LH can	55.52 (21.86)	220.27 (86.72)	276.10 (108.7)	2	Vert	S-261304
8051	1410	LH can	37.69 (14.84)	237.97 (93.69)	270.26 (106.4)	2	Vert	S-261283
8052	1424	LH can	43.15 (16.99)	208.15 (81.95)	271.53 (106.9)	2	Vert	S-261311
8053	1416	LH can	55.45 (21.83)	162.18 (63.85)	272.03 (107.1)	2	Vert	S-261312
8054	1418	LH can	43.36 (17.07)	167.41 (65.91)	270.76 (106.6)	2	Vert	S-261285
8102	27	RH wing	-224.15 (-88.25)	493.01 (194.1)	250.95 (98.8)	10	Vert	S-260878
8103	31	RH wing	-224.79 (-88.5)	521.21 (205.2)	253.75 (99.9)	15	Vert	S-260957
8114	193	RH wing	-175.51 (-69.1)	448.44 (176.55)	248.84 (97.97)	5	Vert	S-260196
8115	201	RH wing	-156.84 (-61.75)	472.19 (185.9)	253.03 (99.62)	5	Vert	S-260191
8125	423	RH wing	-86.36 (-34.0)	438.15 (172.5)	251.92 (99.18)	2	Vert	S-261306
8127	440	RH wing	-86.36 (-34.0)	357.94 (140.92)	247.04 (97.26)	2	Vert	S-261277

Table V

LOCATION OF DEFLECTION TRANSDUCERS (Concluded)

Gage No.	Nominal Grid No.	Location	Coord X_F cm (in.)	Coord Y_F cm (in.)	Coord Z_F cm (in.)	Size	Gage Dir	Prop No.
8132	1565	RH can	-127.00 (-50.0)	277.49 (109.25)	302.77 (119.2)	10	Vert	S-260877
8133	1572	RH can	-127.00 (-50.0)	290.32 (114.3)	303.78 (119.6)	10	Vert	S-260899
8071	75	LH wing	210.31 (82.8)	508.63 (200.25)	252.22 (99.3)	15	Vert	S-260187

* Accuracy of transducer is one percent around center reading. Therefore, as example, size 10, has an accuracy of ±.05 inches.

Table VI

COORDINATE LOCATIONS FOR GROUND STRAIN GAGES

Gage Number	Gage Type	Location	Coordinates			Angle
			X_F m (in.)	Y_F m (in.)	Z_F m (in.)	β°
1	Rosette	Lower surface outboard wing	1.186 (46.7)	4.383 (172.55)	2.52 (99.2046)	0
2	Rosette	Lower surface outboard wing	1.336 (42.6)	4.371 (172.1)	2.51 (98.8771)	2.0
3	Rosette	Lower surface outboard wing	1.476 (58.1)	4.483 (176.5)	2.51 (98.8944)	1.5
4	Rosette	Lower surface outboard wing	2.12 (83.459)	4.922 (193.77)	2.5 (98.5629)	3.0
5	Rosette	Lower surface canard	.514 (20.22)	2.11 (83.07)	2.75 (108.2405)	0
6	Rosette	Lower surface canard	.591 (23.28)	2.007 (79.02)	2.77 (109.1796)	3.5
7	Rosette	Lower surface canard	.603 (23.73)	2.216 (87.23)	2.78 (109.6227)	0
8	Rosette	Lower surface canard	.821 (32.33)	2.439 (96.02)	2.86 (112.6112)	0
101	Rosette	Upper surface outboard wing leading edge	1.516 (59.7)	4.145 (163.17)	2.498 (98.3594)	-90.0
102	Rosette	Upper surface outboard wing leading edge	1.746 (68.76)	4.368 (171.97)	2.495 (98.2427)	-90.0
103	Rosette	Lower surface outboard wing leading edge	1.746 (68.76)	4.368 (171.97)	2.477 (97.5011)	0
105	Rosette	Upper surface canard leading edge	.683 (26.9)	1.922 (76.65)	2.808 (110.5508)	-90.0
106	Rosette	Lower surface canard	.861 (33.9)	2.19 (86.22)	2.86 (112.6411)	0

Table VI

COORDINATE LOCATIONS FOR GROUND STRAIN GAGE (Concluded)

Gage Number	Gage Type	Location	Coordinates			Angle
			X_F m (in.)	Y_F m (in.)	Z_F m (in.)	$\beta°$
108	Rosette	Lower surface outboard wing trailing edge	1.793 (70.609)	4.956 (195.12)	2.536 (99.8457)	89.5
109	Rosette	Lower surface outboard wing trailing edge	1.934 (76.159)	5.055 (199.03)	2.535 (99.7897)	.50
110	Rosette	Lower surface outboard wing trailing edge	1.3 (51.2)	4.629 (182.24)	2.538 (99.9278)	-3.5
111	Rosette	Lower surface aft inboard wing	.599 (23.6)	4.746 (186.85)	2.553 (100.531)	-16.8
112	Rosette	Lower surface canard trailing edge	.836 (32.91)	2.539 (99.97)	2.902 (114.2693)	-2.8
115	Rosette	Lower surface canard	.919 (36.17)	2.544 (100.18)	2.898 (114.095)	0
117	Rosette	Lower surface outboard wing	1.107 (43.6)	4.336 (170.7)	2.518 (99.1436)	0
118	Rosette	Lower surface canard leading edge	.79 (31.12)	2.09 (82.27)	2.837 (111.6966)	0

Table VII

COORDINATE LOCATIONS FOR NASA FLIGHT TEST STRAIN GAGES

Number	Gage Type	Location	Coordinates			
			X_F m (in.)	Y_F m (in.)	Z_F m (in.) Upper	Z_F m (in.) Lower
1015	Shear	Front spar canard	.37 (14.7)	1.58 (62.12)	2.7 (106.2)	
1016	Shear	Rear spar canard	.37 (14.7)	2.01 (79.2)	2.69 (106.08)	
1017	Shear	Canard (root)	.3 (11.69)	1.58 (62.16)	2.68 (105.41)	
1018	Bending bridge	Canard Upper and lower surfaces	.37 (14.7)	1.93 (76.12)	2.72 (107.18)	2.69 (105.9)
1019	Bending bridge	Upper and lower surfaces Outboard wing	2.06 (81.0)	4.94 (194.37)	2.55 (100.24)	2.51 (98.82)
1020	Bending bridge	Upper and lower surfaces Outboard wing	1.26 (49.76)	4.25 (167.13)	2.57 (101.08)	2.50 (98.59)
1021	Bending bridge	Upper and lower surfaces Outboard wing	1.24 (49.00)	4.27 (168.04)	2.54 (100.1395)	2.51 (98.70)
1022	Shear	Front spar outboard wing	1.37 (53.95)	4.12 (162.05)	2.51 (98.9)	
1023	Shear	Rear spar outboard wing	1.12 (44.27)	4.41 (173.81)	2.55 (100.37)	
1025	Bending bridge	Upper and lower surfaces Outboard wing	1.36 (53.64)	4.33 (170.3)	2.56 (100.84)	2.51 (98.64)

Table VII

COORDINATE LOCATIONS FOR NASA FLIGHT TEST STRAIN GAGES (Continued)

Number	Gage Type	Location	Coordinates			
			X_F m (in.)	Y_F m (in.)	Z_F m (in.) Upper	Z_F m (in.) Lower
1026	Bending bridge	Upper and lower surfaces Outboard wing	1.34 (52.87)	4.35 (171.23)	2.56 (100.92)	2.51 (98.76)
1029	Shear	Inboard wing	.4 (15.64)	4.05 (159.5)	2.57 (101.34)	
1030	Shear	Inboard wing	.4 (15.64)	4.38 (172.5)	2.57 (101.01)	
1035	Shear	Inboard wing	.78 (30.9)	4.38 (172.5)	2.55 (100.52)	
1036	Shear	Inboard wing	.81 (32.0)	4.05 (159.5)	2.55 (100.49)	
1037	Shear	Inboard wing	.82 (32.2)	3.81 (150.)	2.55 (100.29)	
1038	Shear	Inboard wing	.82 (32.2)	3.56 (140.)	2.53 (99.79)	
1115	Shear	Front spar canard	.61 (24.09)	1.91 (75.35)	2.8 (110.21)	
1116	Shear	Rear spar canard	.44 (17.5)	2.08 (81.94)	2.73 (107.39)	
1118	Bending bridge	Canard upper and lower surfaces	0.52 (20.61)	2.00 (109.69)	2.79 (109.69)	2.75 (108.31)
2020	Bending bridge	Upper and lower surfaces Outboard wing	1.3 (51.02)	4.21 (165.6)	2.56 (100.82)	2.5 (98.3)
2021	Bending bridge	Upper and lower surfaces Outboard wing	1.21 (47.72)	4.31 (169.62)	2.57 (101.2569)	2.51 (98.91)

Table VII

COORDINATE LOCATIONS FOR NASA FLIGHT TEST STRAIN GAGES (Concluded)

Number	Gage Type	Location	Coordinates			
			X_F m (in.)	Y_F m (in.)	Z_F m (in.) Upper	Z_F m (in.) Lower
2025	Bending bridge	Upper and lower surfaces Outboard wing	1.39 (54.9)	4.29 (168.77)	2.55 (100.55)	2.5 (98.32)
2026	Bending bridge	Upper and lower surfaces Outboard wing	1.31 (51.6)	4.39 (172.78)	2.57 (101.07)	2.51 (98.98)

Table VIII

HiMAT 8g STATIC TEST RESULTS-GROUND STRAIN GAGES

Gage No.	Type		Average Gage Stress kN/m^2 (psi)	Predicted Stress kN/m^2 (psi)	Percent Difference
1	Rosette	σ_x	18523.4 (2686.5)	60099.6 (8716.4)	-69
		σ_y	-4123.2 (-598.)	35800.9 (5192.3)	-112
		τ_{xy}	10349.4 (1501.)	-29393.4 (-4263.)	-135
2	Rosette	σ_x	26735.4 (3877.5)	44159.7 (6404.6)	-39
		σ_y	7739.6 (1122.5)	19167.4 (2779.9)	-60
		τ_{xy}	4454.2 (646.)	-18037.3 (-2616.)	-125
3	Rosette	σ_x	27390.4 (3972.5)	38956.7 (5650.)	-30
		σ_y	9284.1 (1346.5)	12581.9 (1824.8)	-26
		τ_{xy}	492.9 (71.5)	-7119.1 (-1032.5)	-110
4	Rosette	σ_x	3426.8 (497.)	16155. (2343.)	-79
		σ_y	117.2 (17.)	209.6 (30.4)	-44
		τ_{xy}	48478.7 (7031.)	-13250.8 (-1921.8)	-466

Table VIII

HiMAT 8g STATIC TEST RESULTS-GROUND STRAIN GAGES (Continued)

Gage No.	Type		Average Gage Stress kN/m^2 (psi)	Predicted Stress kN/m^2 (psi)	Percent Difference
5	Rosette	σ_x	85427. (12389.7)	83113. (12054.1)	3
		σ_y	24895.1 (3610.6)	20089.9 (2913.7)	24
		τ_{xy}	26409.2 (3830.2)	-12545.4 (-1819.5)	-310
6	Rosette	σ_x	66653.9 (9667.)	65759. (9537.2)	1.4
		σ_y	20822.9 (3020.)	16370.8 (2374.3)	27
		τ_{xy}	-9480.6 (-1375.)	-1886.5 (-273.6)	403
7	Rosette	σ_x	80509.5 (11676.5)	107208.3 (15548.7)	-25
		σ_y	8708.4 (1263.)	9515.1 (1380.)	-8
		τ_{xy}	-7398.3 (-1073.)	-11846.3 (-1718.1)	-38
8	Rosette	σ_x	31365.4 (4549.)	48895.2 (7091.4)	-36
		σ_y	3351. (486.)	8265. (1198.7)	-59
		τ_{xy}	5736.6 (832.)	5753.2 (834.4)	-

Table VIII

HiMAT 8g STATIC TEST RESULTS-GROUND STRAIN GAGES (Continued)

Gage No.	Type		Average Gage Stress kN/m^2 (psi)	Predicted Stress kN/m^2 (psi)	Percent Difference
101	Rosette	σ_x	19505 (2829)	-34260 (-4969)	-157
		σ_y	15231 (2209)	-3144 (-456)	-584
		τ_{xy}	-6267 (-909)	-669 (-97)	—
102	Rosette	σ_x	26862 (3896)	-36990 (-5365)	-173
		σ_y	18292 (2653)	-1606 (-233)	—
		τ_{xy}	13045 (1892)	-655 (-95)	—
103	Rosette	σ_x	14913 (2163)	51400 (7455)	-71
		σ_y	13017 (1888)	-41 (-6)	—
		τ_{xy}	11356 (1647)	4137 (600)	-374

Table VIII

HiMAT 8g STATIC TEST RESULTS-GROUND STRAIN GAGES (Continued)

Gage No.	Type		Average Gage Stress kN/m^2 (psi)	Predicted Stress kN/m^2 (psi)	Percent Difference
106	Rosette	σ_x	26352 (3822)	66107 (9588)	-60
		σ_y	-14955 (-2169)	17258 (2503)	-187
		τ_{xy}	4261 (618)	30323 (4398)	-86
108	Rosette	σ_x	11909.7 (1727.3)	18579.3 (2694.6)	-36
		σ_y	2855.2 (414.1)	-39.3 (-5.7)	-
		τ_{xy}	841.5 (122.04)	6513.7 (944.7)	-87
109	Rosette	σ_x	6665.4 (966.7)	59297. (8600.)	-89
		σ_y	3032.4 (439.8)	25661.1 (3721.7)	-88
		τ_{xy}	-3613.7 (-524.1)	-7124.6 (-1033.3)	-49
110	Rosette	σ_x	176 (25.5)	-379 (-551)	-146
		σ_y	-400 (-58)	-483 (-70)	-17
		τ_{xy}	2592 376	2923 (-424)	-11

Table VIII

HiMAT 8g STATIC TEST RESULTS-GROUND STRAIN GAGES (Concluded)

Gage No.	Type		Average Gage Stress kN/m^2 (psi)	Predicted Stress kN/m^2 (psi)	Percent Difference
112	Rosette	σ_x	-2199 (-319	4902 (711)	-145
		σ_y	-565 (-82)	-2461 (-357)	-77
		τ_{xy}	213 (31)	5385 (781)	-96
115	Rosette	σ_x	15455.1 (2241.5)	21972.3 (3186.7)	-30
		σ_y	-903.2 (-131.)	2443.6 (354.4)	-137
		τ_{xy}	4030.1 (584.5)	5727.7 (830.7)	-30
117	Rosette	σ_x	37818 (5485)	69189 (10035)	-45
		σ_y	-5916 (-858)	11749 (1704)	-150
		τ_{xy}	21008 3047	-24387 (-35371)	-186
118	Rosette	σ_x	68175 (9888)	83813 (12156)	-19
		σ_y	-3289 (-477)	9618 (1395)	-134
		τ_{xy}	4902 (711)	15093 (2189)	-68

Table IX

HiMAT 8g STATIC TEST-FLIGHT TEST STRAIN GAGES

Gage Number	Type
1015	Shear
1016	Shear
1017	Shear
1019	Bending bridge
1020	Bending bridge
1021	Bending bridge
1022	Shear
1023	Shear
1025	Bending bridge
1026	Bending bridge
1027	Bending bridge
1028	Bending bridge
1029	Shear
1030	Shear
1031	Bending bridge

Table IX

HiMAT 8g STATIC TEST-FLIGHT TEST STRAIN GAGES
(Concluded)

Gage Number	Type
1032	Bending bridge
1033	Bending bridge
1034	Bending bridge
1035	Shear
1036	Shear
1037	Shear
1038	Shear
1115	Shear
1116	Shear
1118	Bending bridge
2020	Bending bridge
2021	Bending bridge
2025	Bending bridge
2026	Bending bridge

Table X

FLIGHT TEST STRAIN GAGES-INNER ROW TEST RESULTS

Gage Number	Type	Strain (ϵ_x) 100% Load Loading (μ - m/m)	Strain (ϵ_x) 100% Load Unloading (μ - m/m)	Average (μ - m/m)
2020	Bending bridge	2009.	2107.	2058.
1020	Bending bridge	2219.	2330.	2274.5
1021	Bending bridge	2311.	2423.	2367.
2021	Bending bridge	2398.5	2513.	2456.

Table XI

LONGITUDINAL PANEL STRAIN-NASTRAN
$X_F \sim 130.3$ cm

$G_{LT} = 2.413 \times 10^6$ kN/m^2 (0.35×10^6 lb/in^2)		
Nastran Panel Number	Longitudinal Strain (ϵ_x) (μ - m/m)	Average Strain [(L)-(U)]/2. (μ - m/m)
1021117 (U)	-2029.6	1975.2
1021118 (L)	1920.9	
1021119 (U)	-2440.4	2176.8
1021120 (L)	1913.3	
1021121 (U)	-2729.9	2383.7
1021122 (L)	2037.5	
1021123 (U)	-2874.5	2801.7
1021124 (L)	2729.0	

Table XII

FLIGHT TEST STRAIN GAGES-OUTER ROW TEST RESULTS

Gage Number	Type	Strain (ϵ_x) 100% Load Loading (μ - m/m)	Strain (ϵ_x) 100% Load Unloading (μ - m/m)	Average (μ - m/m)
1025	Bending bridge	2195.	2301.	2248.
2025	Bending bridge	2260.	2373.	2316.5
1026	Bending bridge	2223.	2331.	2277.
2026	Bending bridge	2341.	2460.	2400.5

Table XIII

LONGITUDINAL PANEL STRAIN - NASTRAN PANELS 1021109-1021116

Nastran Panel Number	Type	CG Location (Dist. From Front Spar) m (in.)	Longitudinal Strain (ϵ_x) (μ-m/m)	Average Strain [(L)-(U)]/2. (μ-m/m)
G_{LT} = 2.413 x 10^6 kN/m^2 (0.35 x 10^6 lb/in^2)				
(U) 1021109	CQDMEM	0.042 m (1.65 in.)	-2712.0	2673.2
(L) 1021110	CQDMEM	0.042 m (1.65 in.)	2634.5	
(U) 1021111	CQDMEM	0.122 m (4.8 in.)	-3218.2	2857.7
(L) 1021112	CQDMEM	0.122 m (4.8 in.)	2497.2	
(U) 1021113	CQDMEM	0.218 m (8.5 in.)	-3295.6	2885.8
(L) 1021114	CQDMEM	0.218 m (8.5 in.)	2476.1	
(U) 1021115	CQDMEM	0.32 m (12.6 in.)	-2912.2	2815.9
(L) 1021116	CQDMEM	0.32 m (12.6 in.)	2719.6	
G_{LT} = 4.689 x 10^6 kN/m^2 (0.68 x 10^6 lb/in^2)				
(U) 1021109			-2283.9	2363.4
(L) 1021110			2443.0	
(U) 1021111			-2769.4	2520.7
(L) 1021112			2272.0	
(U) 1021113			-2888.8	2547.4
(L) 1021114			2206.0	
(U) 1021115			-2601.0	2490.5
(L) 1021116			2380.0	

(U) = Upper panel
(L) = Lower panel

Table XIV

LONGITUDINAL PANEL STRAIN-NASTRAN
$X_F \sim 130.3$

G_{LT} = 4.689 x 10^6 kN/m^2 (0.68 x 10^6 lb/in^2)		
Nastran Panel Number	Longitudinal Strain (ϵ_x) (μ-m/m)	Average Strain [(L)-(U)]/2. (μ-m/m)
1021117 (U)	-1711.9	1795.
1021118 (L)	1878.	
1021119 (U)	-2095.6	1963.3
1021120 (L)	1831.	
1021121 (U)	-2387.	2148.7
1021122 (L)	1910.5	
1021123 (U)	-2594.8	2568.9
1021124 (L)	2543.0	

Table XV
TEST DEFLECTIONS

HiMAT A/V-2, Cond 8g to 110%, 27 April 1978

Gage	8001	8002	8003	8004	8005	8006
Slot	174	175	176	177	178	179
Chan	112	113	114	115	116	117
(%)						
0.0	-0.000	0.000	-0.000	-0.000	-0.000	-0.000
20.0	0.675	0.679	0.797	0.897	0.848	0.602
40.0	1.491	1.526	1.789	1.984	1.786	1.345
60.0	2.379	2.450	2.865	3.211	2.777	2.148
80.0	3.314	3.412	4.026	4.516	3.825	2.992
90.0	3.804	3.924	4.650	5.211	4.379	3.436
100.0	4.293	4.427	5.274	5.921	4.945	3.881
110.0	4.808	4.965	5.921	6.657	5.335	4.338
100.0	4.561	4.714	5.619	6.312	5.225	4.116
90.0	4.164	4.307	5.129	5.744	4.820	3.767
80.0	3.747	3.872	4.597	5.145	4.358	3.391
60.0	2.866	2.945	3.487	3.898	3.349	2.593
40.0	1.964	2.019	2.369	2.641	2.336	1.780
20.0	1.042	1.058	1.252	1.390	1.300	0.946
0.0	0.063	0.053	0.082	0.089	0.035	0.058

Gage	8007	8008	8009	8010	8011	8012
Slot	180	181	182	183	184	185
Chan	118	9016	9017	9018	9019	9020
(%)						
0.0	-0.000	-0.000	-0.000	-0.000	0.000	0.000
20.0	0.565	0.695	0.512	0.465	0.410	0.562
40.0	1.281	1.448	1.100	1.033	0.928	1.152
60.0	2.061	2.234	1.736	1.655	1.489	1.753
80.0	2.876	3.063	2.380	2.296	2.079	2.398
90.0	3.310	3.504	2.725	2.628	2.380	2.731
100.0	3.754	3.957	3.065	2.969	2.689	3.080
110.0	4.197	4.408	3.410	3.316	3.014	3.419
100.0	4.008	4.228	3.248	3.169	2.882	3.293
90.0	3.666	3.899	2.991	2.908	2.641	3.051
80.0	3.291	3.542	2.704	2.622	2.381	2.786
60.0	2.518	2.750	2.086	2.023	1.832	2.183
40.0	1.725	1.932	1.464	1.401	1.258	1.544
20.0	0.915	1.106	0.796	0.755	0.680	0.912
0.0	0.058	0.041	0.052	0.047	0.046	0.031

Table XV
TEST DEFLECTIONS (Continued)

Gage Slot Chan (%)	8013 186 9021	8014 187 9022	8015 188 9023	8016 189 9024	8017 190 9025	8018 191 9026
0.0	0.000	0.000	-0.000	0.000	0.000	0.000
20.0	0.430	0.293	0.273	0.305	0.285	0.183
40.0	0.921	0.668	0.610	0.758	0.617	0.417
60.0	1.422	1.066	0.979	1.122	0.949	0.678
80.0	1.938	1.490	1.368	1.521	1.281	0.938
90.0	2.208	1.702	1.564	1.712	1.463	1.074
100.0	2.475	1.922	1.767	1.947	1.645	1.209
110.0	2.701	2.155	1.976	2.160	1.838	1.345
100.0	2.631	2.046	1.884	2.086	1.762	1.287
90.0	2.432	1.876	1.732	1.956	1.635	1.190
80.0	2.216	1.697	1.570	1.803	1.490	1.084
60.0	1.741	1.316	1.211	1.430	1.180	0.848
40.0	1.240	0.912	0.846	1.038	0.848	0.592
20.0	0.700	0.497	0.456	0.647	0.486	0.321
0.0	0.053	0.038	0.039	0.039	0.045	0.017

Gage Slot Chan (%)	8019 192 9027	8020 193 9028	8021 194 9029	8022 195 9030	8023 196 9031	8024 197 9032
0.0	-0.000	0.000	-0.000	0.000	0.000	0.000
20.0	0.122	0.202	0.160	0.056	0.148	0.053
40.0	0.304	0.574	0.477	0.165	0.330	0.141
60.0	0.501	0.825	0.659	0.285	0.510	0.234
80.0	0.704	1.097	0.859	0.412	0.691	0.336
90.0	0.809	1.244	0.973	0.477	0.785	0.388
100.0	0.914	1.400	1.091	0.541	0.879	0.439
110.0	1.022	1.556	1.195	0.606	0.985	0.490
100.0	0.992	1.530	1.182	0.603	0.968	0.489
90.0	0.917	1.449	1.136	0.559	0.902	0.452
80.0	0.834	1.350	1.075	0.512	0.831	0.413
60.0	0.650	1.091	0.882	0.397	0.663	0.323
40.0	0.454	0.803	0.669	0.274	0.479	0.225
20.0	0.247	0.538	0.488	0.148	0.275	0.123
0.0	0.019	0.025	0.025	0.013	0.028	0.013

Table XV
TEST DEFLECTIONS (Continued)

Gage Slot Chan (%)	8025 198 9033	8026 199 9034	8027 200 9035	8028 201 9036	8029 202 9037	8030 203 9038
0.0	0.000	0.000	0.000	0.000	0.000	0.000
20.0	0.005	0.004	0.006	0.000	0.000	0.000
40.0	0.039	0.036	0.040	-0.000	-0.000	0.005
60.0	0.079	0.073	0.072	0.002	-0.000	0.017
80.0	0.124	0.112	0.107	0.014	0.005	0.031
90.0	0.147	0.133	0.127	0.021	0.009	0.039
100.0	0.170	0.154	0.145	0.028	0.015	0.047
110.0	0.193	0.174	0.162	0.034	0.018	0.053
100.0	0.200	0.180	0.166	0.039	0.023	0.057
90.0	0.191	0.175	0.164	0.042	0.025	0.057
80.0	0.174	0.159	0.150	0.041	0.025	0.057
60.0	0.133	0.121	0.117	0.037	0.025	0.053
40.0	0.090	0.083	0.081	0.024	0.021	0.040
20.0	0.047	0.044	0.043	0.013	0.012	0.022
0.0	0.005	0.005	0.004	0.003	0.002	0.003

Gage Slot Chan (%)	8031 204 9039	8032 205 9040	8033 206 9041	8034 207 9042	8035 208 9043	8036 209 9044
0.0	0.000	-0.000	0.000	0.000	0.000	0.000
20.0	0.564	0.602	0.647	0.702	0.631	0.566
40.0	1.204	1.288	1.387	1.486	1.342	1.208
60.0	1.815	1.933	2.075	2.226	2.004	1.817
80.0	2.388	2.550	2.734	2.927	2.643	2.397
90.0	2.668	2.846	3.052	3.269	2.955	2.671
100.0	2.918	3.107	3.329	3.565	3.225	2.918
110.0	3.175	3.380	3.619	3.865	3.501	3.175
100.0	3.082	3.280	3.519	3.762	3.400	3.085
90.0	2.883	3.071	3.294	3.527	3.182	2.889
80.0	2.658	2.833	3.040	3.256	2.942	2.668
60.0	2.130	2.265	2.432	2.598	2.350	2.145
40.0	1.538	1.636	1.752	1.876	1.692	1.543
20.0	0.844	0.896	0.961	1.026	0.929	0.851
0.0	0.051	0.050	0.052	0.059	0.050	0.054

Table XV
TEST DEFLECTIONS (Continued)

Gage Slot Chan (%)	8037 210 9045	8038 211 9046	8039 212 9047	8040 213 9048	8041 214 9049	8042 215 9050
0.0	-0.000	0.000	0.000	0.000	0.000	0.000
20.0	0.554	0.531	0.436	0.410	0.399	0.446
40.0	1.184	1.143	0.935	0.877	0.851	0.960
60.0	1.778	1.710	1.404	1.315	1.273	1.447
80.0	2.339	2.256	1.857	1.729	1.671	1.902
90.0	2.614	2.524	2.076	1.939	1.868	2.128
100.0	2.855	2.753	2.269	2.118	2.035	2.331
110.0	3.100	2.979	2.468	2.302	2.206	2.539
100.0	3.010	2.905	2.393	2.239	2.143	2.460
90.0	2.823	2.737	2.238	2.096	2.012	2.298
80.0	2.604	2.524	2.065	1.934	1.861	2.119
60.0	2.082	2.013	1.652	1.545	1.486	1.696
40.0	1.504	1.460	1.194	1.126	1.074	1.224
20.0	0.823	0.793	0.655	0.617	0.587	0.673
0.0	0.047	0.051	0.037	0.035	0.031	0.040

Gage Slot Chan (%)	8043 216 9051	8044 217 9052	8045 218 9053	8046 219 9054	8047 220 9055	8048 221 9056
0.0	-0.000	0.000	0.000	-0.000	0.000	0.000
20.0	0.476	0.263	0.235	0.202	0.432	0.138
40.0	0.966	0.572	0.522	0.477	0.835	0.328
60.0	1.379	0.860	0.790	0.711	1.148	0.500
80.0	1.691	1.131	1.042	0.931	1.338	0.662
90.0	1.844	1.264	1.166	1.051	1.428	0.742
100.0	1.990	1.382	1.280	1.149	1.506	0.815
110.0	2.138	1.508	1.396	1.258	1.583	0.892
100.0	2.096	1.459	1.363	1.246	1.567	0.876
90.0	1.987	1.362	1.274	1.169	1.513	0.818
80.0	1.872	1.258	1.175	1.080	1.455	0.757
60.0	1.620	1.014	0.946	0.875	1.325	0.615
40.0	1.327	0.742	0.693	0.645	1.161	0.456
20.0	0.764	0.412	0.384	0.360	0.686	0.253
0.0	0.044	0.026	0.027	0.030	0.045	0.016

Table XV
TEST DEFLECTIONS (Continued)

Gage	8049	8050	8051	8052	8053	8054
Slot	222	223	224	225	226	227
Chan	9057	9058	9059	9060	9061	9062
(%)						
0.0	0.000	0.000	0.000	0.000	-0.000	0.000
20.0	0.114	0.085	0.354	0.000	0.067	0.051
40.0	0.271	0.206	0.664	0.000	0.180	0.123
60.0	0.412	0.304	0.870	0.000	0.273	0.179
80.0	0.544	0.396	0.943	0.001	0.363	0.233
90.0	0.610	0.441	0.972	0.002	0.408	0.261
100.0	0.672	0.485	0.997	0.002	0.453	0.285
110.0	0.737	0.534	1.017	0.002	0.498	0.310
100.0	0.733	0.532	1.021	0.002	0.501	0.311
90.0	0.684	0.495	1.021	0.002	0.471	0.292
80.0	0.633	0.458	1.021	0.002	0.437	0.272
60.0	0.515	0.375	1.011	0.001	0.355	0.226
40.0	0.383	0.282	0.975	0.000	0.268	0.172
20.0	0.214	0.158	0.595	0.000	0.150	0.099
0.0	0.014	0.011	0.042	0.000	0.011	0.006

Gage	8102	8103	8114	8115	8125	8127
Slot	244	245	246	247	248	249
Chan	9079	9080	9081	9082	9083	9084
(%)						
0.0	0.000	-0.000	-0.000	0.000	-0.000	0.000
20.0	0.733	0.818	0.324	0.297	0.025	0.038
40.0	1.632	1.830	0.724	0.664	0.076	0.087
60.0	2.580	2.909	1.133	1.045	0.127	0.133
80.0	3.589	4.070	1.571	1.444	0.183	0.182
90.0	4.104	4.670	1.789	1.648	0.211	0.207
100.0	4.626	5.275	2.014	1.852	0.239	0.230
110.0	5.218	5.955	2.270	2.081	0.271	0.259
100.0	4.913	5.624	2.137	1.965	0.274	0.260
90.0	4.483	5.123	1.953	1.801	0.253	0.240
80.0	4.022	4.587	1.753	1.624	0.228	0.218
60.0	3.076	3.488	1.362	1.249	0.177	0.172
40.0	2.092	2.365	0.939	0.862	0.121	0.125
20.0	1.082	1.221	0.502	0.449	0.061	0.066
0.0	0.028	0.031	0.017	0.016	-0.003	0.004

Table XV

TEST DEFLECTIONS (Concluded)

Gage Slot Chan (%)	8132 250 9085	8133 251 9086	8071 420 9087
0.0	0.000	-0.000	-0.000
20.0	0.658	0.716	0.670
40.0	1.375	1.492	1.479
60.0	2.044	2.218	2.373
80.0	2.656	2.871	3.321
90.0	2.931	3.170	3.815
100.0	3.183	3.439	4.321
110.0	3.470	3.744	4.845
100.0	3.365	3.622	4.600
90.0	3.157	3.407	4.208
80.0	2.915	3.147	3.774
60.0	2.326	2.509	2.868
40.0	1.644	1.772	1.975
20.0	0.882	0.945	1.047
0.0	-0.001	-0.002	0.067

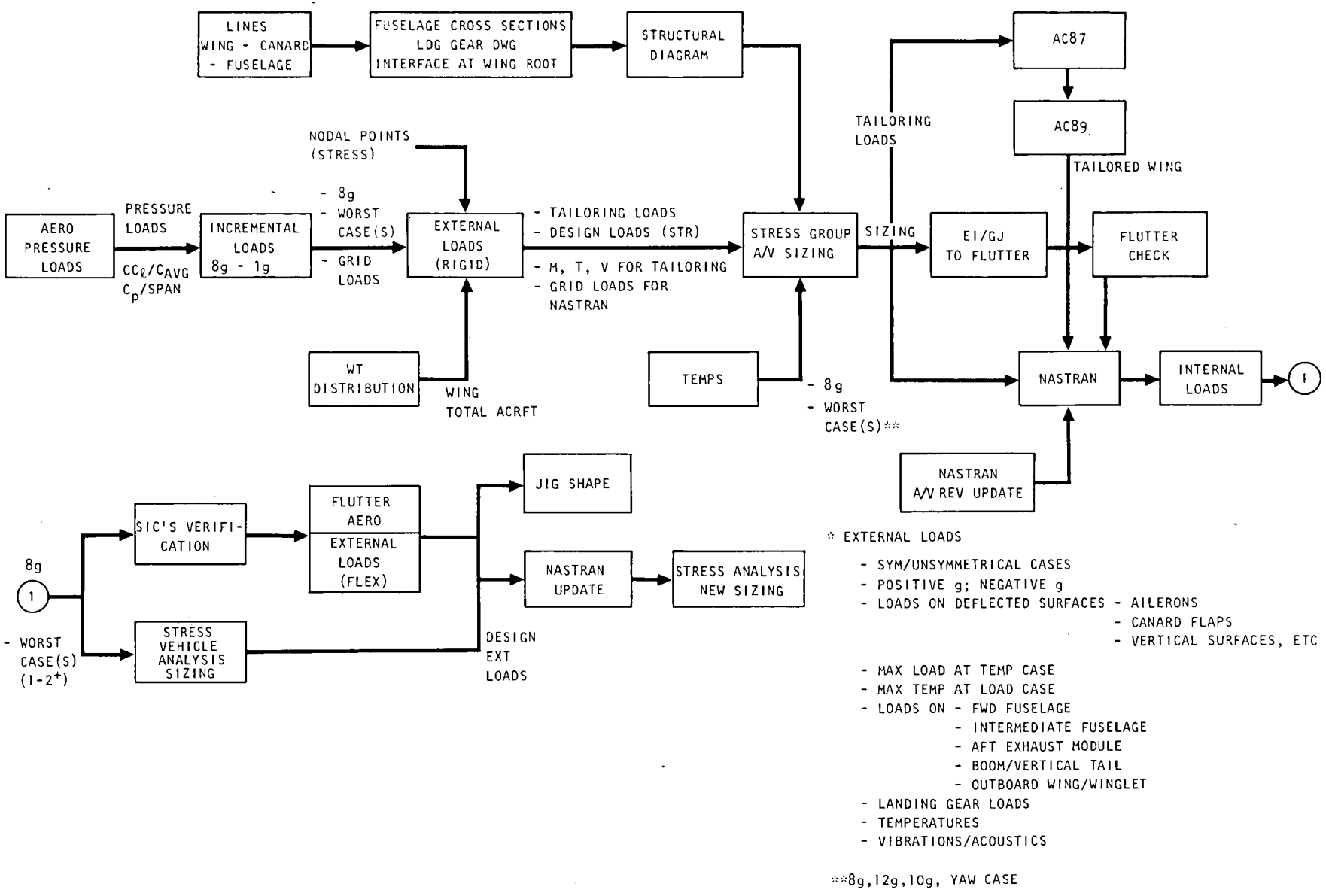

Figure 1. Engineering Analysis Cycle

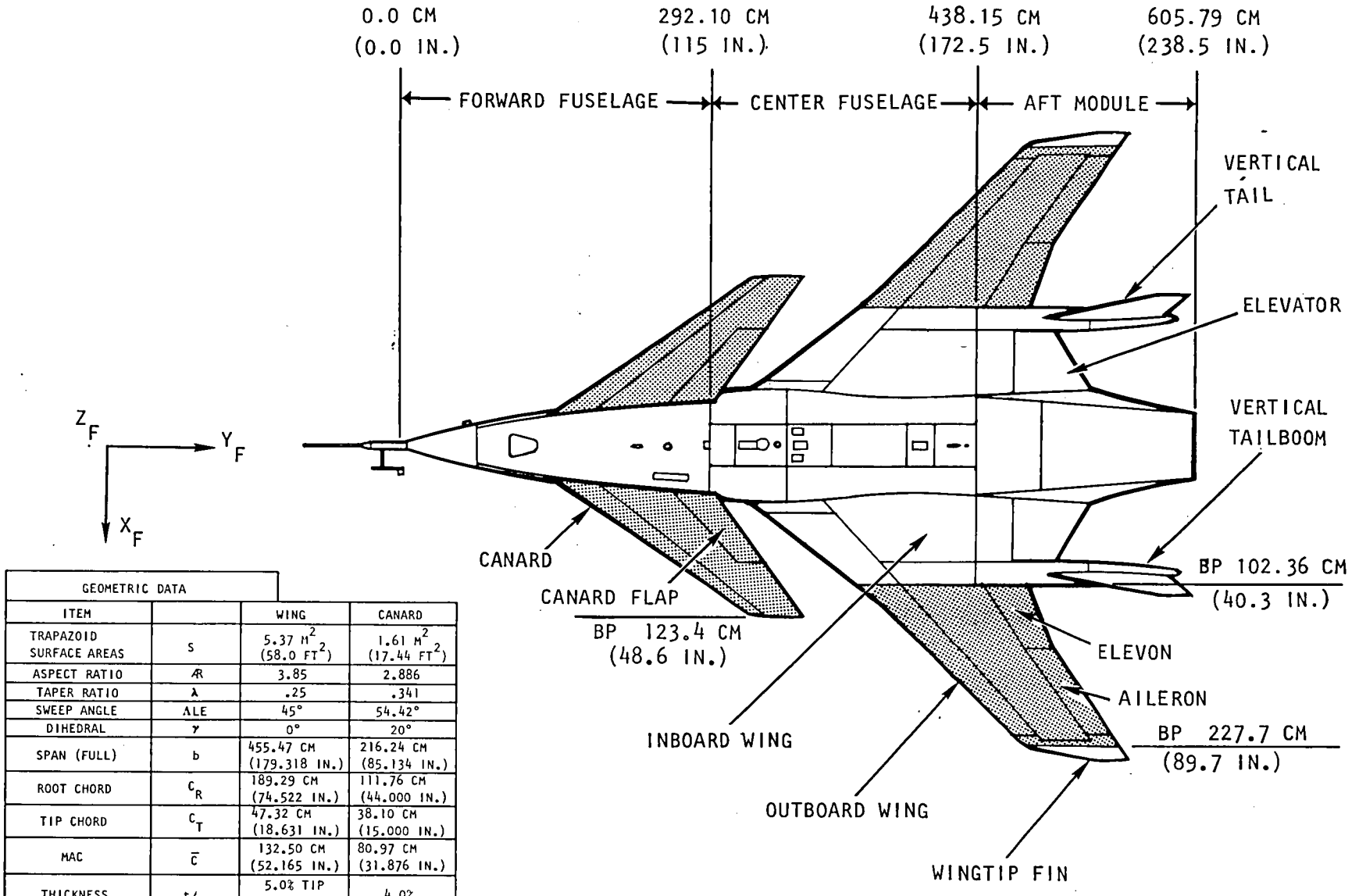

GEOMETRIC DATA			
ITEM		WING	CANARD
TRAPAZOID SURFACE AREAS	S	5.37 M^2 (58.0 FT^2)	1.61 M^2 (17.44 FT^2)
ASPECT RATIO	$\mathcal{R}$	3.85	2.886
TAPER RATIO	λ	.25	.341
SWEEP ANGLE	Λ_{LE}	45°	54.42°
DIHEDRAL	γ	0°	20°
SPAN (FULL)	b	455.47 CM (179.318 IN.)	216.24 CM (85.134 IN.)
ROOT CHORD	c_R	189.29 CM (74.522 IN.)	111.76 CM (44.000 IN.)
TIP CHORD	c_T	47.32 CM (18.631 IN.)	38.10 CM (15.000 IN.)
MAC	$\bar{c}$	132.50 CM (52.165 IN.)	80.97 CM (31.876 IN.)
THICKNESS	t/c	5.0% TIP 7.5% ROOT	4.0%

Figure 2. HiMAT Aeroelastically Tailored Surfaces

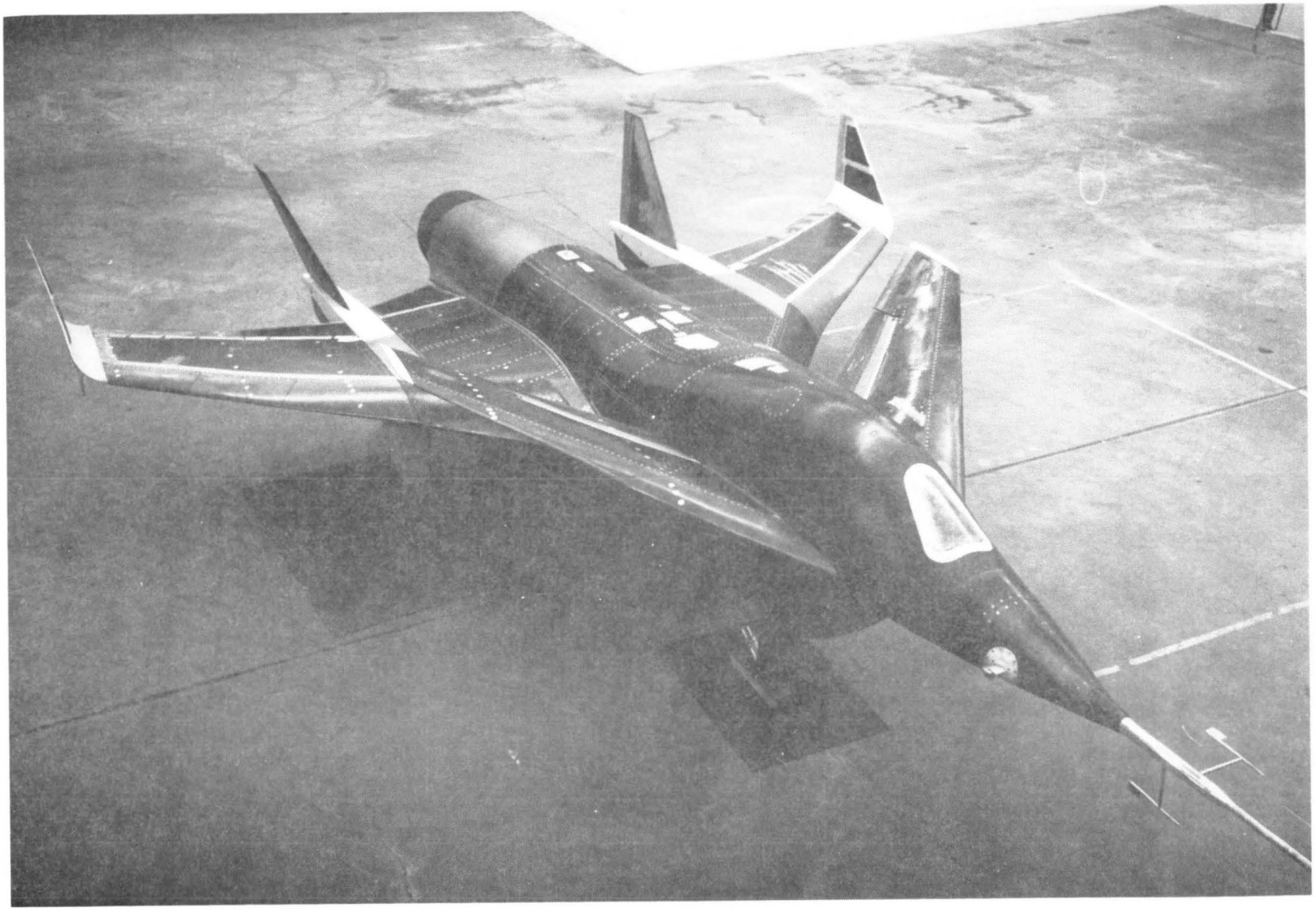

Figure 3. HiMAT Aircraft - A/V-2

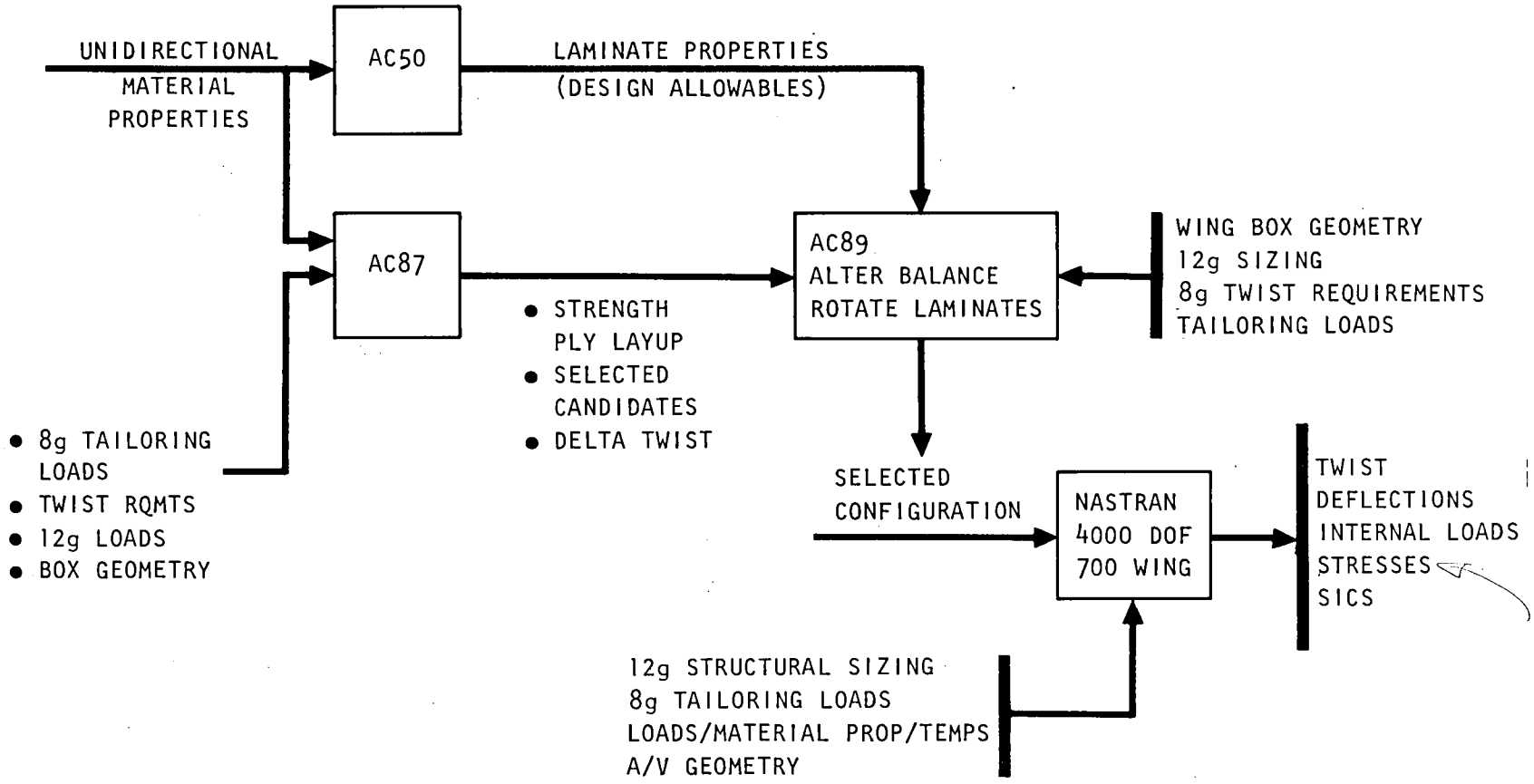

Figure 4. Wing and Canard Tailoring Procedure

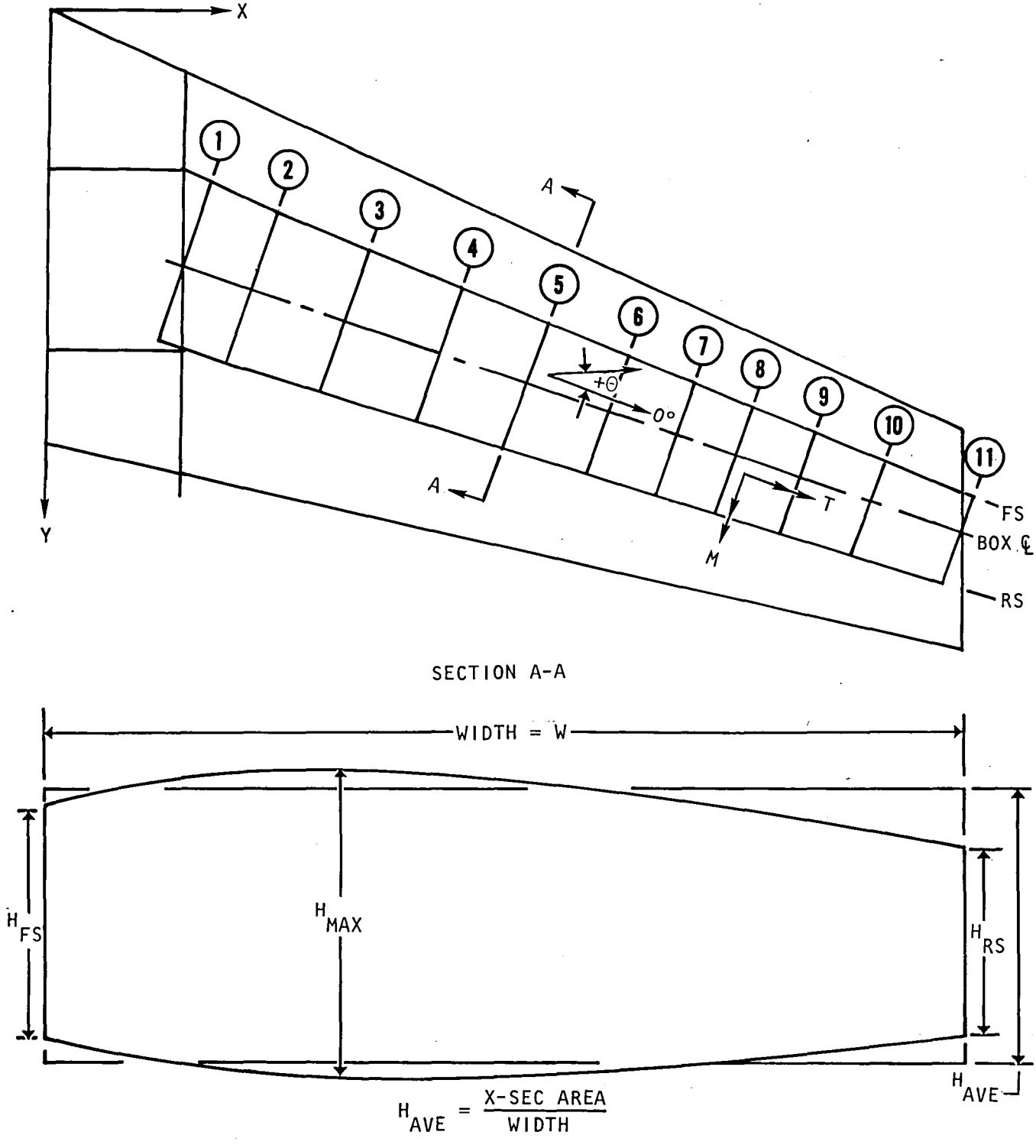

Figure 5. Idealized Cross Section - AC87

$$N_X = \frac{M}{WH} \; ; \quad N_{XY} = \frac{T}{2WH} \; ; \quad N'_{XY} = \frac{V_Z}{2H} + \frac{T}{2WH} \; ; \quad N''_{XY} = \frac{V_Z}{2H} + \frac{T}{2WH}$$

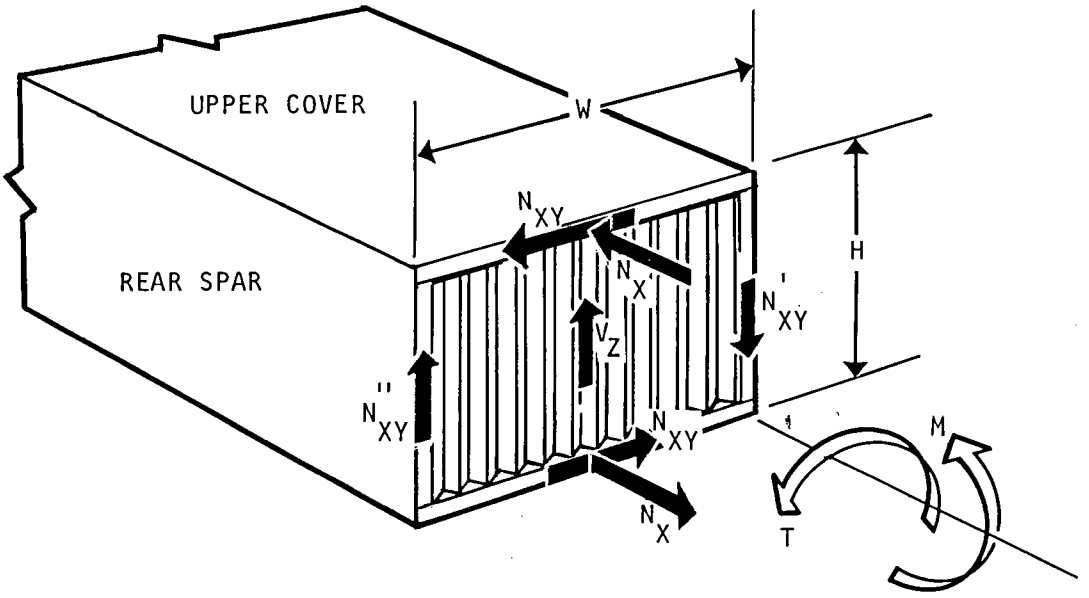

Figure 6. AC87Q Loading Model

$$N_X = \frac{M}{WH} \; ; \quad N_{XY} = \frac{T}{2WH}$$

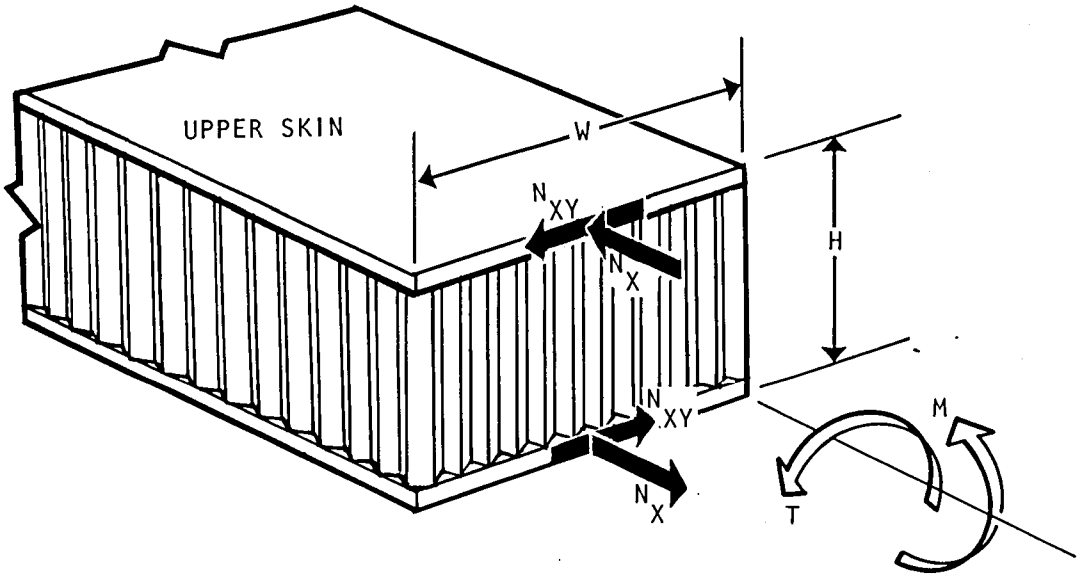

Figure 7. AC87 Loading Model

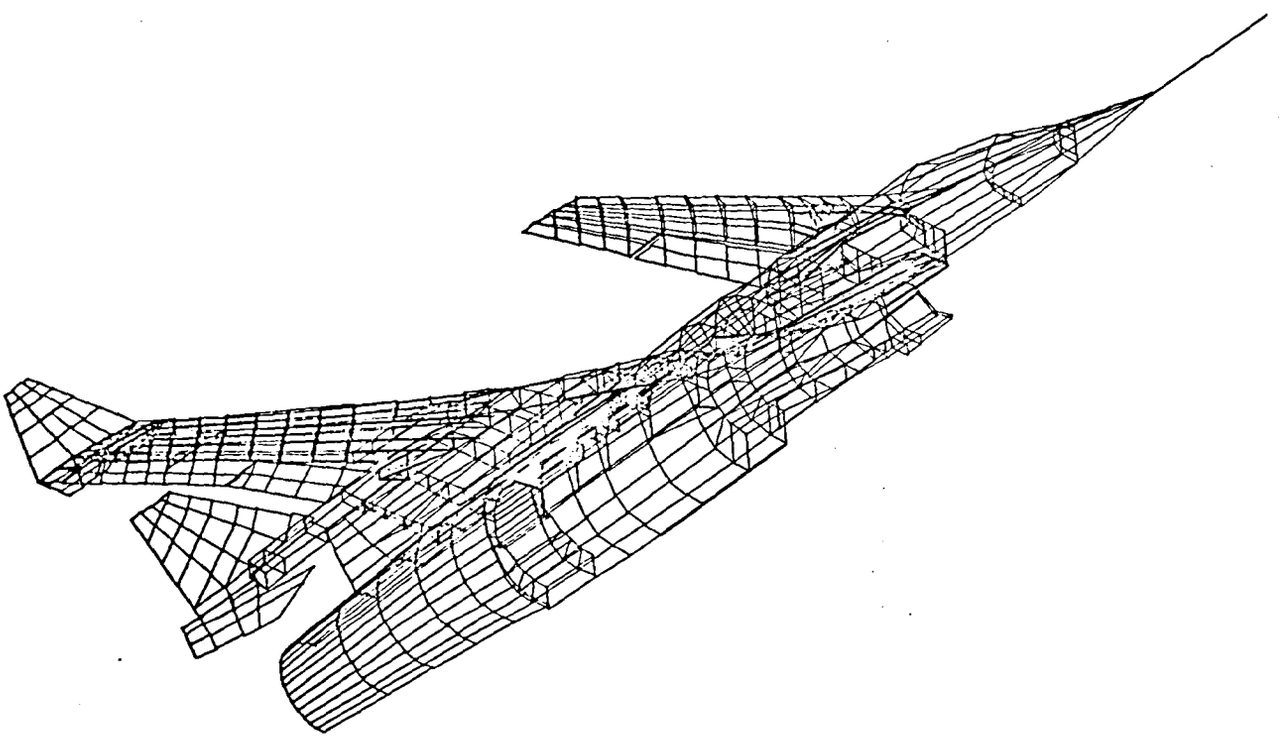

Figure 8. HiMAT Aircraft - FEM Perspective View

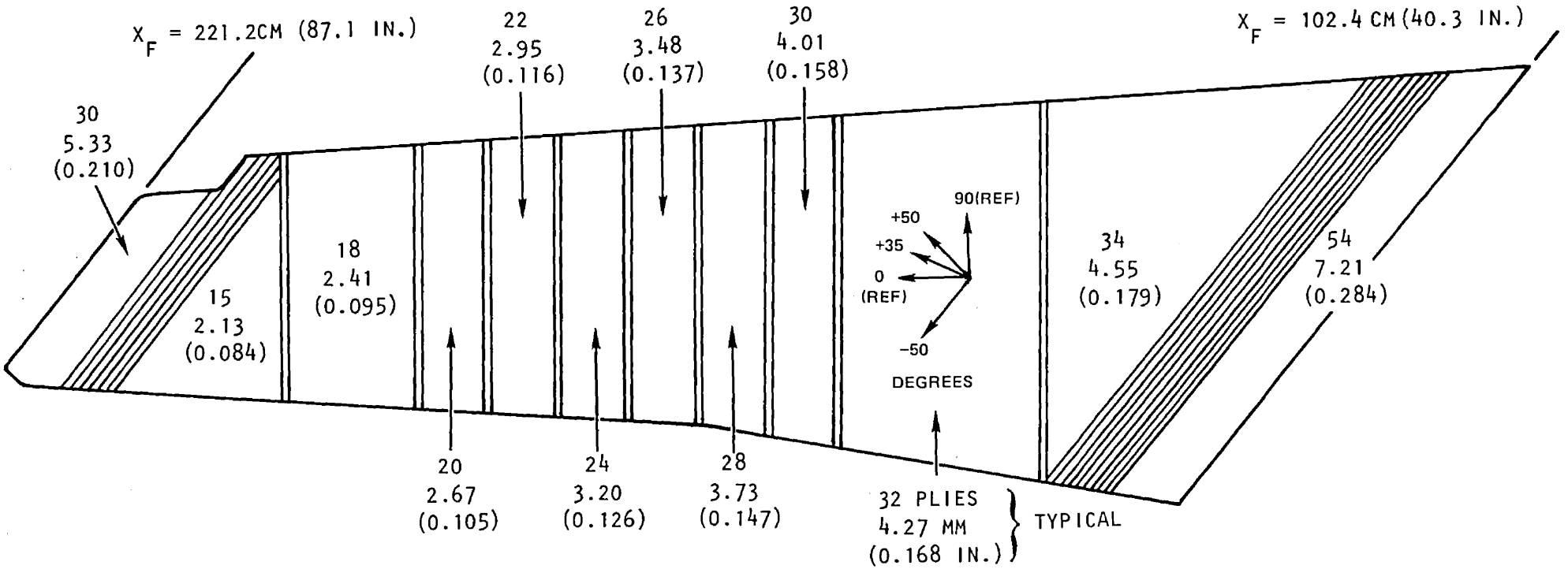

Figure 9. HiMAT Outboard Wing Ply Orientation and Layup

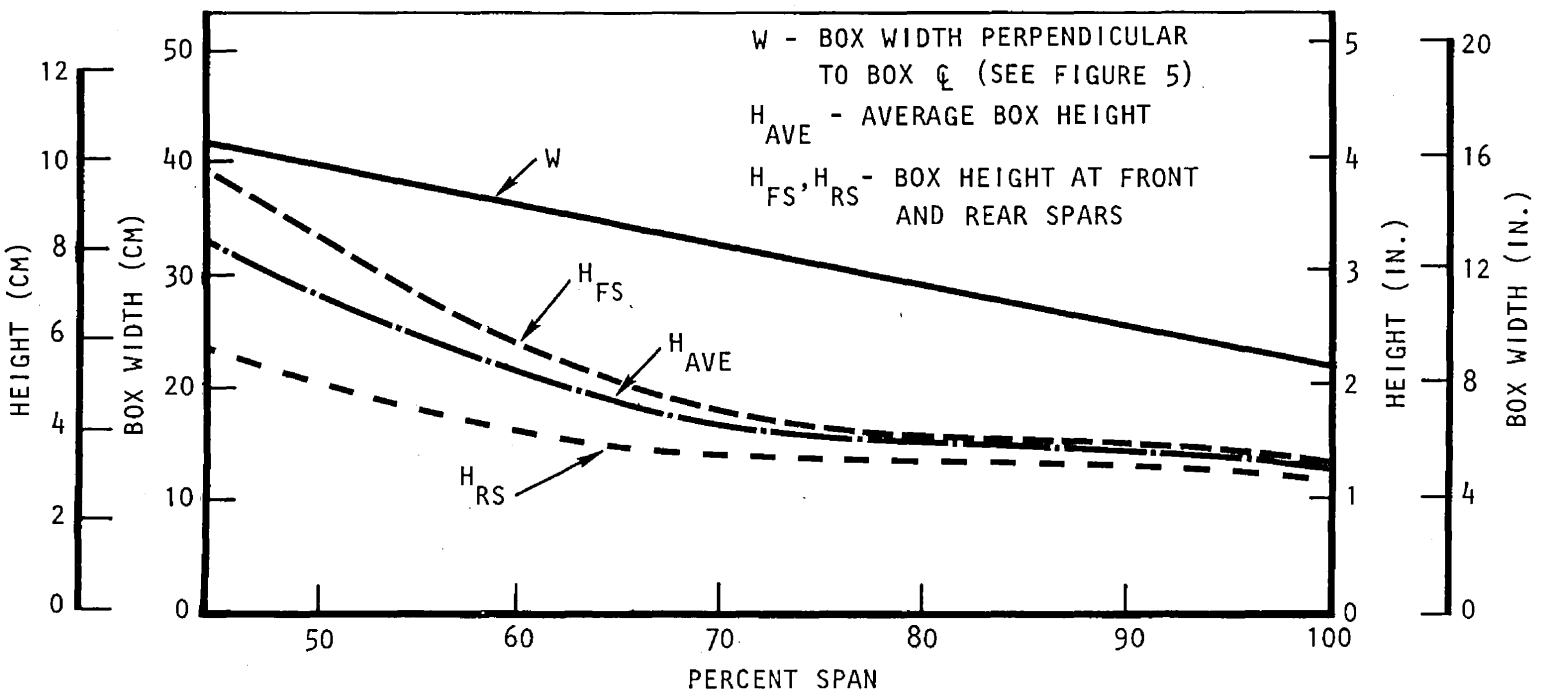

Figure 10. HiMAT Outboard Wing Box Geometry

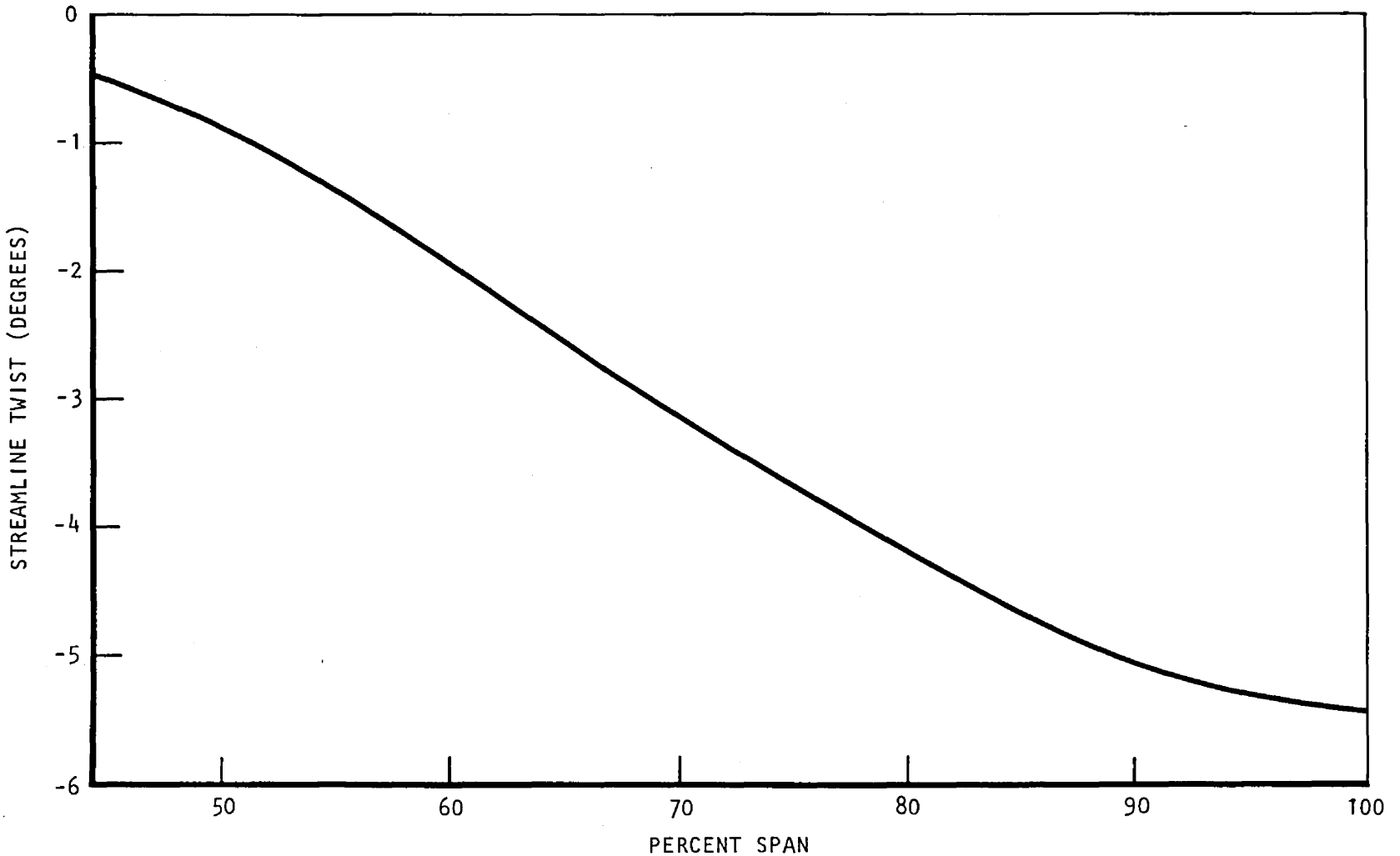

Figure 11. HiMAT Outboard Wing Required Structual Deflections

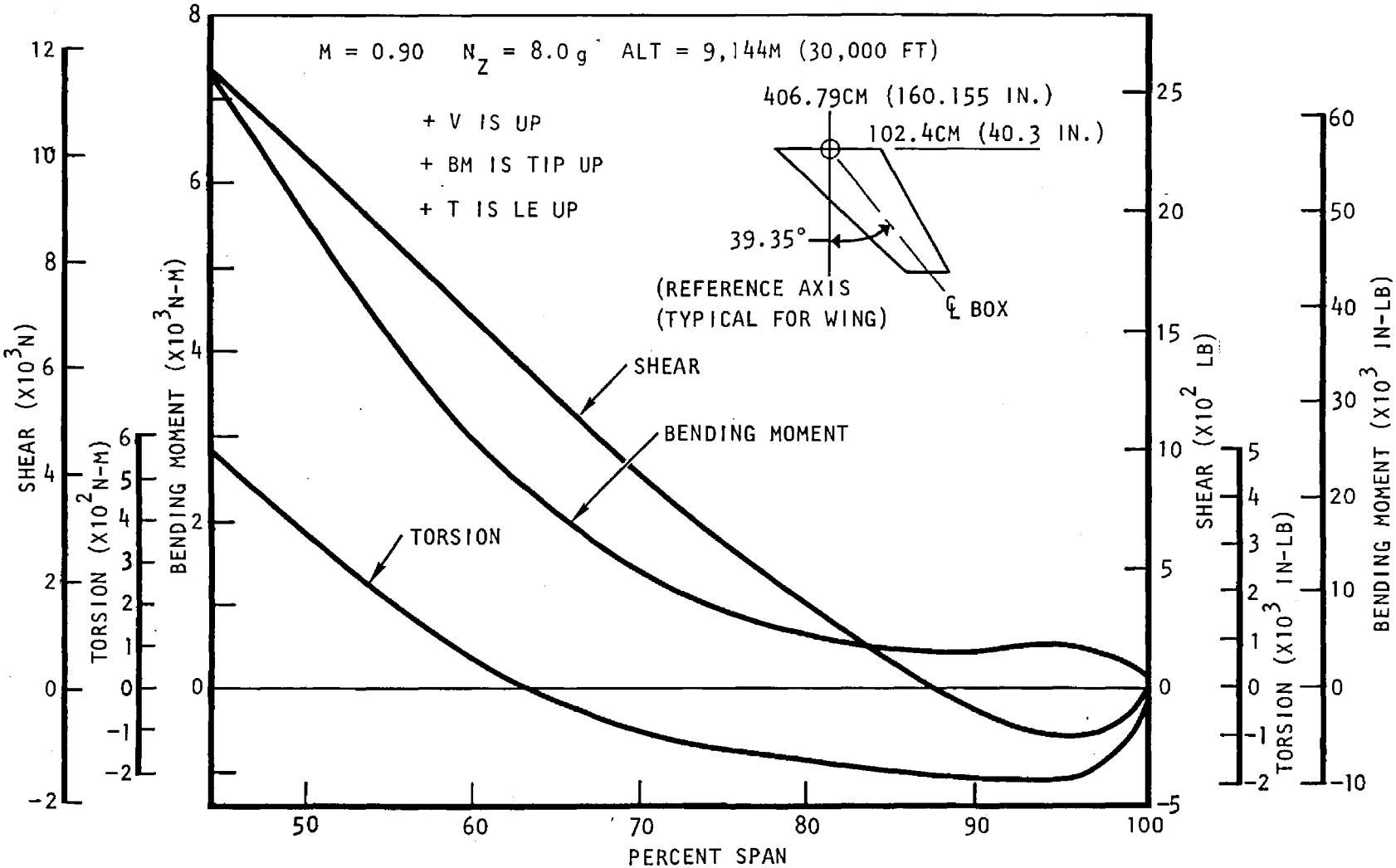

Figure 12. HiMAT Outboard Wing 8g Limit Loads (Net)

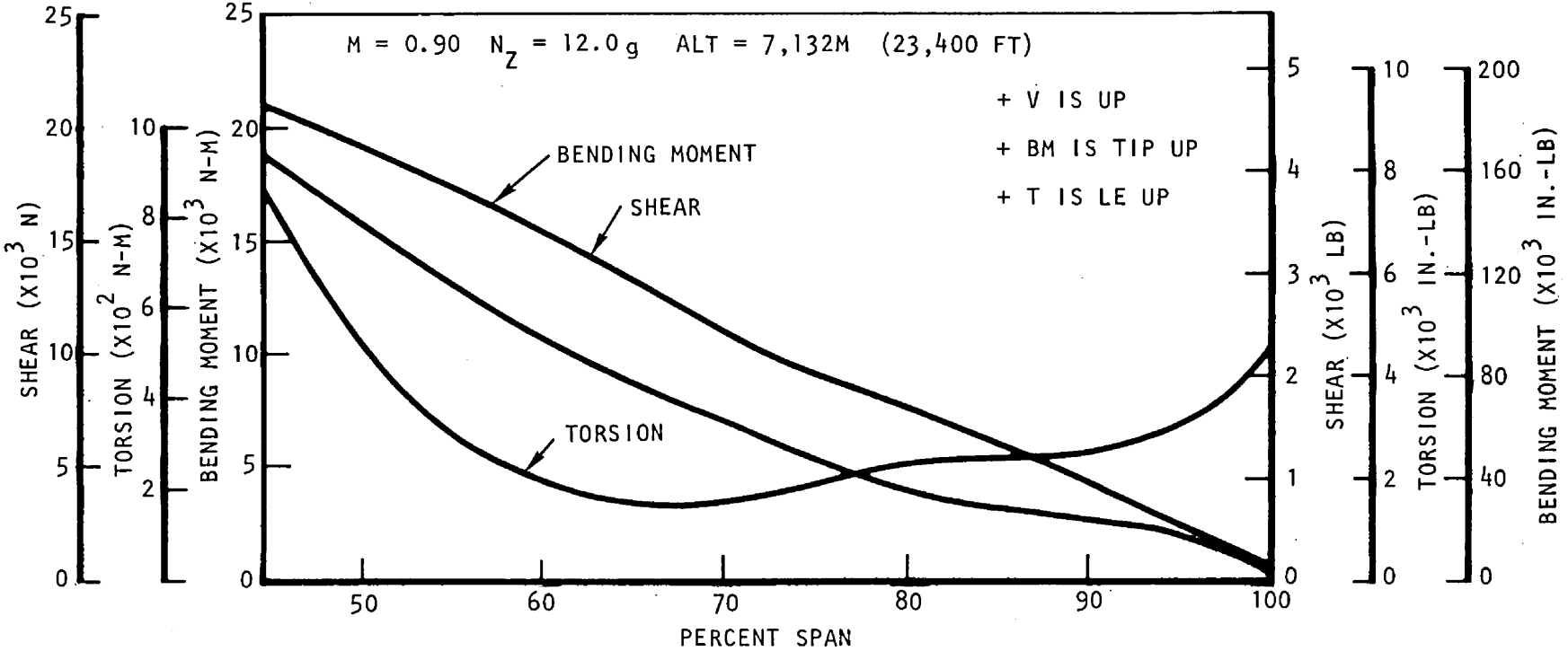

Figure 13. HiMAT Outboard Wing 12 g Limit Loads (Net)

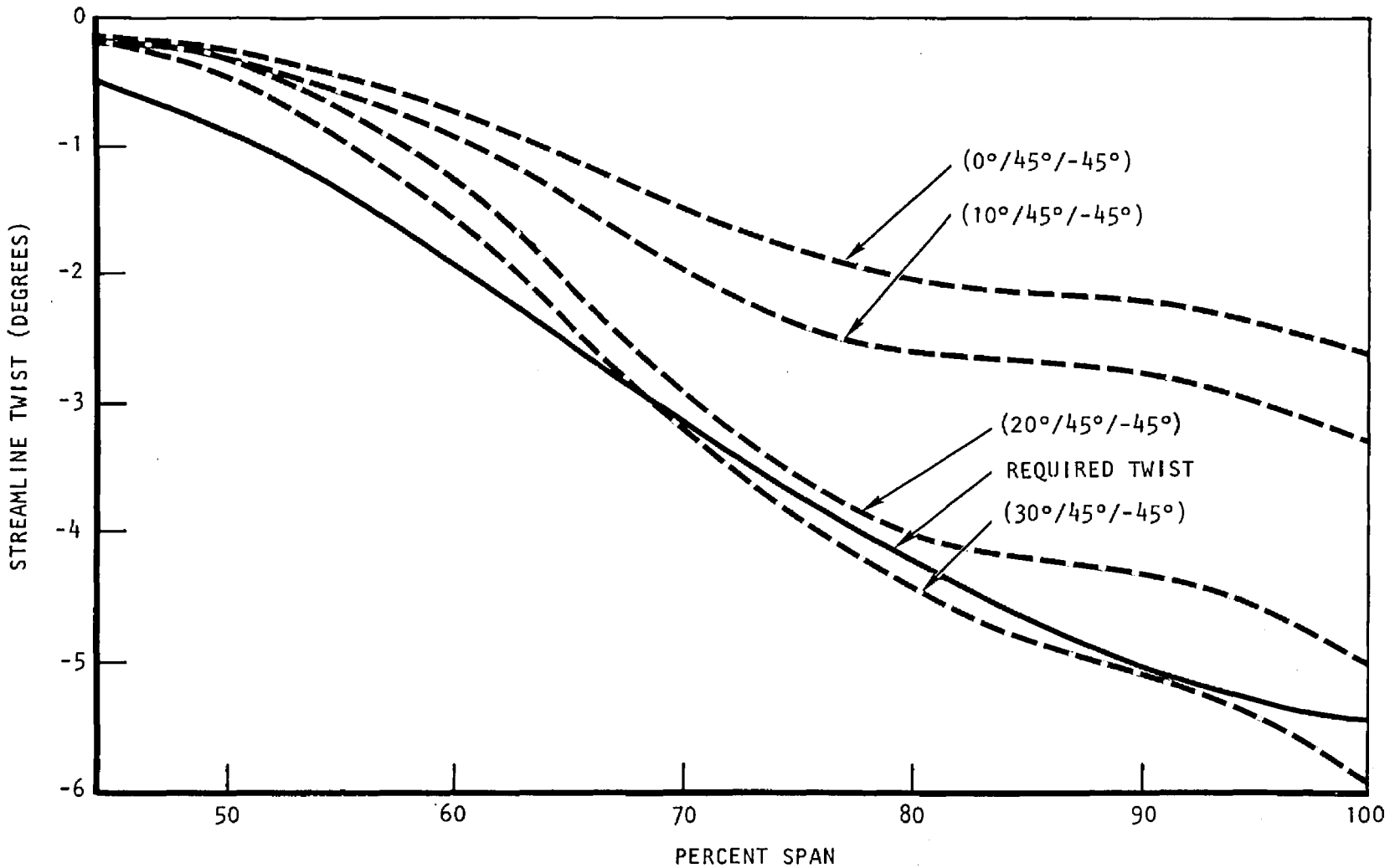

Figure 14. HiMAT Outboard Wing Cover Laminate
AC87 Results (θ°/45°/-45°)

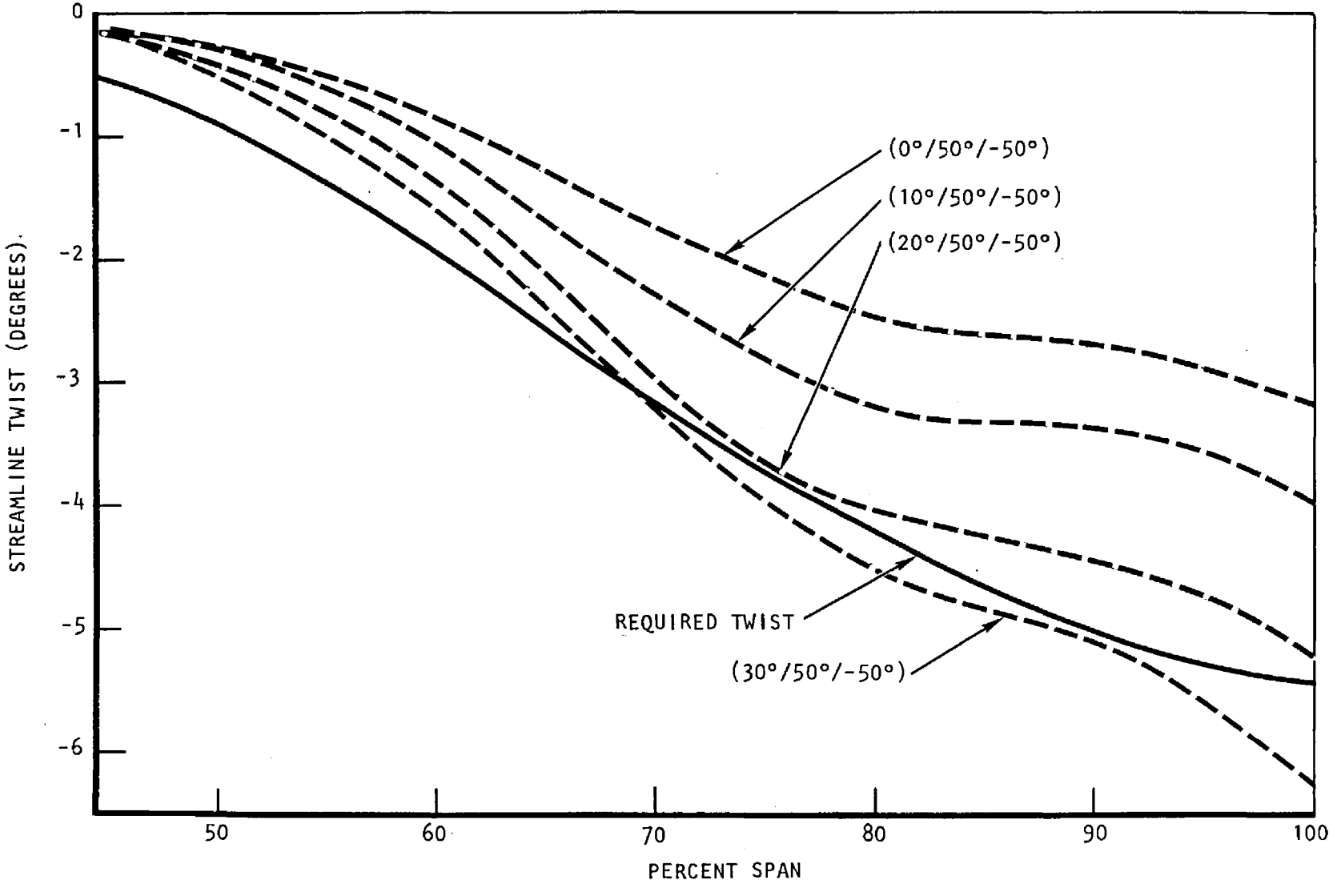

Figure 15. HiMAT Outboard Wing Cover Laminate
AC87 Results (0°/50°/-50°)

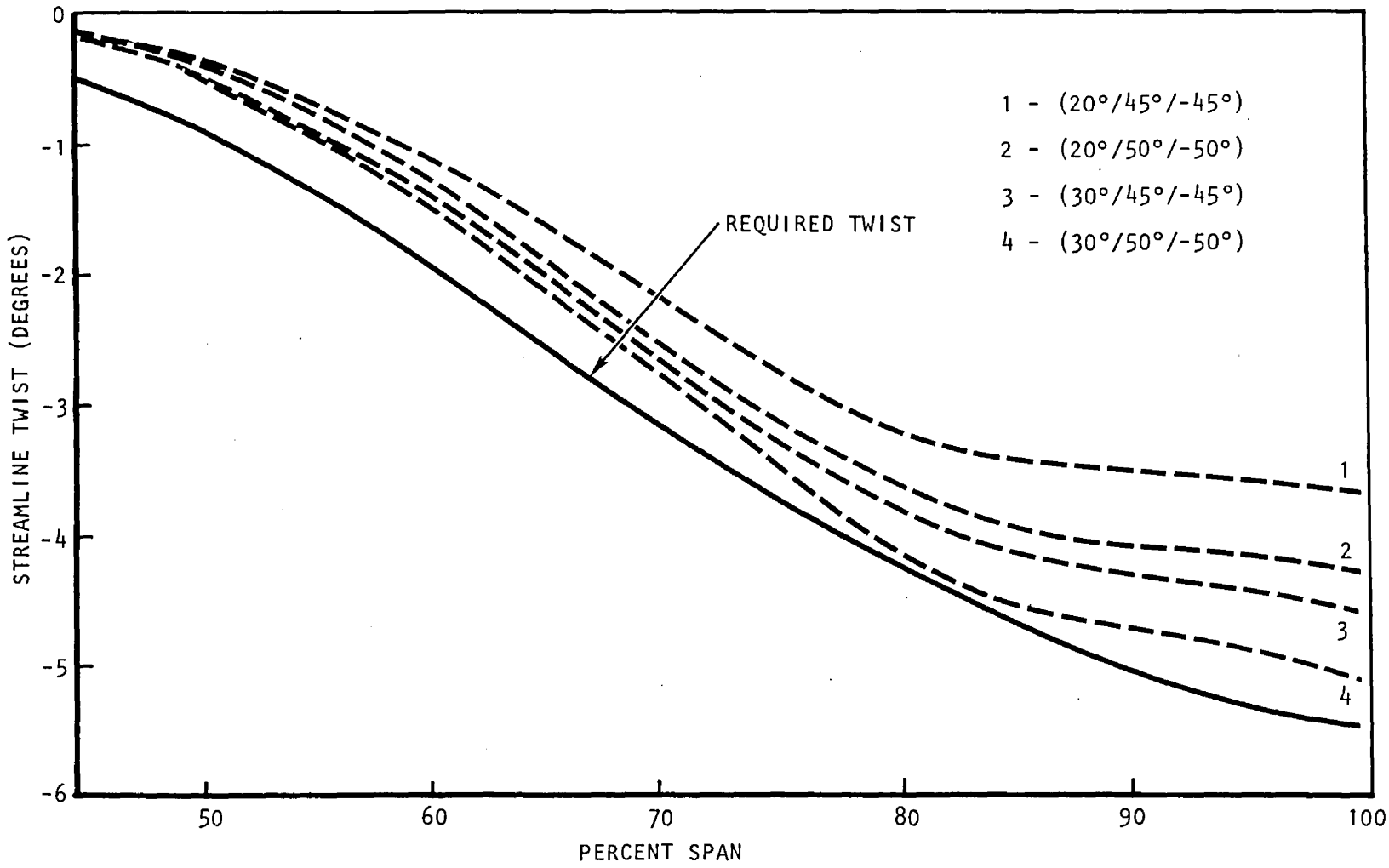

Figure 16. HiMAT Outboard Wing-AC89 Results

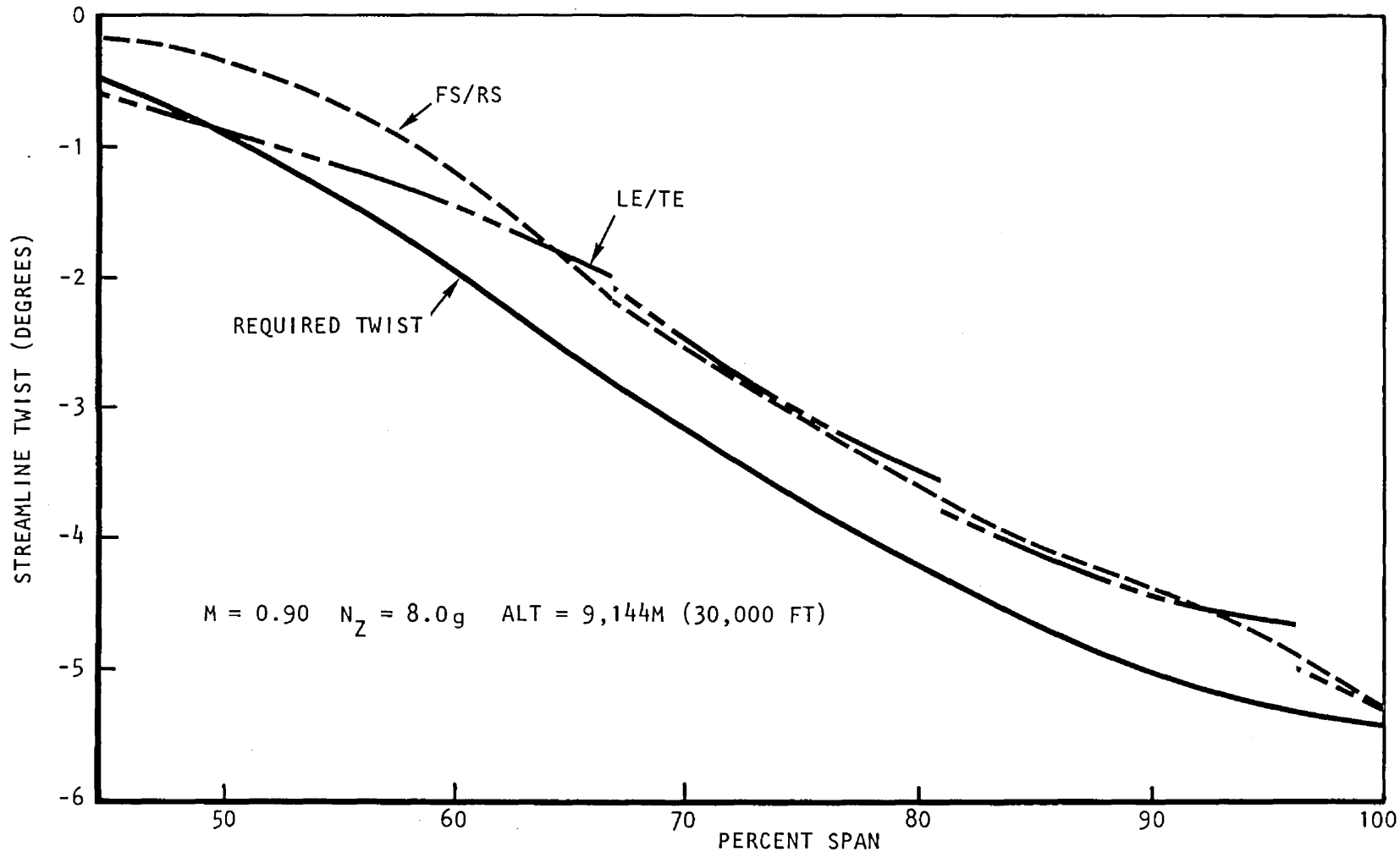

Figure 17. HiMAT Outboard Wing - AC87 Designed Covers (30°/50°/-50°) NASTRAN Results

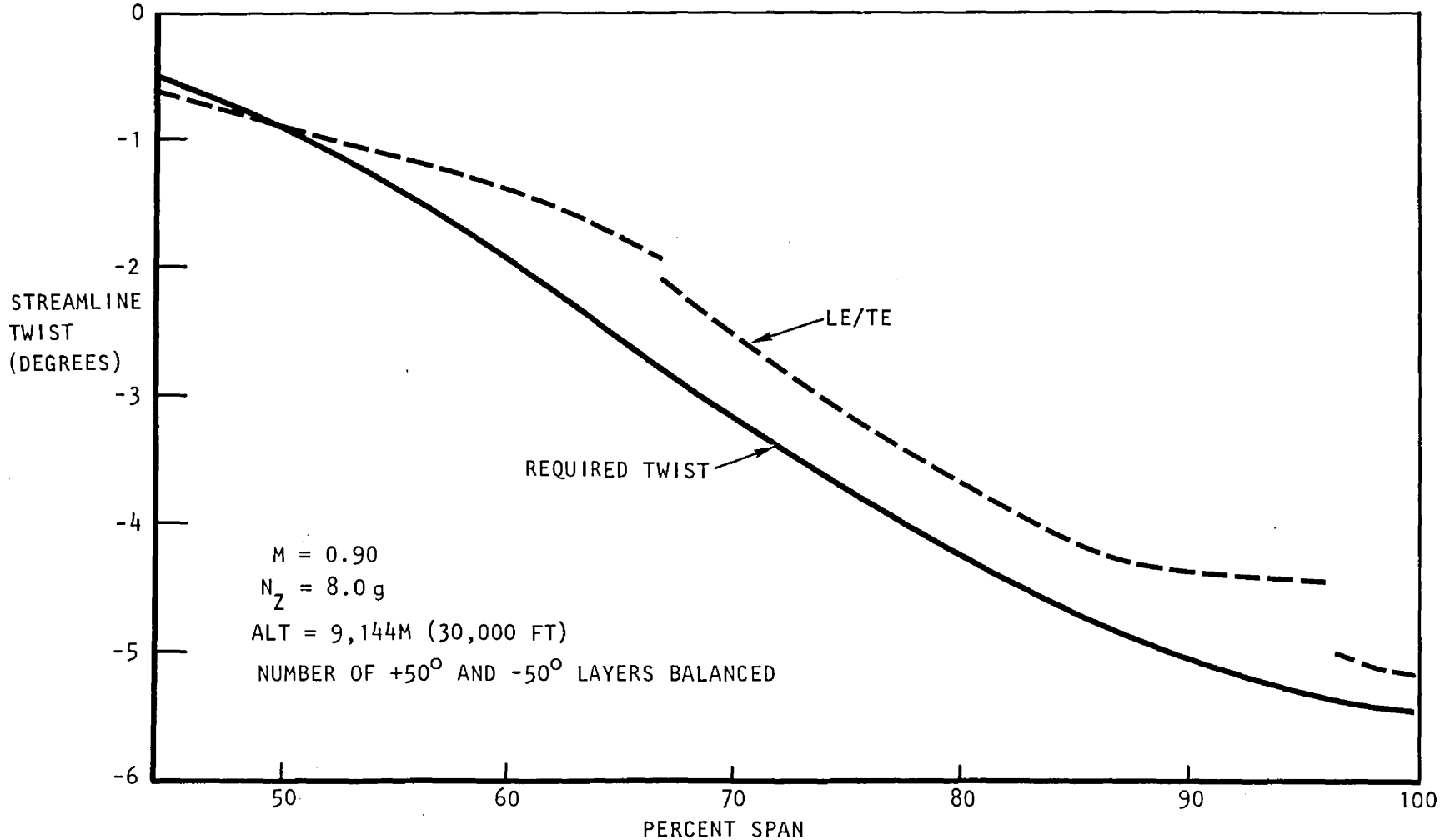

Figure 18. HiMAT Outboard Wing - Revised AC87 Covers (30°/50°/-50°) NASTRAN Results

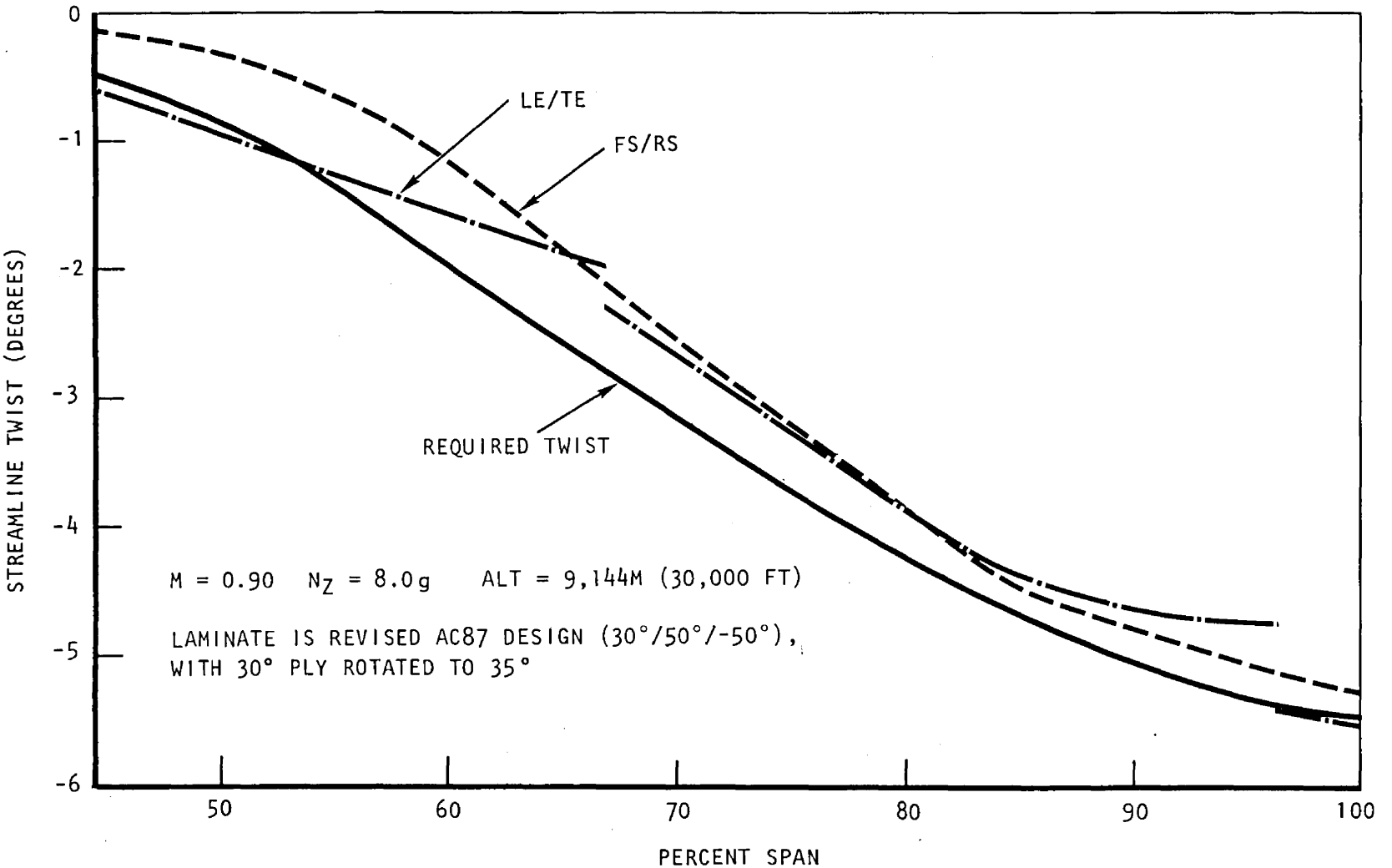

Figure 19. HiMAT Outboard Wing Cover Laminates (35°/50°/-50°)
NASTRAN Results-Selected Design

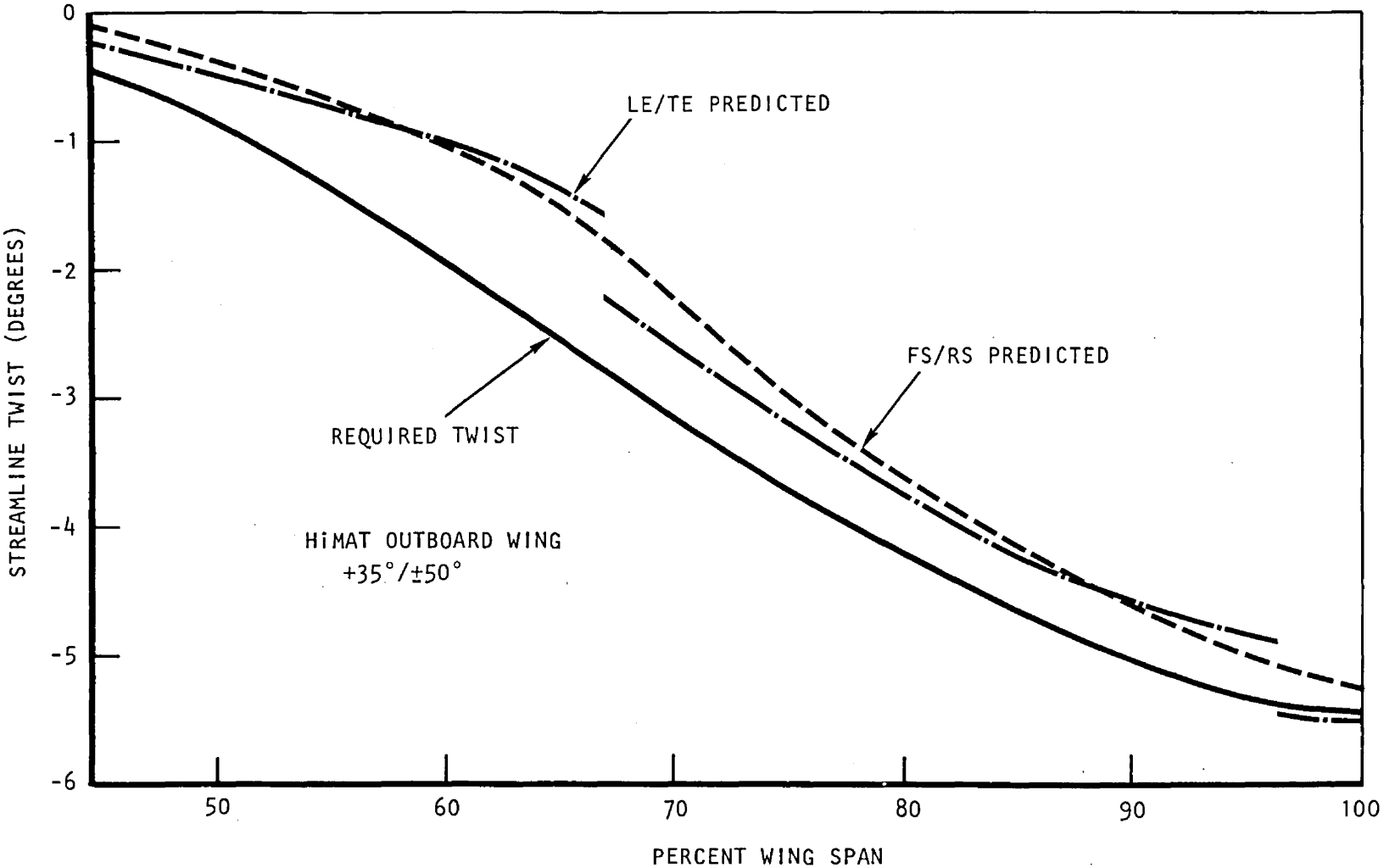

Figure 20. Wing Structural Twist at 7,620 M (25,000 Ft)

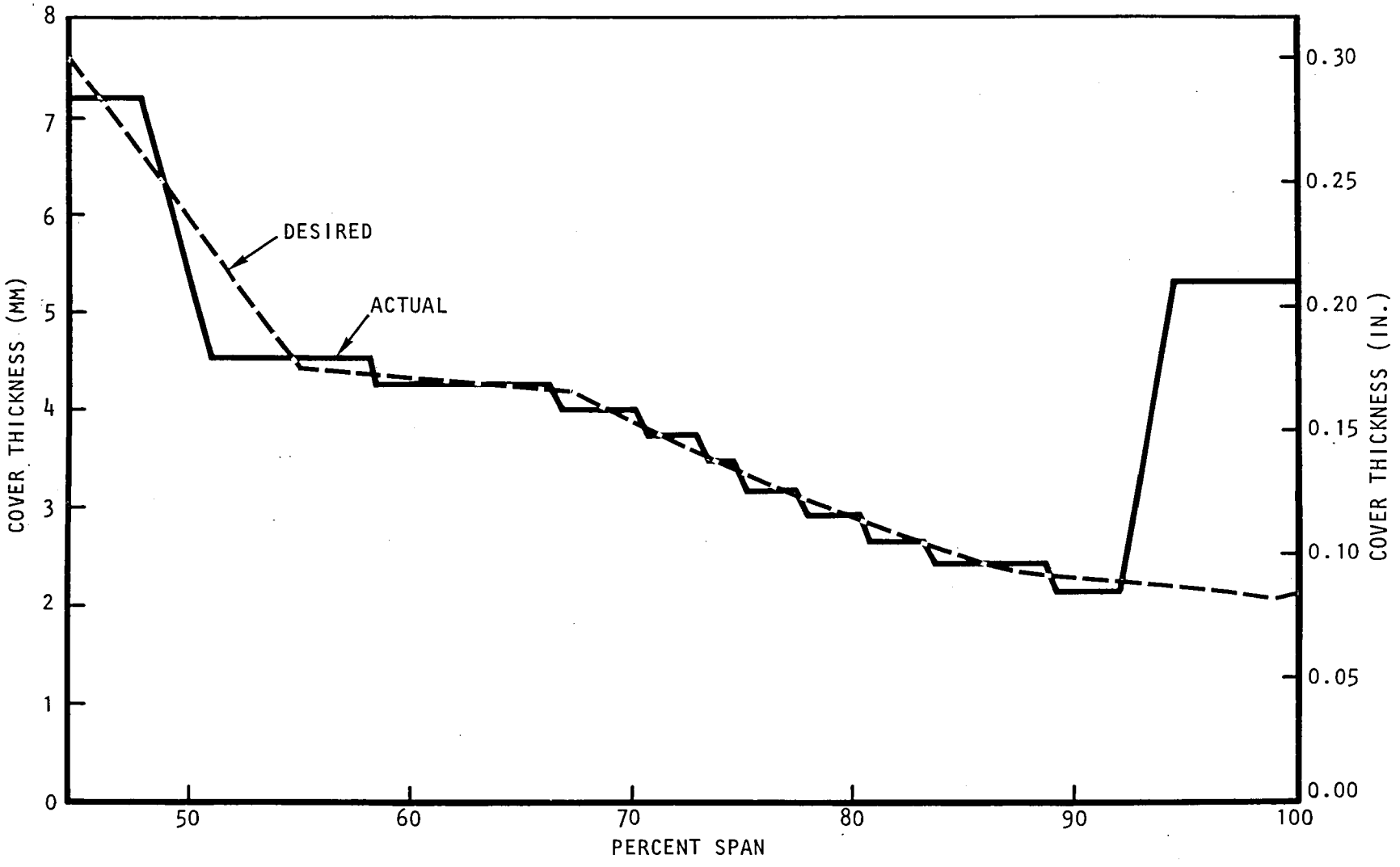

Figure 21. HiMAT Outboard Wing Cover Laminate Thickness

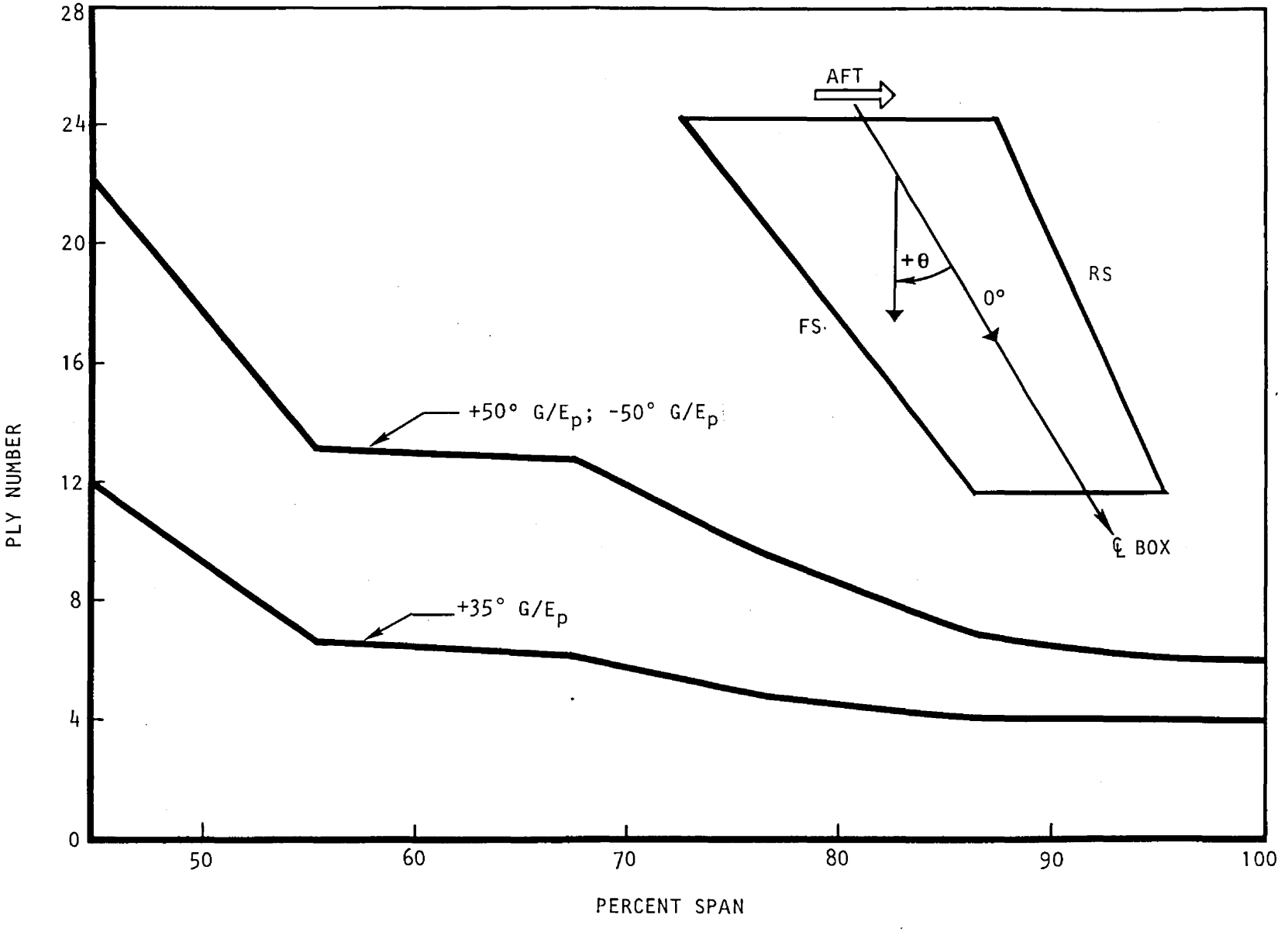

Figure 22. HiMAT Outboard Wing - Desired Cover Ply Distributions

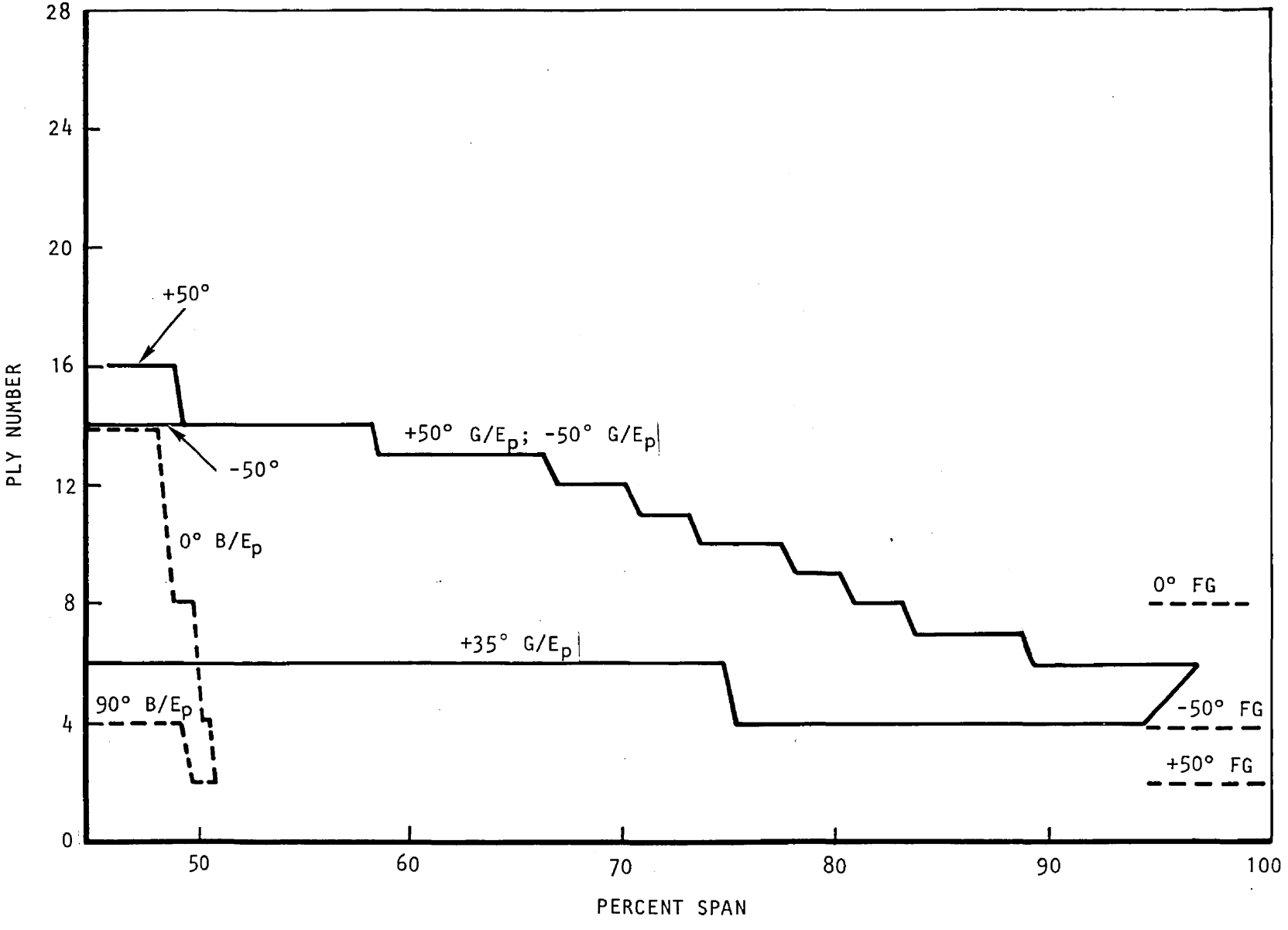

Figure 23. HiMAT Outboard Wing - Actual Cover Ply Distributions

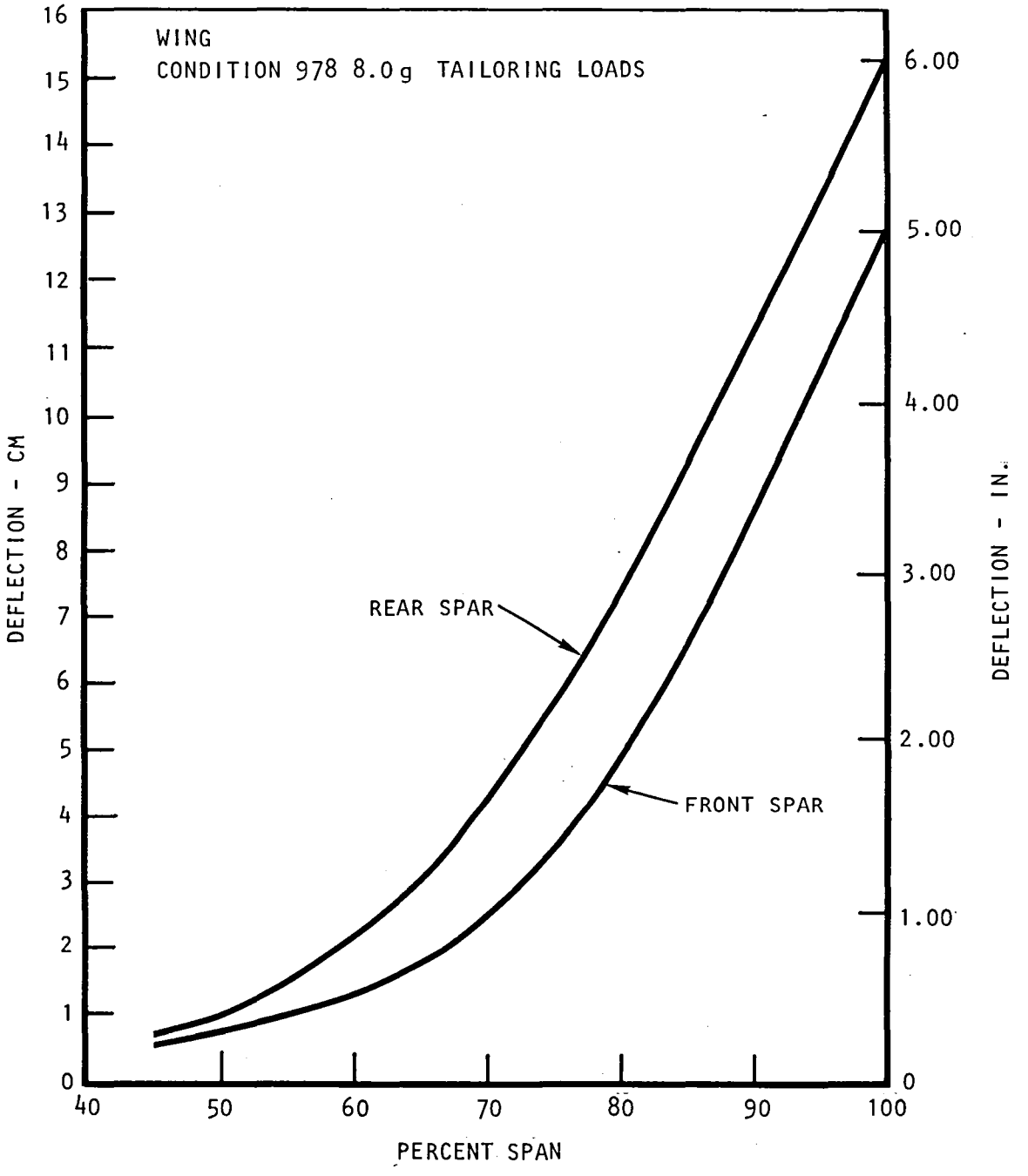

Figure 24. Wing Front Spar/Rear Spar Deflections

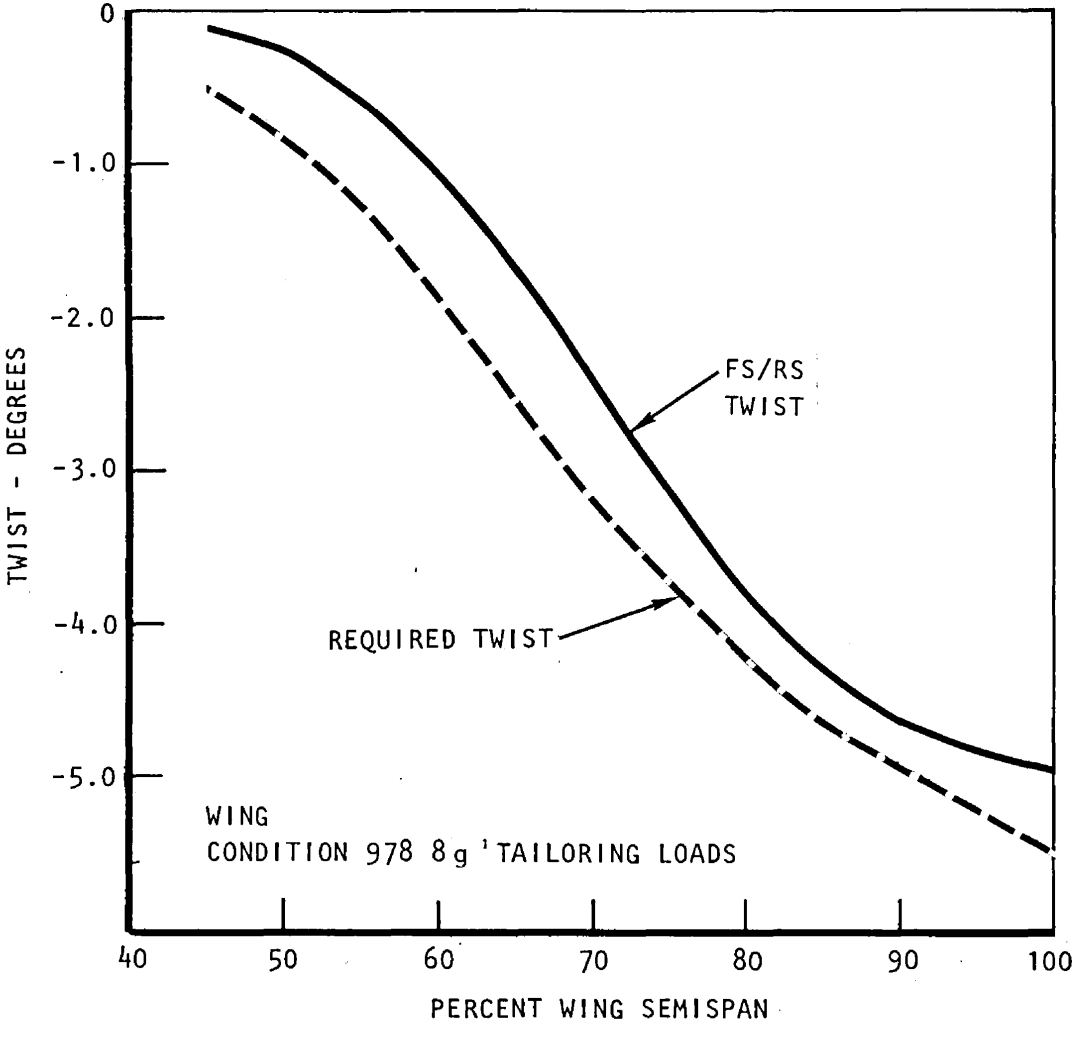

Figure 25. Final Predicted Wing Twist - Front and Rear Spars

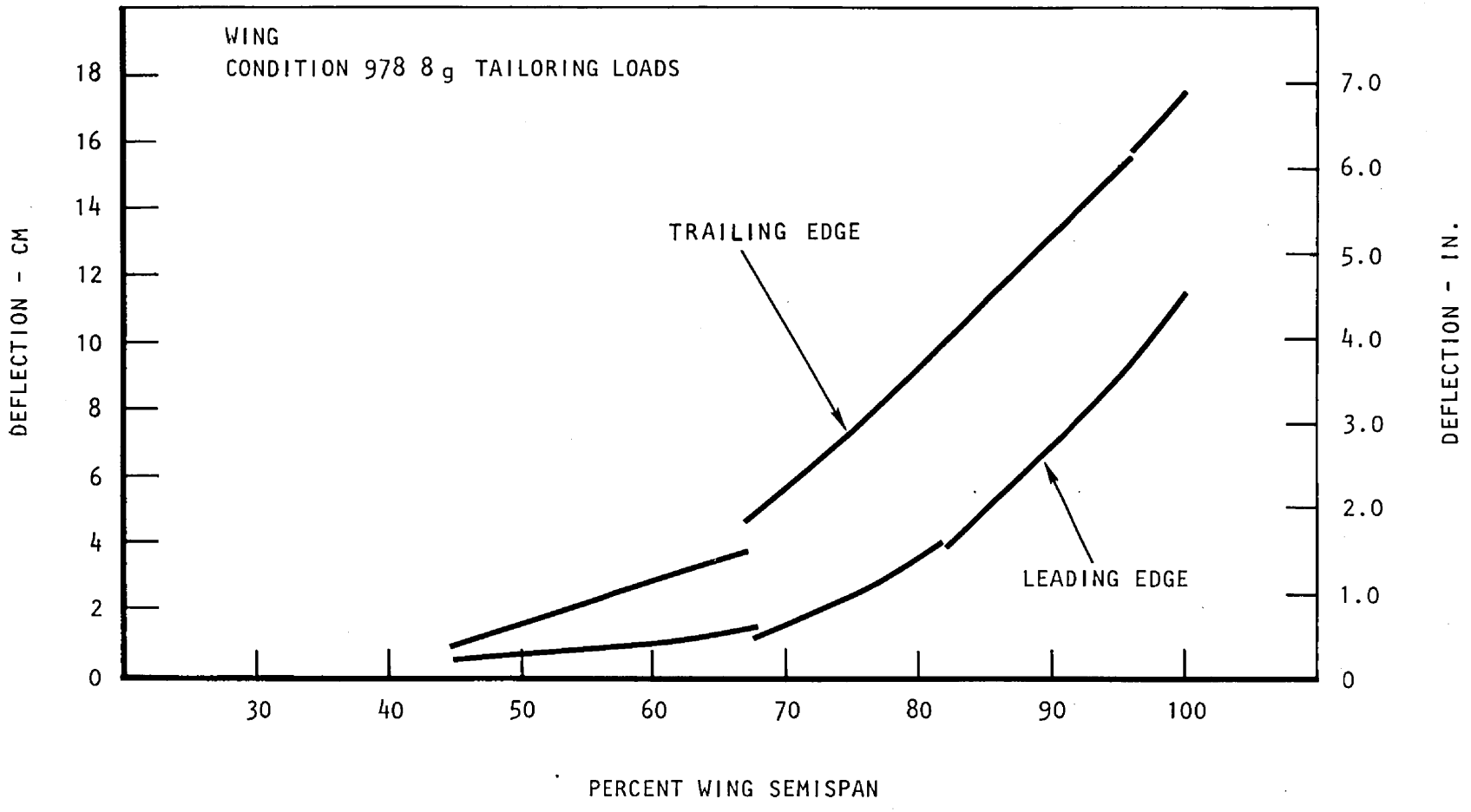

Figure 26. Wing Deflection - Leading/Trailing Edge

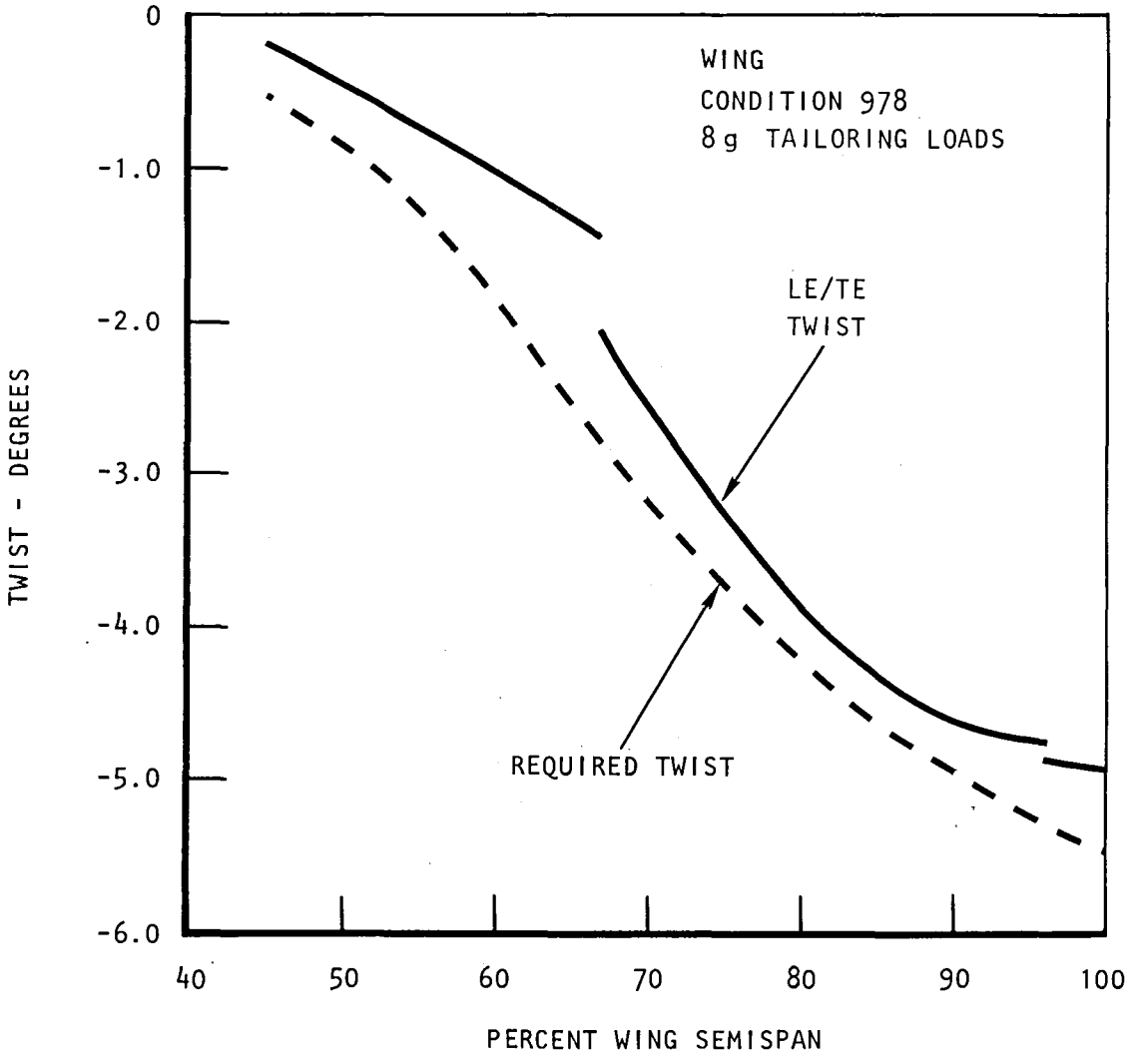

Figure 27. Final Prediction Wing Twist - Leading/Trailing Edge

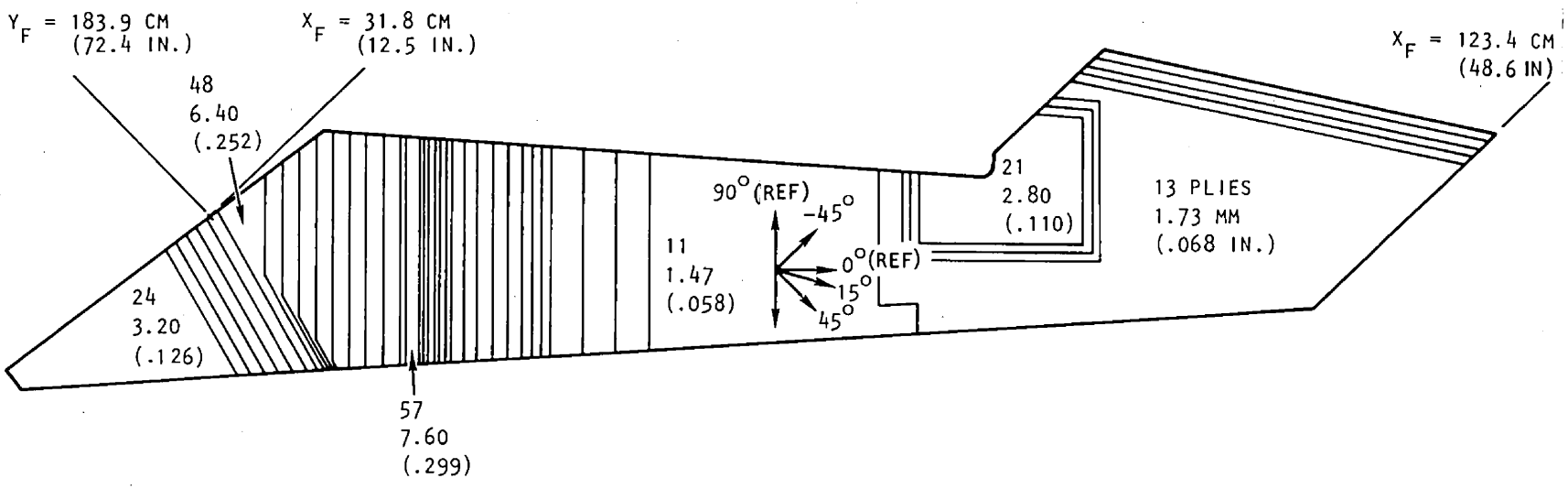

Figure 28. HiMAT Canard Ply Orientation and Layup

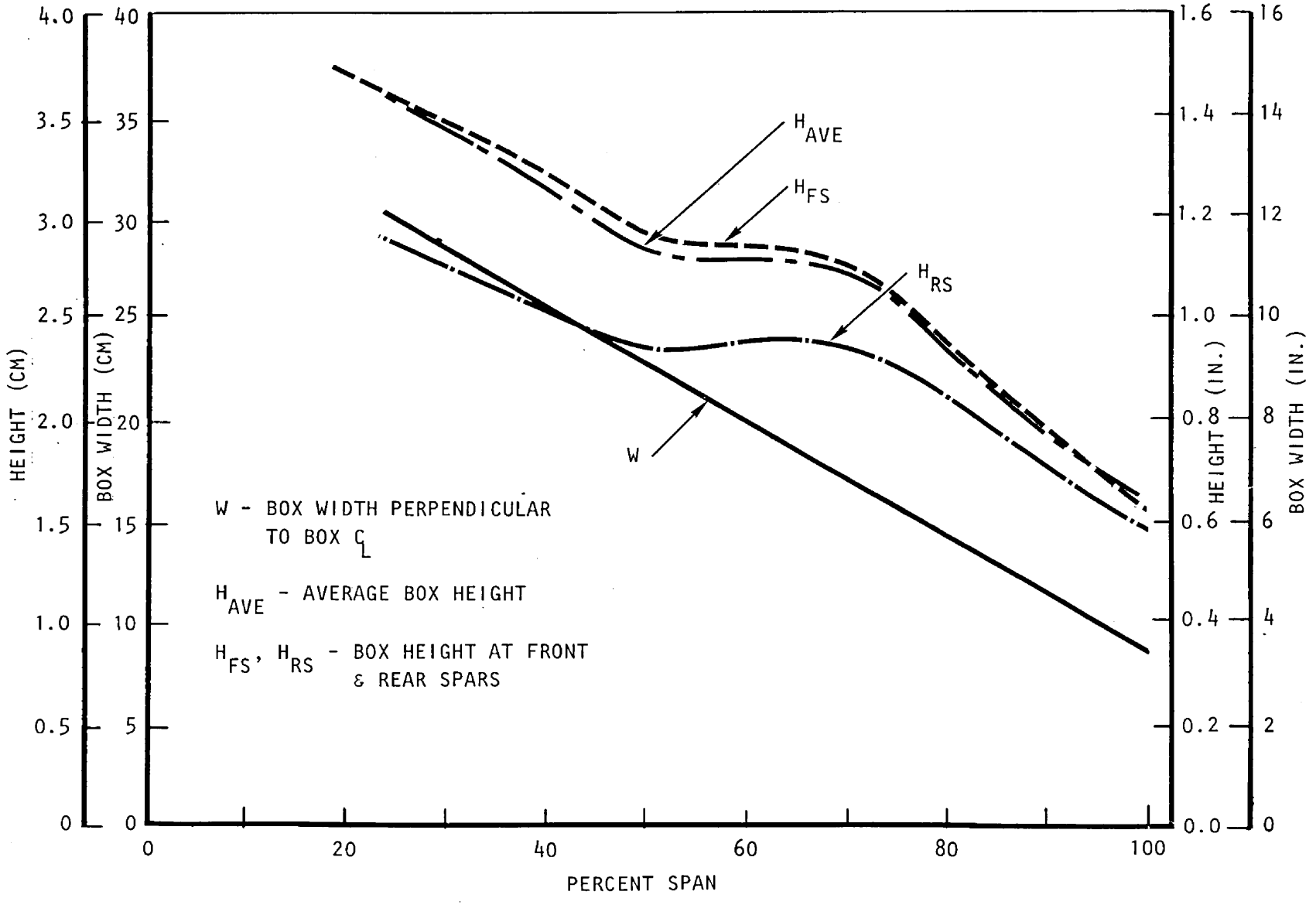

Figure 29. HiMAT Canard Box Geometry

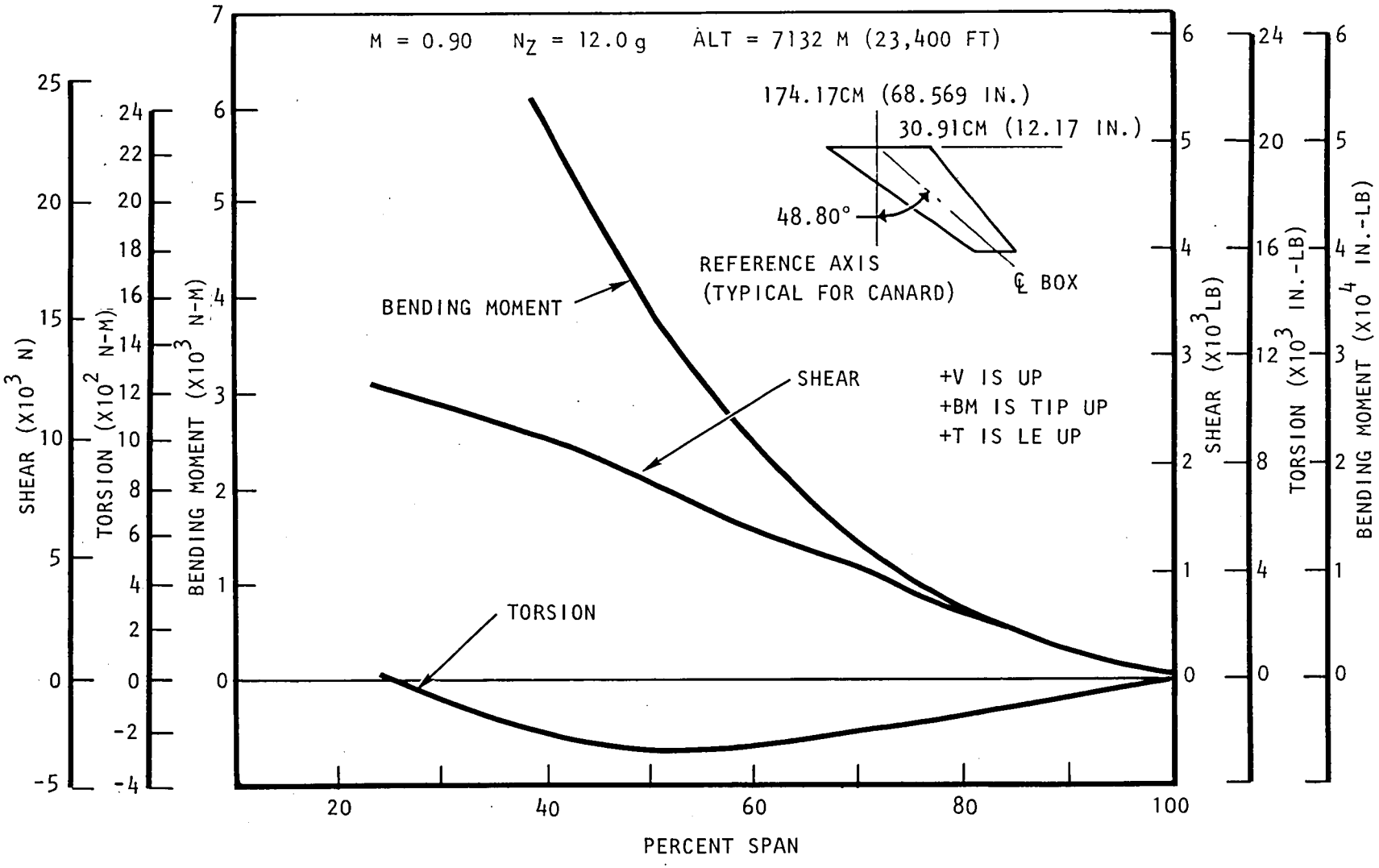

Figure 30. HiMAT Canard 12 g Net Limit Loads

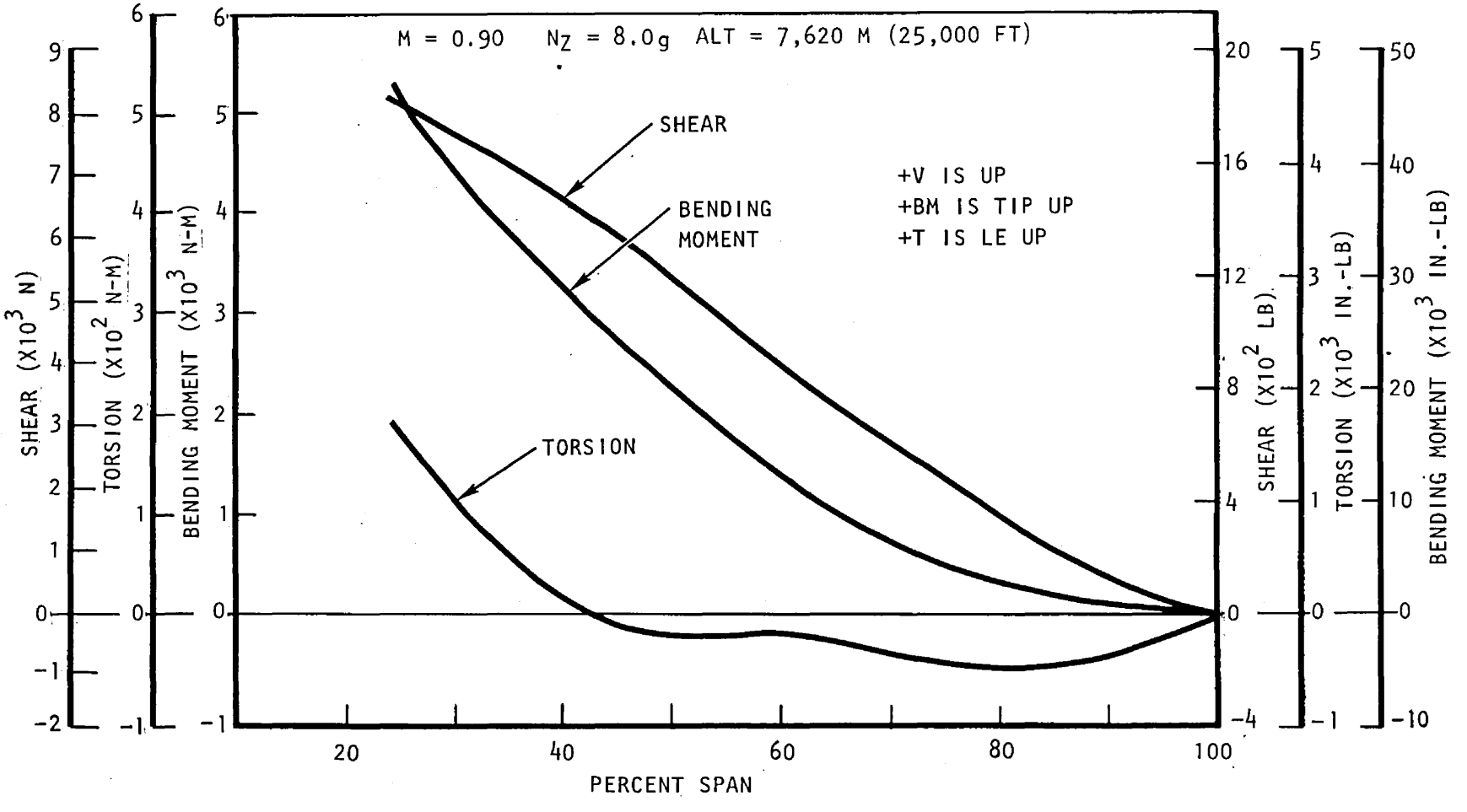

Figure 31. HiMAT Canard 8 g Net Limit Loads

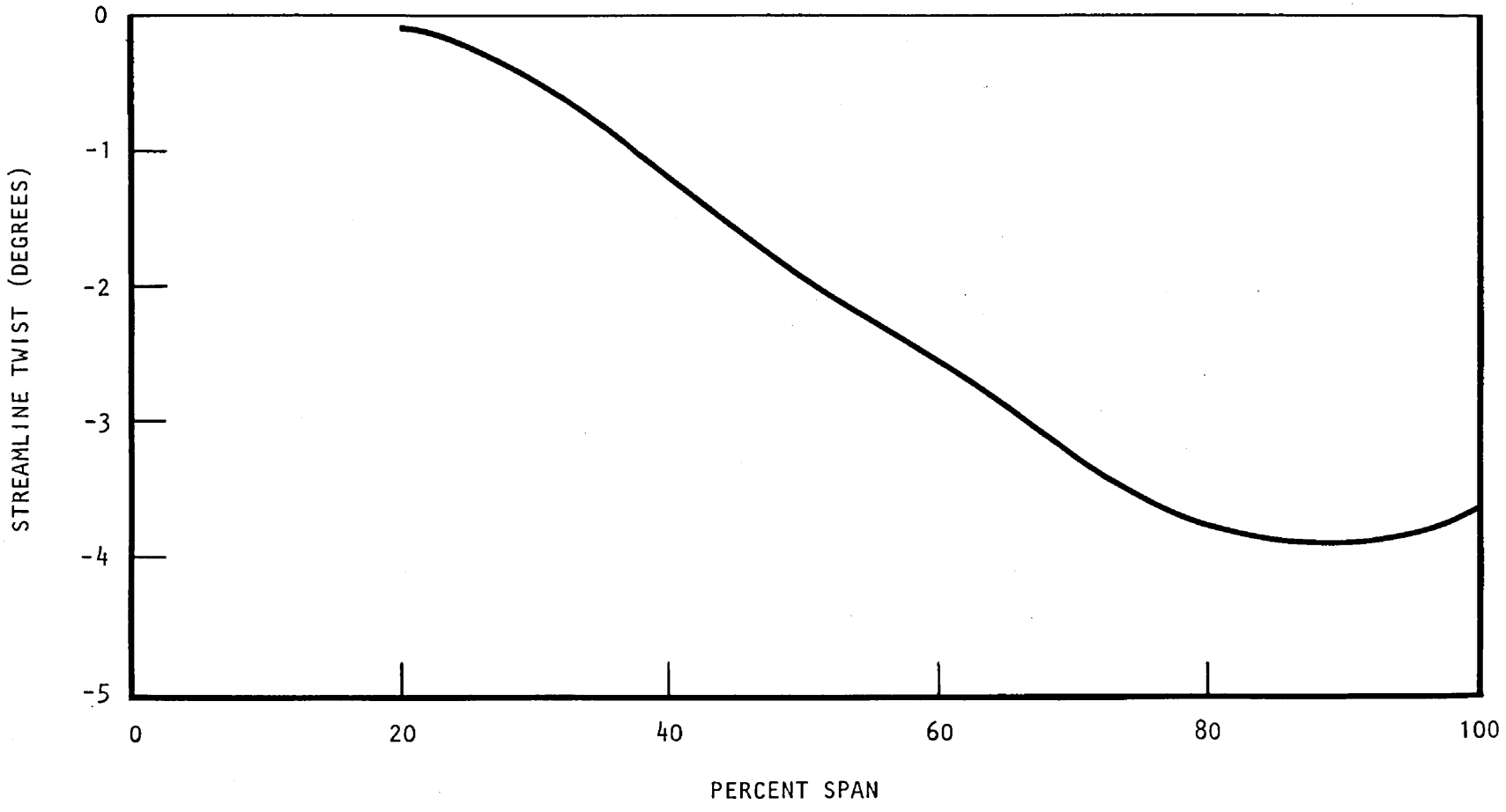

Figure 32. HiMAT Canard Required Structural Deflections - 8g Maneuver Condition

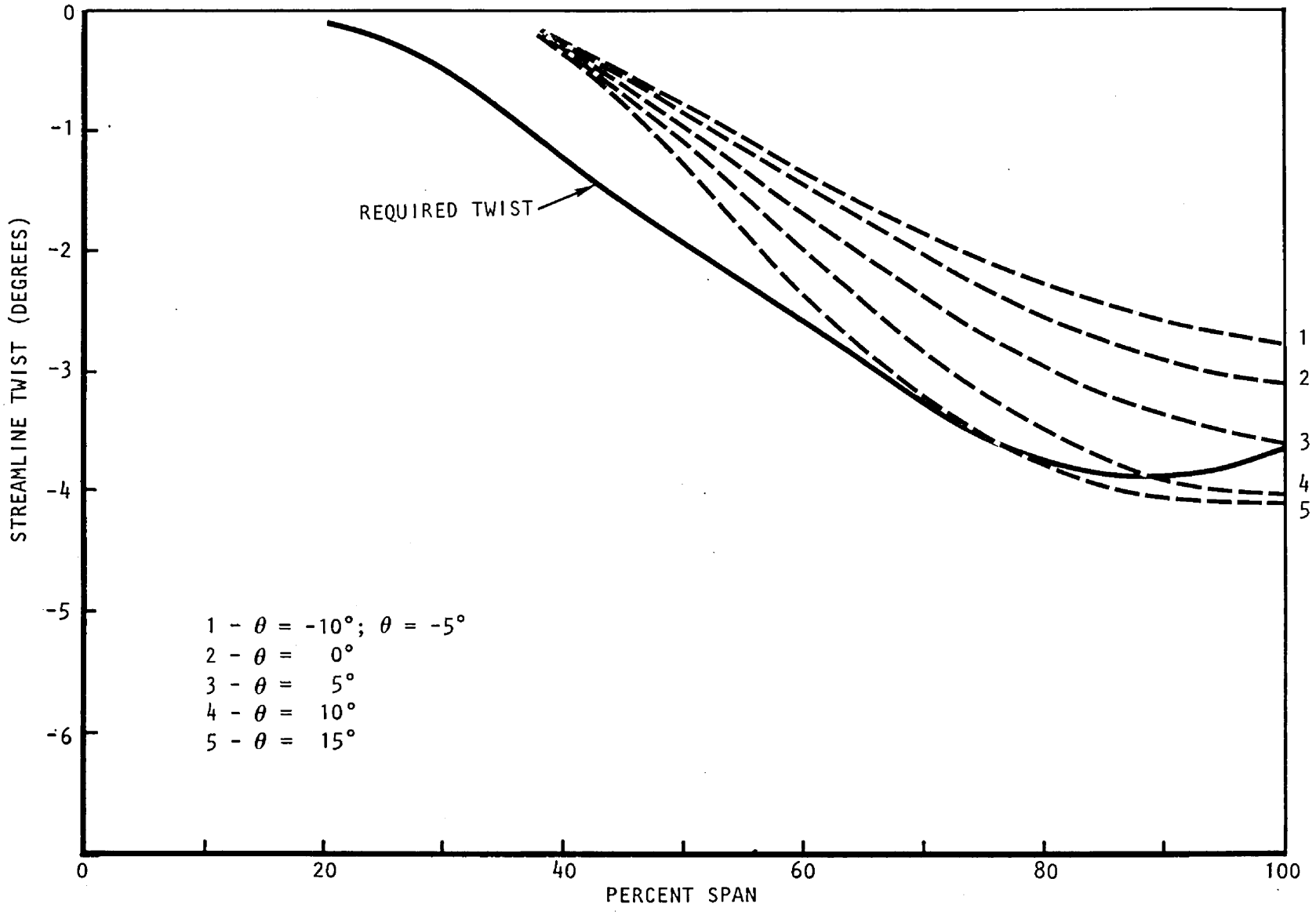

Figure 33. HiMAT Canard AC87 Results - Cover Laminate ($\theta°/45°/-45°$)

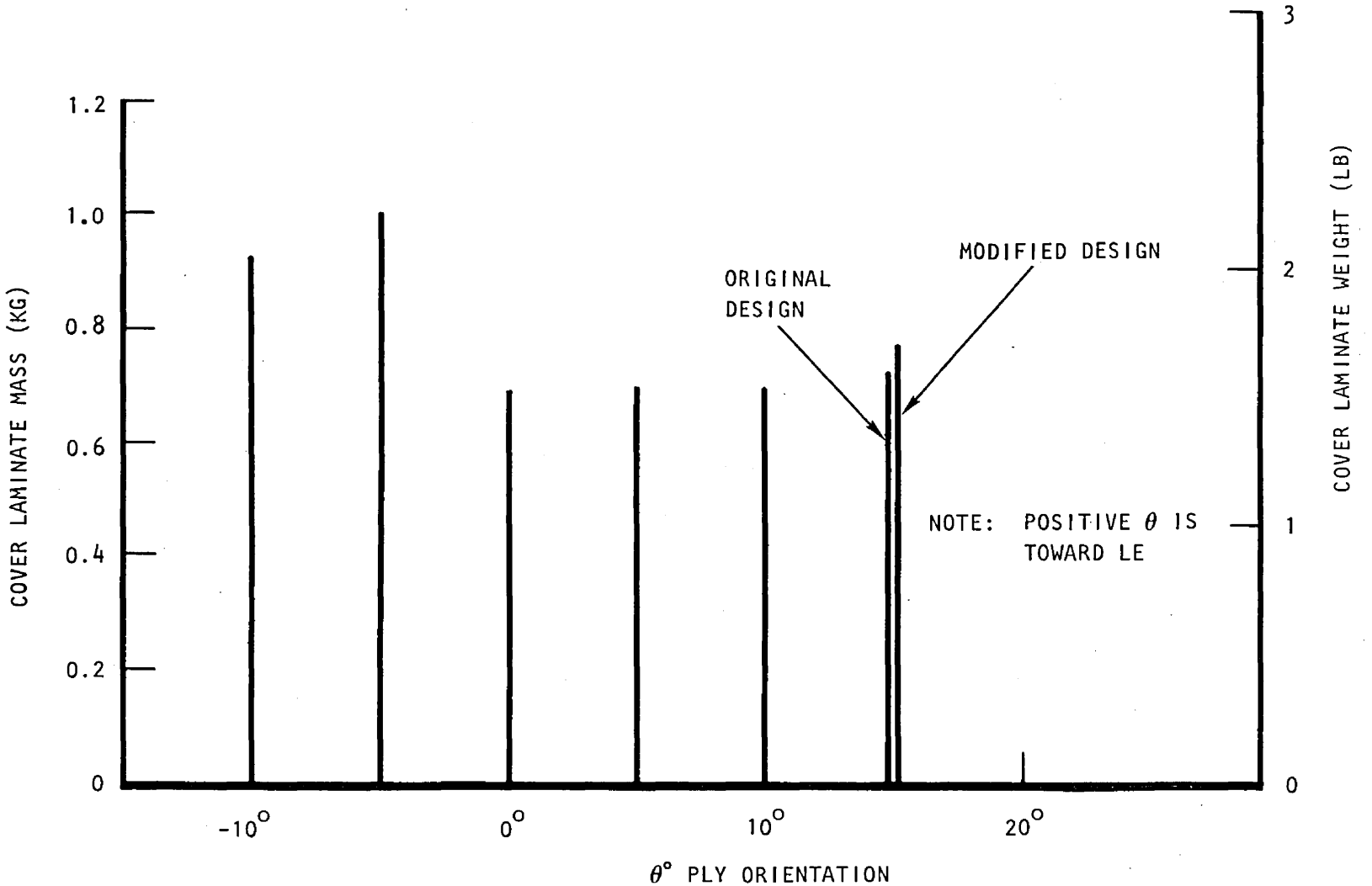

Figure 34. HiMAT Canard Cover Mass - AC87 Designs (θ°/45°/-45°)

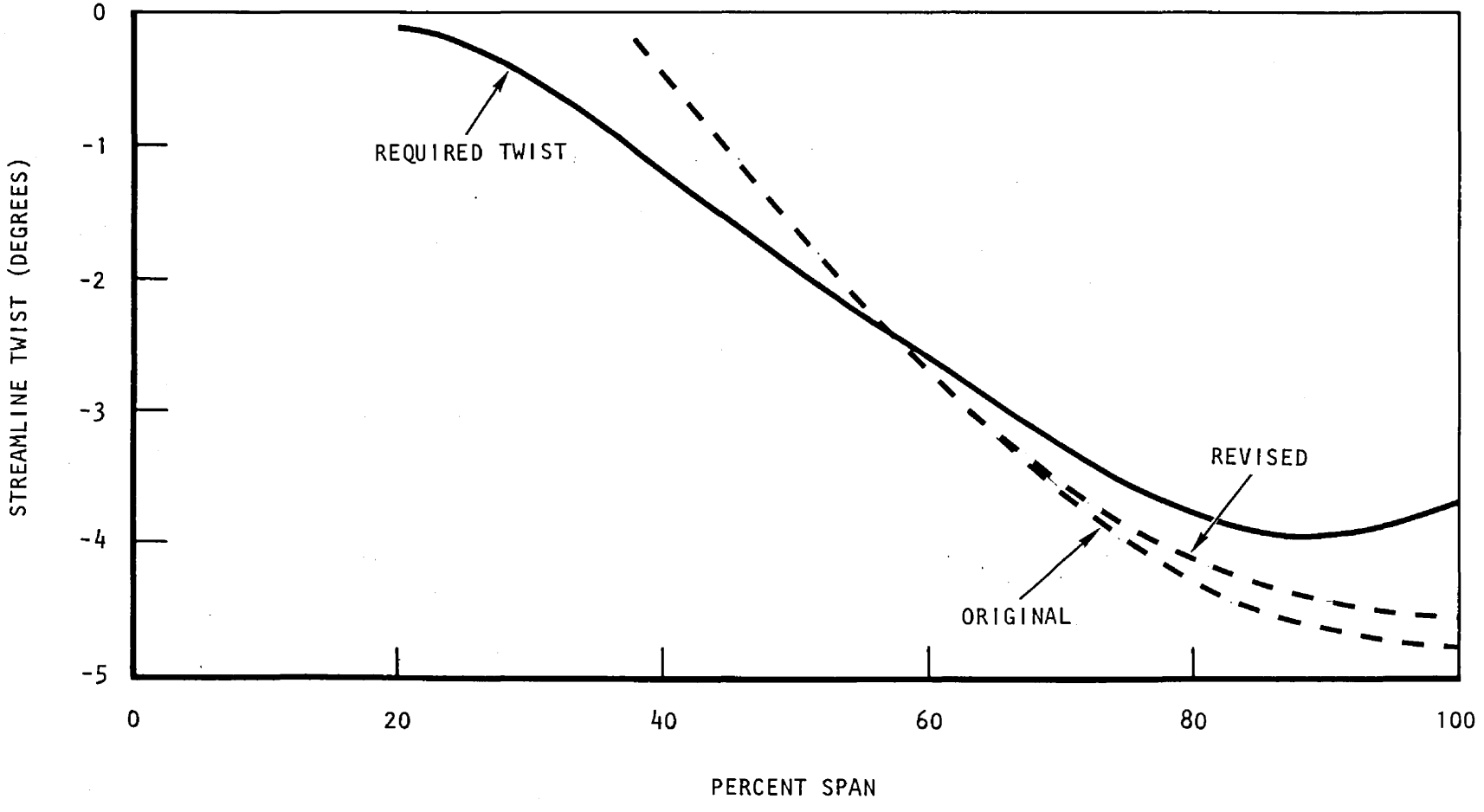

Figure 35. HiMAT Canard AC89 Results - Cover Laminate (15°/45°/-45°)

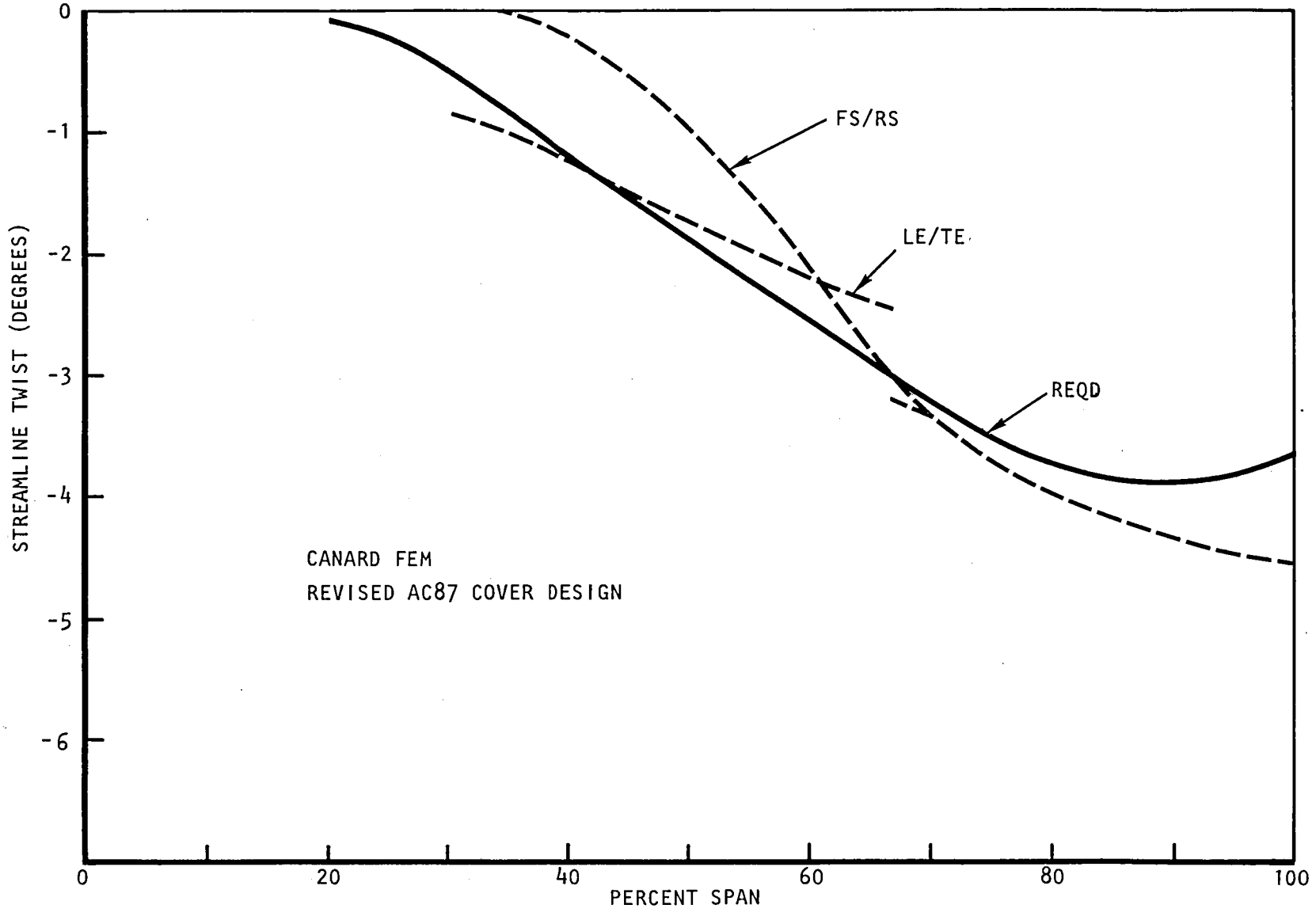

Figure 36. HiMAT Canard NASTRAN Results (15°/45°/-45°) - Selected Ply Layup

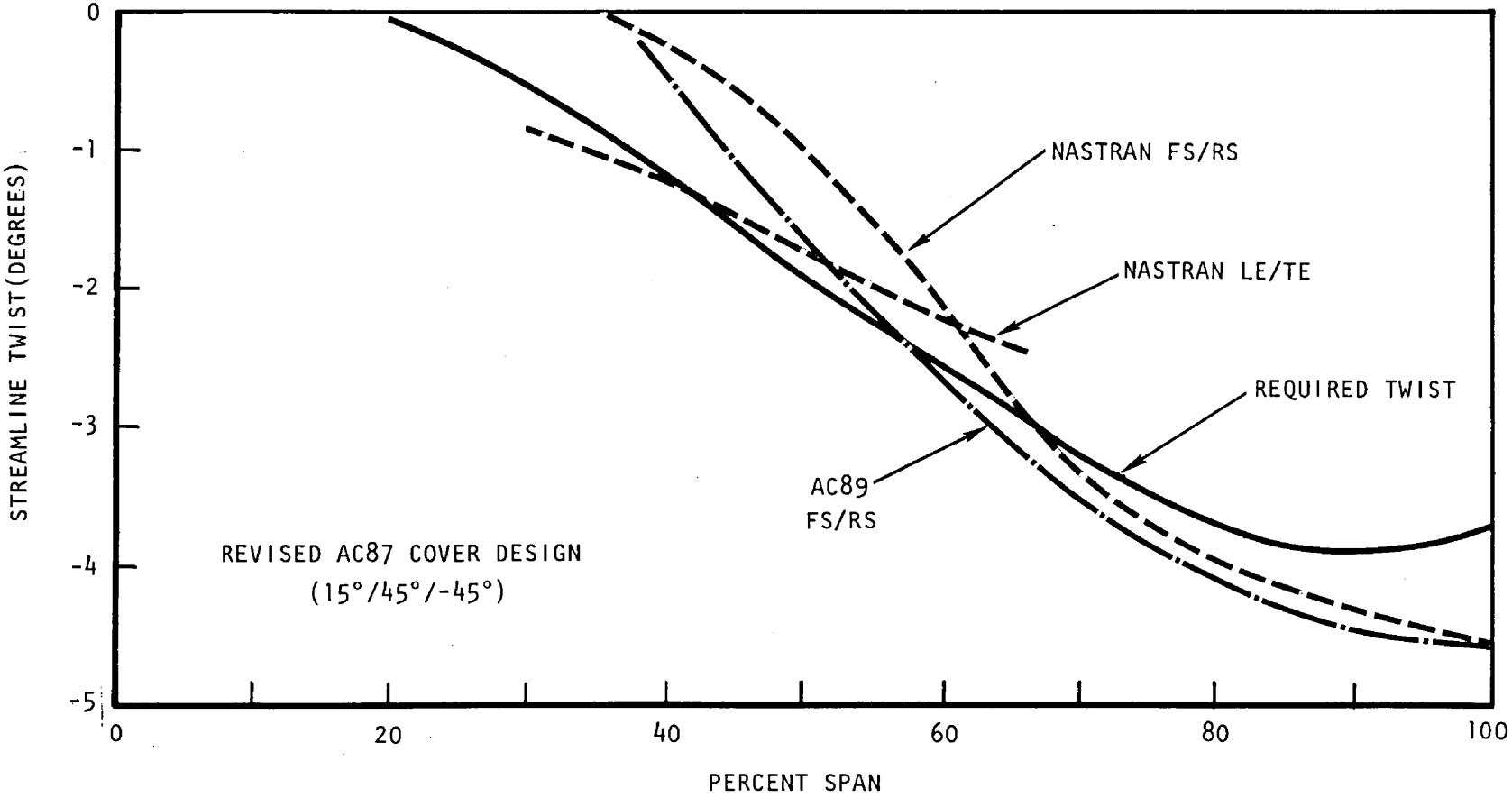

Figure 37. HiMAT Canard-AC89 Versus NASTRAN Twist

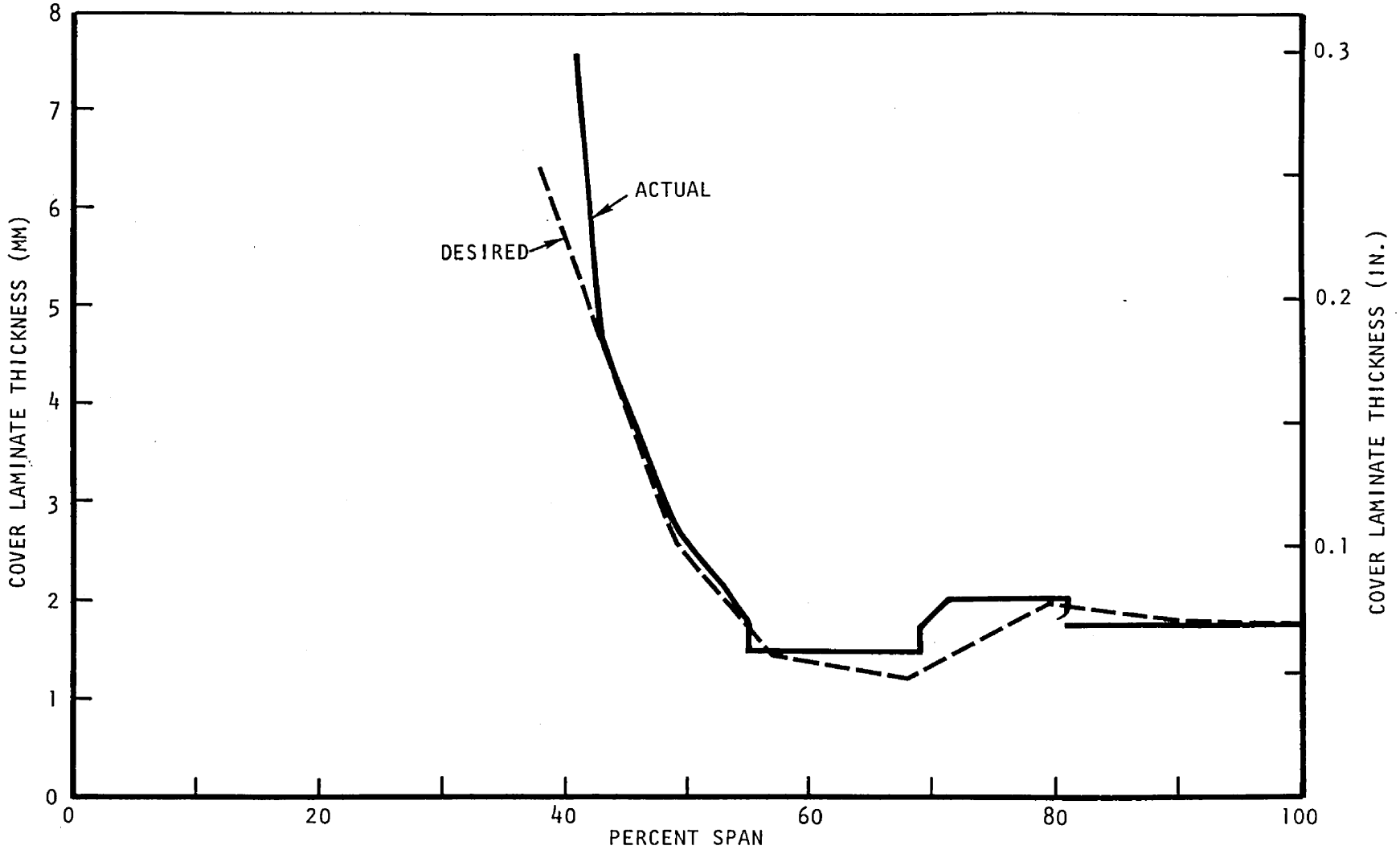

Figure 38. HiMAT Canard Cover Laminate Thickness

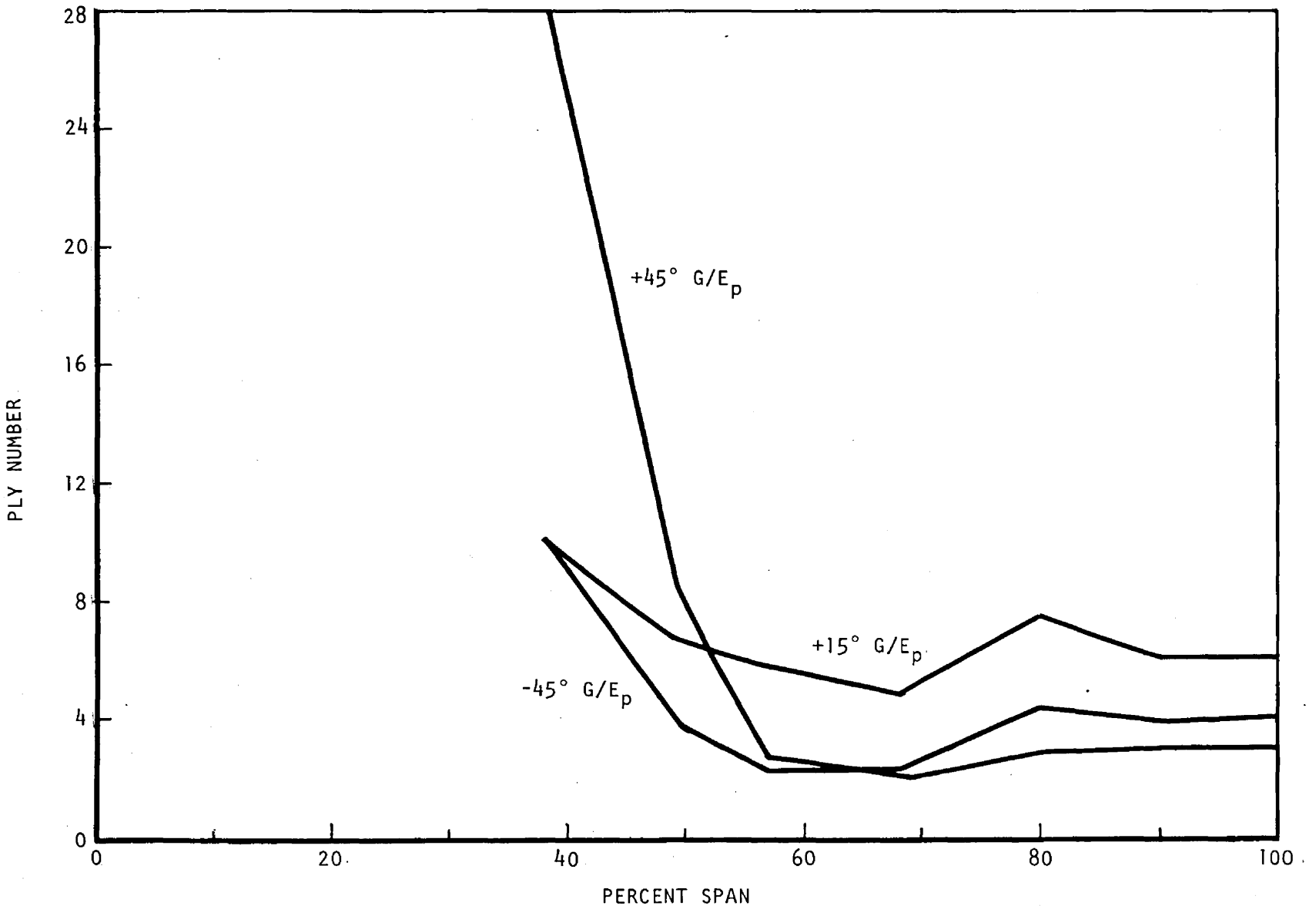

Figure 39. HiMAT Canard Cover Laminate - Desired Ply Distributions

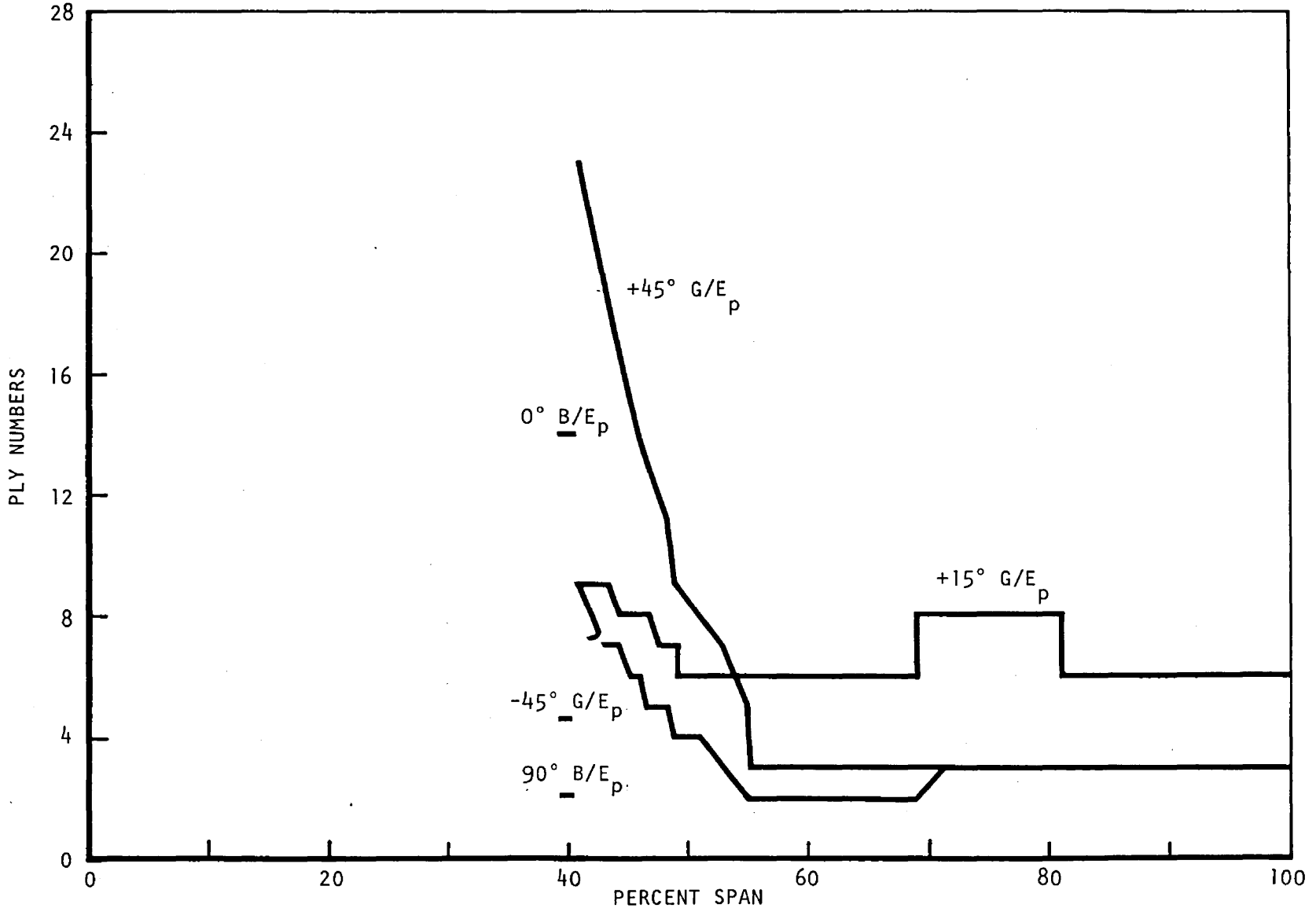

Figure 40. HiMAT Canard Cover Laminate - Actual Ply Distributions

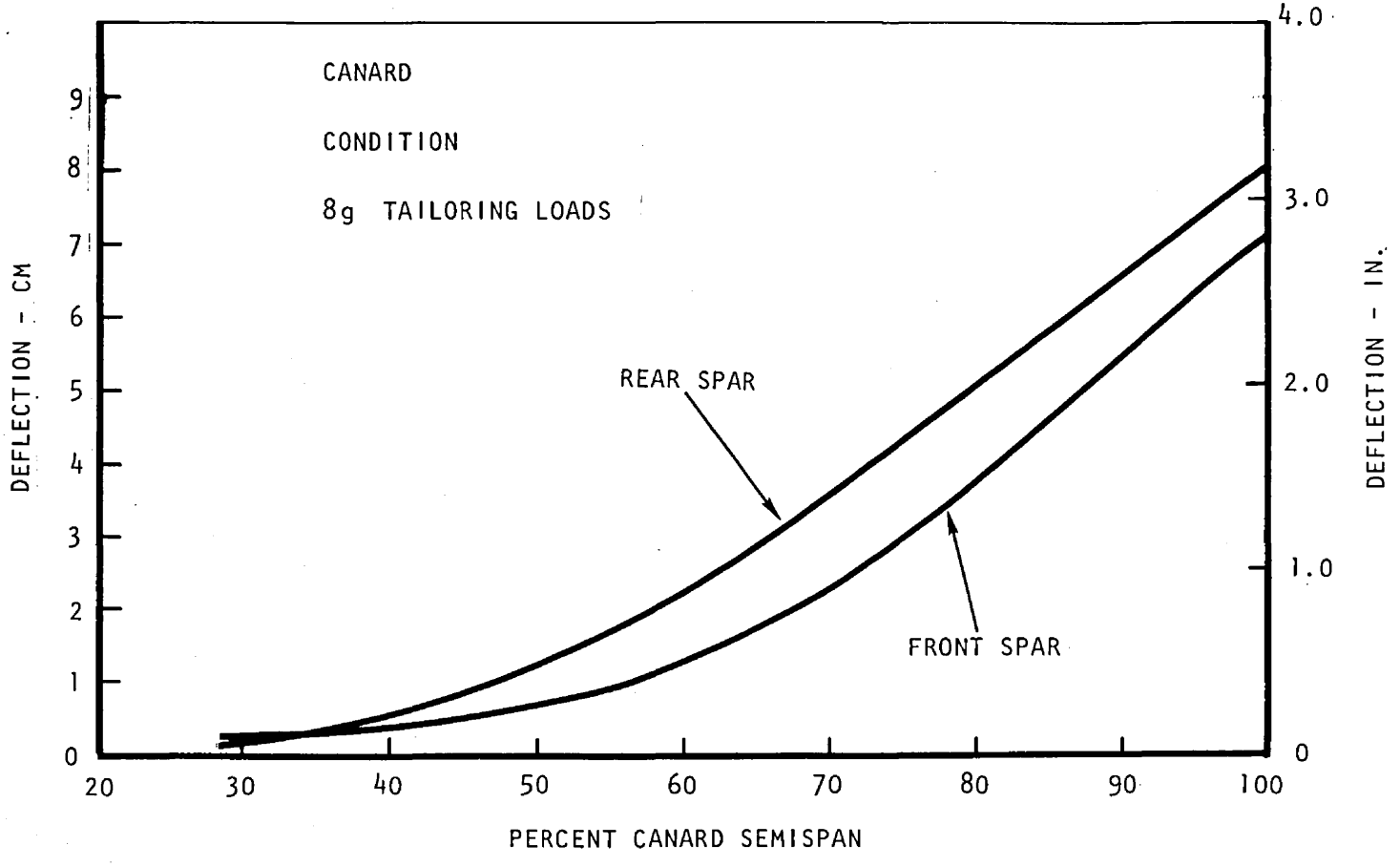

Figure 41. Deflection of Front/Rear Spars - Canard

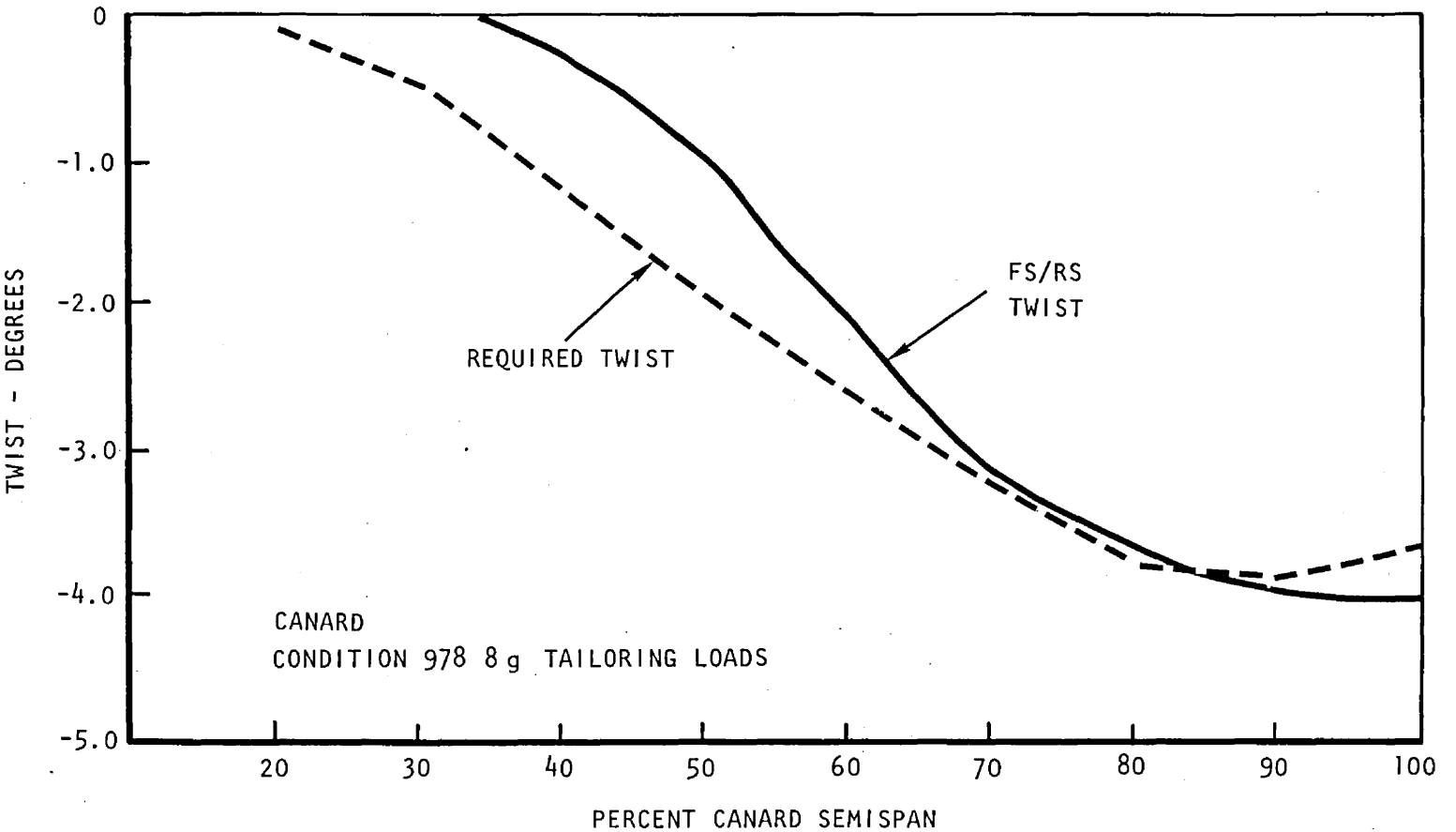

Figure 42. Canard Final Predicted Flight Twist - Canard FS/RS

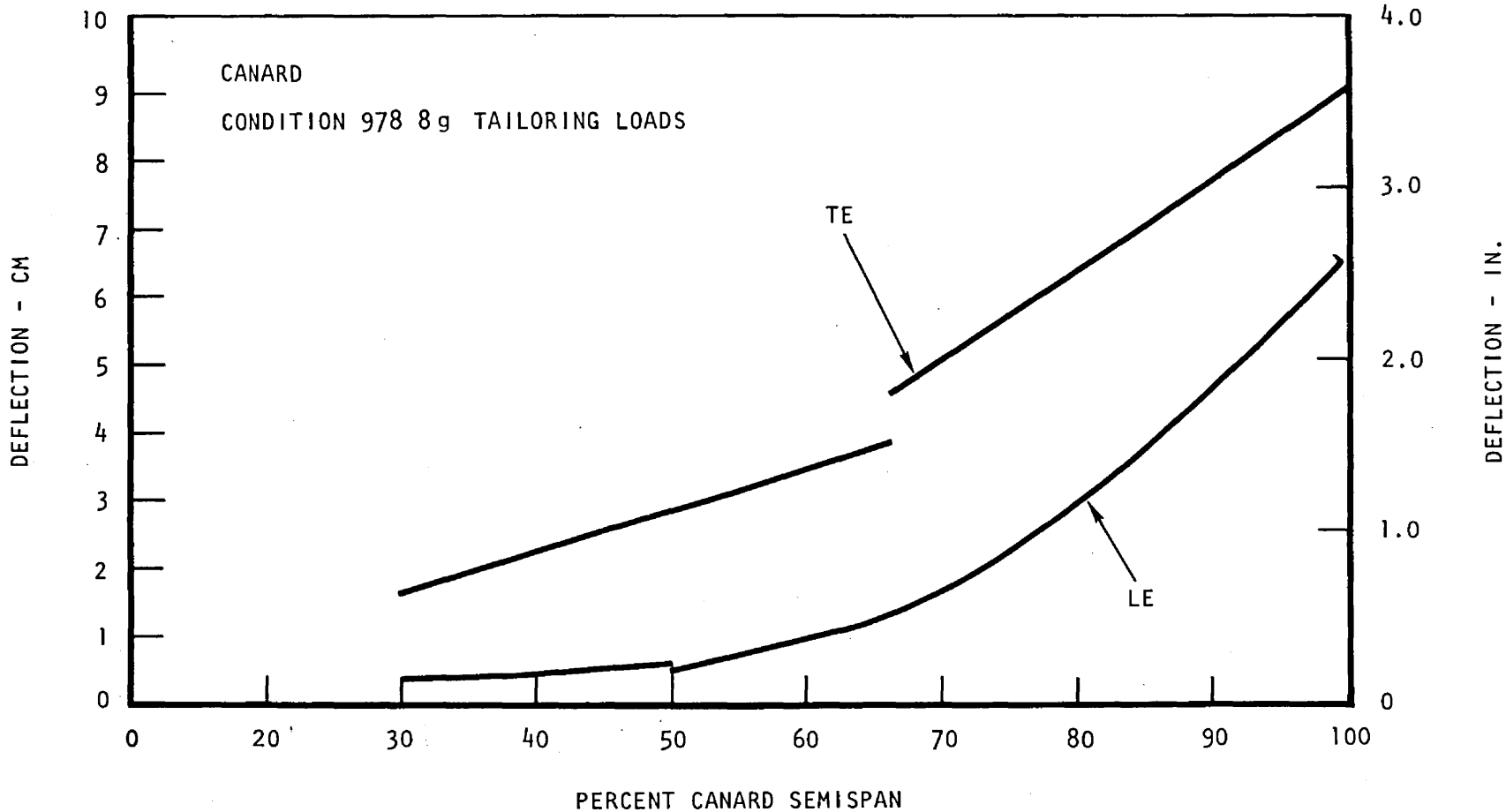

Figure 43. Canard LE/TE Deflection

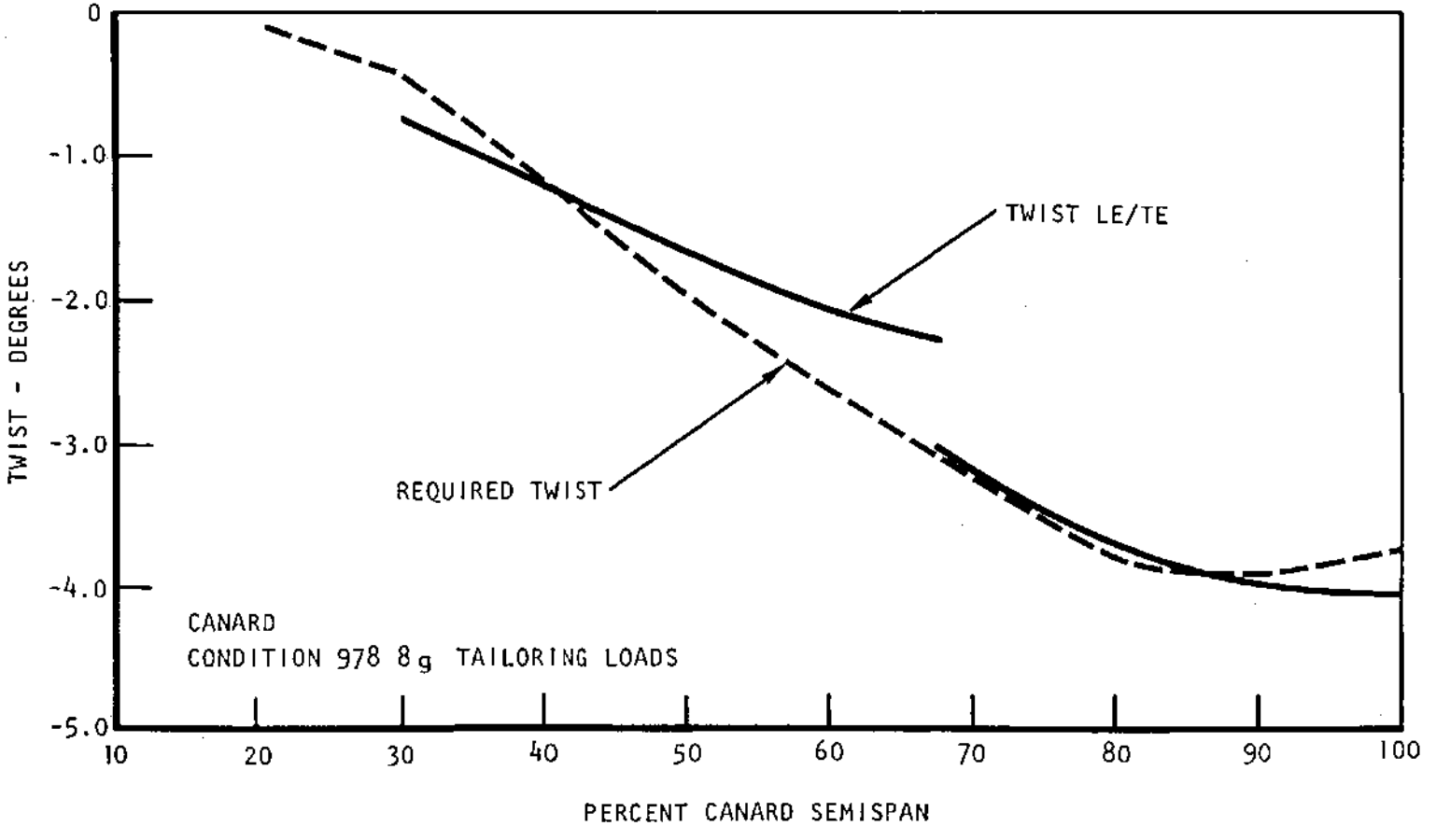

Figure 44. Canard Final Predicted Flight Twist - LE/TE

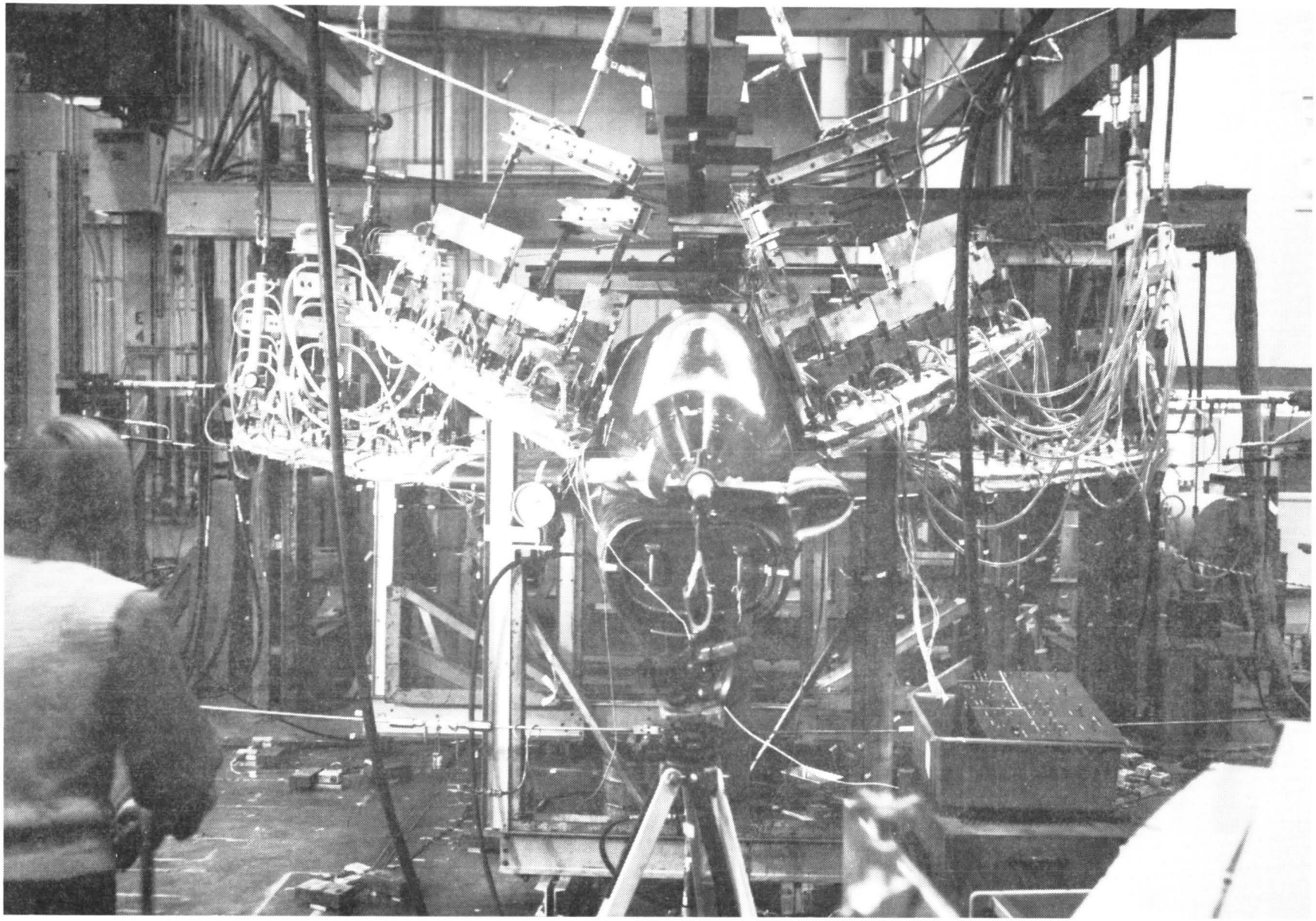

Figure 45. Front View of HiMAT A/V-2 in Test Setup

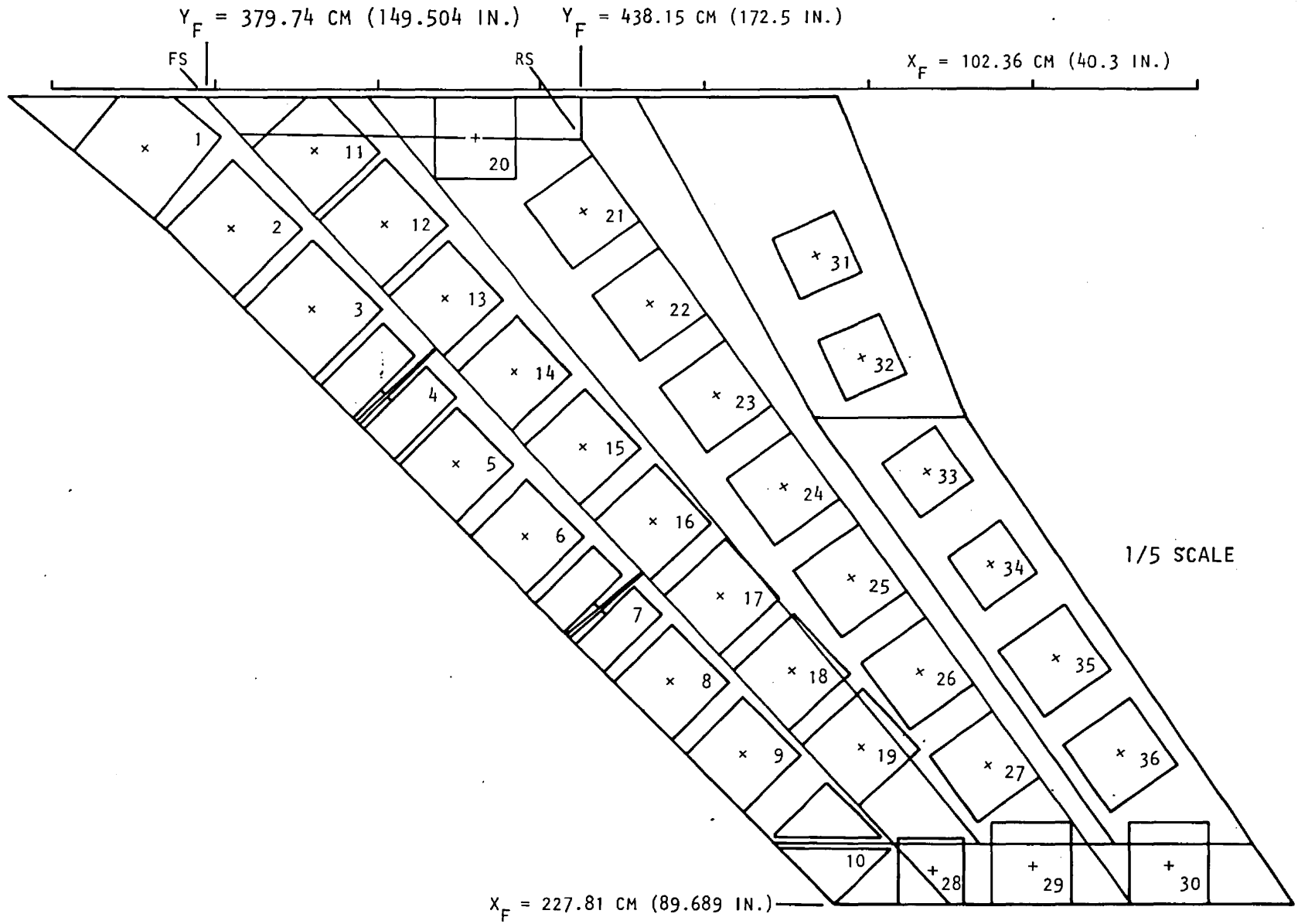

Figure 46. Outboard Wing Pad Locations

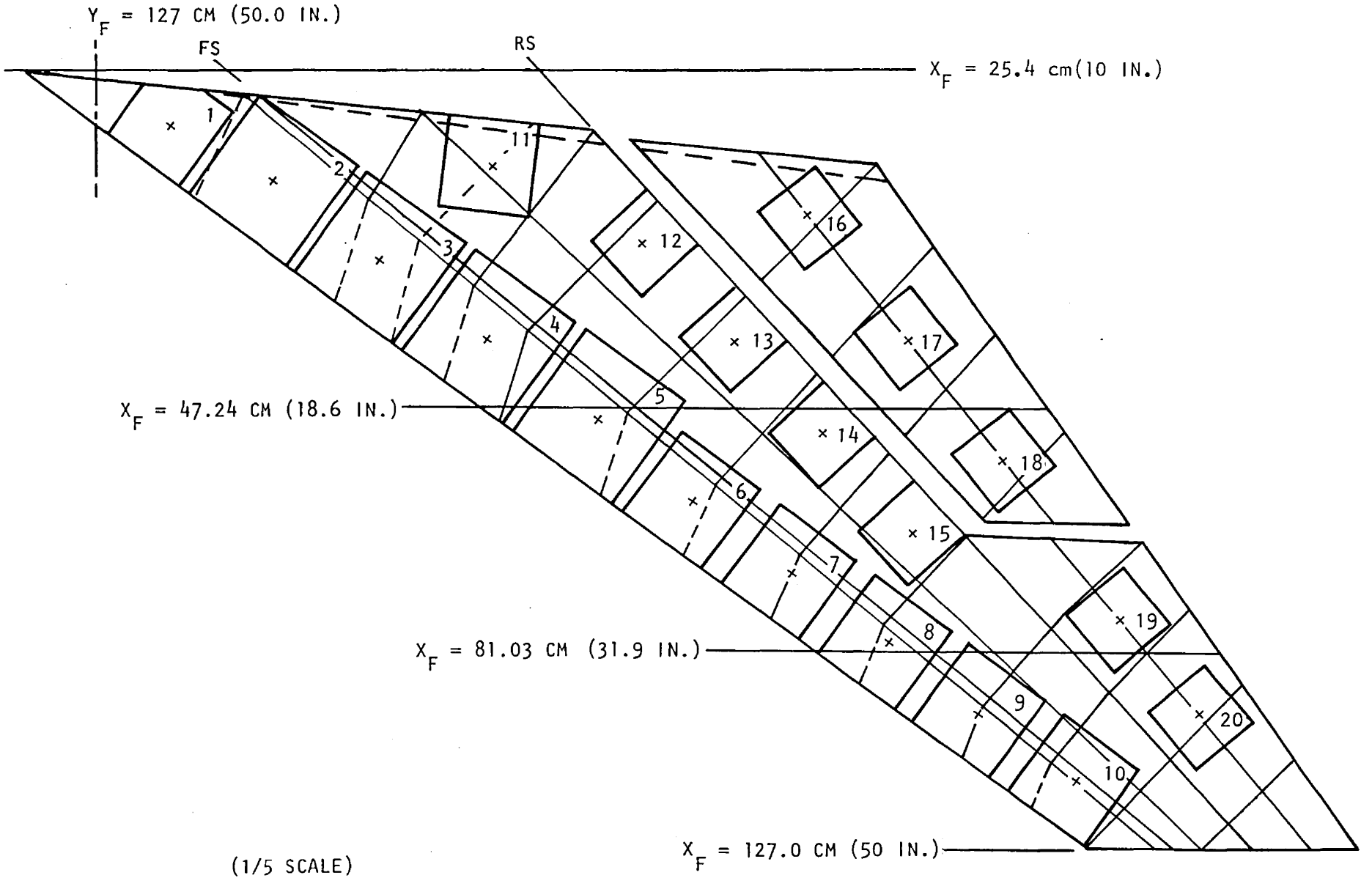

Figure 47. Canard Pad Locations

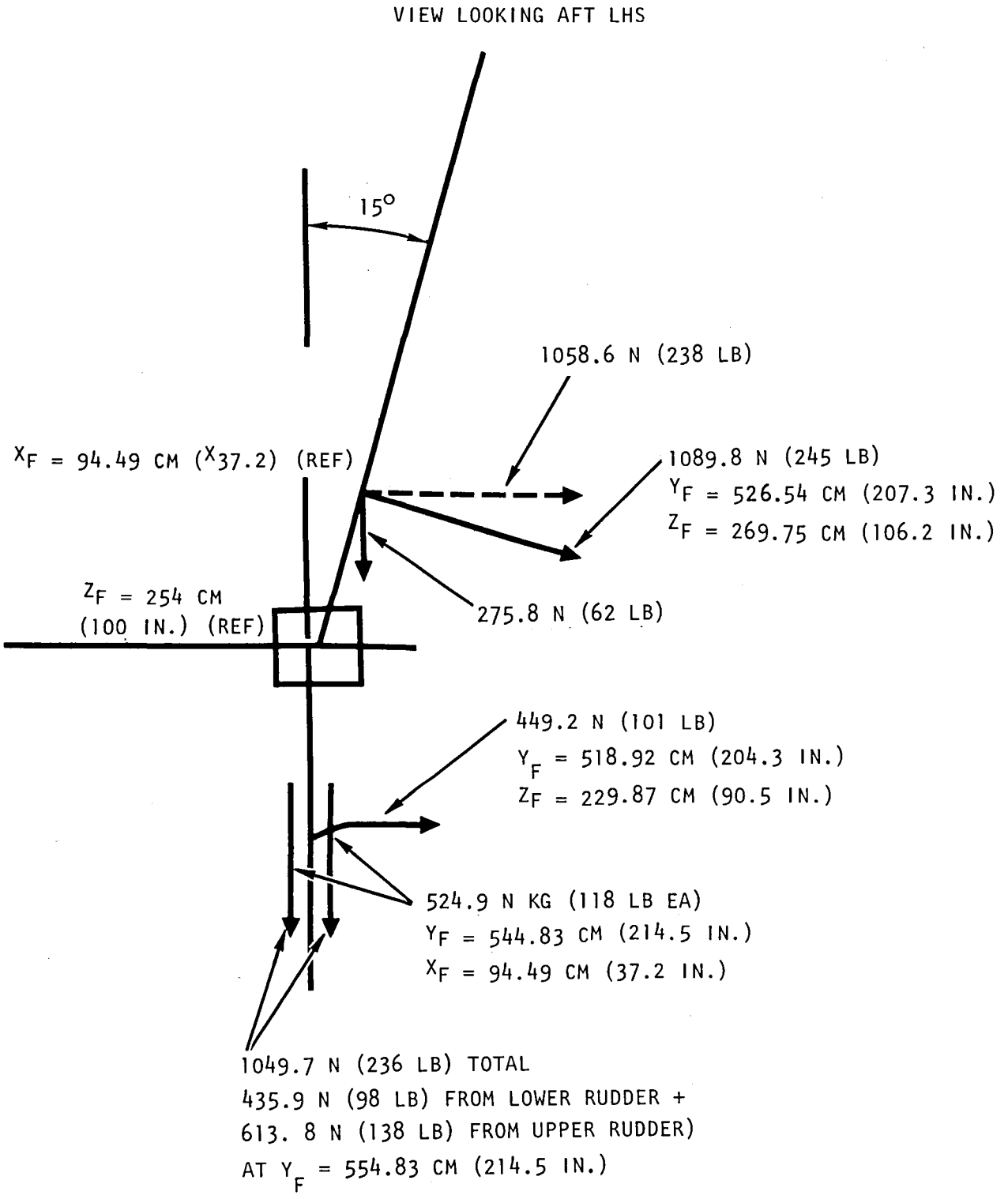

Figure 48. Rudder Pad Loads

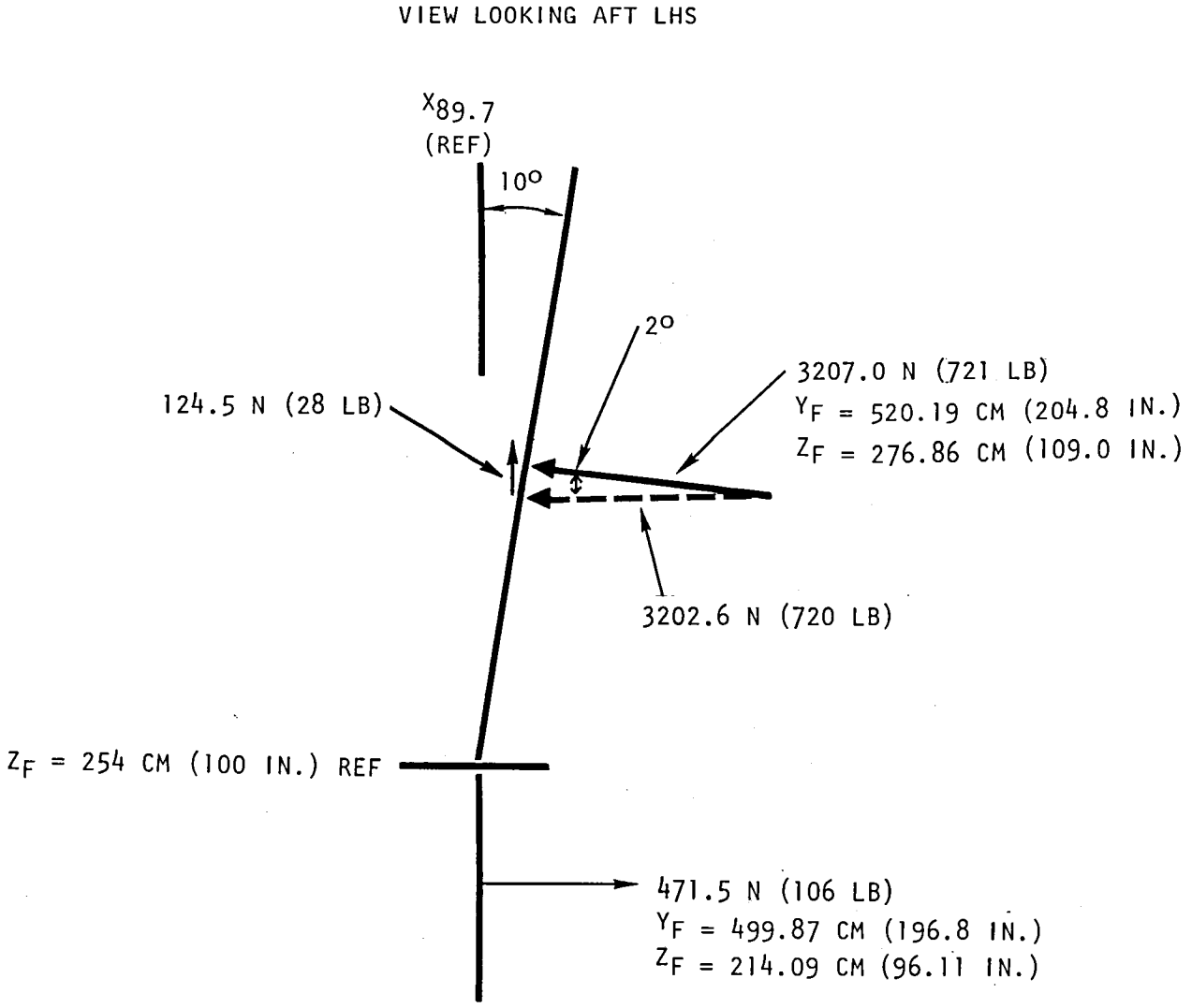

Figure 49. Wing Tip Fin Pad Loads

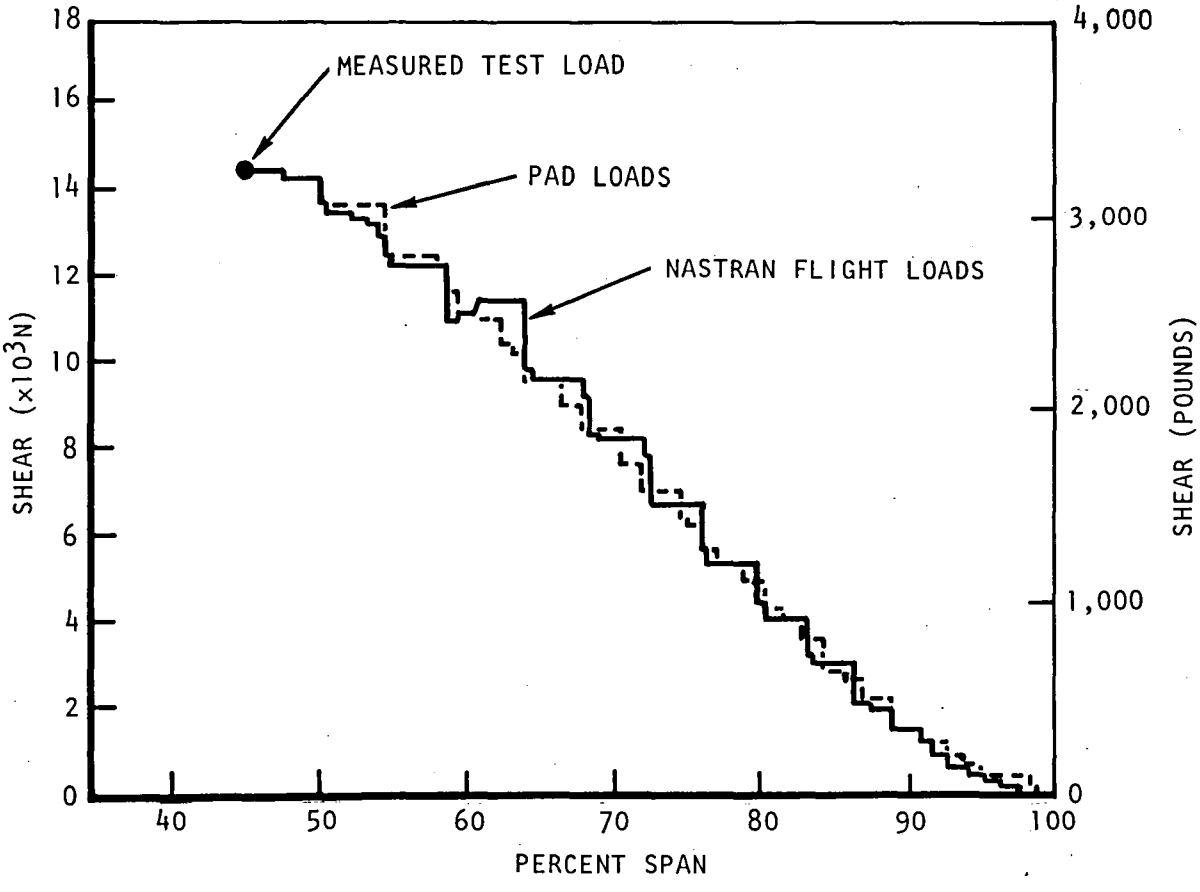

	V N (LB)	M CM-N (IN.-LB)	T CM-N (IN.-LB)	C_P X_F CM (IN.)	C_P Y_F CM (IN.)
NAS	14.3 (3.22)	957.7 (84.8)	518.7 (45.9)	169.14 (66.59)	441.36 (173.74)
PAD	14.5 (3.26)	962.3 (85.2)	539.2 (47.7)	168.7 (66.41)	442.29 (174.13)

(MULTIPLY ABOVE BY 10^3)

Figure 50. Correlation of Shear Test Loads - Outboard Wing

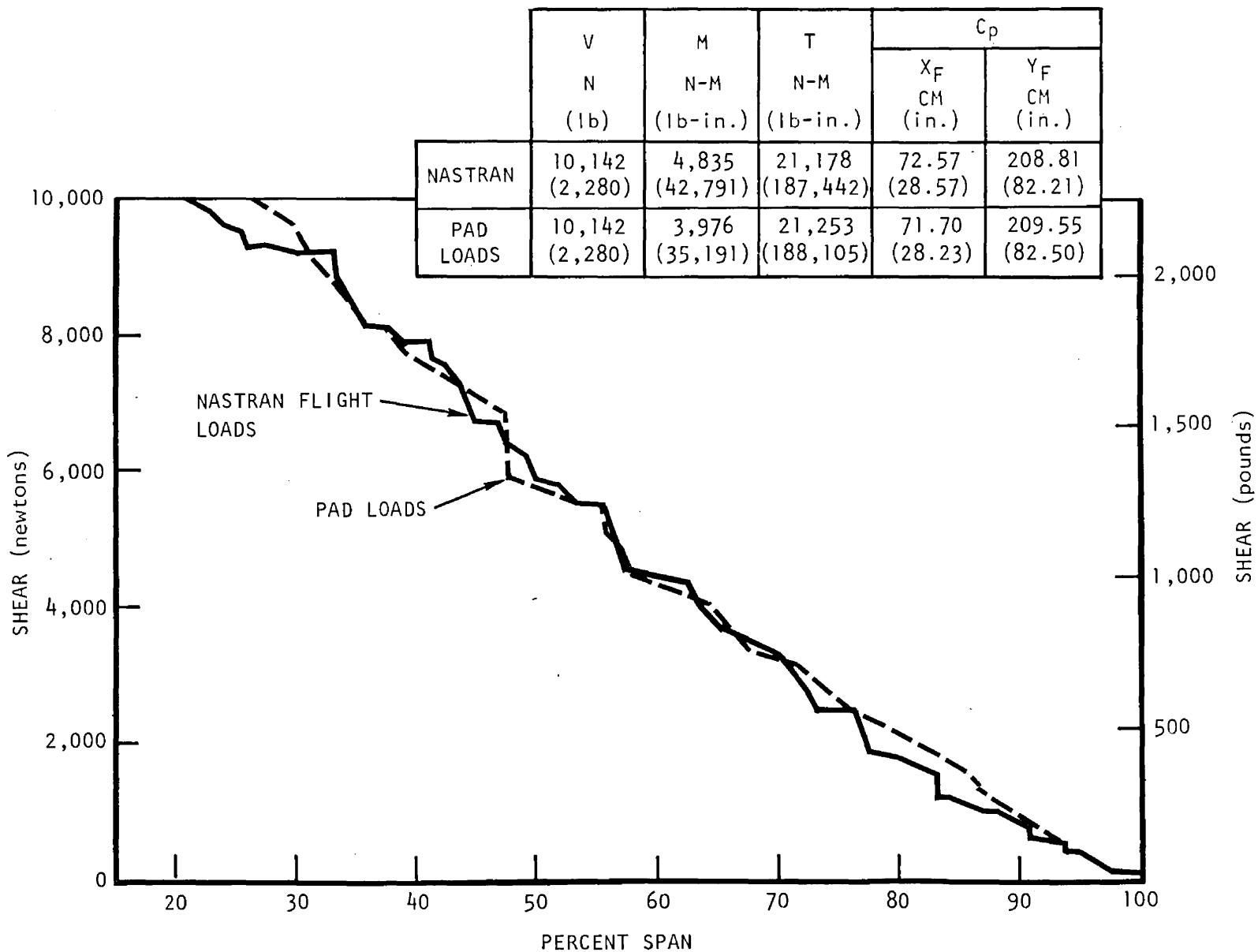

Figure 51. Correlation of Shear Test Loads - Canard

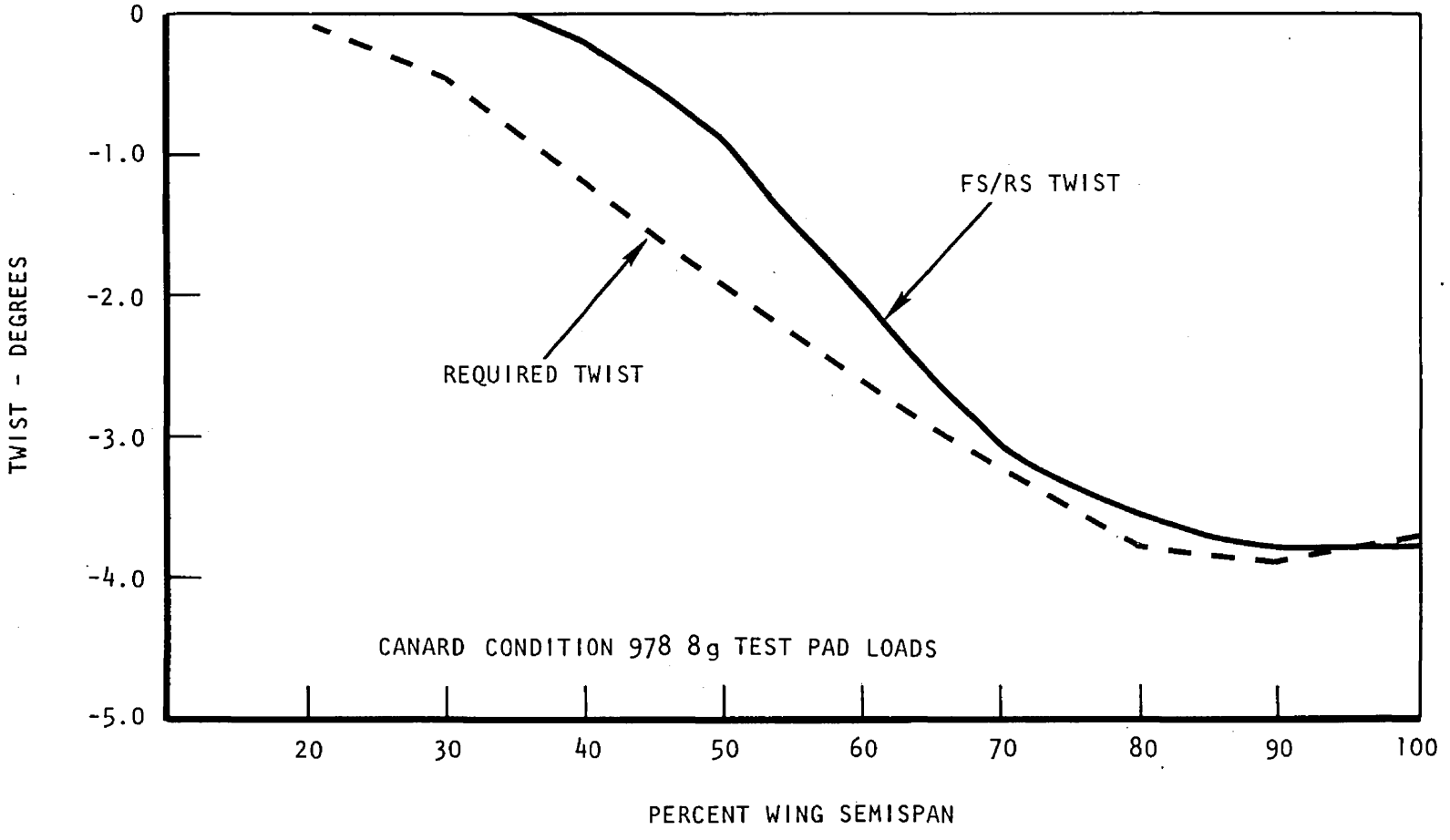

Figure 52. Canard Predicted Test Twist - FS/RS

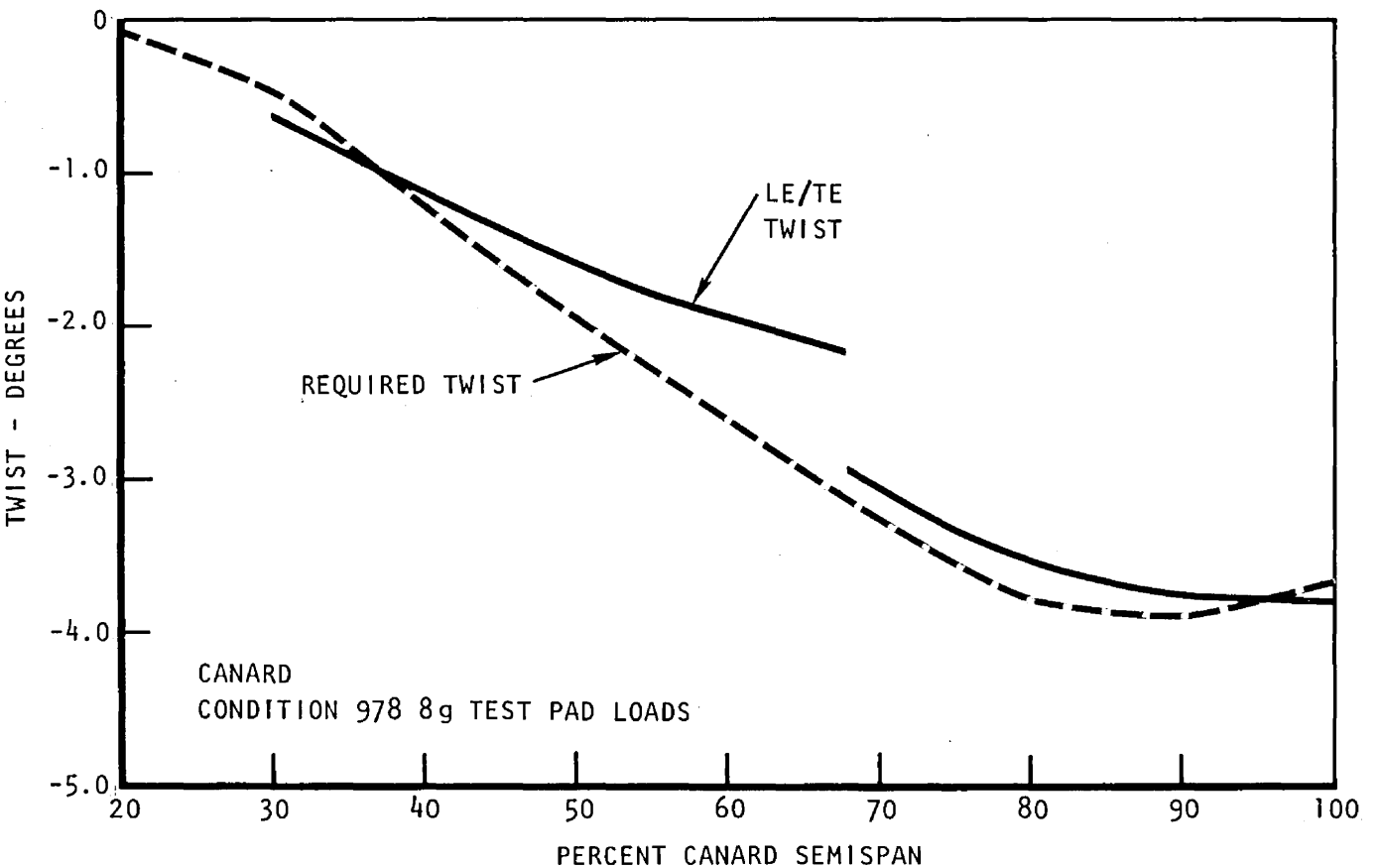

Figure 53. Canard Predicted Test Twist - LE/TE

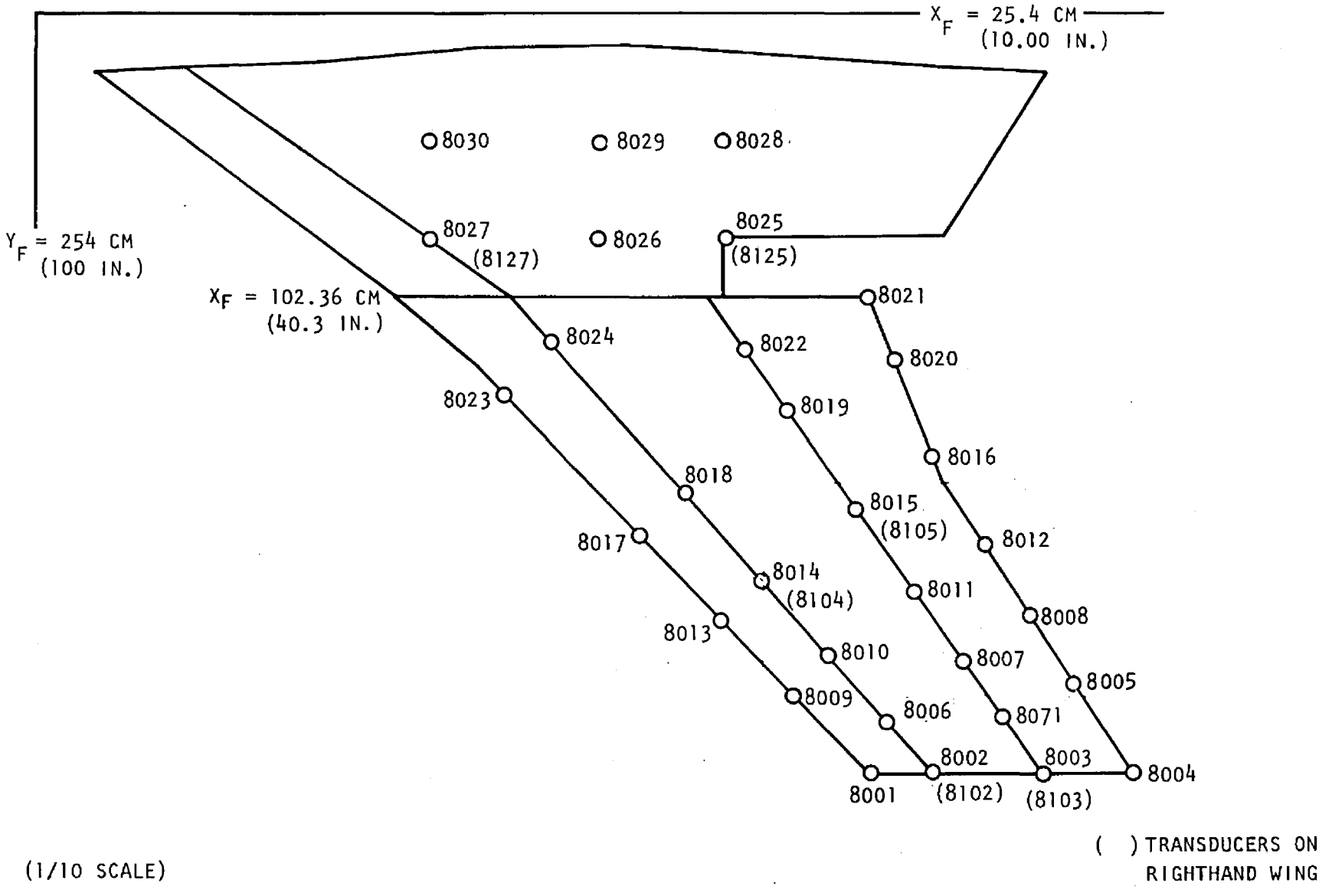

Figure 54. Wing Deflection Transducer Points

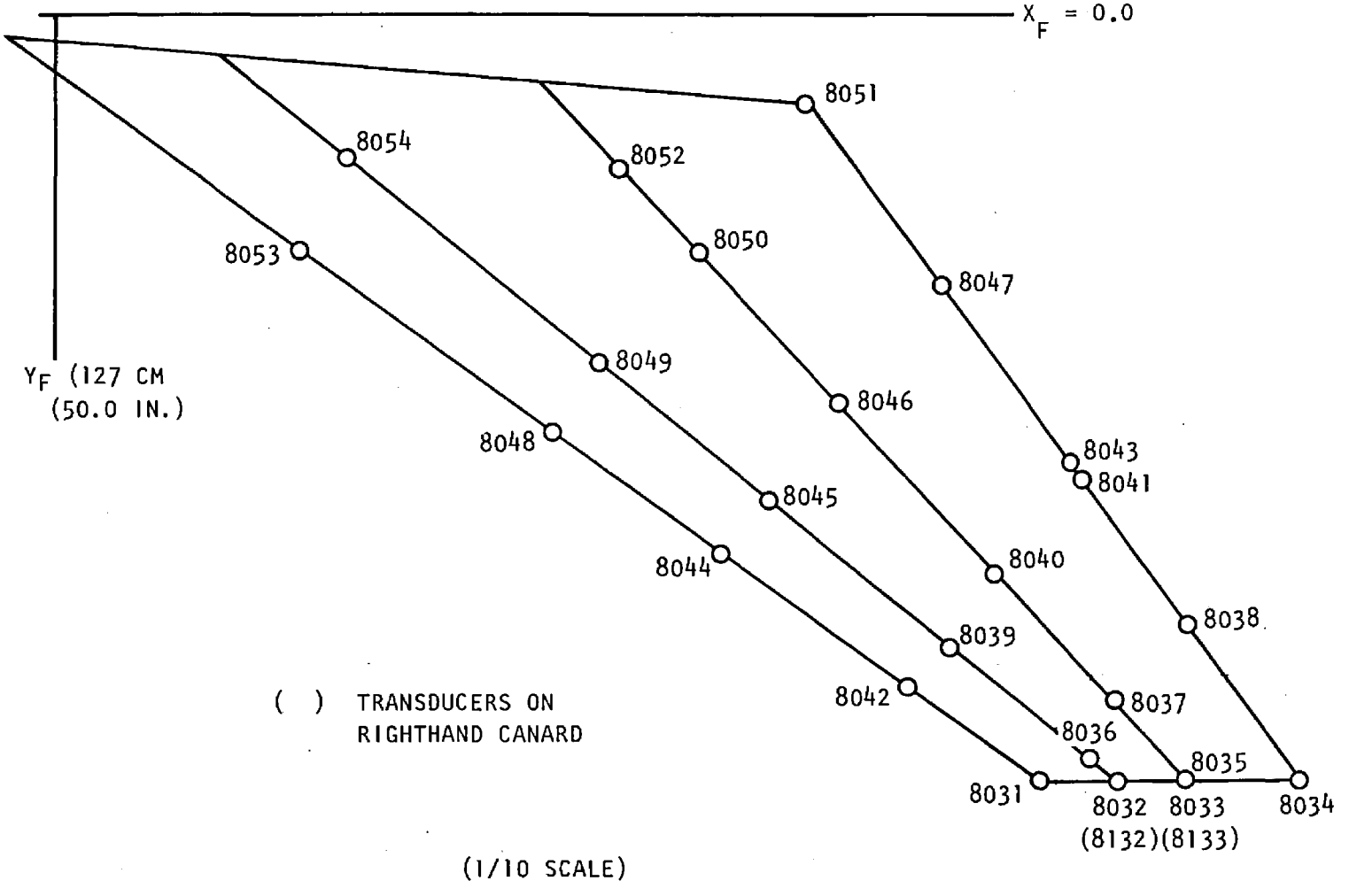

Figure 55. Canard Deflection Transducer Points

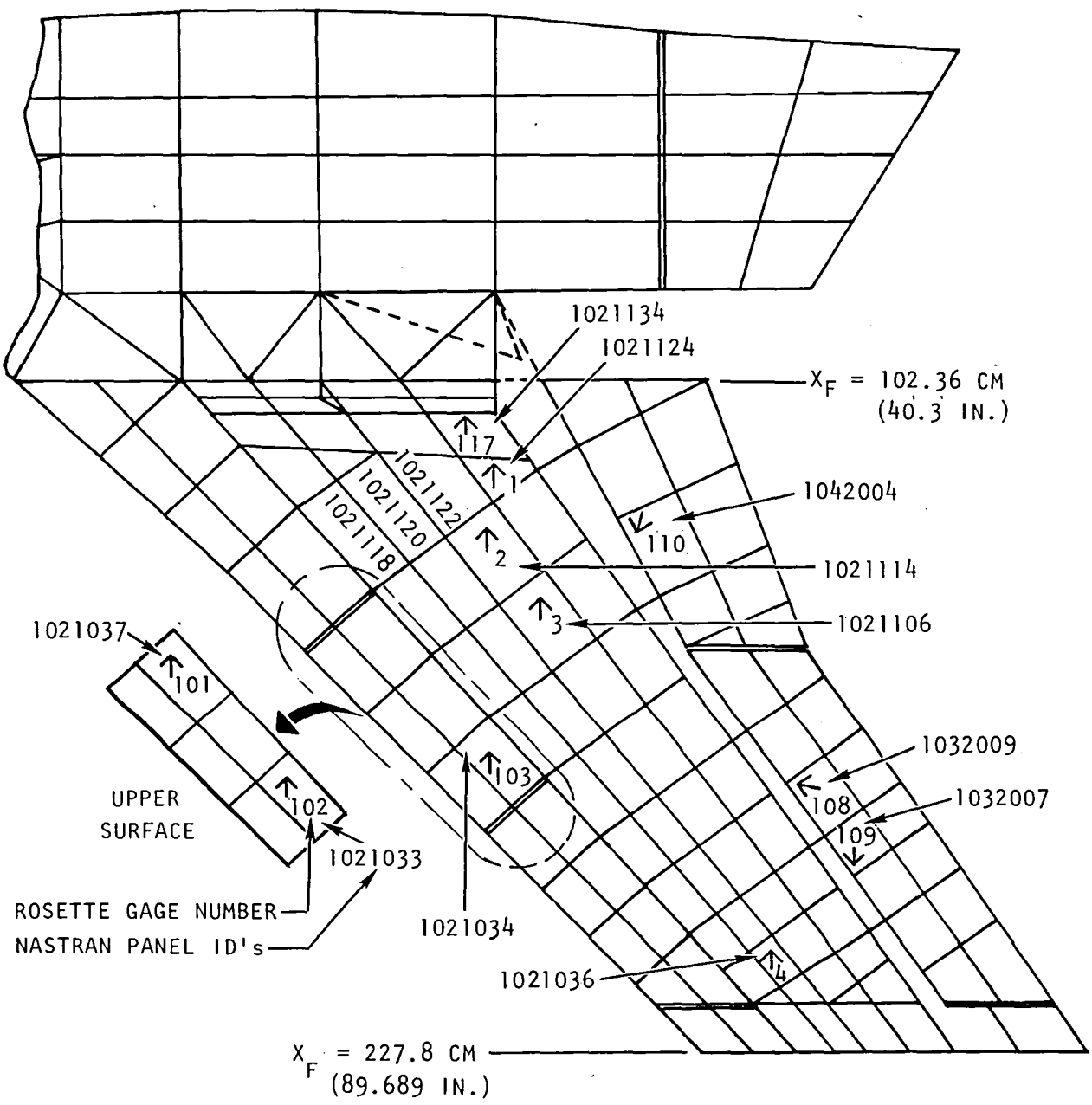

Figure 56. Ground Test Strain Gages - Lower and Upper Surfaces - Outboard Wing

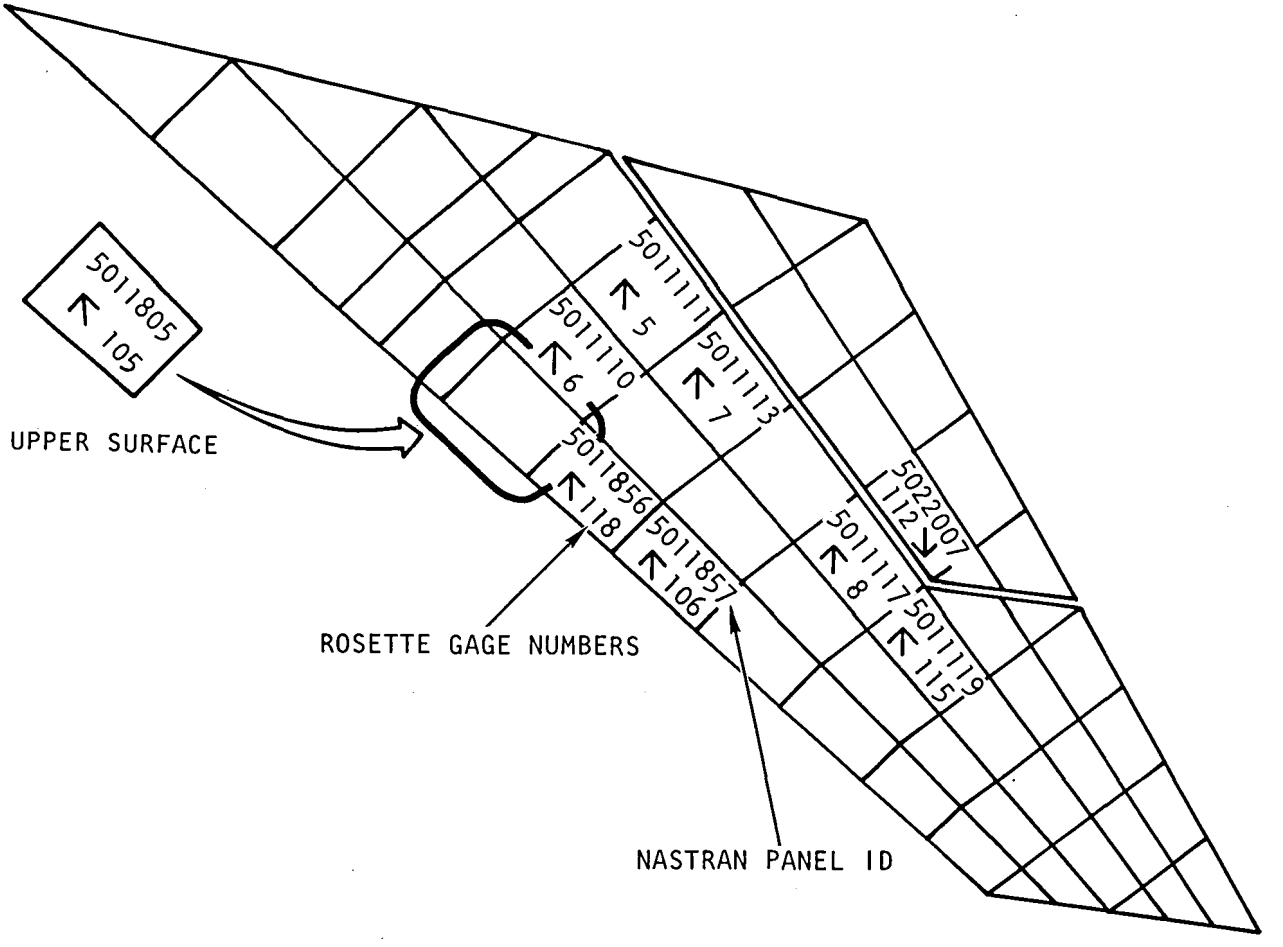

Figure 57. Ground Test Strain Gages - Canard Lower and Upper Surfaces

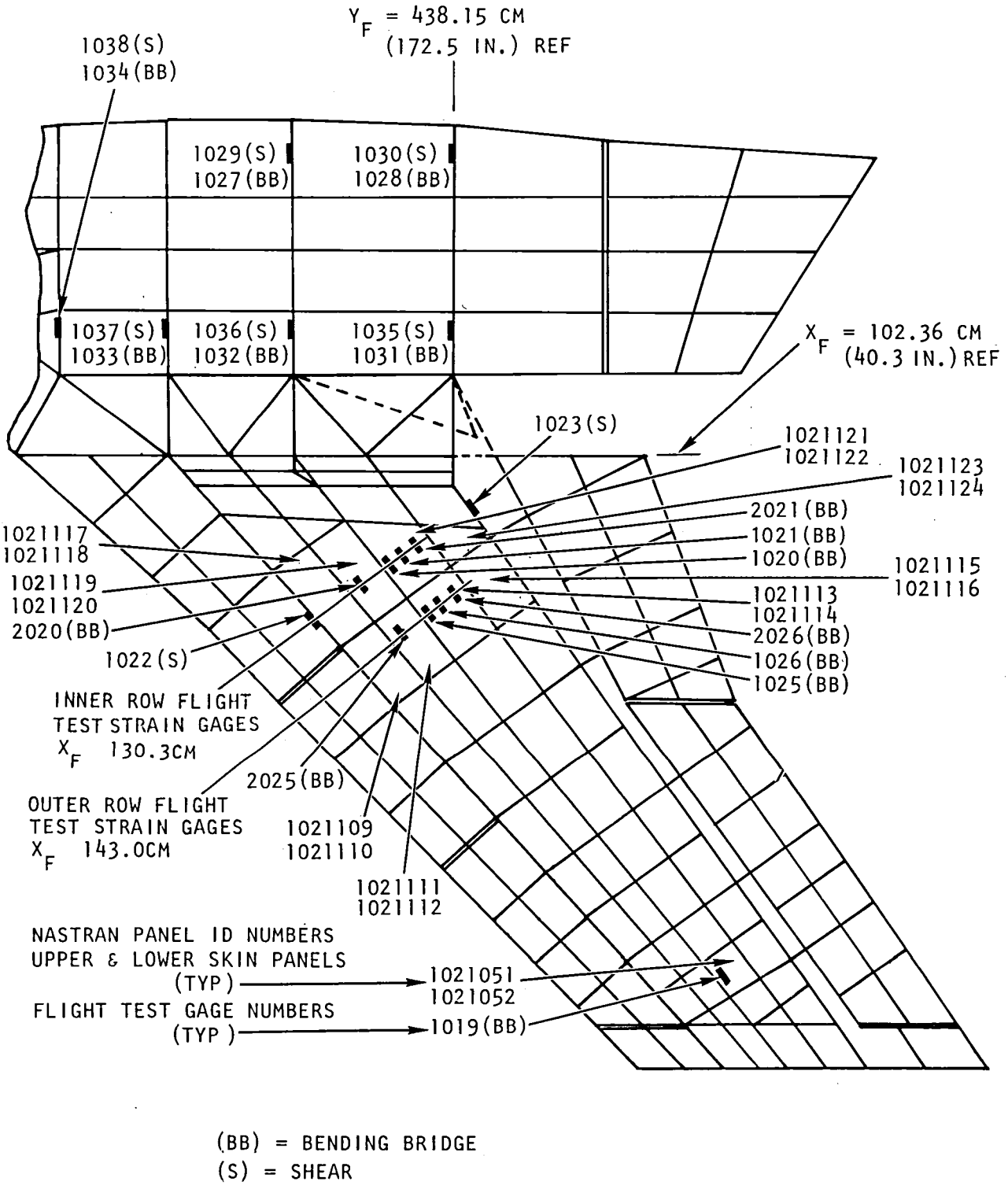

Figure 58. Flight Test Strain Gages - Inboard/Outboard Wing

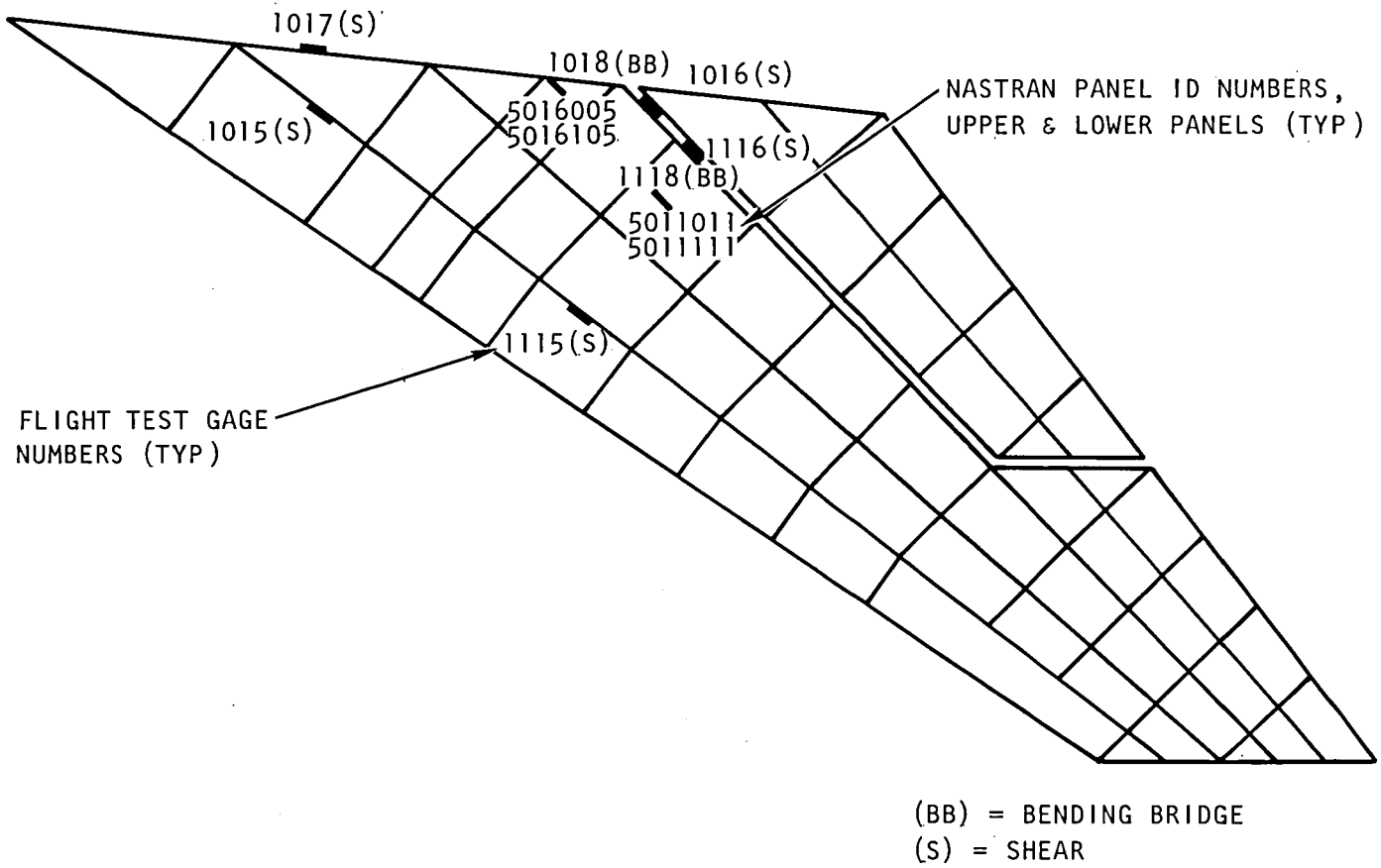

Figure 59. Flight Test Strain Gages - Canard

TYPE A1-1 AXIAL

TYPE S1-2 SHEAR (SINGLE SURFACE)

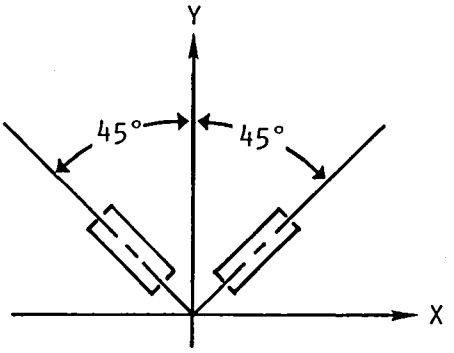

TYPE R3-1 ROSETTE

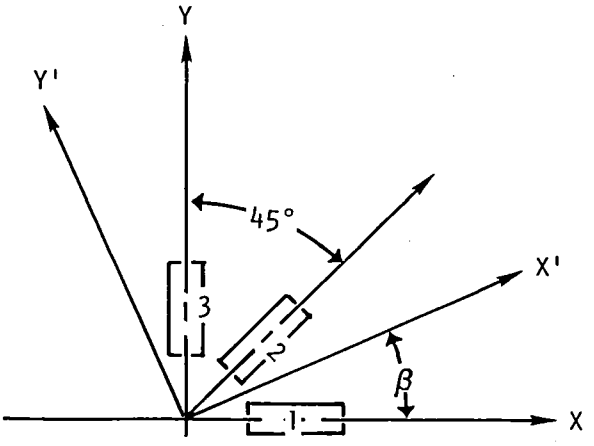

NOTE: X,Y REFERS TO GAGE AXIS SYSTEM
X', Y' LOCATES COORDINATE AXIS OF NASTRAN ELEMENT

β ANGLE BETWEEN GAGE AXIS AND FINITE ELEMENT AXIS

Figure 60. Strain Gage Axis System - Ground Gages

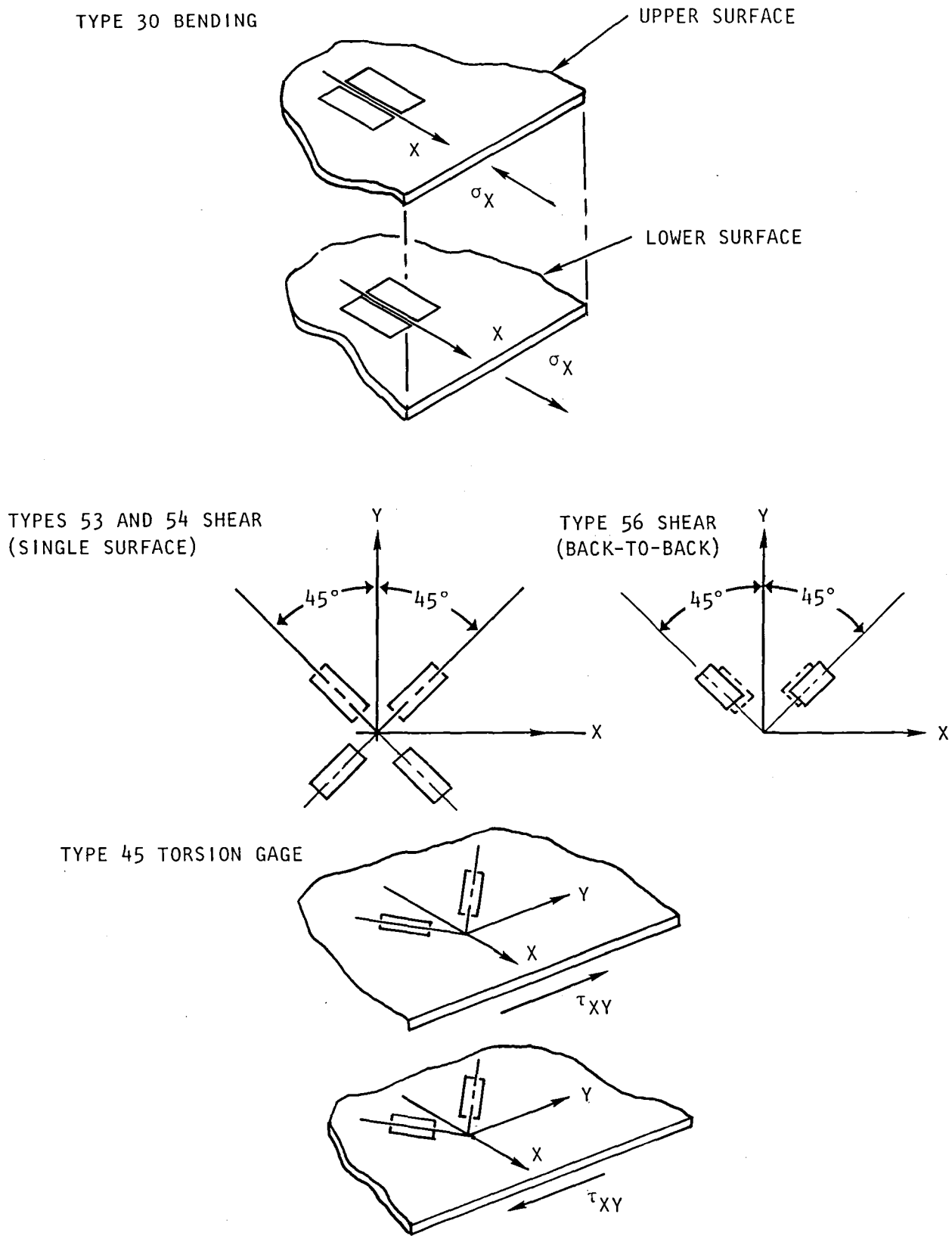

Figure 61. Strain Gage Axis System - Flight Gages

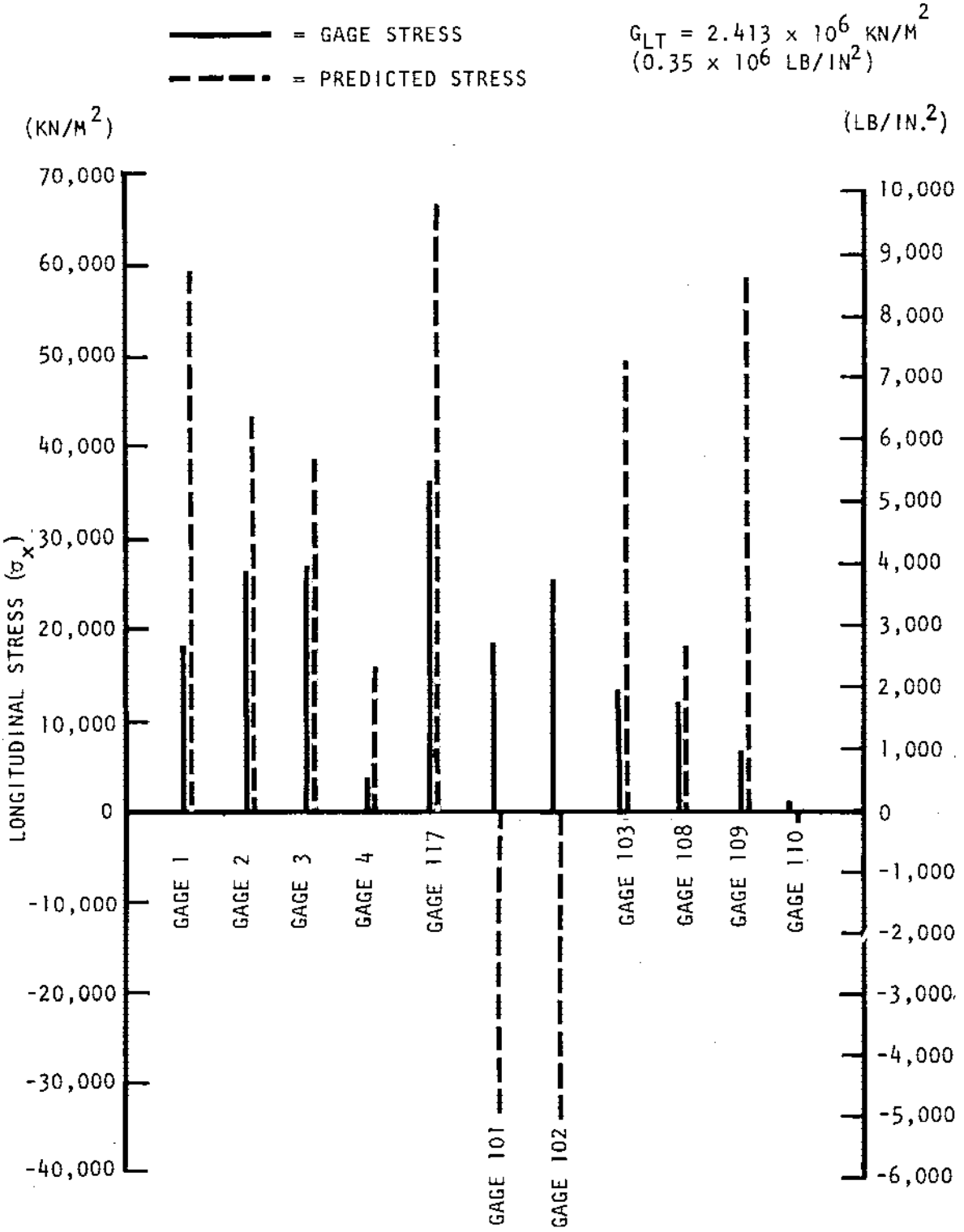

Figure 62. Outboard Wing Ground Test Gages - $\sigma_{x\ \text{gage}}$ Versus $\sigma_{x\ \text{predicted}}$

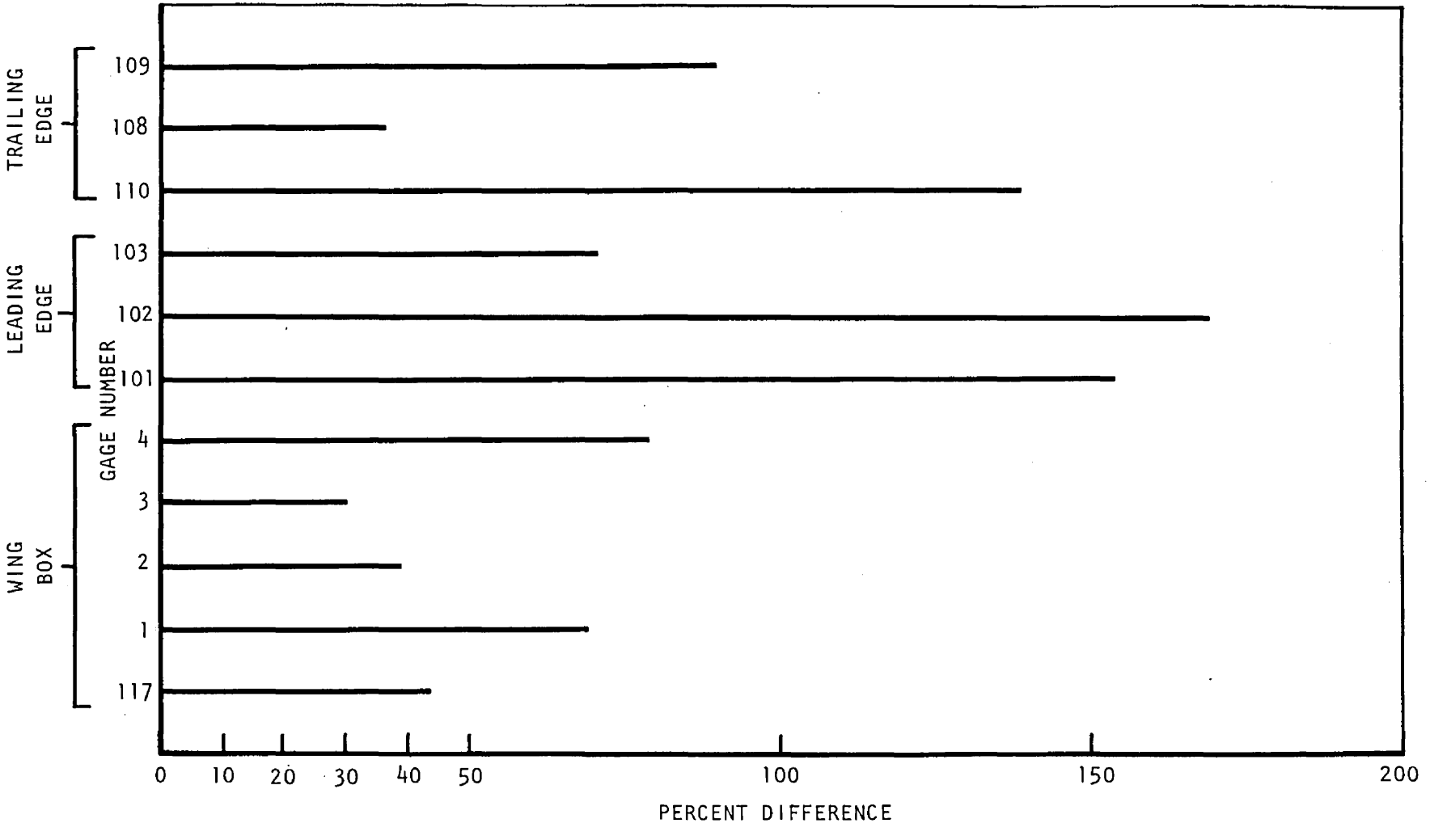

Figure 63. Outboard Wing - σ_x Percentage Correlation

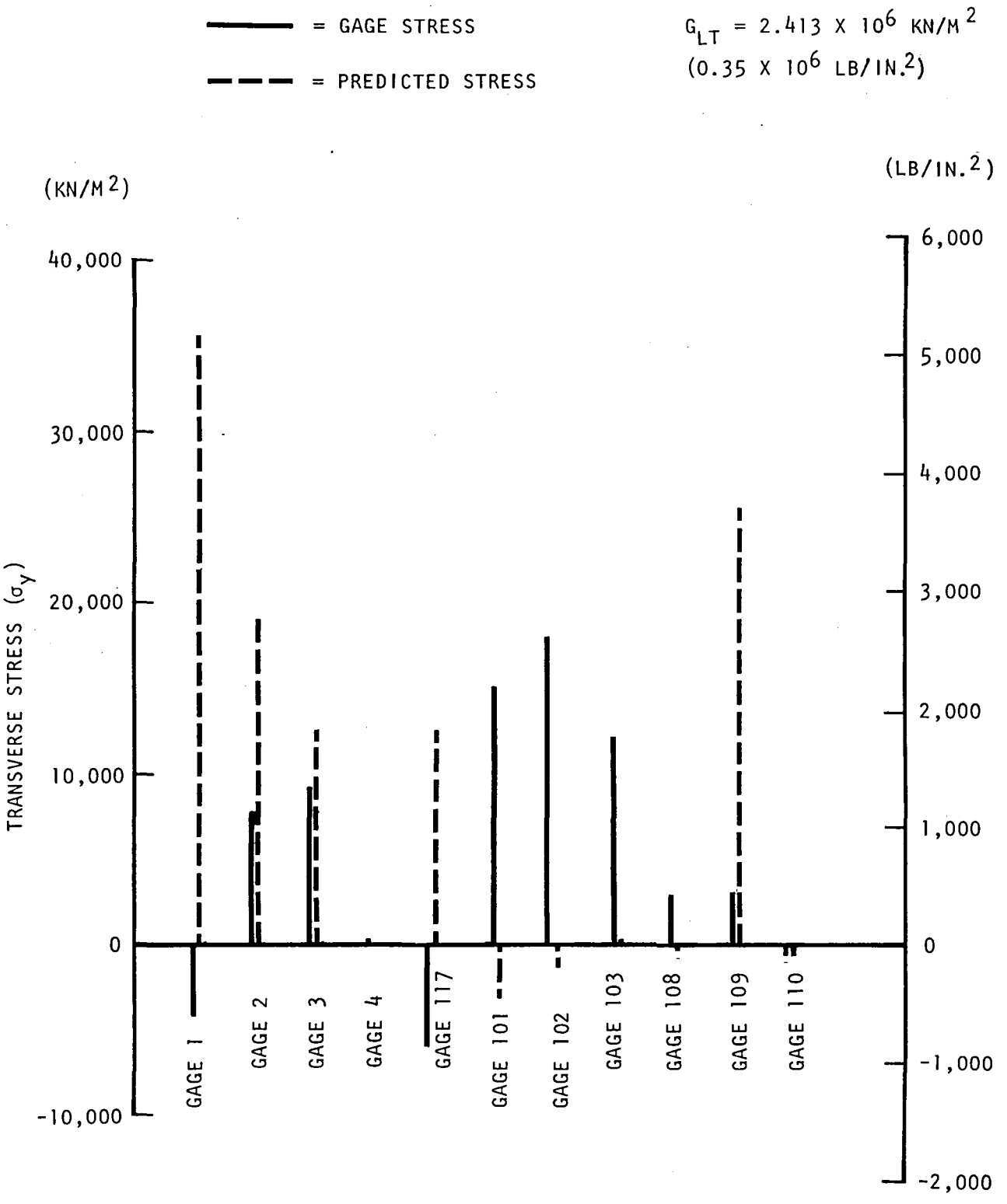

Figure 64. Outboard Wing Ground Test Gages - $\sigma_{y\ gage}$ Versus $\sigma_{y\ predicted}$

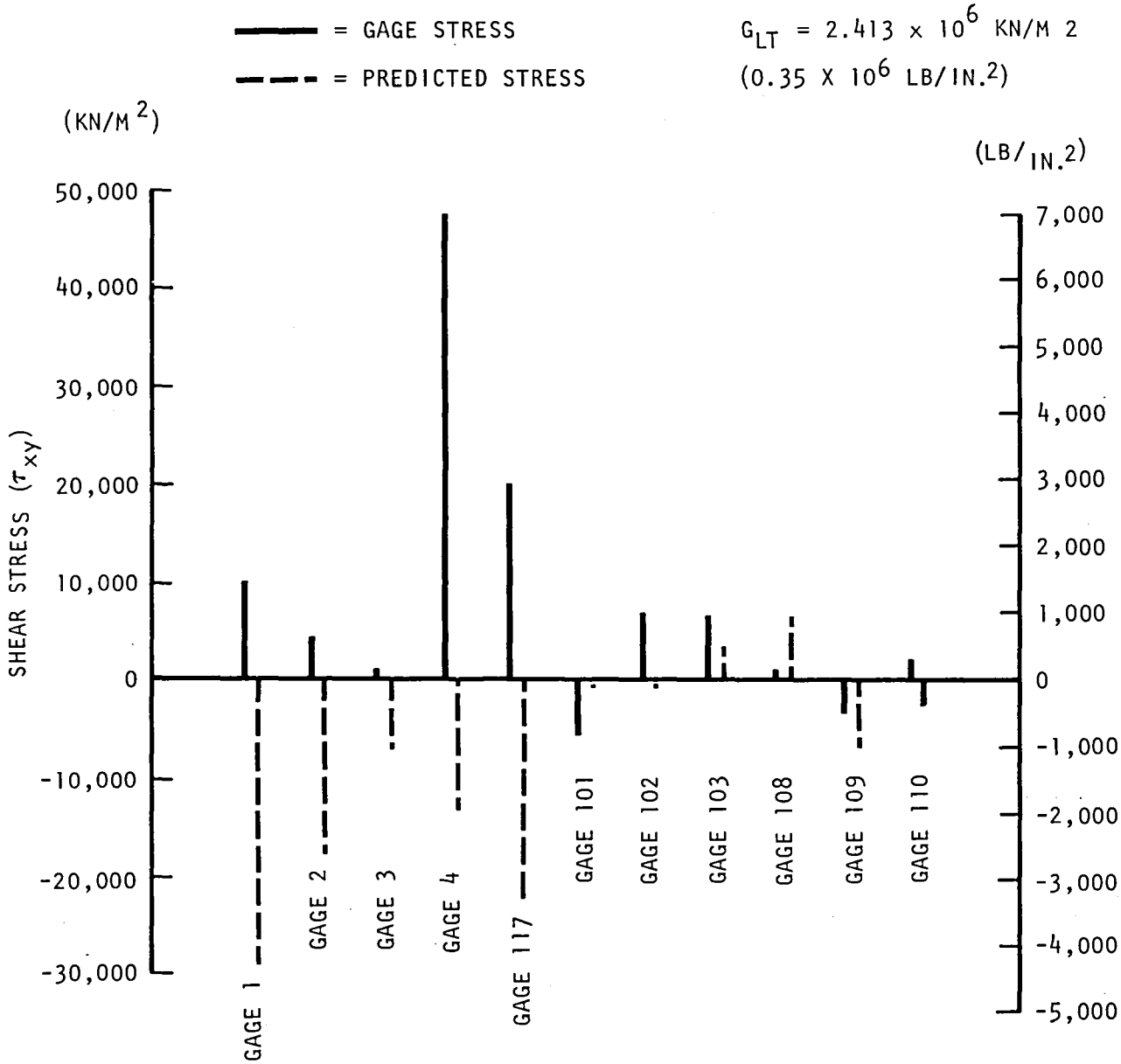

Figure 65. Outboard Wing Ground Test Gages - τ_{xy} gage Versus τ_{xy} predicted

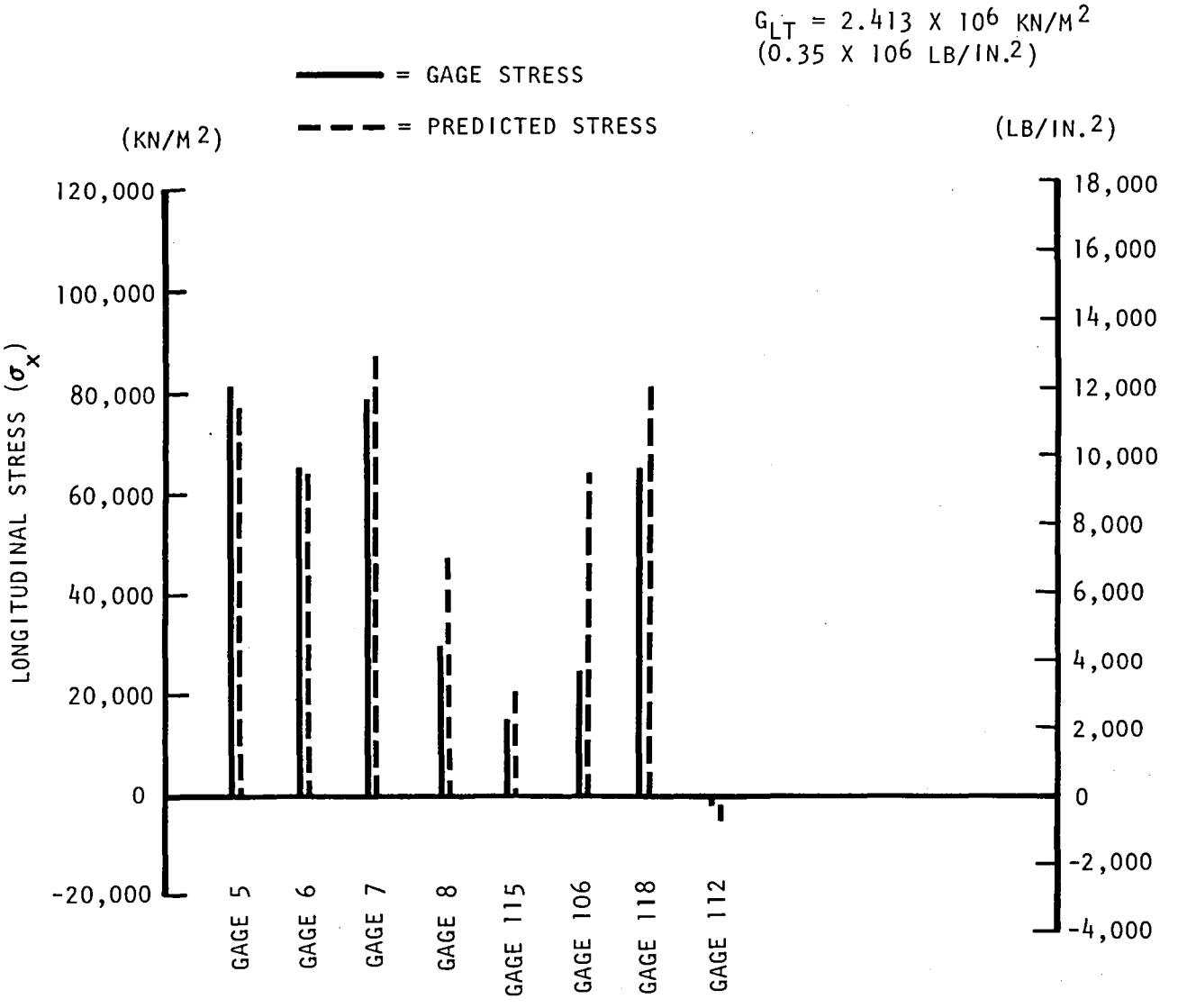

Figure 66. Canard Ground Test Gages - $\sigma_{x_{gage}}$ Versus $\sigma_{x_{predicted}}$

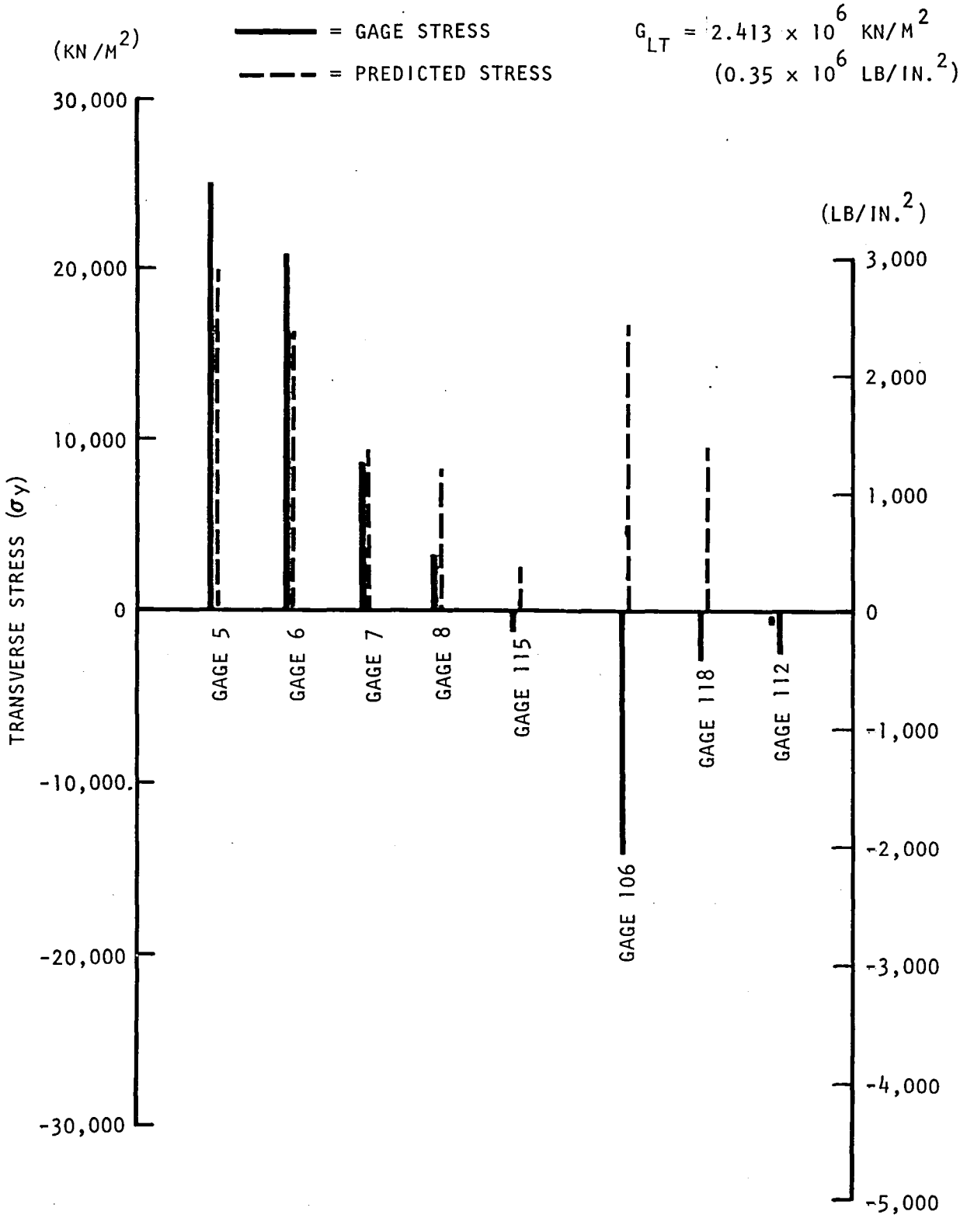

Figure 67. Canard Ground Test Gages - $\sigma_{y_{gage}}$ Versus $\sigma_{y_{predicted}}$

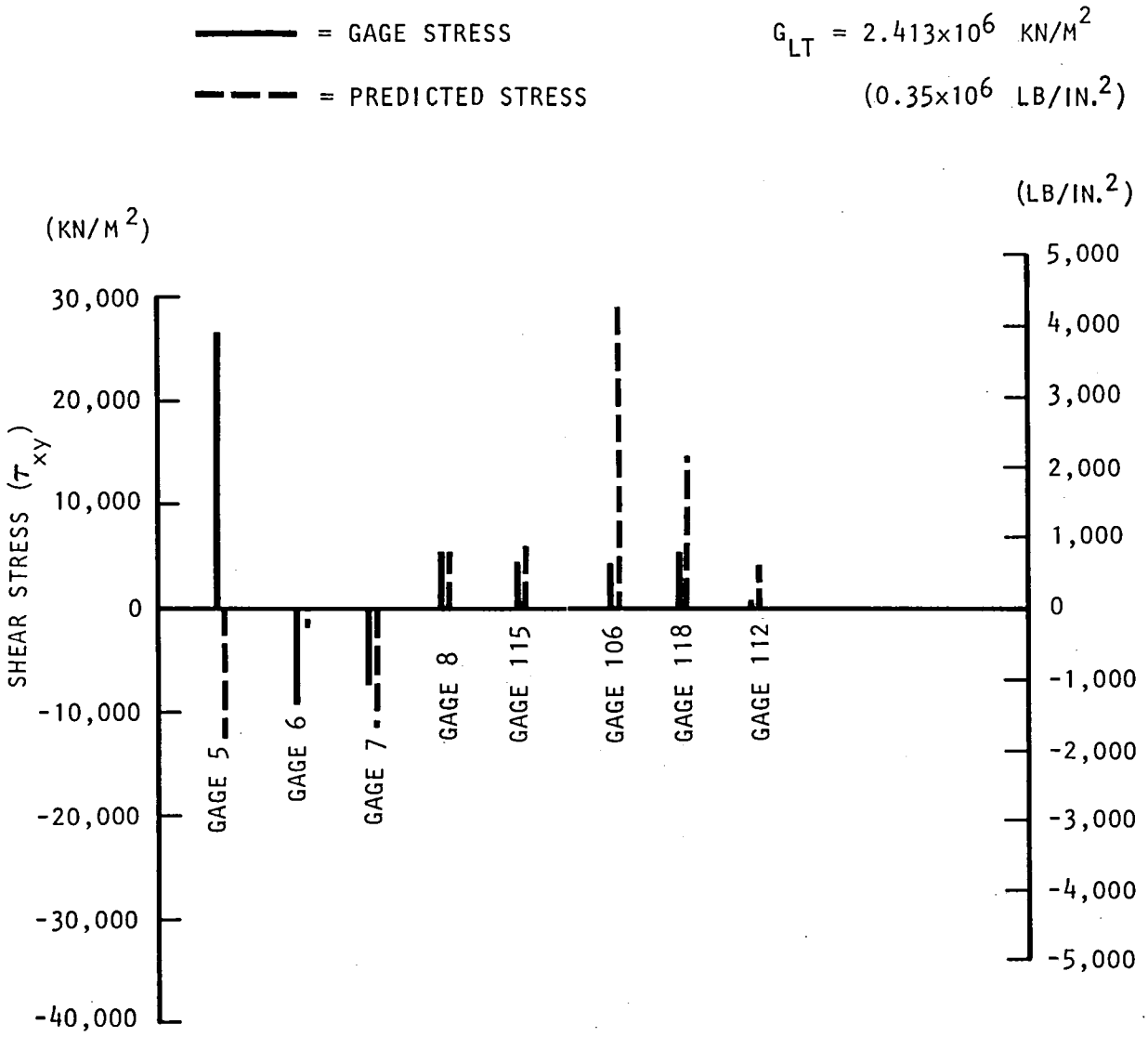

Figure 68. Canard Ground Test Gages - $\tau_{xy_{gage}}$ Versus $\tau_{xy_{predicted}}$

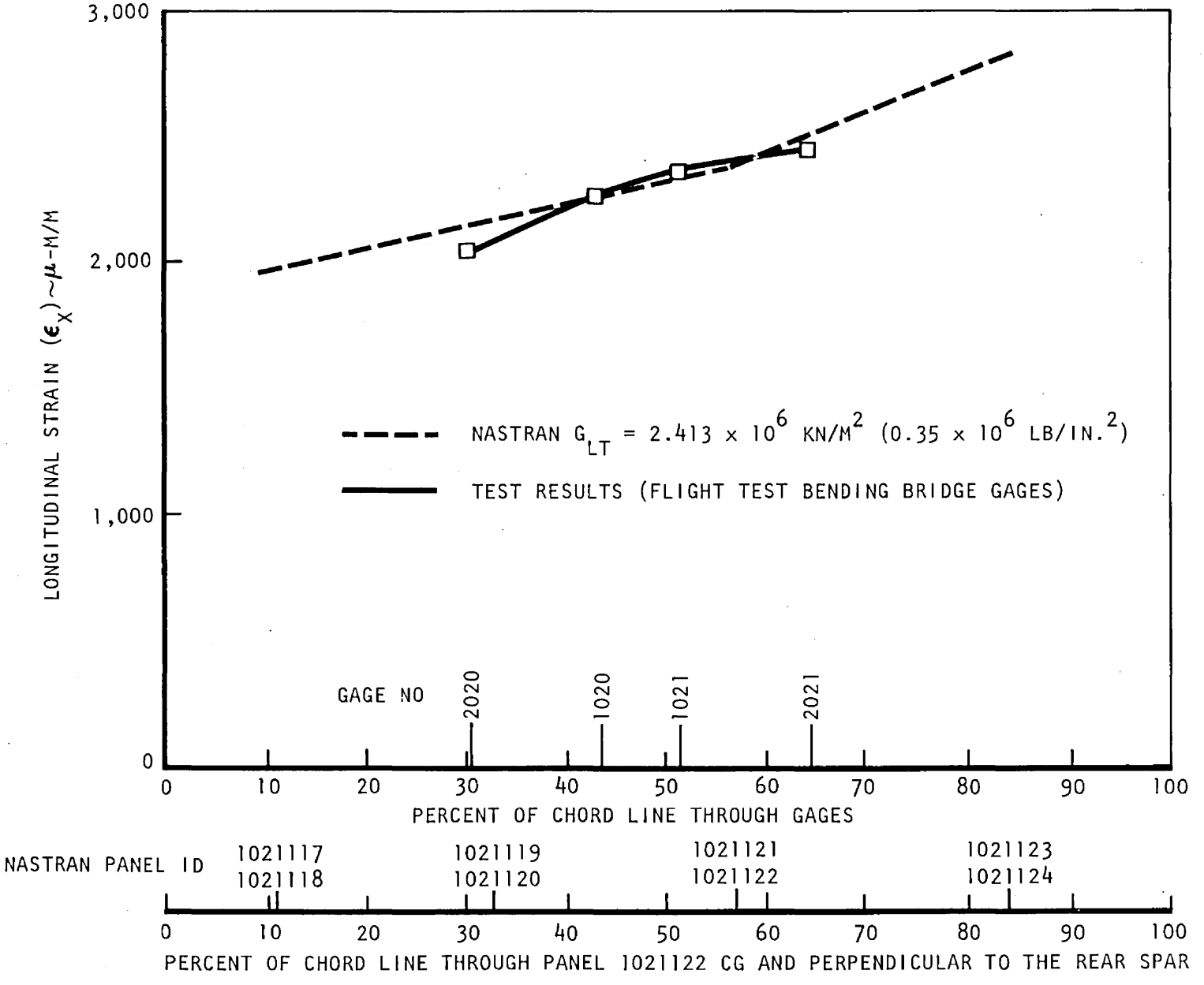

Figure 69. Flight Test Strain Gages Versus Predicted Strains X_F = 130.3 CM

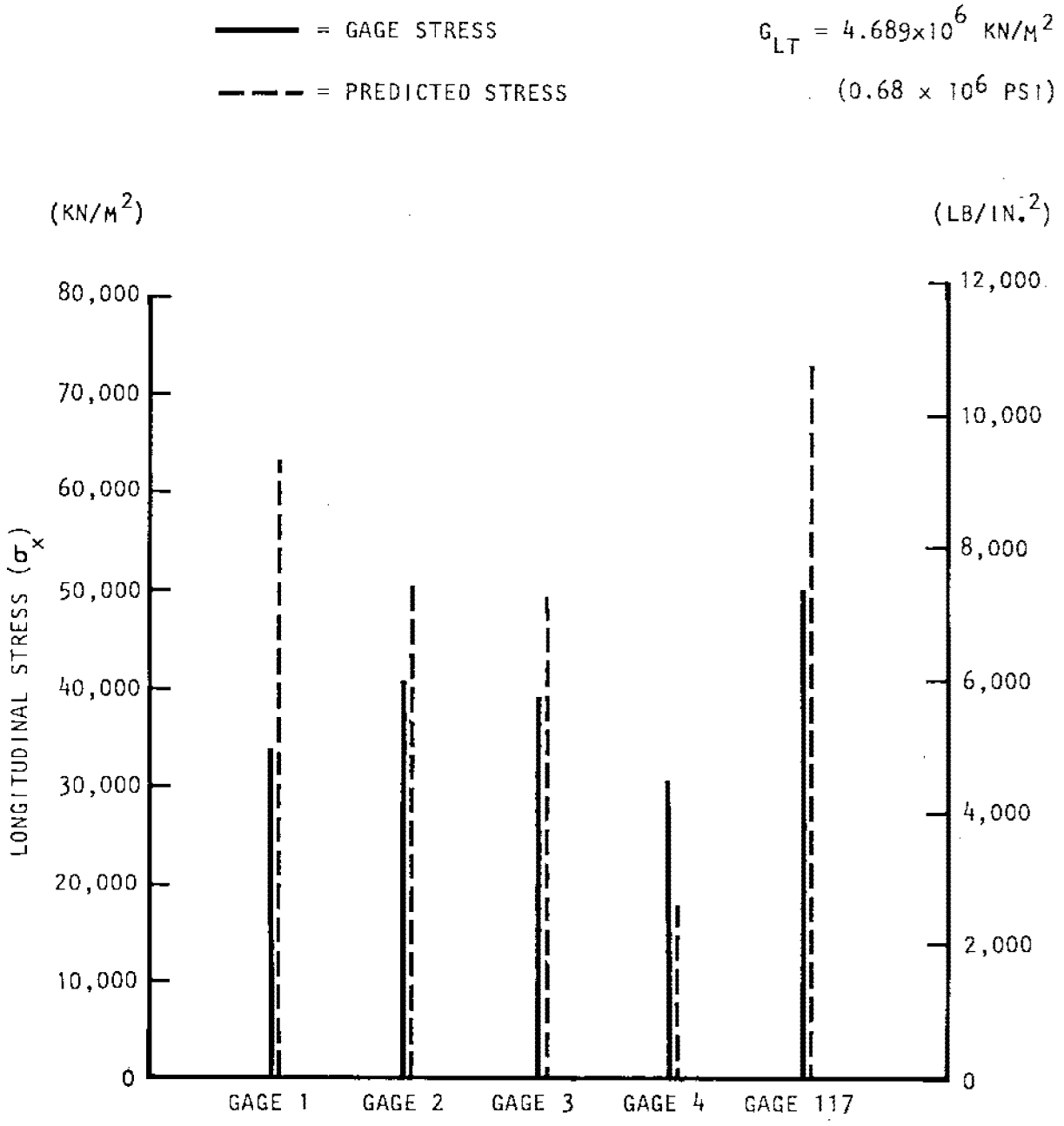

Figure 70. Outboard Wing Box Ground Test Gages- $\sigma_{x_{gage}}$ Versus $\sigma_{x_{predicted}}$

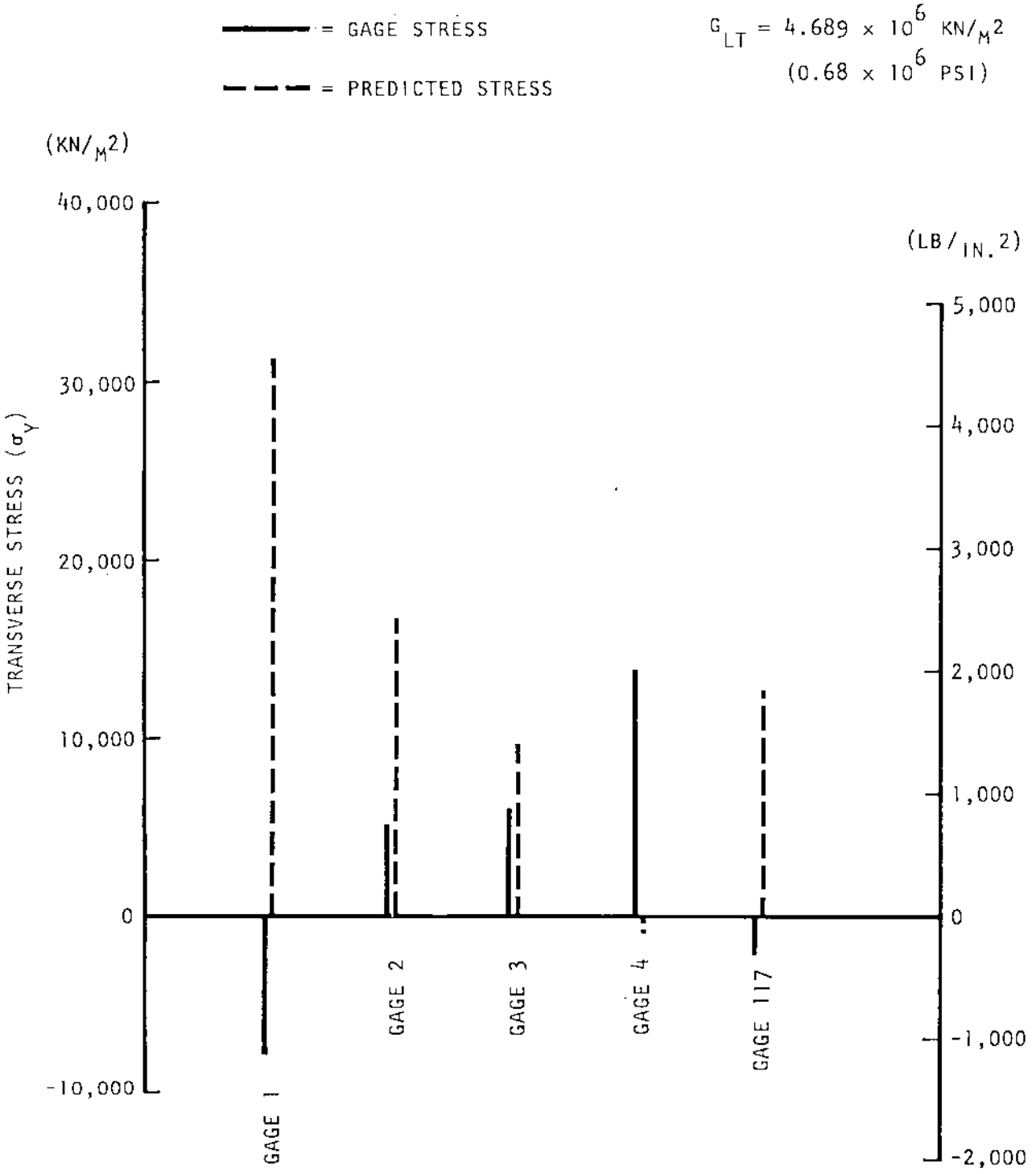

Figure 71. Outboard Wing Box Ground Test Gages - $\sigma_{y_{gage}}$ Versus $\sigma_{y_{predicted}}$

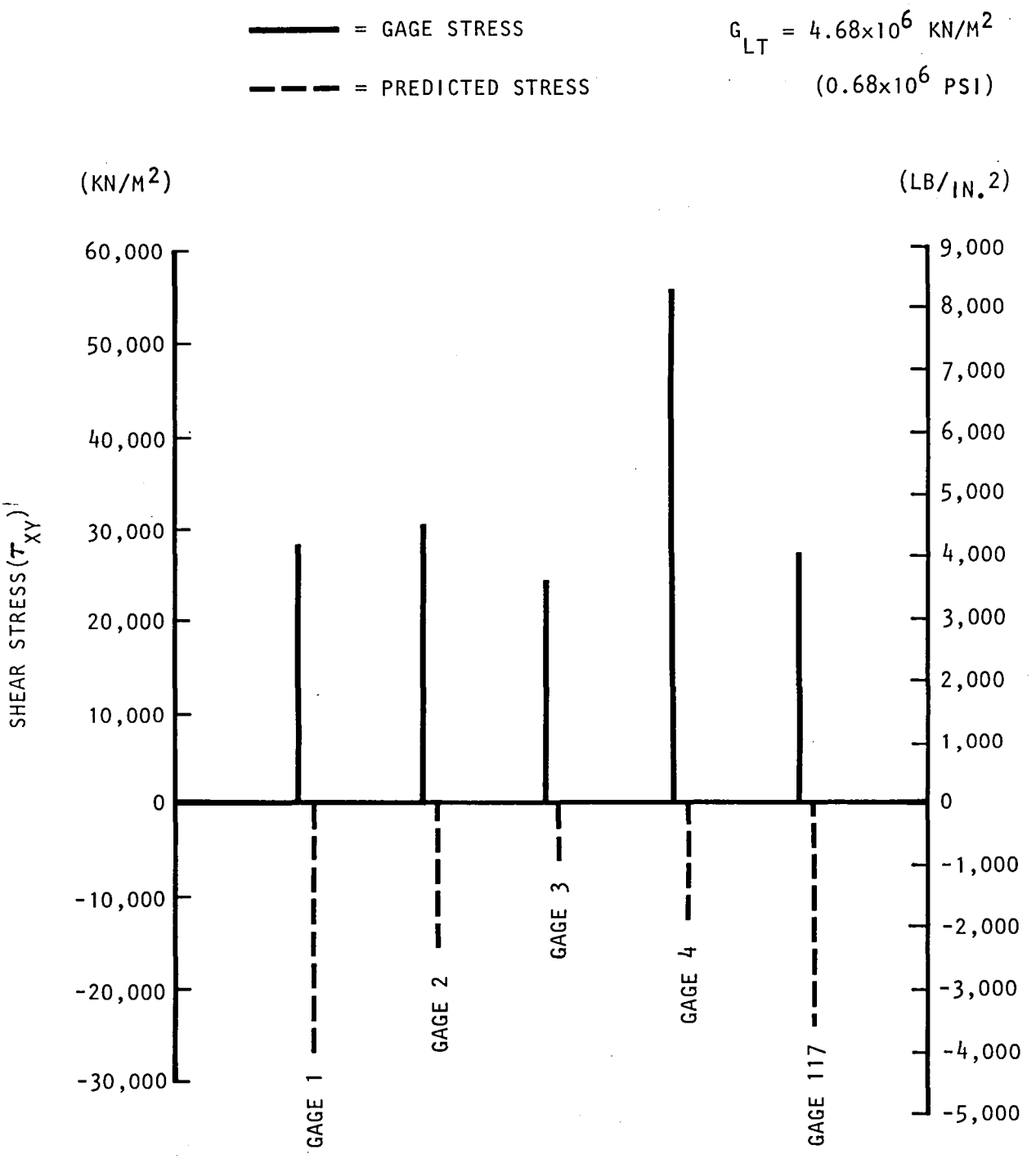

Figure 72. Outboard Wing Box Ground Test Gages - $\tau_{xy_{gage}}$ Versus $\tau_{xy_{predicted}}$

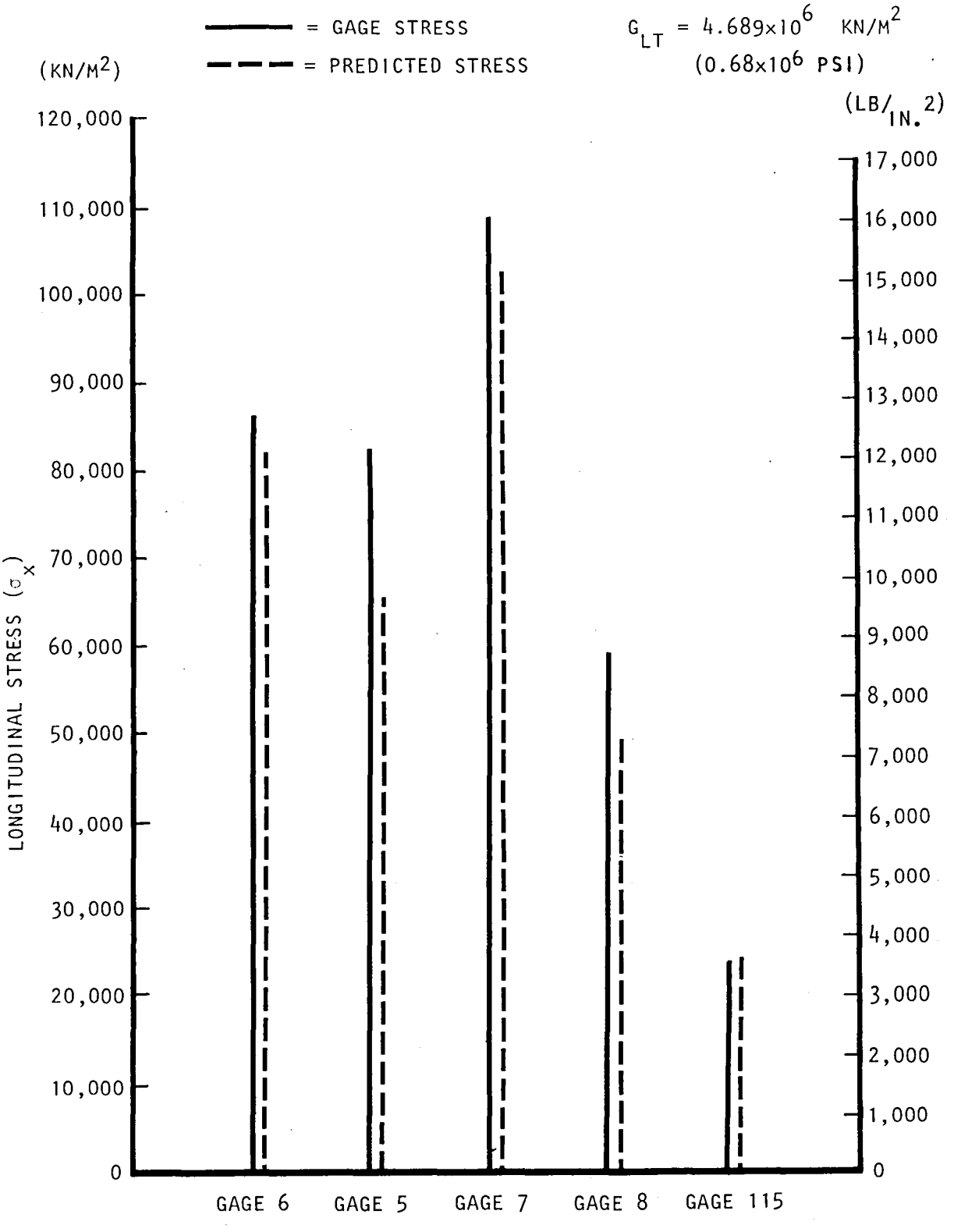

Figure 73. Canard Ground Test Gages - Structural Box - $\sigma_{x_{gage}}$ Versus $\sigma_{x_{predicted}}$

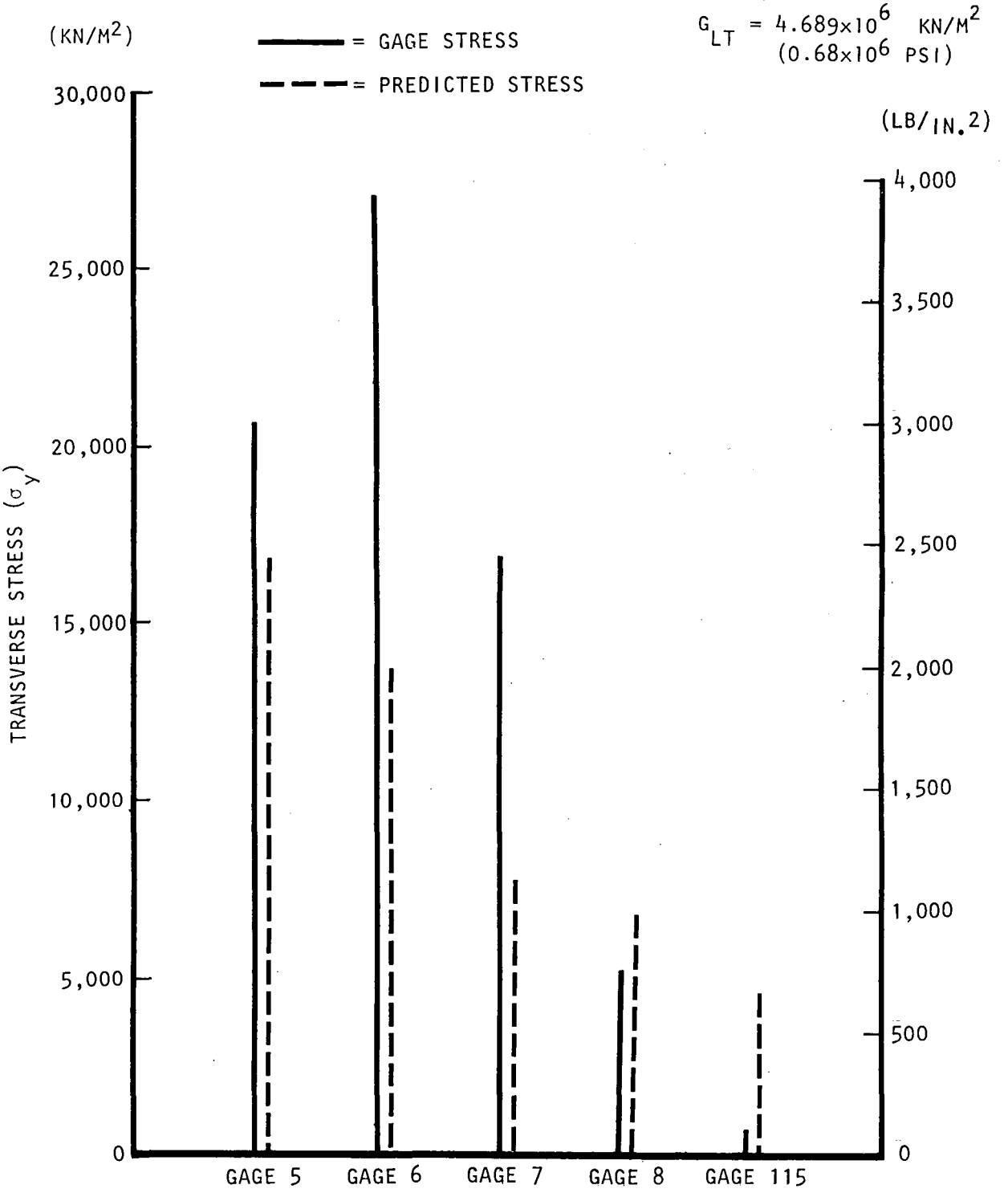

Figure 74. Canard Ground Test Gages - Structural Box - $\sigma_{y_{gage}}$ Versus $\sigma_{y_{predicted}}$

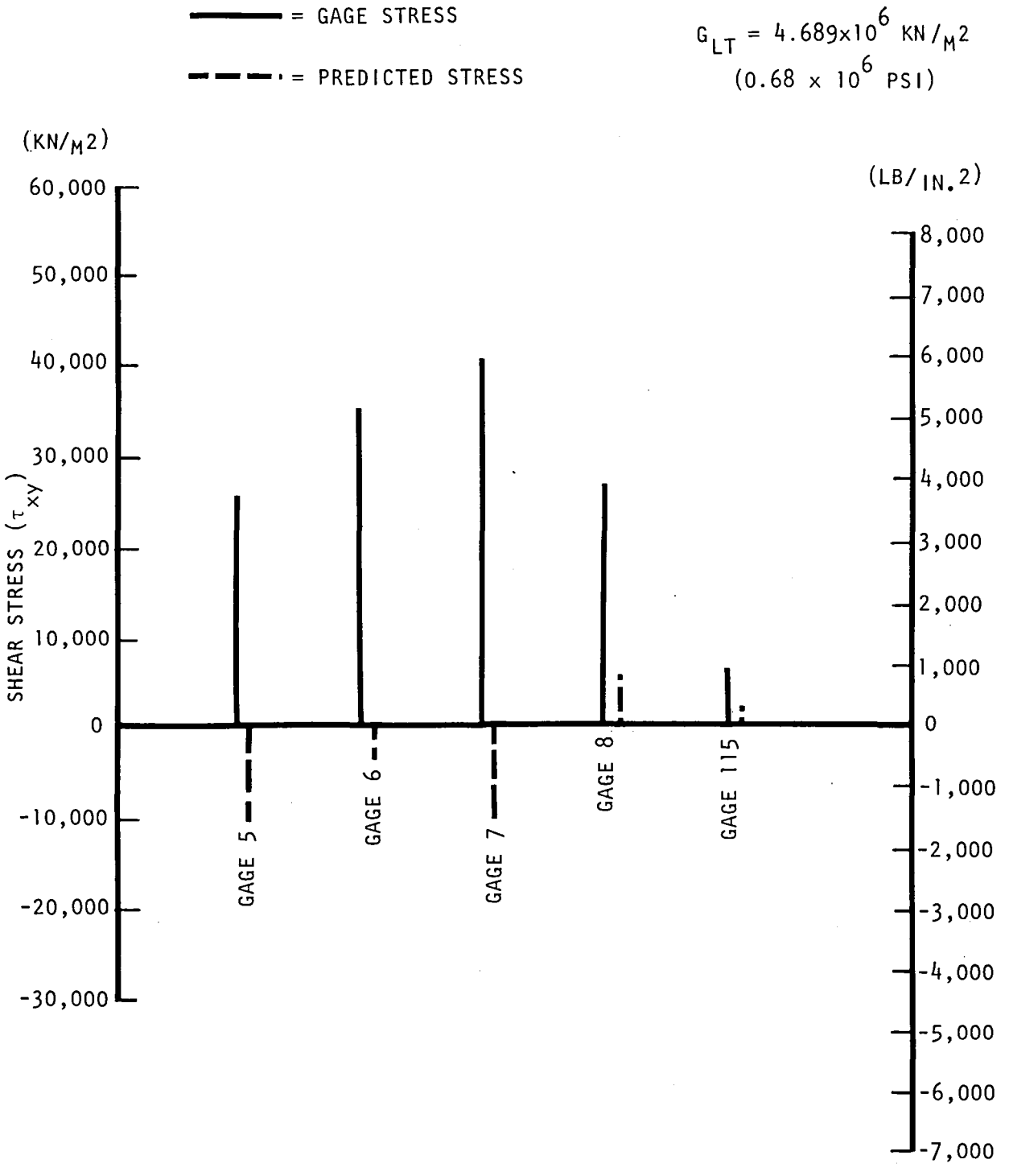

Figure 75. Canard Ground Test Gages - Structural Box - $\tau_{xy_{gage}}$ Versus $\tau_{xy_{predicted}}$

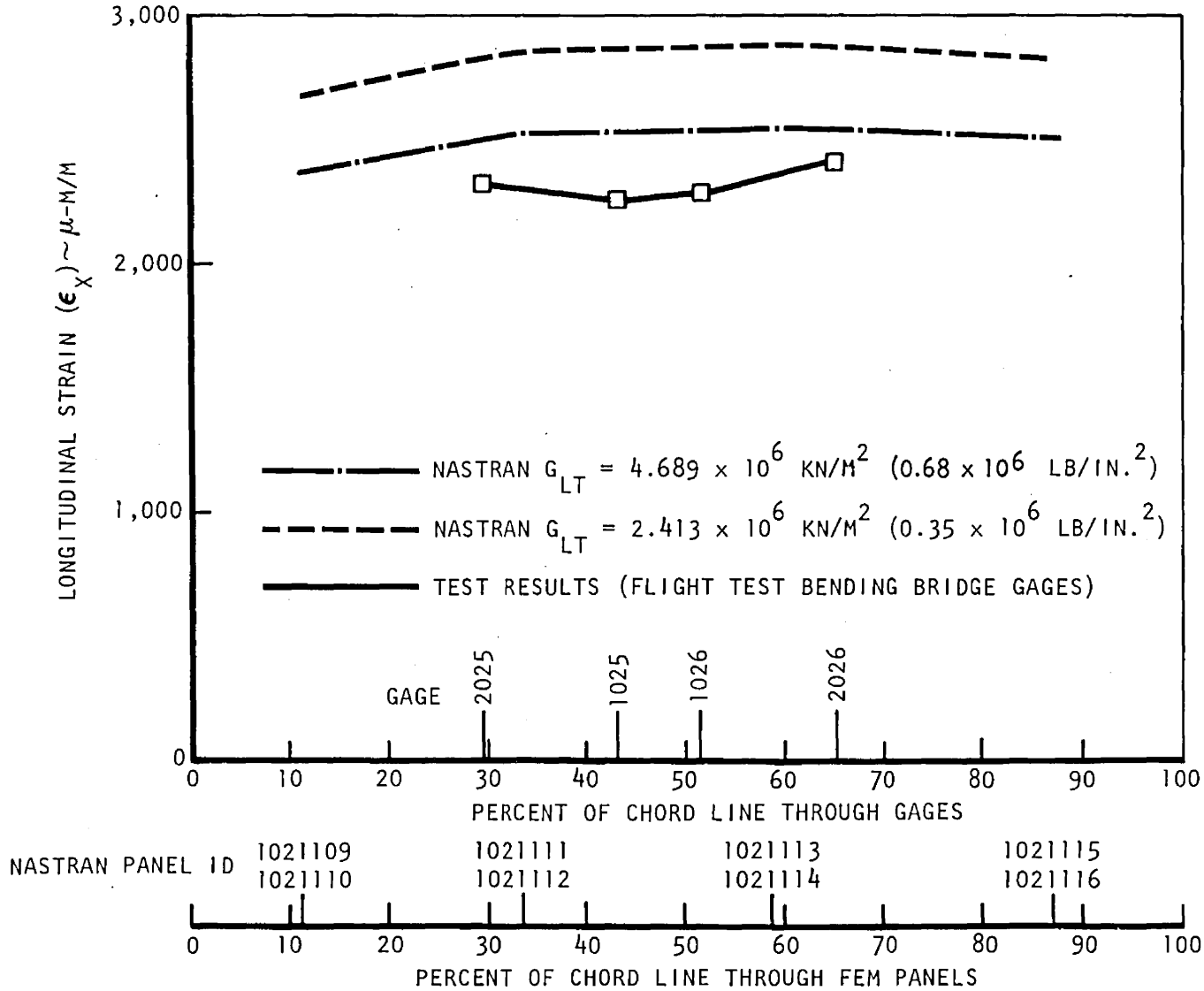

Figure 76. Wing Flight Test Gage Strains Versus Predicted Strains, X_F = 143.0 CM

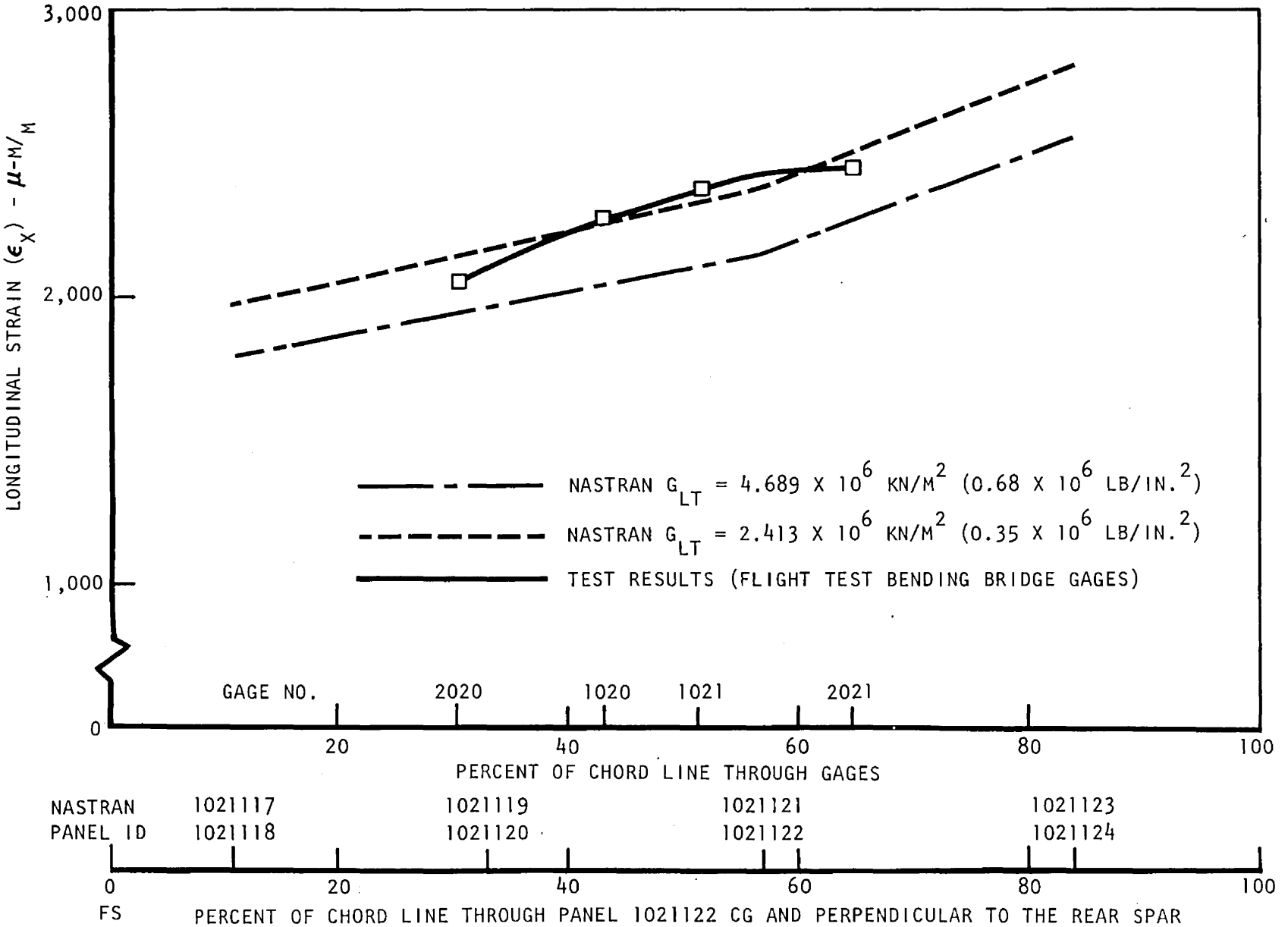

Figure 77. Wing Flight Test Strain Gages Versus Predicted Strains, X_F = 143.0 CM

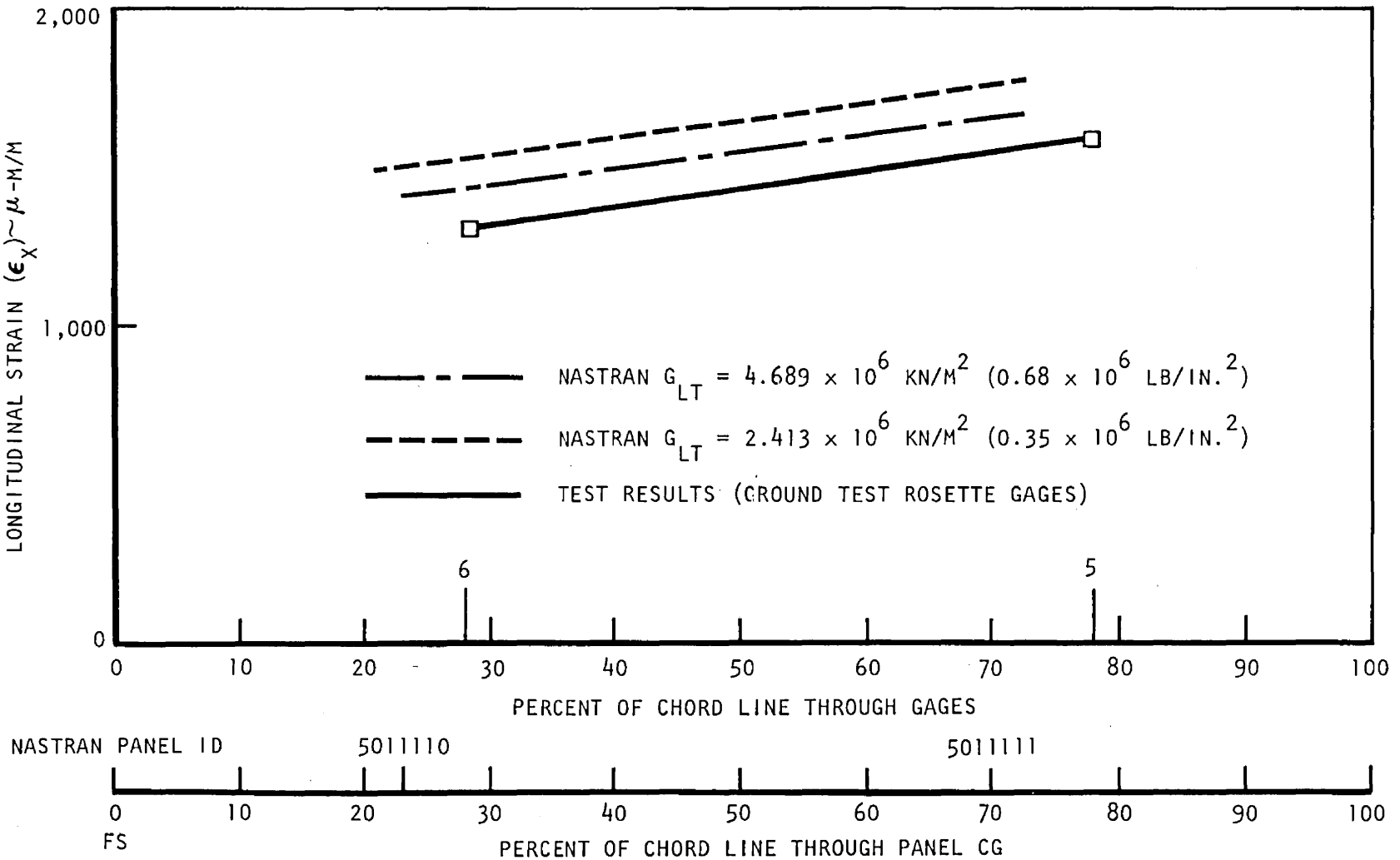

Figure 78. Ground Test Gages Versus Predicted Strains

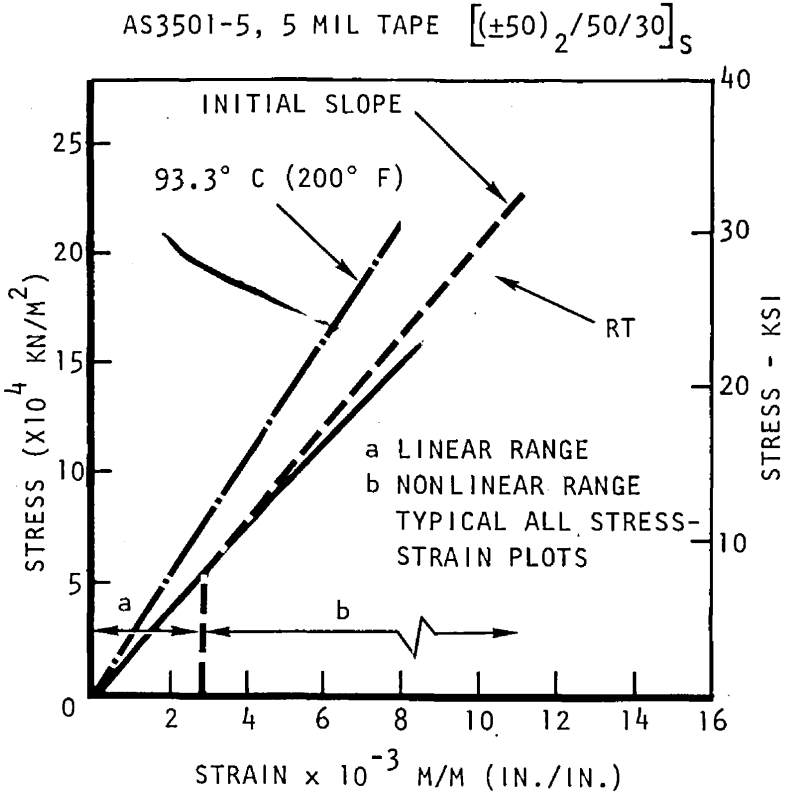

Figure 79. Longitudinal Tension Stress Versus Strain Curve at RT and 93.3° C (200° F)

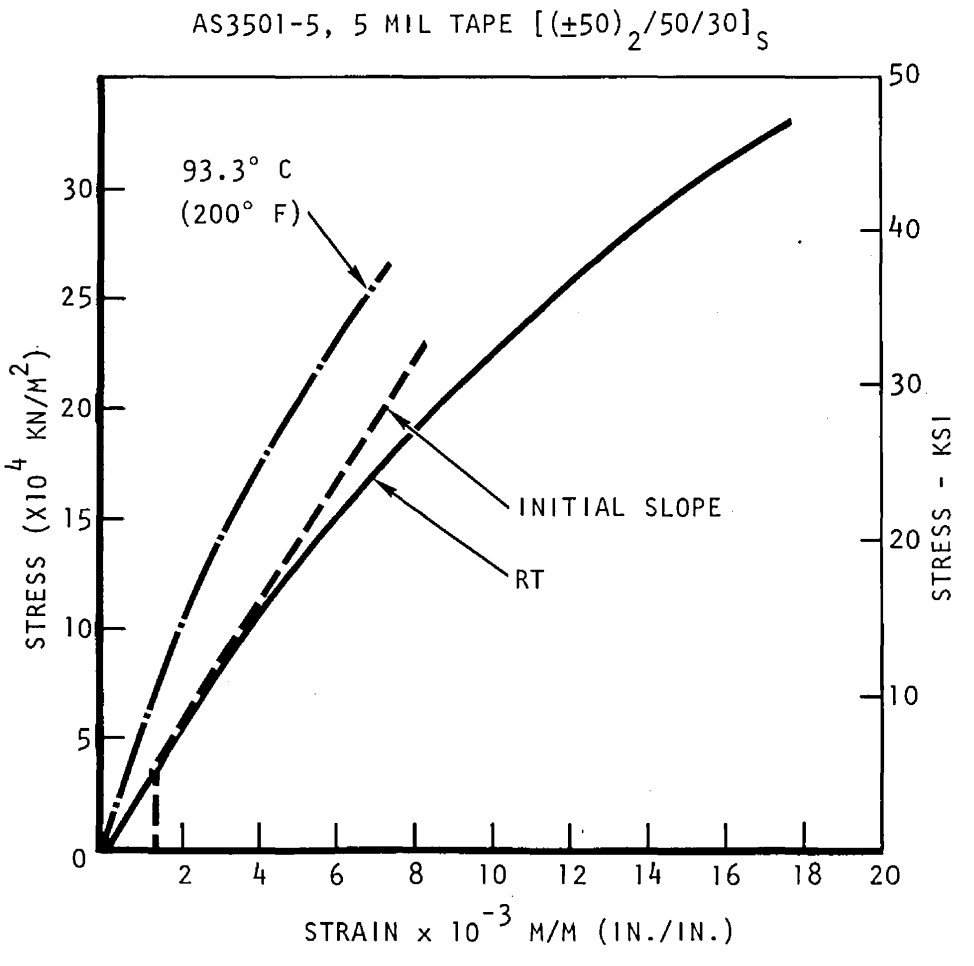

Figure 80. Transverse Tension Stress Versus Strain Curve at RT and 93.3° C (200° F)

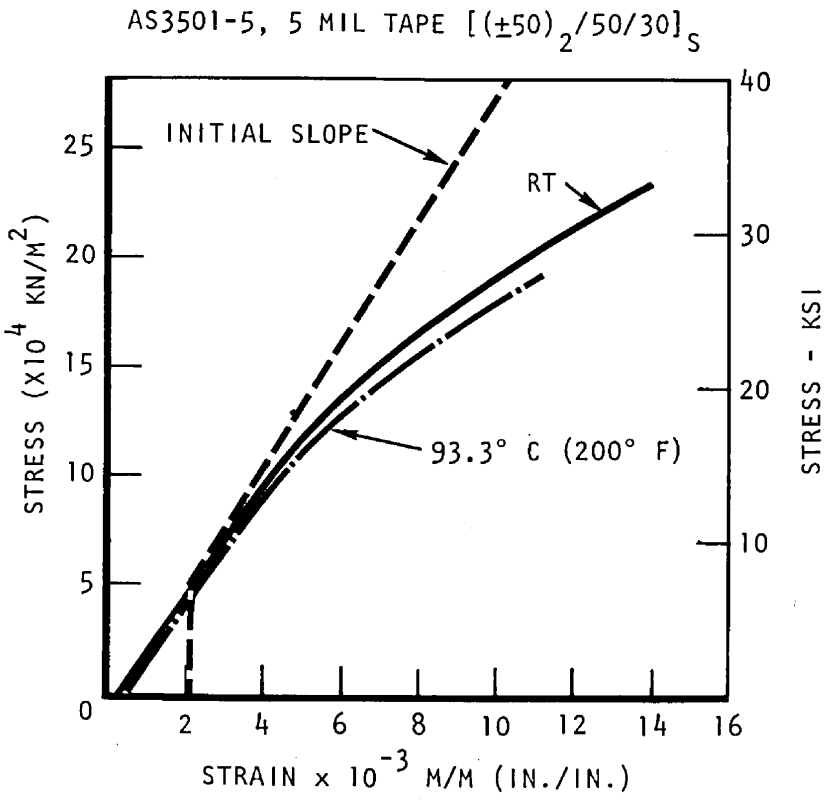

Figure 81. Longitudinal Compression Stress Versus Strain Curve at RT and 93.3° C (200° F)

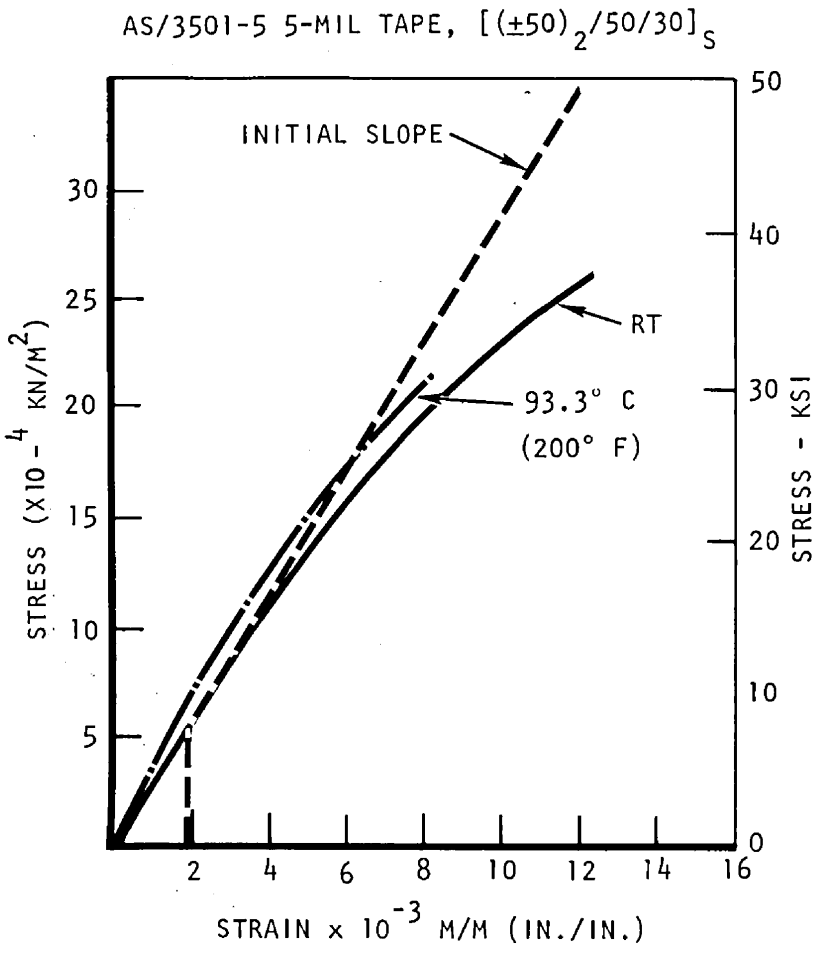

Figure 82. Transverse Compression Stress Versus Strain Curve at RT and 93.3° C (200° F)

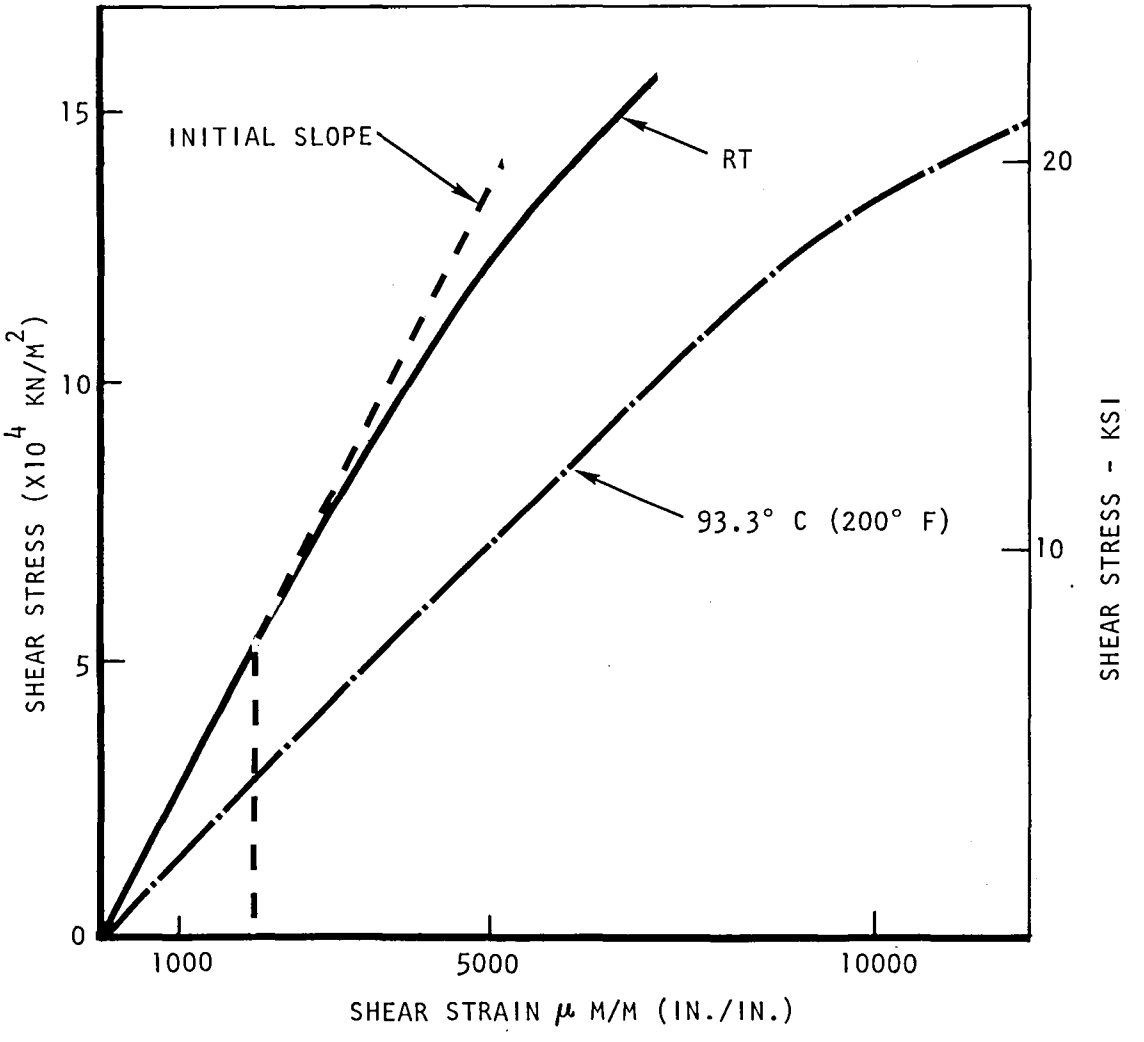

Figure 83. Shear Stress-Strain Curve RT and 93.3° C (200° F)

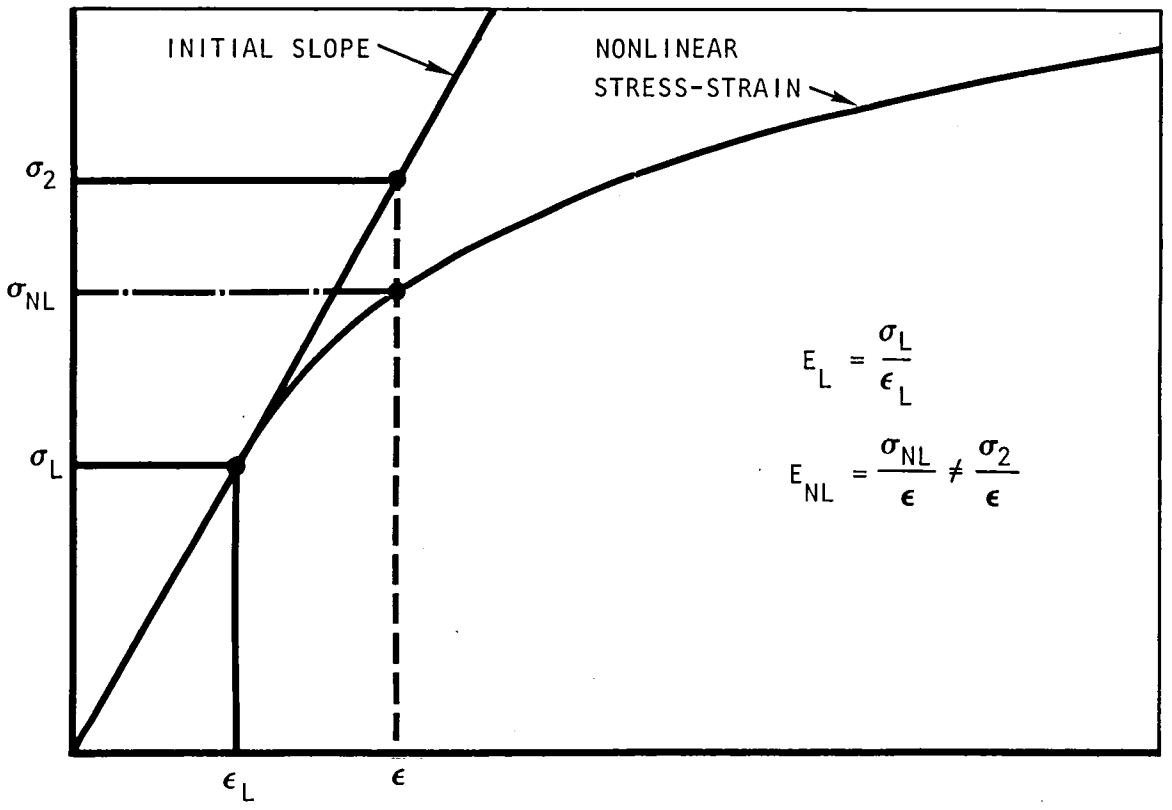

Figure 84. Typical Stress-Strain Plot

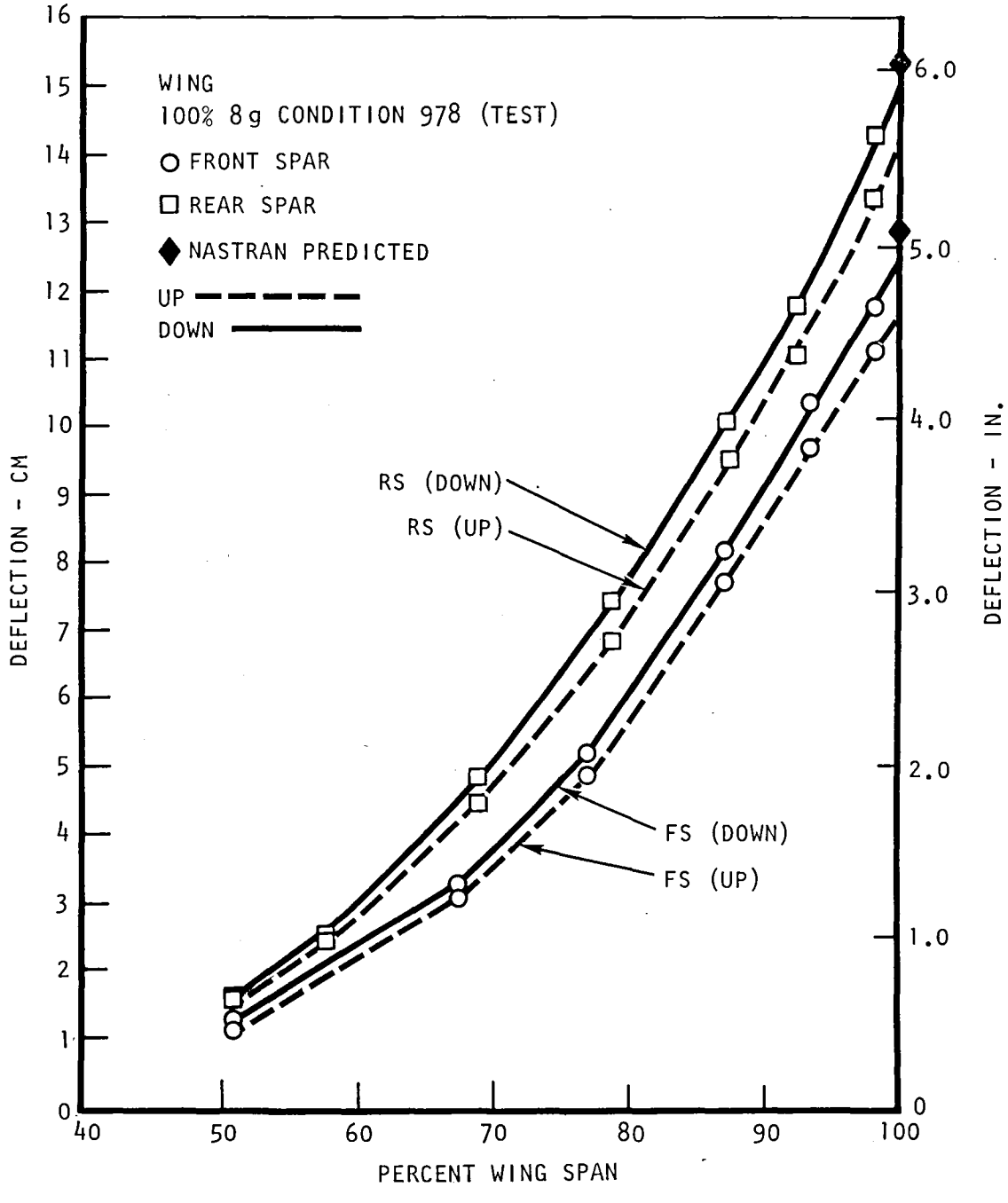

Figure 85. Wing Test Deflections - Front Spar/Rear Spar

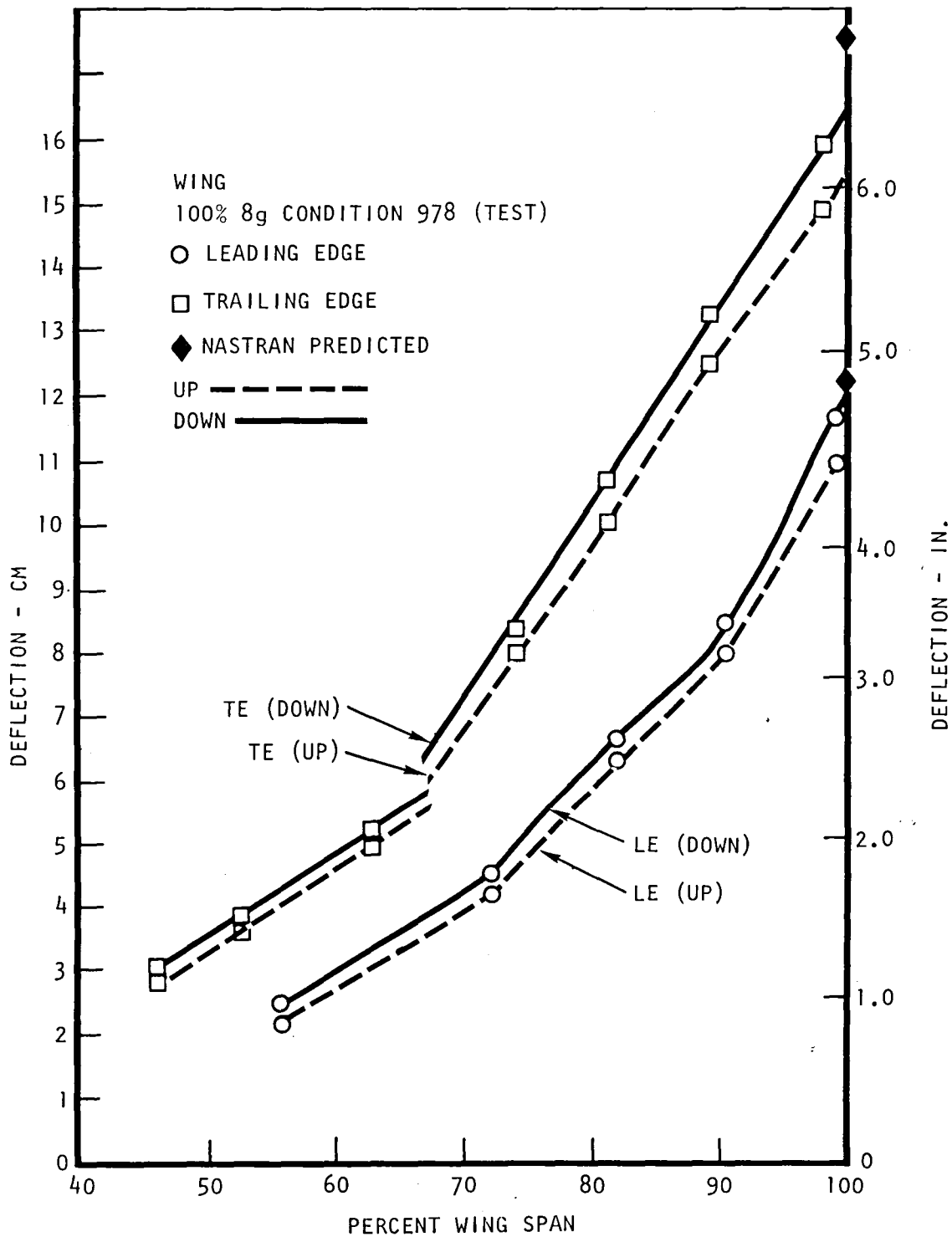

Figure 86. Wing Test Deflections - Leading Edge/Trailing Edge

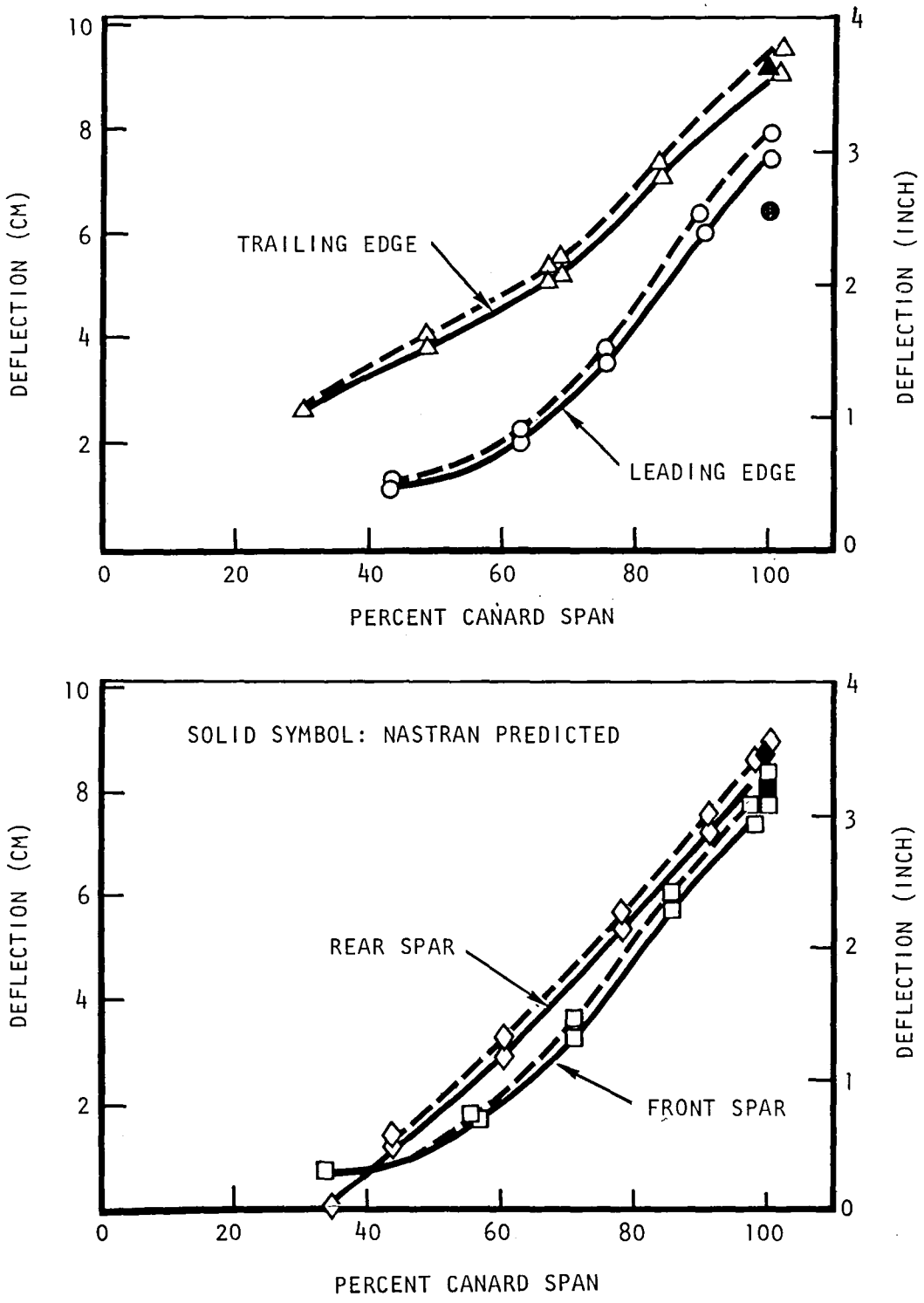

Figure 87. Test Deflections for Canard

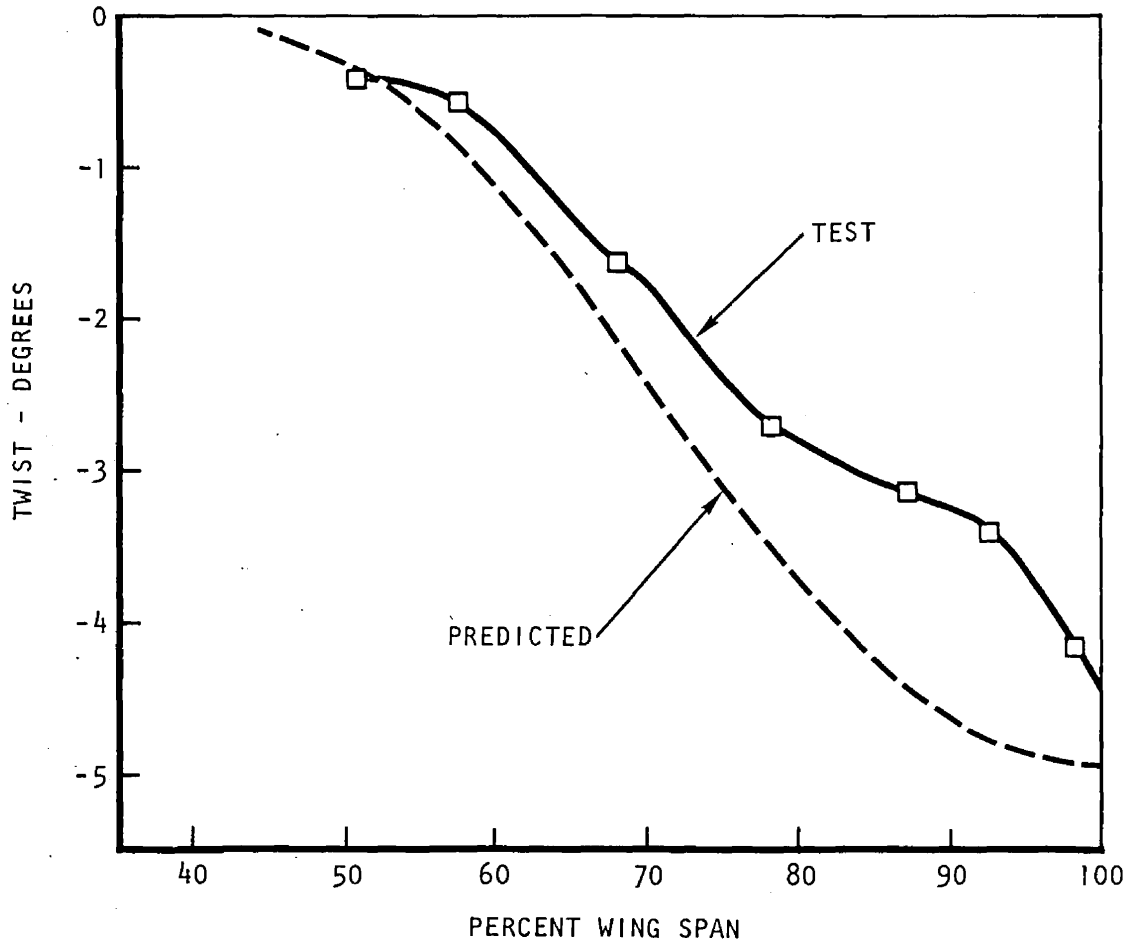

Figure 88. Wing Twist - Test Versus Predicted - FS/RS

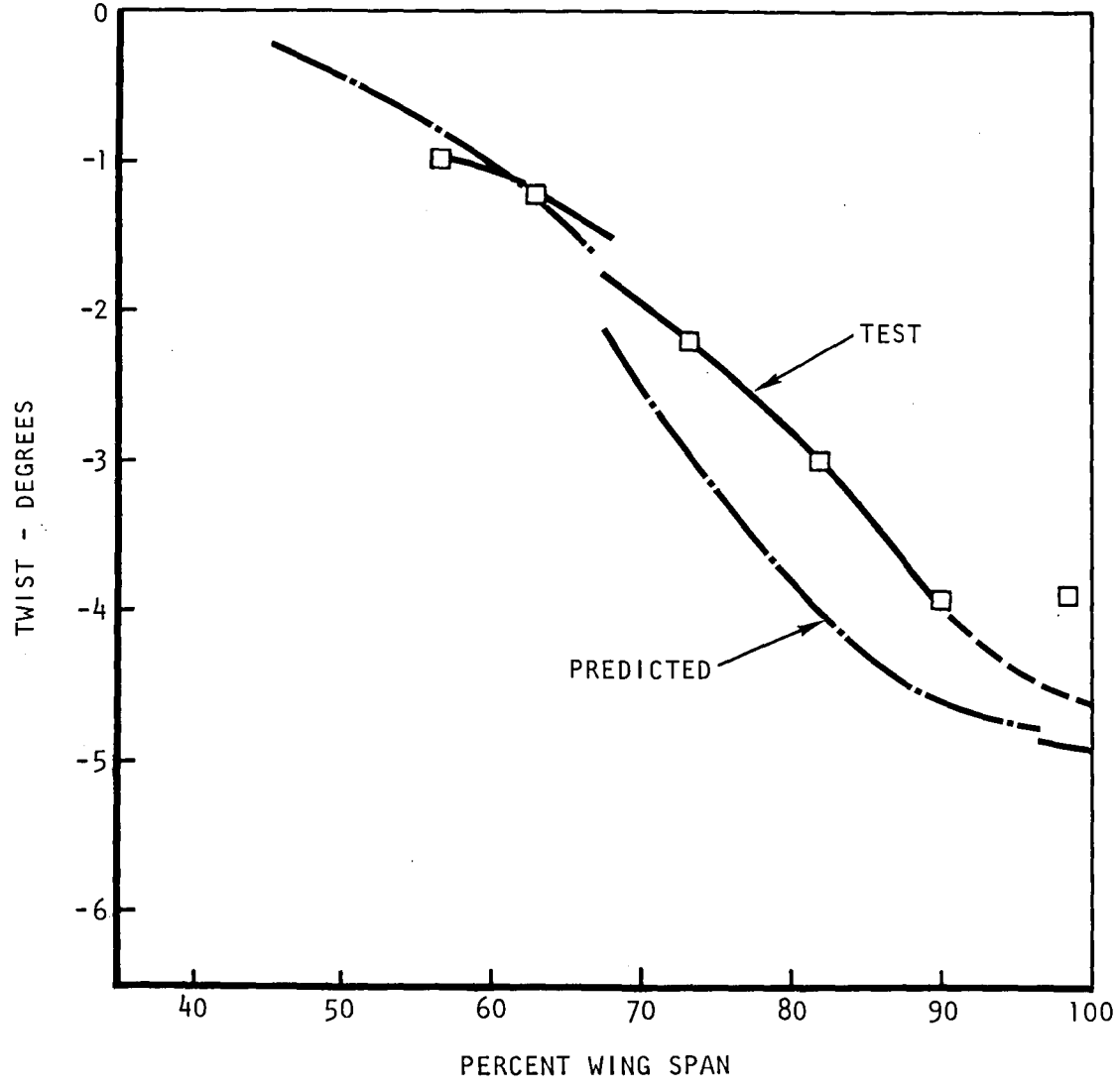

Figure 89. Wing Twist - Test Versus Predicted - LE/TE

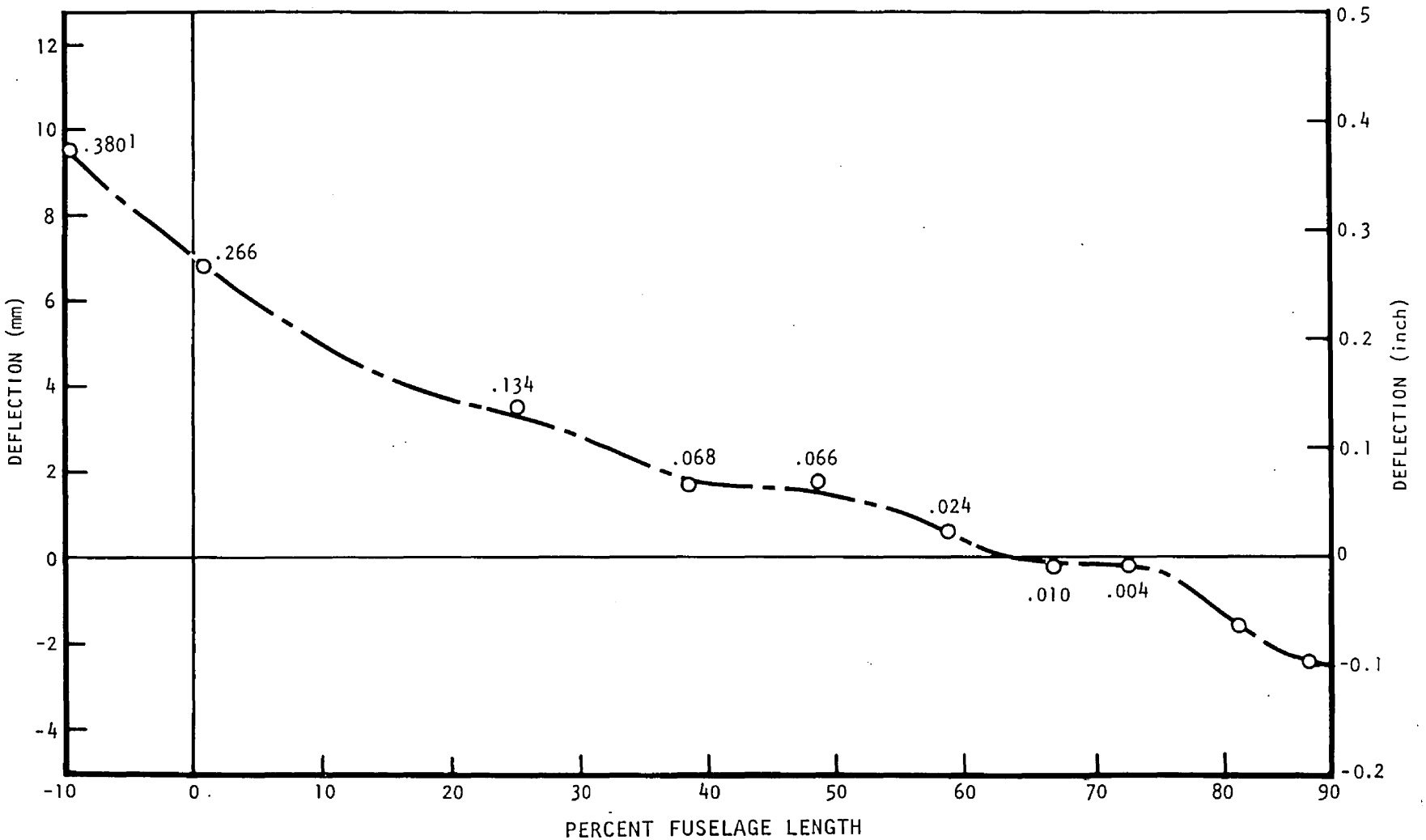

Figure 90. Fuselage Deflections

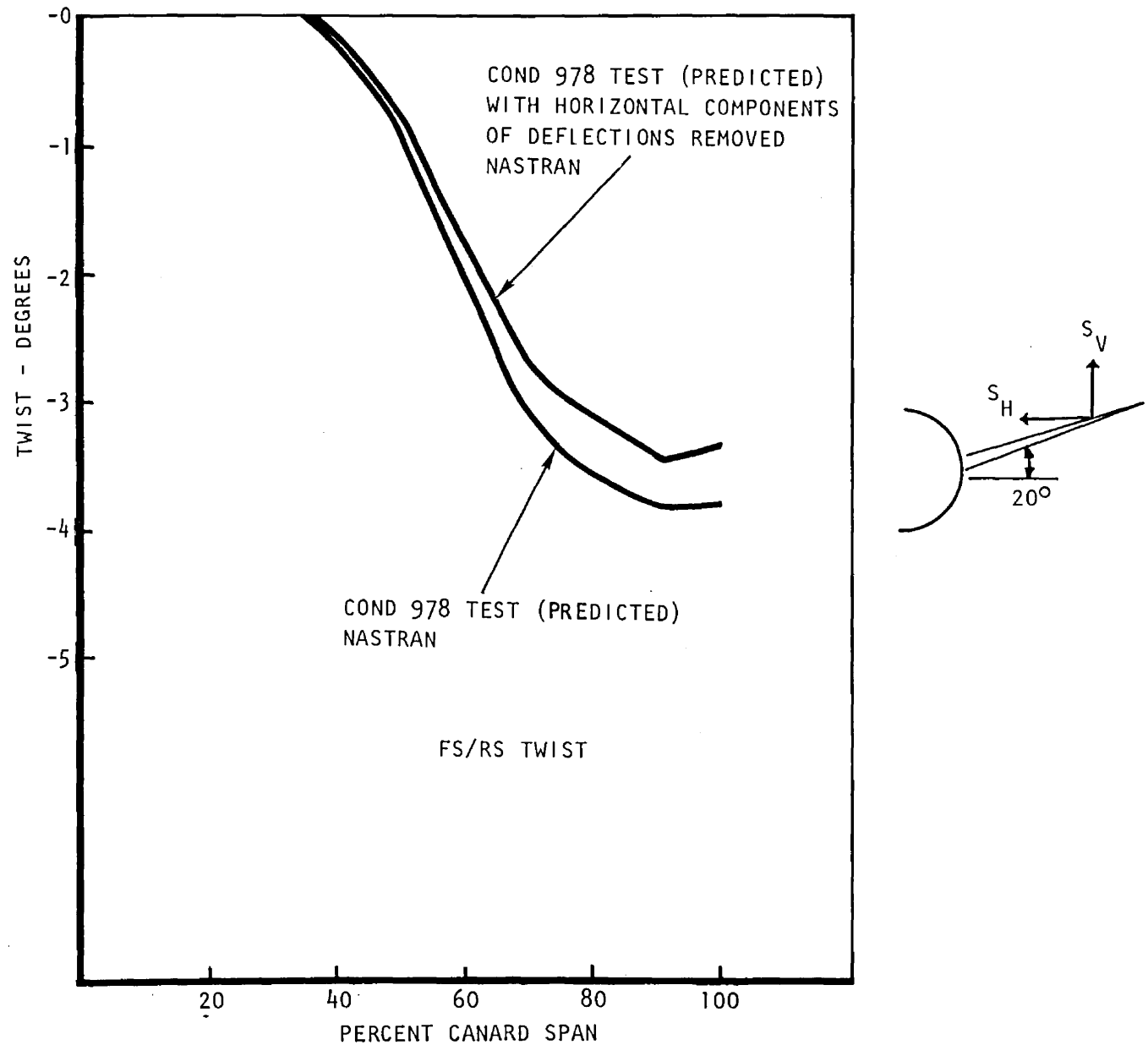

Figure 91. Effect of Horizontal Component on Twist

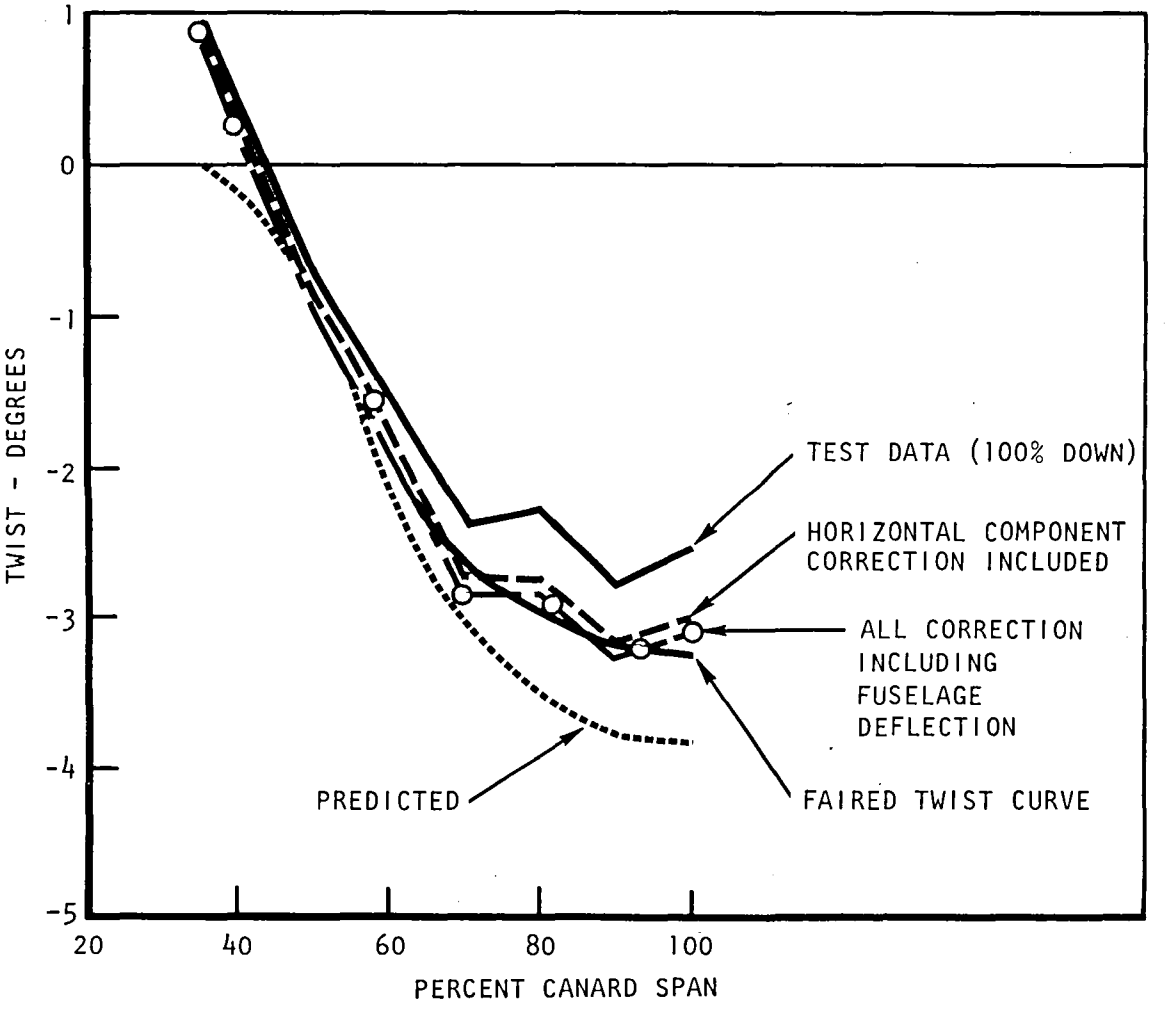

Figure 92. Canard Test Twist Versus Predicted - FS/RS

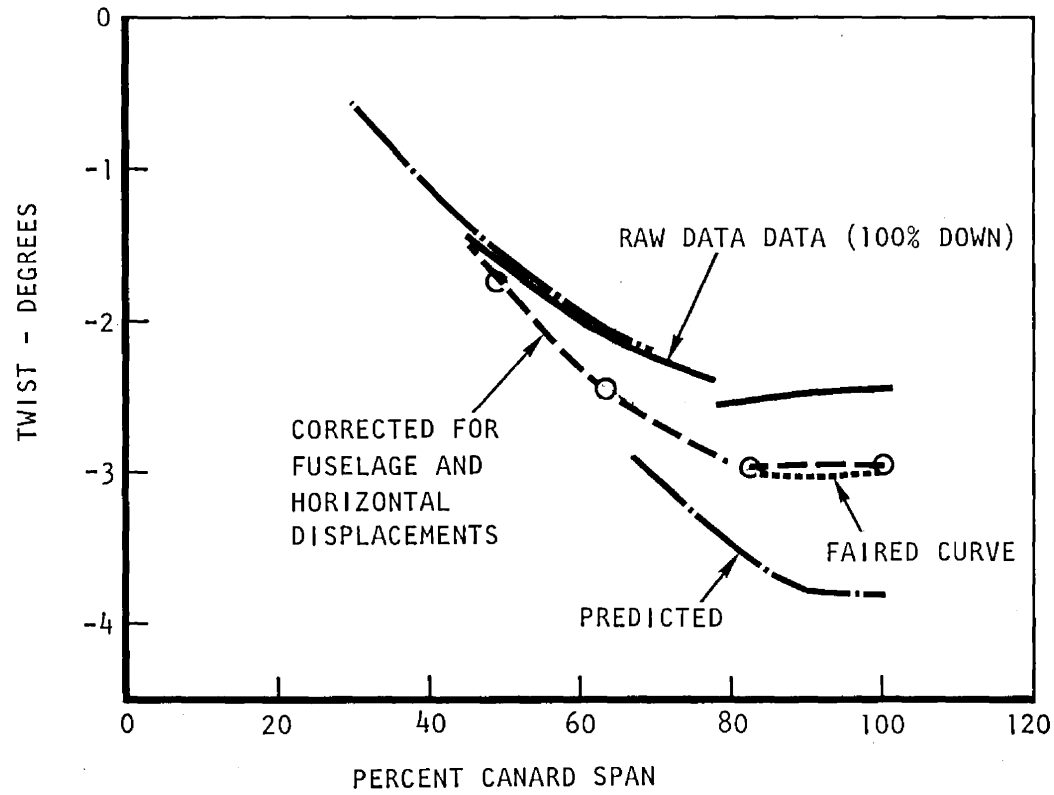

Figure 93. Canard Test Twist Versus Predicted - LE/TE

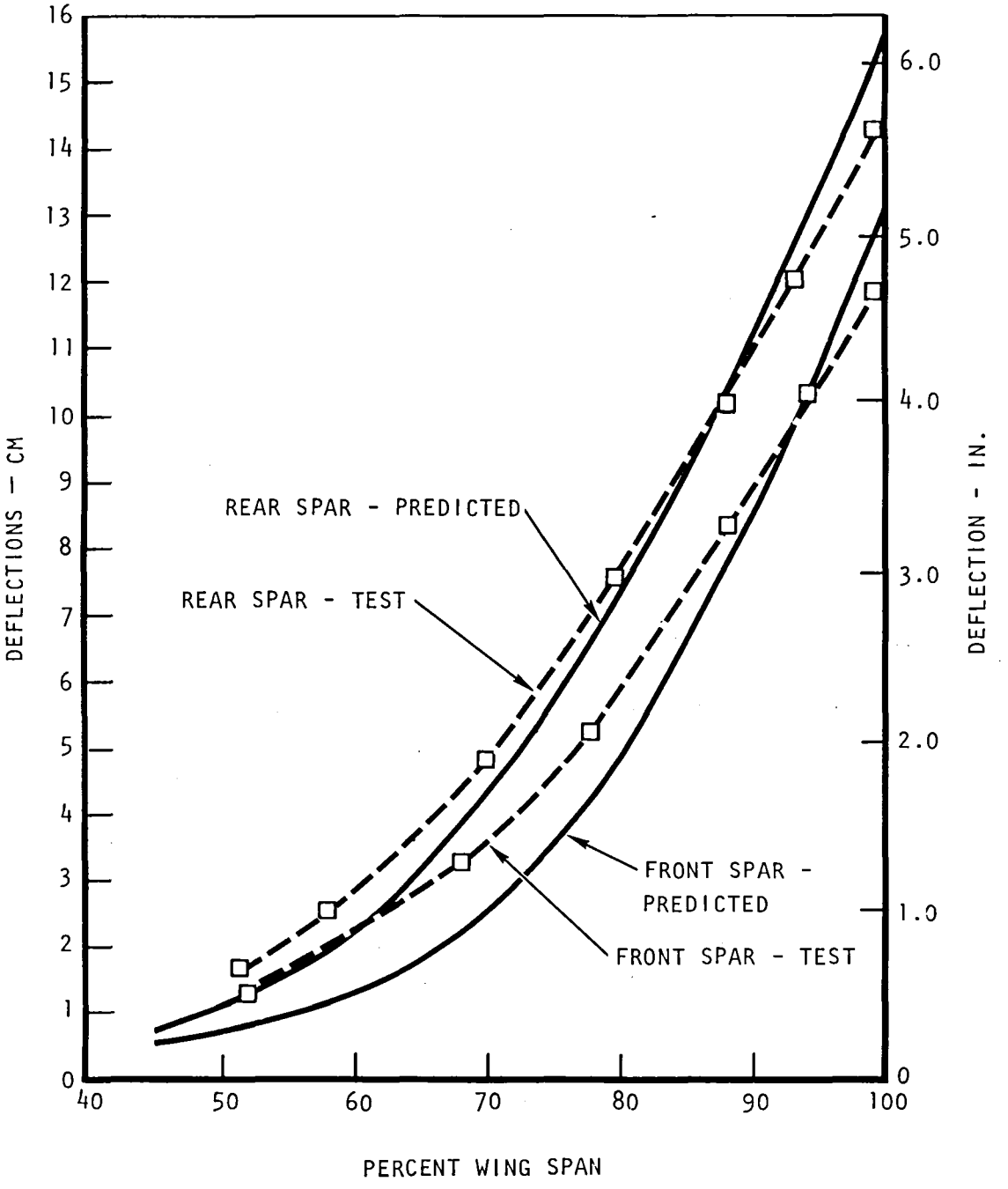

Figure 94. Wing Deflections - Test Versus Predicted

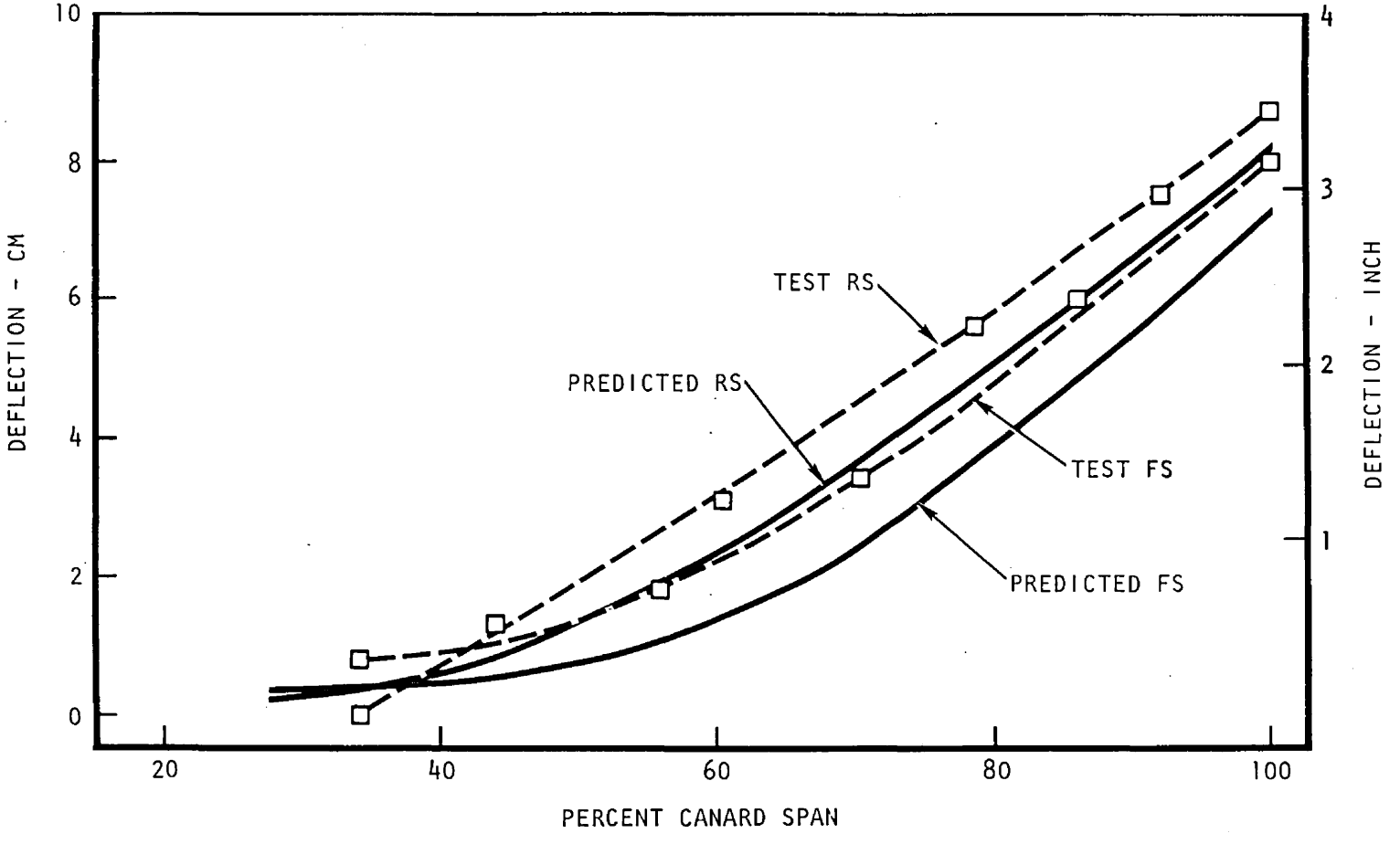

Figure 95. Canard Test Deflections Versus Predicted - FS/RS

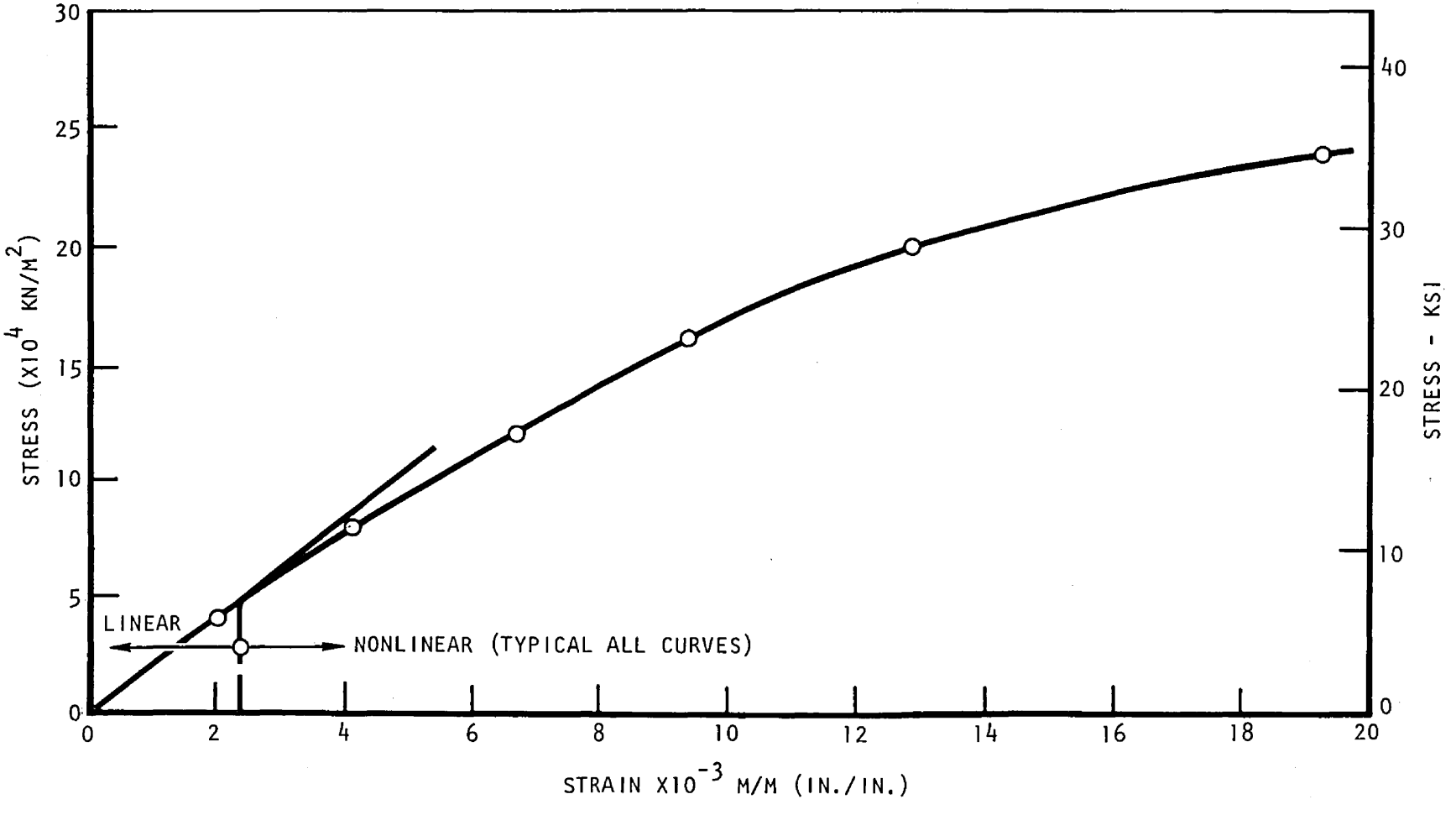

Figure 96. Longitudinal Tension Stress Versus Strain

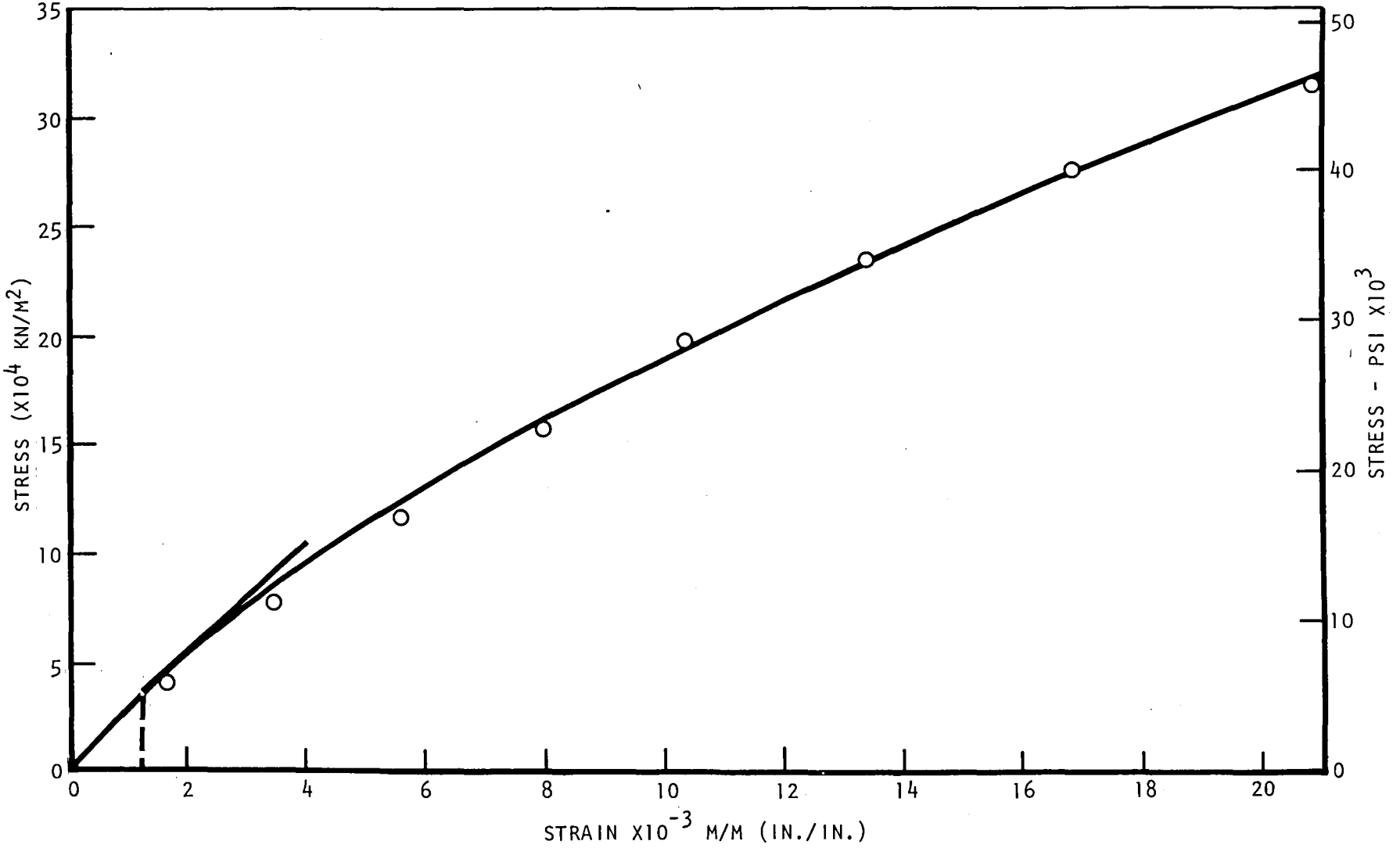

Figure 97. Longitudinal Transverse Stress Versus Shear

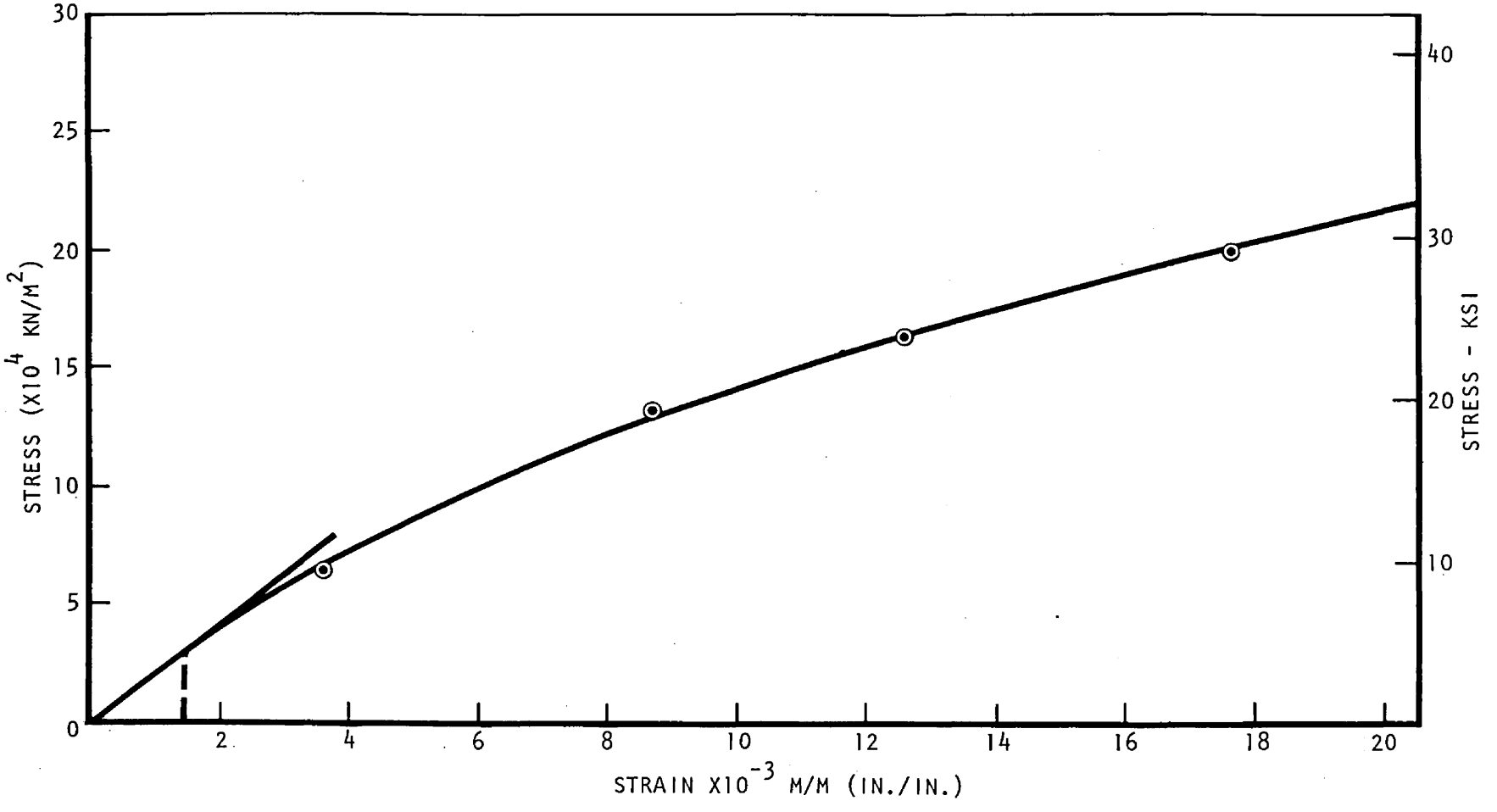

Figure 98. Longitudinal Compression Stress Versus Strain

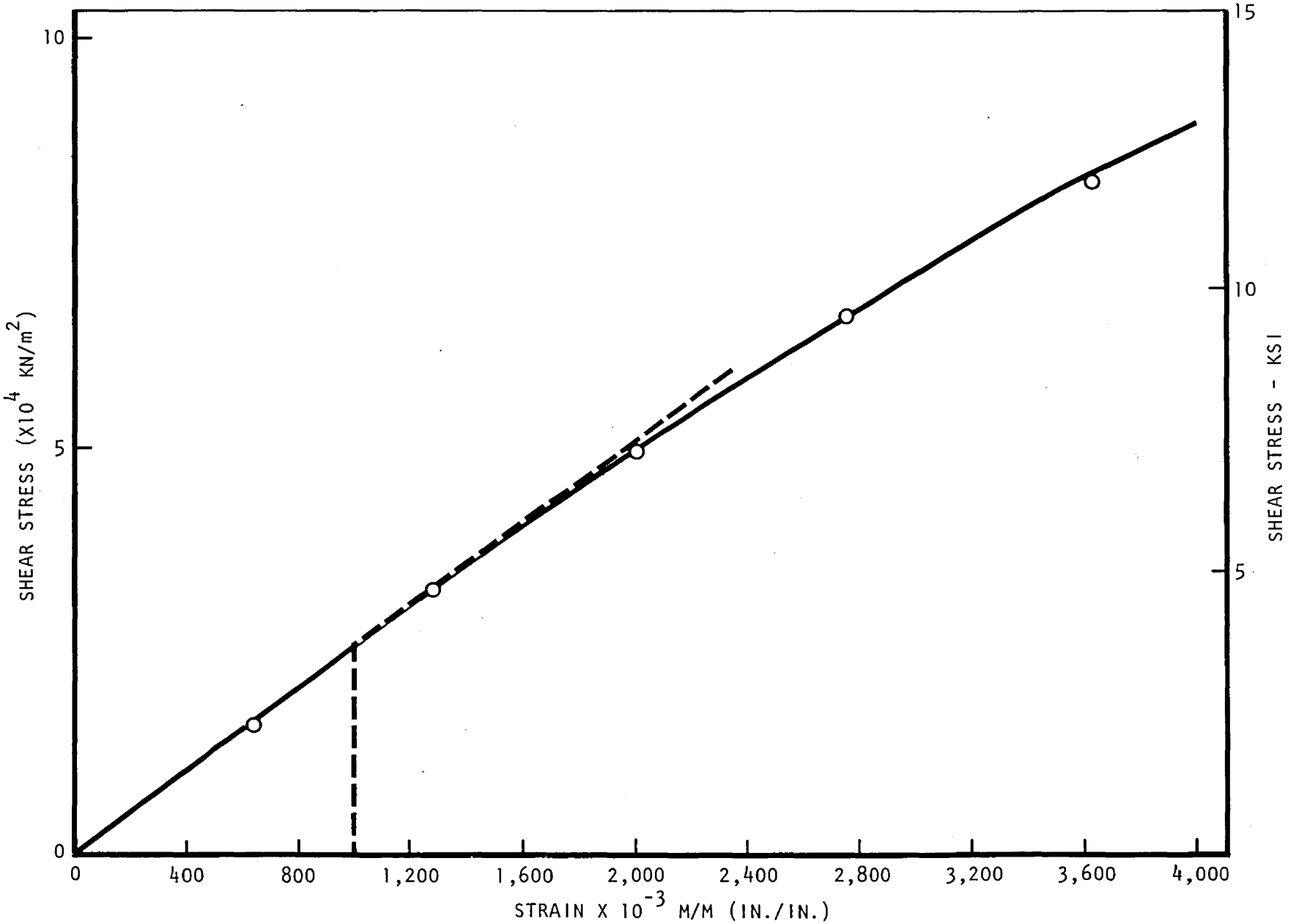

Figure 99. Shear Stress-Strain Curve

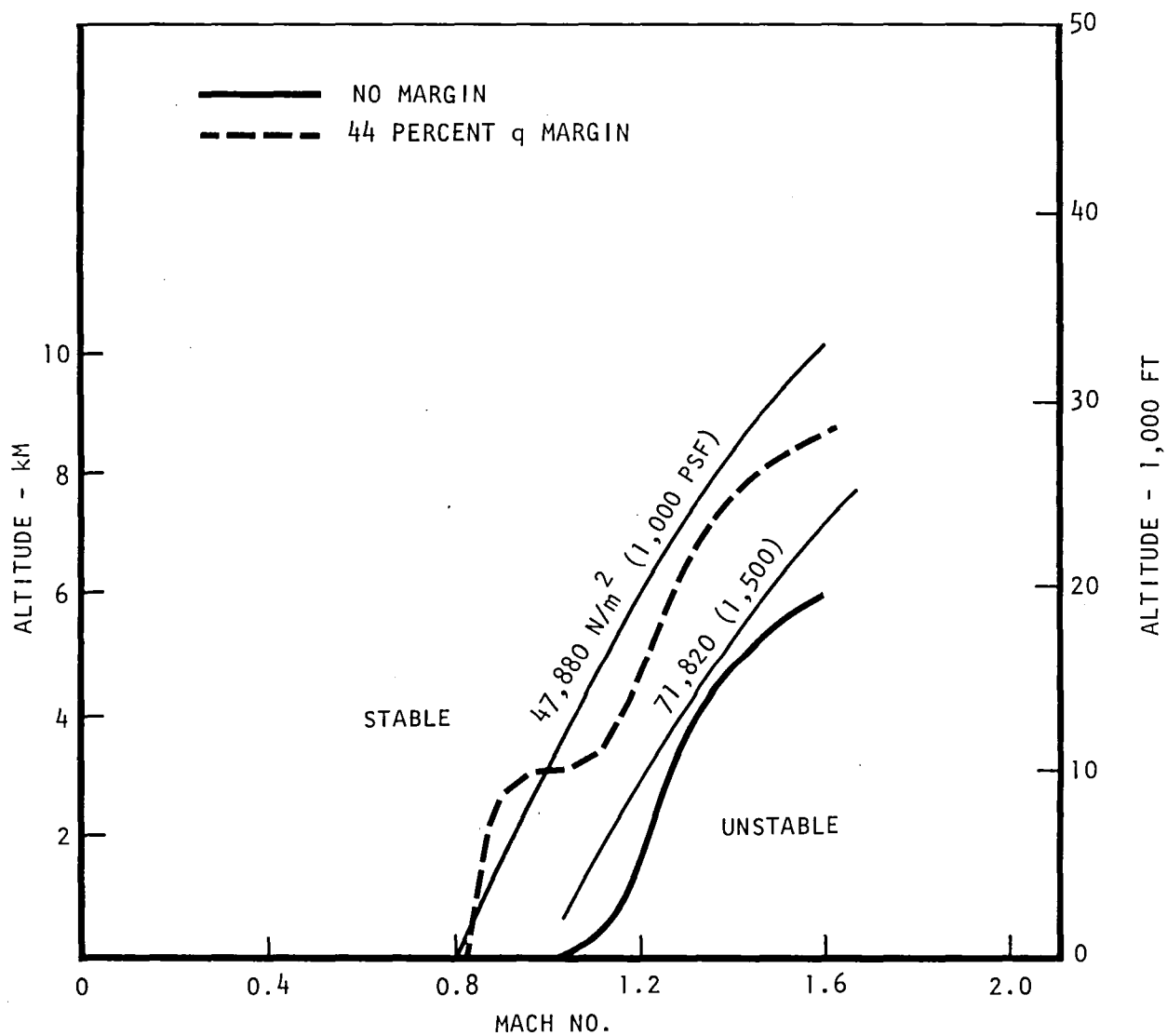

Figure 100. Flutter Limit for the Unballasted Configuration

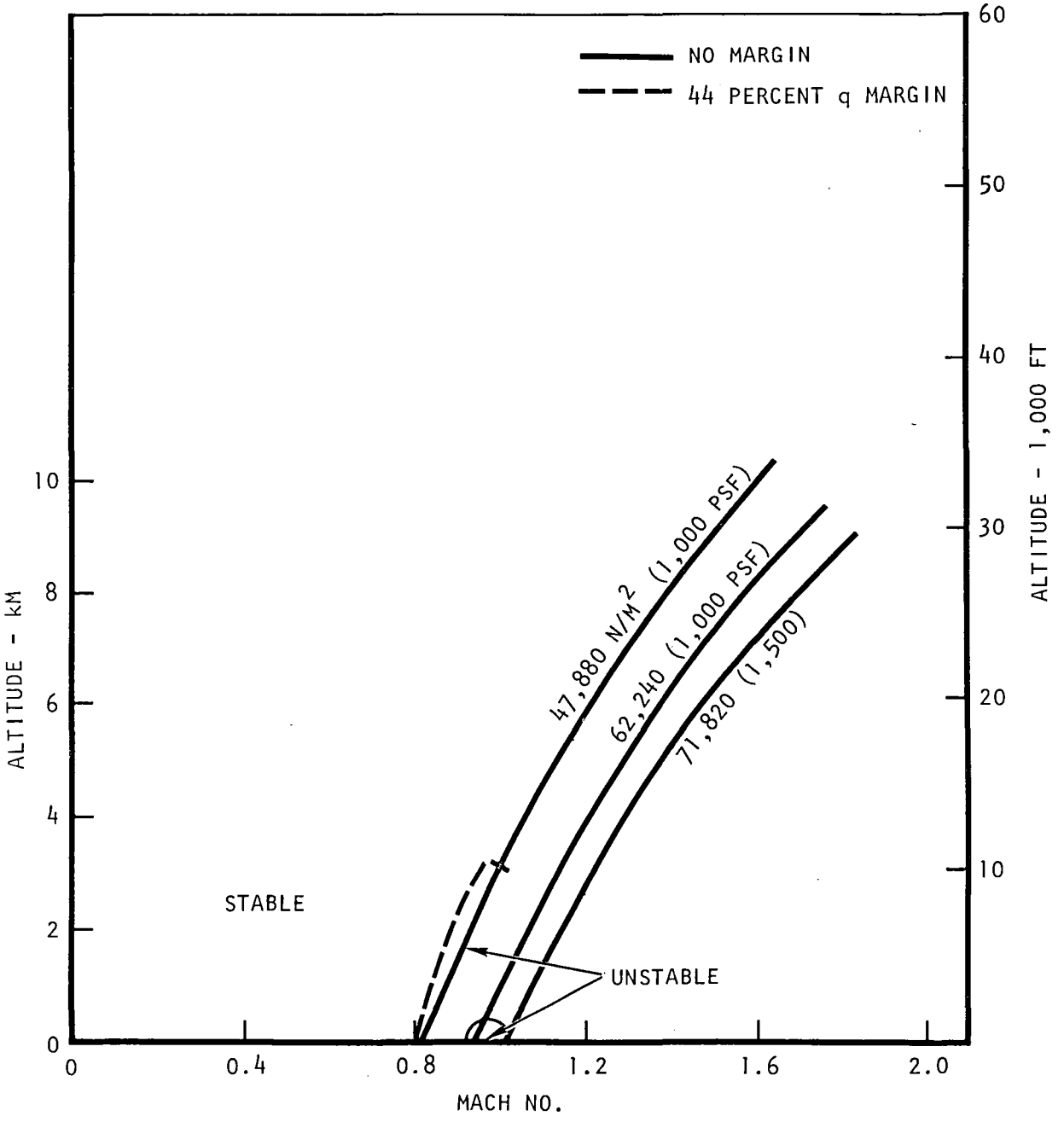

Figure 101. Flutter Limit for the Ballasted Configuration

1. Report No.	2. Government Accession No.	3. Recipient's Catalog No.
NASA CR-144886		

4. Title and Subtitle	5. Report Date
HiMAT STRUCTURAL DEVELOPMENT DESIGN METHODOLOGY	October 1979
	6. Performing Organization Code

7. Author(s)	8. Performing Organization Report No.
M. A. Price	NA-79-3
	10. Work Unit No. 723-01-04

9. Performing Organization Name and Address	11. Contract or Grant No.
Rockwell International Corporation Los Angeles Aircraft Division Los Angeles, California 90009	NAS4-2560
	13. Type of Report and Period Covered Contractor Report - Final

12. Sponsoring Agency Name and Address	14. Sponsoring Agency Code
National Aeronautics and Space Administration Washington, D.C. 20546	H-1103

15. Supplementary Notes

NASA Technical Monitor: Paul C. Loschke, Dryden Flight Research Center

16. Abstract

Two graphite-epoxy research aircraft were developed and built by Rockwell International in order to explore the highly maneuverable aircraft technology (HiMAT) area for NASA/Dryden Flight Research Center (DFRC). In order to improve aerodynamic performance, a twist criterion was used to design the canard and wing lifting surfaces. In order to meet that twist criterion, the lifting surfaces were tailored using graphite-epoxy tape. The outer surface of the aircraft is essentially constructed of 95% graphite epoxy materials.

This report presents the analytical tools and methodology used to design those lifting surfaces. In addition, one aircraft was subjected to an 8g ground test. The test was conducted in order to verify structural integrity and to determine how well the desired twist was achieved. This report presents those test results, including a discussion of the reductions of both flight and ground strain test gages and their associated stresses.

17. Key Words (Suggested by Author(s))	18. Distribution Statement
HiMAT structure Graphite-epoxy composites Aeroelastic tailoring	Unclassified—Unlimited STAR Category: 05

19. Security Classif. (of this report)	20. Security Classif. (of this page)	21. No. of Pages	22. Price*
Unclassified	Unclassified	238	

For sale by the National Technical Information Service, Springfield, Virginia 22161